Measurements and modelling of shelf sea productivity using oxygen-argon ratios and oxygen triple isotopes

A thesis submitted to the School of Environmental Sciences at the

University of East Anglia in partial fulfilment of the requirements for the degree of

Doctor of Philosophy

Francesco Pallottino

December 2022

I. Abstract

This thesis provides net (N) and gross (G) oxygen production estimates for North Sea surface waters during late summer 2019. Net production rates ($N(O_2/Ar)$) were based on the O_2/Ar saturation anomaly $\Delta(O_2/Ar)$, while triple oxygen isotopes were used as tracer for gross production ($G(^{17}O)$). The research revealed that on average, surface waters were in metabolic balance ($N(O_2/Ar)$ = (–3±40) mmol m^{-2} d^{-1}). Stations located closest to UK coasts were net heterotrophic ($N(O_2/Ar)$ = (–29±21) mmol m^{-2} d^{-1} < 0) despite high $G(^{17}O)$ values of (500±90) mmol m^{-2} d^{-1}. This result suggests strong remineralisation occurring in the area.

Using a modelling approach, this thesis also investigated the robustness of the steady-state assumption for net and gross production estimates in a shelf sea environment. Station L4 (Western English Channel), was used as case study. Results showed that the steady-state approach can be improved by using a repeat discrete sampling strategy to estimate as non-steady-state contributions to $G(^{17}O)$ and $N(O_2/Ar)$ and reduce the prediction error by 53 % and 75 %, respectively. We also used model simulations to investigate the impact of phytoplankton species-specific isotope effects in photosynthesis on diagnosed $G(^{17}O)$. We found that neglecting these isotope effects can cause a small systematic overestimate of $G(^{17}O)$, rising to up to +50 % during the spring bloom at Station L4. Taken together, these results can be used to design observational studies aimed at determining $G(^{17}O)$ and $N(O_2/Ar)$ in dynamic shelf-sea environments like Station L4.

II. Table of contents

I. Abstract 2

II. Table of contents 3

III. List of figures 6

IV. List of tables 11

V. Acknowledgements 12

Chapter 1: Introduction 14

1.1 Conservation regulations for shelf-sea ecosystems 14

1.2 Ocean carbon pump and community production 15

1.3 Estimating community production from water sample measurements 17

1.3.1 Frequently used *in vitro* methods 17

1.3.2 Frequently used *In-situ* methods 18

1.4 Implications for this study 22

1.5 Aims of this thesis 22

Chapter 2: Measurements of pelagic net metabolic rates in the North Sea 24

2.1 Abstract 24

2.2 Introduction 25

2.3 Aims 27

2.4 Methods 27

2.4.1 Sampling strategy 27

2.4.2 Experimental procedure 29

2.4.3 Calculations and calibrations 30

2.4.3.1 Calibration of the RINKO optode using discrete dissolved oxygen data 30

2.4.3.2 Correction of $\delta(^{i}O)$ for dual-inlet pressure imbalance 31

2.4.3.3 Correction of $\delta(^{i}O)$ for N_2 interference 33

2.4.4 O_2/Ar from IRMS discrete samples 34

2.4.5 Dry air and water saturated air calibration for $\delta(^{i}O)$ and Δ (O_2/Ar) 35

2.4.6 Calculating $^{17}\Delta$ from IRMS discrete samples 36

2.4.7 Air-sea gas exchange, gas transfer velocity and wind speed 37

2.5 Results 41

2.5.1 Temperature, salinity, and stratification: 41

2.5.2 Dissolved oxygen concentration, supersaturation, and air-sea exchange: 48

2.5.3 Results from MAT 253 analyses: $G(^{17}O)$ and $N(O_2/Ar)$ 50

2.6 Discussion 55

2.6.4 North Sea hydrography and oxygen cycling in late summer 2019 55

2.6.4.4 North Sea metabolic rates in late summer 2019 57

2.6.4.5 Fully mixed coastal waters 57
2.6.4.6 Stratified waters in the southern North Sea 58
2.6.4.7 Stratified waters in the central and northern North Sea 60
2.7 Conclusions 61
Chapter 3: Using the ERSEM model to determine best practice for net community production measurements at station L4, Western English Channel 63
3.1 Abstract 63
3.2 Introduction 65
3.3 Aims 67
3.4 Methods 67
3.4.1 Study Area 67
3.4.2 The ERSEM-FABM-GOTM model 68
3.4.2.1 The marine ecosystem model: ERSEM 68
3.4.2.2 Argon 69
3.4.2.3 Numerics 70
3.4.2.4 Simulation setups 73
3.4.3 Calculating *N* from the biological oxygen saturation anomaly 75
3.4.3.1 $F_{bio}(O_2/Ar)$: the net air-sea gas exchange of biologically processed oxygen 75
3.4.3.2 $F_n(O_2/Ar)$: the time disequilibrium of biological oxygen 77
3.4.3.3 $F_v(O_2/Ar)$: the vertical diffusion of biological oxygen 78
3.4.4 Post processing calculations for $N(O_2/Ar)$ and N(ERSEM) 78
3.4.4.1 $F_{bio}(O_2/Ar)$: the air-sea gas exchange component 79
3.4.4.2 $F_n(O_2/Ar)$: the time disequilibrium term 80
3.4.4.3 $F_v(O_2/Ar)$: the vertical diffusive mixing term 80
3.4.4.4 Model evaluation against observations 80
3.4.5 Experimental procedure 81
3.4.5.1 Q1: uncertainties derived from steady-state assumption 82
3.4.5.2 Q2: $N(O_2/Ar)$ sensitivity to integration depth in shallow dynamic waters 82
3.4.5.3 Q3: Determination of the optimal sampling interval 82
3.5 Results 84
3.5.1 Model evaluation against observed dataset at L4 84
3.5.2 Evaluating the diagnostic model ($N(O_2/Ar)$) in post processing calculations: N(ERSEM) vs $N(O_2/Ar)$ 93
3.5.3 Q1: uncertainties derived from steady-state assumption 95
3.5.3.4 Assuming steady-state during the growing season 96
3.5.3.5 Assuming *N* in steady-state during winter 101
3.5.3.6 Assuming steady-state at coarser sampling frequency 104

3.5.4 Q2: $N(O_2/Ar)$ sensitivity to integration depth in shallow dynamic waters 106
3.5.5 Q3: $N(O_2/Ar)$ model sensitivity to the sampling interval and sampling error. . 110
3.6 Discussion 117
3.6.1 Q1: uncertainties derived from steady-state assumption 117
3.6.2 Q2: $N(O_2/Ar)$ sensitivity to integration depth in shallow dynamic waters. 118
3.6.3 Q3: $N(O_2/Ar)$ model sensitivity to sampling intervals and sampling error. 118
3.7 Conclusions 119
Chapter 4: Chapter 4: Using the ERSEM model to simulate gross production with oxygen triple isotopes at L4, Western English Channel 121
4.1 Abstract 121
4.2 Introduction 122
4.3 Aims 124
4.4 Methods 125
4.4.1 The ERSEM-FABM-GOTM model 125
4.4.2 Notations and definitions in isotopic calculations: 125
4.4.3 Adding Oxygen isotopes ^{16}O, ^{17}O and ^{18}O to ERSEM 126
4.4.3.1 Fractionation during biological processes: 129
4.4.3.2 Contribution of temporal changes in isotopic composition to $G(^{17}O)$: 130
4.4.3.3 Contribution of vertical diffusive mixing to $G(^{17}O)$: 130
4.4.4 Post-processing calculations for G(ERSEM) and $G(^{17}O)$ 130
4.4.4.1 $F_{bio}(^{17}O)$: the air-sea gas exchange component 132
4.4.4.2 $F_n(^{17}O)$: the time disequilibrium term 132
4.4.4.3 $F_v(^{17}O)$: the vertical diffusive mixing term 132
4.4.5 Experimental procedure 133
4.4.5.1 Q1: uncertainties derived from steady-state assumption at L4 133
4.4.5.2 Q2: $G(^{17}O)$ sensitivity to the integration depth at L4…….. 133
4.4.5.3 Q3: Determination of the optimal sampling interval 133
4.4.5.4 Q4: uncertainty derived from oxygen fractionation during photosynthesis. 135
4.5 Results 137
4.5.1 Diagnostic model performance 137
4.5.2 Q1: uncertainties derived from steady-state assumption at L4 139
4.5.3 Q2: Influence of integration depth on $G(^{17}O)$ at L4 142
4.5.4 Q3: Determination of the optimal sampling interval 145
4.5.5 Q4: uncertainty derived from oxygen fractionation during photosynthesis 150
4.6 Discussion 155
4.6.1 Q1: Uncertainties derived from steady-state assumption at L4 155
4.6.2 Q2: $G(^{17}O)$ sensitivity to integration depth in shallow dynamic waters 156

4.6.3 Q3: Determination of the optimal sampling interval..... 156
4.6.4 Q4: Uncertainty from photosynthetic oxygen fractionation..... 157
4.7 Conclusions..... 158
4.7.1 Q1: Uncertainties derived from steady-state assumption at L4..... 158
4.7.2 Q2: $G(^{17}O)$ sensitivity to integration depth in shallow dynamic waters..... 158
4.7.3 Q3: Determination of the optimal sampling interval..... 158
4.7.4 Q4: Uncertainty from photosynthetic oxygen fractionation..... 159
4.7.5 Future remarks..... 159
Chapter 5: Conclusions and future work..... 160
5.1 Measurements of net and gross metabolic rates in the North Sea..... 160
5.1.1 Research questions and summary of the results..... 160
5.1.2 Future work..... 161
5.2 Using the ERSEM model to determine best practice for net and gross community production measurements at station L4, Western English Channel..... 161
5.2.1 Research questions and summary of the results..... 161
5.2.2 Future work..... 163
References..... 164

III. List of figures

Figure 1: Schematic of *in-vitro* and *in-situ* methods estimating marine net and gross community production. 21

Figure 2: North Sea map showing the position of the sampling stations measured between August and September 2019. 29

Figure 3: Linear regression analysis used to calibrate the oxygen optode used in the North Sea. 31

Figure 4: Illustration of a classic dual inlet mass spectrometer. 32

Figure 5: The linear regression analysis used for the mass spectrometer imbalance test. 33

Figure 6: The linear regression analysis used to correct the effects of N_2 contamination on $\delta(^{17}O)$ and $\delta(^{18}O)$ in the mass spectrometer ion chamber..... 34

Figure 7: A North Sea map showing the cruise track and wind speed measurements.. 39

Figure 8: A comparison of ERA5 and ship observed wind speeds along the time dimension. 40

Figure 9: Linear regression analysis between wind speeds measured in this survey with ERA5 data.. 41

Figure 10: A comparison between measured temperature and matching values from the North Sea Biogeochemical Climatology (NSBC) 42

Figure 11: A comparison between measured salinity and matching values from the North Sea Biogeochemical Climatology (NSBC) 43

Figure 12: A North Sea map showing 2D interpolations of temperature and salinity. 44

Figure 13: Examples of T, S, $c(O_2)$, $\Delta(O_2)$ profiles in the fully mixed area of the southern North Sea and off Scotland 45

Figure 14: Examples of T, S, $c(O_2)$, $\Delta(O_2)$ profiles for the stratified areas in the southern North Sea with water columns deeper than 30 m 46

Figure 15: Examples of T, S, $c(O_2)$, $\Delta(O_2)$ profiles for the stratified areas showing salinity reversals and $c(O_2)$ maximum at thermocline depths 46

Figure 16: Examples of T, S, $c(O_2)$, $\Delta(O_2)$ profiles for the stratified waters in the central and northern North Sea.. 47

Figure 17: A North Sea map showing 2D interpolations of water stratification. 47

Figure 18: A comparison between measured dissolved oxygen concentrations and matching values from the North Sea Biogeochemical Climatology (NSBC) 48

Figure 19: A North Sea map showing 2D interpolations of dissolved oxygen concentrations and supersaturations. 50

Figure 20: A North Sea map showing 2D interpolations of air-sea gas exchange of O_2 and oxygen gas transfer velocity. 50

Figure 21: $\delta(^{18}O)$ and $^{17}\Delta$ vs sampling depth, and $\delta(^{17}O)$ vs $\delta(^{18}O)$.. 51

Figure 22: $^{17}\Delta$ and $\Delta(O_2/Ar)$ vs depth. 52

Figure 23: $\Delta(O_2/Ar)$ vs $^{17}\Delta$. 53

Figure 24: A North Sea map showing 2D interpolations of $\delta(^{18}O)$ and $^{17}\Delta$. 53

Figure 25: A North Sea map showing 2D interpolations of $N(O_2/Ar)$ and $G(^{17}O)$ estimates. . 55

Figure 26: Schematic of the ERSEM model including the addition of argon made in this study. 69

Figure 27: ERSEM-FABM-GOTM time and space organisation, discretisation, and sign convention. 73

Figure 28: Vertical discretisation setup used for model simulations. 74

Figure 29: Robust target diagram representing overall model validation. 84

Figure 30: A time series showing modelled and observed temperature at various depths. 86

Figure 31: A time series showing modelled and observed salinity at various depths. 87

Figure 32: A time series showing modelled and observed dissolved oxygen concentration at various depths. 89

Figure 33: A time series showing modelled and observed dissolved argon concentration at various depths. 90

Figure 34: A time series showing modelled and observed oxygen supersaturation at various depths. 91

Figure 35: A time series showing modelled and observed argon supersaturation at various depths. 92

Figure 36: A time series showing modelled and observed biological oxygen supersaturation at various depths. 93

Figure 37: A time series and residuals comparing N(ERSEM) to $N(O_2/Ar)$. 95

Figure 38: Time series and Hovmoller for simulated $N(O_2/Ar)$, N(ERSEM), photosynthetic active radiation, net primary production, and heterotrophic respiration, during late spring 2010 at Station L4. 97

Figure 39: Time series and Hovmoller for simulated $N(O_2/Ar)$, N(ERSEM), windspeeds, vertical turbulent diffusivity and biological oxygen supersaturation, during late spring 2010 at Station L4. 98

Figure 40: A time series showing prediction error derived by the steady-state assumption (N(ERSEM) = $F_{bio}(O_2/Ar)$ - $F_v(O_2/Ar)$) during late spring 2010. 100

Figure 41: Time series and Hovmoller for simulated $N(O_2/Ar)$, N(ERSEM), photosynthetic active radiation, net primary production, and heterotrophic respiration, during winter at Station L4 101

Figure 42: Time series and Hovmoller for simulated $N(O_2/Ar)$, N(ERSEM), windspeeds, vertical turbulent diffusivity and biological oxygen supersaturation, during winter at Station L4.. 102

Figure 43: A time series showing prediction error derived by the steady-state assumption (N(ERSEM) = $F_{bio}(O_2/Ar)$ - $F_v(O_2/Ar)$) during winter..... 103

Figure 44: A time series showing prediction error derived by the steady-state assumption (N(ERSEM) = $F_{bio}(O_2/Ar)$ - $F_v(O_2/Ar)$) from 2009 until 2011. Sampling intervals are 7 days long. N(ERSEM) is averaged at each sampling interval using the values of the previous week..... 105

Figure 45: Month-by-month box model for $N(O_2/Ar)$ (in grey) and its constituent terms such as air-sea flux ($F_{bio}(O_2/Ar)$ in blue), vertical diffusivity ($F_v(O_2/Ar)$ in red) and time disequilibrium ($F_n(O_2/Ar)$ in green). 109

Figure 46: Direct timeseries comparison between time averaged N(ERSEM) ($N_{\Delta t}$(ERSEM)) and $N(O_2/Ar)$ calculated from subsampled at various intervals ($N_{\Delta t}(O_2/Ar)$) : every minute, hour, day, week and 21 days.. 111

Figure 47: Direct timeseries comparison between $N_{\Delta t}$(ERSEM) and $N_{\Delta t}(O_2/Ar)$ calculated from concentrations affected by experimental random error 113

Figure 48: A bar plot showing the optimal sampling strategy for $N_{\Delta t}(O_2/Ar)$ at Station L4. 114

Figure 49: A bar plot showing the seasonal optimal sampling strategy for $N_{\Delta t}(O_2/Ar)$ at Station L4. 115

Figure 50: A time series showing why random sampling error majorly affects estimates based on high resolution data 116

Figure 51: Schematic of the ERSEM model including the addition of oxygen isotopes ^{17}O and ^{18}O made in this study. 128

Figure 52: Application of experimental error to oxygen concentrations showing the effects on concentrations, $\delta(^{i}O)$ values and $^{17}\Delta$. 135

Figure 53: Hovmoller plots showing the succesful implementation of triple oxygen isotope scheme within ERSEM. 138

Figure 54: A time series showing prediction error derived by the steady-state assumption (G(ERSEM) = $F_{bio}(^{17}O)$ - $F_{v}(^{17}O)$) during late spring 2010. 140

Figure 55: A time series showing prediction error derived by the steady-state assumption (G(ERSEM) = $F_{bio}(^{17}O)$ - $F_{v}(^{17}O)$) from 2009 until 2011. Sampling intervals are 7 days long. 141

Figure 56: Month-by-month box model for $G(^{17}O)$ and its constituent terms such as air-sea flux ($F_{bio}(^{17}O)$), vertical diffusivity ($F_{v}(^{17}O)$) and time disequilibrium ($F_{n}(^{17}O)$). 144

Figure 57: A time series of G(ERSEM) and $G(^{17}O)$ over 5 years at different and increasing sampling intervals. 146

Figure 58: A time series of G(ERSEM) and $G(^{17}O)$ over 5 years at different and increasing sampling intervals where $G(^{17}O)$ is calculated using oxygen concentrations affected by random experimental error.. 147

Figure 59: A bar plot showing the annual optimal sampling interval for $G(^{17}O)$ at Station L4. 148

Figure 60: A bar plot showing the seasonal optimal sampling interval for G(17O) at Station L4.. 149

Figure 61: A time series showing why random sampling error majorly affects estimates based on high resolution data. 150

Figure 62: Effects of group specific $\delta_P(^iO)$ values on modelled $^{17}\Delta$. Where the diatom group was assigned a photosynthetic fractionation factor 152

Figure 63: Effects of group specific $\delta_P(^iO)$ values on $G(^{17}O)$. Where the diatom group was assigned a photosynthetic fractionation factor. 153

Figure 64: Effects of group specific $\delta_P(^iO)$ values on $G(^{17}O)$. Where all photosynthetic functional group was assigned a different photosynthetic fractionation factor 154

IV. List of tables

Table 1: Analyses of dry air against working reference in this study compared with results of Seguro (2017) 35

Table 2:Coefficients and check result (at 20 °C) for the Schmidt numbers of O_2 and Ar (Wanninkhof, 2014). 38

Table 3: Physical properties of N_2, Ar, and O_2 in sea water 76

Table 4: Summary statistics for the overall net oxygen production from oxygen argon ratios ($N(O_2/Ar)$) 107

Table 5: Summary statistics for the terms composing $N(O_2/Ar)$ 108

Table 6: Isotopic composition of photosynthetic O_2 assigned to ERSEM functional groups 136

Table 7: Summary statistics for $G(^{17}O)$ 142

Table 8: Summary statistics for the terms composing $G(^{17}O)$ 143

V. Acknowledgements

“M'affaccio alla finestra, e vedo il mare:

vanno le stelle, tremolano l'onde.

Vedo stelle passare, onde passare:

un guizzo chiama, un palpito risponde.

Ecco sospira l'acqua, alita il vento:

sul mare è apparso un bel ponte d'argento.

Ponte gettato sui laghi sereni,

per chi dunque sei fatto e dove meni?”

“I look out my window, I see the sea:

a flitting of stars, a quivering of waves.

I see stars passing, waves passing;

a flicker calls, a throb replies.

Now the water sighs, the winds exhales:

on the sea a silver bridge appears.

Bridge thrown over silent lakes,

for whom are you made, where do you lead?”

Giovanni Pascoli, from Myricae (1891)

I would like to dedicate this poem to my supervisors: Jan, James, Sue, Johan, and Gennadi. I am grateful for all their individual contribution and guidance during my PhD. All my gratitude goes to James and Jan. I now consider them both my mentors and friends. Without their enthusiasm for science and guidance this piece of work would not have been completed. I would like to thank Sue for helping me organising my sampling campaign in the North Sea and always spending a word of comfort during periods of low morale, and for cheering the accomplishments. Thanks to Johan and his wise comments I was able to untangle the *operator splitting dilemma* afflicting my calculations for years. A particular thanks goes to Gennadi especially during my early years for helping me on my several (and always googleable) questions on python and Fortran code. I am particularly grateful to Alina for patiently teaching me how to operate a mass spectrometer. Alina, I promise I will not break the gas separation line again! I would like to thank all the staff that was working on the RV Cefas Endeavour Survey CEND12/19, and all my colleagues and superiors working at Plymouth Marine Laboratory.

Most importantly all my gratitude goes to Valeria, Ettore, and Carlo. You are my silver bridge thrown over the sea, leading to a future made of happiness and joy.

Chapter 1: Introduction

1.2 Conservation regulations for shelf-sea ecosystems

Shelf seas cover about 7 % of the world's ocean surface area and have disproportionate importance in terms of resources, biogeochemistry, and human impact compared to the open oceans. Biogeochemical processes impacting the carbon cycle such as primary production, remineralisation, and sediment burial are enhanced in shelf seas, so that they represent 10 to 30 % of all marine primary production, 30 to 50 % of total inorganic carbon burial and 80 % of organic carbon burial (Sharples et al., 2019). Consequently, shelf seas play a key role in marine productivity, sustaining 90 % of global fish catches (Pauly et al., 2002).

Human activity causing environmental degradation of shelf seas, for example through fishing, shipping and pollution is a global concern (Halpern et al., 2015; Harris, 2020; Bastardie et al., 2021). Extensive urbanisation threatens shelf sea ecosystems through processes such as anthropogenic nutrient enrichment, especially in developed agricultural regions such as in Europe (Topcu and Brockmann, 2015). Formation of harmful algal blooms (HABs) such as red tides, bottom water oxygen deficiency, mass mortality of benthic fauna and fish are also linked to anthropogenic fertilisation of coastal environments (Glibert et al., 2010, 2014) causing severe economic loss in regions such as the Greater North Sea, the Baltic Sea, the Black Sea and the Adriatic Sea (Diaz and Rosenberg, 2008). In Europe, the growing problem of coastal pollution has led to the formulation of marine and coastal ecosystem-based risk and management assessments (ERA and EMA respectively) (e.g., Linkov et al., 2006; Ferreira et al., 2011; Pinkau and Schiele, 2021), which have led to the development of monitoring programmes in regions considered to be as at risk. Policy drivers include international agreements such as the 1982 Oslo-Paris Convention for the Protection of the North Atlantic (OSPAR Commission, 2003) and European Directives such as the Water Framework Directive (EU, 2000), and the Marine Strategy Framework Directive (EU, 2008). These are typically transcribed into national law, and implemented by government institutions (Bean et al., 2017). In the UK, for example, by the Department for Environment, Food and Rural Affairs (DEFRA) and agencies such as the Environment Agency and Natural England (Johnson, 2008; Boyes and Elliott, 2014) as well as the devolved administrations of Northern Ireland, Scotland and Wales. Under

the Water Framework Directive, River Basin Management Plans are focused on nutrient reduction plans and based on the assumption of reversibility, which means that ecosystem functioning can reverse back to reference conditions (Duarte et al., 2009). Therefore, studies on the sensitivity of marine systems, internal buffers and historical environmental baselines are essential to conserve biodiversity, preserve environmental health and restore ecosystem functioning (Steckbauer et al., 2011).

1.3 Ocean carbon pump and community production

The term ocean biological pump refers to the flux of CO_2 from the atmosphere to ocean surface water and to the subsequent storage of carbon into the deep ocean, mediated by direct or indirect biological activity. The biological ocean pump can be divided into two distinct processes namely the soft-tissue pump and the carbonate pump (Volk and Hoffert, 2013). The carbonate pump refers to the biological formation of hard structures made out of calcium carbonate ($CaCO_3$), which releases CO_2 as by-product:

$$Ca^{2+} + 2\,HCO_3 \leftrightarrow CaCO_3 + CO_2 + H_2O \quad (1)$$

The soft-tissue pump refers to the sequestration of CO_2 via photosynthesis:

$$CO_2 + H_2O \leftrightarrow CH_2O + O_2 \quad (2)$$

The two reactions have opposing effects on atmospheric CO_2, where over a time scale of thousands of years the soft tissue pump lowers atmospheric CO_2 while the carbonate pump raises it (Sarmiento and Gruber, 2006). The carbonate pump will not be considered further in this thesis.

The soft-tissue pump is quantified in terms of net community production (N). N is defined as the balance between primary production (P), which is the net production rate of biomass from inorganic molecules (Eq. (2), forward) done by phytoplankton and heterotrophic respiration (R_H), which is the consumption rate of organic material releasing inorganic carbon (Eq. (2), backward) done by grazers and decomposers (Falkowski and Raven, 2007):

$$N = P - R_H \quad (3)$$

When N is positive the whole ecosystem community is net autotrophic, meaning that rates of photosynthesis exceed rates of respiration. On the other hand, when N is

negative the total respiration is greater than the photosynthesis and CO_2 is released into the environment (net heterotrophy).

Autotrophs (e.g., phytoplankton) also contribute to the total community respiration releasing CO_2. Therefore, primary production needs to be defined as the balance between gross primary production (G) and autotrophic respiration (R_A):

$$P = G - R_A \tag{4}$$

During photosynthesis, CO_2 is consumed (fixation) while O_2 is released into the environment as a by-product. These processes can be written in terms of carbon, or in terms of oxygen, and that the latter will be used here. This means that rates of gross primary production can be theoretically quantified by measuring the O_2 released into the environment, and in this case, G refers to the gross oxygen production. Using the same principle, N can also be quantified in oxygen equivalent and in this form is also referred as net oxygen production.

There are some practical details that need to be addressed to make accurate oxygen-based quantification of N, however. The biological proportion of the oxygen concentration dissolved in seawater need to be isolated from its physical counterpart (e.g., concentration change via bubble injection or due to temperature change) (Cassar et al., 2021). Furthermore, there are some water-splitting, oxygen-producing reactions such as the Mehler reaction that do not lead to carbon fixation and reduce oxygen forming hydrogen peroxide (Mehler, 1951), which need to be taken into consideration when estimating N and G from oxygen concentrations (e.g., Laws et al., 2000; Luz et al., 2002).

At a global scale, N has significant impacts on the dissolved oxygen and carbon dioxide content of the oceans and their respective fluxes with the atmosphere (Sarmiento and Gruber, 2006). At an ecosystem scale, N controls food production and energy levels across the planktonic communities of the microbial food web (Williams, 1981; Ducklow and Harris, 1993; Gaichas et al., 2009). However, key processes affecting pelagic metabolic rates, and their importance and effect on observed biological and ecosystem trends are still unclear. Over the past few decades, methods have been developed to measure gross and net community production, using either *in-vitro* or *in-situ* techniques. A brief overview of these methods is given below.

1.4 Estimating community production from water sample measurements: *in-vitro vs in-situ*

Accurate estimates of marine biological activity are important for monitoring and protecting shelf sea environments. Estimating *G* and *N* not only provides information on ecosystem community energy transfer and biogeochemical cycling of carbon and oxygen but also helps evaluate the health status of monitored regions (OSPAR Commission et al., 2017). Community production can not be measured directly but can be estimated from measurements of primary production and respiration.

Primary production can be measured using several differing methods. Each method has its own constituent assumptions and representation of primary production, which can lead to inconsistency in the results when compared to one another. In this section we focus on methodologies based on the direct measurements of tracers dissolved in water samples and deliberately exclude remote-sensing based observational methods. The methodologies used for estimates of *G* or *N* based on the analysis of water samples can be divided into 2 major groups: *in-vitro* and *in-situ* observations. *In-vitro* approaches extract a plankton community into a confined environment and observe rates of production and/or consumption in a controlled environment. These experiments provide local instantaneous primary production rates, which tend to miss episodic phenomena such as algal blooms due to their heterogeneous distribution in time and space. *In-situ* observations can directly measure marine productivity integrated on spatial and temporal scales from the natural habitats and can therefore provide a broader view of marine primary production.

1.4.1 Frequently used *in vitro* methods

Frequently used *in-vitro* methods include the ^{14}C method, the light and dark bottle oxygen method, and the ^{18}O method. The ^{14}C method refers to estimates of *P* based on algal assimilation of artificially introduced ^{14}C ($P(^{14}C)$) as sodium bicarbonate ($NaH^{14}CO_3$) (Nielsen, 1952) (Figure 1). The ^{14}C-method assumes that the biological uptake of dissolved inorganic carbon (DIC) labelled with ^{14}C is proportional to the naturally occurring biological uptake of DIC composed of the most common carbon isotope ^{12}C. Therefore, uptake can be calculated knowing the amount ^{14}C introduced to label DIC, the amount of ^{14}C found in particulate organic matter (POC) formed at the end of production processes, and the concentration of DIC naturally occurring in the

sample water. However, $P(^{14}C)$ interpretations have often been controversial because the rates observed *in vitro* may not reflect the production rates occurring in the natural environments (e.g., Harris et al., 1989; Legendre et al., 1983). Depending on incubation times, the method measures neither G nor N but some rate in between. For example, zooplankton grazing, and bacterial consumption may be sources of error in interpreting ^{14}C uptake, since with the increasing time such processes increasingly include ingestion of ^{14}C. Furthermore, rates of grazing can be altered given the confined space of the bottle further increasing the consumption effect (Bender et al., 1987).

The light and dark bottle oxygen method has also been commonly used for the measurement of primary production in aquatic ecosystems (Gaarder, 1927). This method calculates primary production ($P_{LD}(O_2)$) as the difference between change of oxygen concentration in transparent bottles held in the light minus the change of oxygen in opaque bottles held in the dark. Community respiration (R) representing the sum of autotrophic and heterotrophic respirations ($R = R_A + R_H$), is measured as the integrated oxygen change occurring in the dark bottle $R_D(O_2)$. Gross primary production $G_L(O_2)$ can finally be calculated summing $P_{LD}(O_2)$ to $R\,(O_2)$ (Figure 1). This method is based on a similar basis to the ^{14}C method with the main difference being the tracer being measured, therefore also major uncertainties are shared between the two methods. More specifically bacterial growth on the glass surface of the bottles tends to overestimate respiration rates (Pratt and Berkson, 1959).

The ^{18}O method involves estimating G based on the measurements of photosynthetic release of the oxygen stable isotopologue (isotope molecule) $^{18}O^{16}O$ created when oxygen is split from ^{18}O labelled substrate water ($H_2{}^{18}O$) ($G(^{18}O)$) (Figure 1) (Bender et al., 1987). As for $P(^{14}C)$, and the dark-light bottle oxygen method, $G(^{18}O)$ suffers the same uncertainties associated with the bottle effect (Bender et al., 1987).

1.4.2 Frequently used *In-situ* methods

The development of *in-situ* techniques for the measurements of biogeochemical tracers for gross production and respiration started over 60 years ago with the study of diel evolution of oxygen concentrations in freshwater ecosystems (Odum, 1956). Estimates of net community production using seasonal cycles of oxygen were used for the first time in marine applications in the sub arctic Pacific Ocean surface mixed layer (Emerson, 1987). Similarly, net community production was also recently calculated

from the measurements of dissolved inorganic carbon (*N*(DIC)) (Possenti et al., 2021) (Figure 1). These methods involve predicting change of oxygen or DIC concentrations (*c*(DIC)) caused by physical processes such as water heating and cooling, which are derived by a mass balance model and measurements of water temperature. Then the overall tracer (*c*(O_2), or *c*(DIC)) concentration change is calculated based on *in-situ* measurements. The deviation between predicted and observed concentrations, when calculated over a sufficient amount of time, represents the oxygen flux caused by net community production. Today this approach has found proficient use in autonomous measuring systems profiling the water column from a moored station fixed in place (Bushinsky and Emerson, 2015) or moving along transect with sea gliders (Hull et al., 2021; Possenti et al., 2021). The major uncertainty derived from this approach is that the differentiation between physical and biological fluxes is empirical and not based on direct observations.

Measurements of other major atmospheric gases such as N_2, Ar, and Ne dissolved in sea water (in conjunction with dissolved O_2) became relevant for estimating marine productivity in the upper ocean (Emerson et al., 1991; Hamme and Emerson, 2006; Izett et al., 2018). Apart from O_2 the other gases are completely inert to biological activity. Their utility is represented by their physical properties. Physical properties of Ar and O_2 gas dissolved in sea water are so similar that Ar can be considered the abiotic analogue of O_2 (Craig and Hayward, 1987; García and Gordon, 1992; Hamme and Emerson, 2004). Simultaneous measurements of dissolved O_2 and Ar were able to separate the net biological community production (*N*(O_2/Ar)) (Figure 1) from physical fluxes excluding the need of analytical predictions.

In 1999 differences in isotopic ratios for the stable isotopes of oxygen (^{16}O, ^{17}O and ^{18}O) were detected between biologically processed oxygen (photosynthesis and respiration) and oxygen forming in the stratosphere (Luz et al., 1999). Photosynthesis (Guy et al., 1993) and respiration (Lane and Dole, 1956) are mass-dependent isotope reactions causing an enrichment of environmental ^{18}O and ^{17}O relative to ^{16}O, where ^{17}O enrichment is approximately half of ^{18}O (Luz et al., 1999). Oxygen forming in the stratosphere has equal ^{18}O and ^{17}O isotope ratios relative to ^{16}O due to the action of mass independent photochemical reactions (Luz et al., 1999). Therefore, the difference between the two reservoirs are represented by an excess of ^{17}O relative to ^{16}O ($^{17}\Delta$) in biogenic oxygen. $^{17}\Delta$ in conjunction with air-lake gas transfer velocity was then used

to calculate gross production (G (^{17}O)) over the Lake Tiberias (Israel) (Luz et al., 1999). The same method for gross production was then described for marine applications (B. Luz and Barkan, 2000) (Figure 1). Both $N(O_2/Ar)$ and $G(^{17}O)$ are routinely measured together and have received considerable attention in the past 20 years (Juranek and Quay, 2013). Both methods are centred around two main principles. Firstly, time-varying rates of change in dissolved O_2 concentrations need to be integrated over the O_2 residence time in surface waters. Therefore, both methods require knowledge of the gas exchange rates at the air-sea interface and at the mixed layer depth. Secondly, both methods separate O_2 concentrations into different fractions based on the concentration of analogues to O_2, such as argon (Ar), or O_2 isotopologues (Figure 1).

$G(^{17}O)$ and $N(O_2/Ar)$ methods offer important advantages over the other methods introduced above (Juranek and Quay, 2013). They are *in-situ* tracers, thus do not require isotopic labelling and are not subject to the bottle effect. Samples for the two methods are usually taken simultaneously into discrete water samples collected from conductivity, temperature, and depth (CTD) hydro casts. Samples are analysed via dual-inlet isotope ratio mass spectrometry (IRMS) (Ghosh and Brand, 2003) after the research cruise (Seguro Requejo, 2017). $HgCl_2$ spiked into the sampling bottles, stops all biological activity within the samples and preserves the *in-situ* condition encountered at the time of the sampling (Emerson et al., 1991). Alternatively, $N(O_2/Ar)$ can be measured continuously using a membrane-inlet mass spectrometer (MIMS) (Davey et al., 2011) connected to a ship's underway sampling system producing high frequency real-time N estimates over the research vessel's track (Kaiser et al., 2005; Cassar et al., 2009; Hamme et al., 2012). This approach offers basin-wide estimates of plankton community metabolism including rare episodic blooms at the time of the survey. The ratio between $N(O_2/Ar)$ and $G(^{17}O)$ can be compared with the fraction of new production in P although it is not identical to it (Juranek and Quay, 2013). New production is primary production fuelled by new nitrogen sources (nitrate), while recycled/regenerated production is fuelled by nitrogen-based nutrients recycled by local remineralization of organic material (Seguro et al., 2019).

Despite the many advantages offered by $N(O_2/Ar)$ and $G(^{17}O)$ methods, today there are few applications in dynamic systems such as shelf seas (e.g., Gloël, 2012; Seguro et al., 2019; Smith et al., 2021; Zhu et al., 2021; Jurikova et al., 2022). Both $G(^{17}O)$ and $N(O_2/Ar)$ are usually based on the assumption that biologically processed oxygen

($c_{\mathrm{bio}}(O_2)$) dissolved in surface waters is in steady-state ($\frac{dc_{\mathrm{bio}}(O_2)}{dt} = 0$). When the steady-state assumption is not violated the flux of biological oxygen crossing the air-sea interface (F_{bio}) is equal to G and N respectively. This also entails the assumption that $c_{\mathrm{bio}}(O_2)$ is not affected by water transport. System steady-state is often assumed because measurements are taken along cruise tracks where stations are not repeated with enough intervals to calculate time disequilibrium. Assuming steady-state can be valid in the surface mixed layer of regions where the water column is permanently stratified, and the measured signals are not affected by vertical and lateral transport. However, the steady-state assumption can yield substantial uncertainties in dynamic regions. Past studies used mathematical models of various complexity starting from a simple box model (Jonsson et al., 2013), via a 1D vertical mixed model (Nicholson et al., 2012), to global circulation models (Jonsson et al., 2013; Nicholson et al., 2014) to explain the effects of transport and time disequilibrium. Global circulation models used by Jonsson et al. (2013) and Nicholson et al. (2014) are, however, too coarse in resolution to be representative of shelf seas. At present there is a need to increase the number of observations in shelf seas applications given the importance of this type of marine ecosystem but there is no guidance on how to correct bias. To do so it is necessary to replicate past modelling studies but this time focusing on shelf seas to provide a guideline on how to correct for the uncertainties described above.

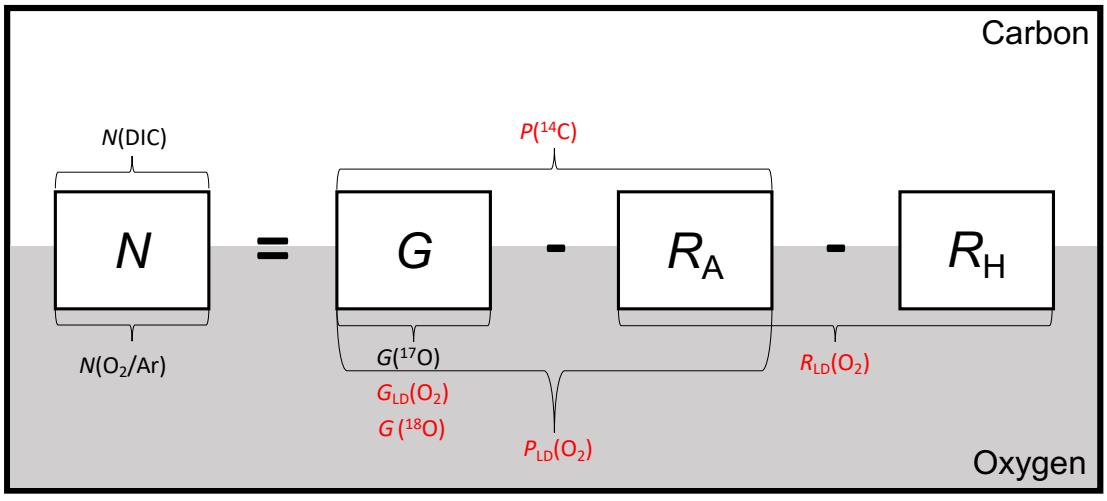

Figure 1: Schematic of the methods (in brackets) estimating marine net and gross community production discussed in this section: ^{14}C is the photosynthetic incorporation of organic carbon into particulate and dissolved fraction (Nielsen, 1952); subscripts with LD refers to the

analysis for dissolved oxygen changes over 24 h in dark and light bottles (Gaarder, 1927); ^{18}O is the bottle method based on photosynthetic release of ^{18}O from $H_2{}^{18}O$ during daytime (Bender et al., 1987); DIC is the method based on measurements of dissolved inorganic carbon (Possenti et al., 2021); O_2/Ar saturation anomaly ($\Delta(O_2/Ar)$) is used as proxy for net biological oxygen supersaturation (Craig and Hayward, 1987); ^{17}O excess ($^{17}\Delta$) dissolved in seawater is used as tracer for pure photosynthetic oxygen (B. Luz and Barkan, 2000). Where N represents net community production, G represents gross community production, R_A represents autotrophic respiration, and R_H heterotrophic respiration. Quantity symbols in red are based on in-vitro observations (black are in-situ). Figure modified from Nicholson et al. (2012).

1.5 Implications for this study

Our understanding of biological metabolic rates in marine ecosystem communities is complicated by several factors resulting in a series of non-linear relationships which are often site-specific. Despite this, all shallow seas are studied assuming spatial uniformity, regularly leading to debates in the scientific community. The spatial extent and time variability of net and gross community production in continental shelf seas and coastal regions represent an obstacle for marine observations. Monitoring programs nowadays benefit from the growing number of methodologies that can be used to assess the efficiency of pelagic net community production within the carbon system. This is particularly true for the development of *in-situ* methods such as $G(^{17}O)$ and $N(O_2/Ar)$, which showed promising results in a past study describing oxygen production rates in the Celtic Sea yet require a quantification of uncertainties (Seguro et al., 2019). Past modelling efforts significantly improved general understanding of the $G(^{17}O)$ (Nicholson et al., 2014) and $N(O_2/Ar)$ (Jonsson et al., 2013) bias in open ocean applications. While these studies were pertinent to oceanic waters, their relevance to shallow, dynamic shelf seas is unclear.

1.6 Aims of this thesis

The overall aim of this thesis was to address gaps in the knowledge of shelf sea pelagic net (N) and gross (G) community production. This was done by achieving two specific aims: 1) To compile the first inventory of dissolved triple oxygen isotopes ($^{17}\Delta$) and oxygen-to-argon saturation anomaly ($\Delta(O_2/Ar)$) as a proxy for net ($N(O_2/Ar)$) and gross ($G(^{17}O)$) oxygen production across the North Sea; and 2) To use a community

ecosystem model to investigate the validity of $N(O_2/Ar)$ and $G(^{17}O)$ estimates in a shelf sea environment.

The main research questions were:

> What is the net metabolic state (producing, consuming, or in balance) in the North Sea surface waters during late summer?
>
> What is the magnitude of the error introduced by approximations often associated to $N(O_2/Ar)$ and $G(^{17}O)$ methods when applied in dynamic environments such as shelf seas?

Chapter 2 contains the rationale, methodologies, results, and discussion for the North Sea sampling campaign measuring both $\Delta(O_2/Ar)$ and $^{17}\Delta$. Sampling was conducted during the RV Cefas Endeavour Survey CEND12/19 (7 August to 5 September 2019). The results of Chapter 2 were used to design and complete model development and scenarios discussed in design and completion of the modelling work shown in Chapter 3 and 4. In Chapter 3, dissolved argon (Ar) was implemented in the European Regional Seas Ecosystem Model (ERSEM) (Butenschön et al., 2016) as a new state variable. The ERSEM model was coupled to the 1-D General Ocean Turbulence Model (GOTM) (Burchard et al., 1999). Chapter 3 aimed to answer question 2 related to $N(O_2/Ar)$ estimates using the L4 time series station (Western English Channel) as case study. Simulation results were validated against $\Delta(O_2/Ar)$ observations at L4 collected by Gloël (2012). Chapter 3 provides the basis for the model scenarios investigated in Chapter 4. In Chapter 4, the oxygen isotopes ^{17}O and ^{18}O were implemented within ERSEM to answer question 2 related to $G(^{17}O)$ using L4 as case study. Chapter 5 offers conclusions, answers to the research questions and suggestions for future work.

Chapter 2: Measurements of pelagic net metabolic rates in the North Sea during late summer 2019

2.1 Abstract

The North Sea is one of the biologically richest and most productive shelf seas in the world. At present, observations on the spatial distribution of pelagic net (N) and gross (G) community production during the growing season are missing. The aim of this study was to measure the spatial distribution of N and G (in oxygen equivalents) during the late growing season across different North Sea regions. N was estimated from oxygen-to-argon ratios, $N(O_2/Ar)$; G was estimated from triple oxygen isotopologue (TOI) ratios, $G(^{17}O)$. This is the first time this methodology has been applied in the North Sea.

A total of 52 stations were sampled by CTD casts across the North Sea during RV Cefas Endeavour Survey CEND12/19 (7 August to 5 September 2019). At each station, vertical profiles of temperature, salinity, dissolved oxygen concentration ($c(O_2)$), turbidity and fluorescence were obtained. Discrete water samples for $c(O_2)$, oxygen-to-argon ratio $R(O_2/Ar)$ and TOI analyses were taken in the surface mixed layer, bottom mixed layer and in between at the deep chlorophyll maximum (detected by the CTD's fluorometer during downcast). Analyses of $c(O_2)$ were carried out on board every 7 days and used to calibrate the oxygen optode used for profiling. TOI and O_2/Ar water samples were stored in poisoned, evacuated glass bottles and transported to UEA for laboratory analysis.

Measured water column in the southern North Sea was fully mixed, instead central, and northern North Sea was stratified. At surface fully mixed waters in the south were warmer than historical means but still within historical standard deviation. Stratified central and northern North Sea was found warmer than the historical standard deviation. On average measured surface waters across the North Sea were found in net metabolic balance. $N(O_2/Ar) = (-3 \pm 40)$ mmol m^{-2} d^{-1}, with $G(^{17}O) = (298 \pm 150)$ mmol m^{-2} d^{-1}. $N(O_2/Ar)$ and $G(^{17}O)$ varied across the region. $G(^{17}O)$ measured in the NW European coastal waters converted in carbon equivalents ($G(C) = (3.09 \pm 0.94)$ g m^{-2} d^{-1}) matched the monthly 90th percentile of primary production (P) given by 21 years long remote sensing dataset. The most productive surface waters were in coastal areas influenced

by the Humber River ($G(^{17}O)$ = (500±220) mmol m^{-2} d^{-1}). This region was found to be net heterotrophic suggesting intense remineralisation. Net autotrophy was observed in the central and northern North Sea. Results shown in this study represents surface observation alone. Therefore, estimated $N(O_2/Ar)$ and $G(^{17}O)$ do not represent production integrated over some depth horizon (e.g., euphotic depth). Future studies could focus on collecting data into locations prone to advection (e.g., Southern Bight) and entrainment (e.g., north-eastern North Sea) to calculate the fluxes with adjacent waters.

2.2 Introduction

The North-West European Shelf (NWS) is a temperate marine region located on the eastern boundary of the North Atlantic Ocean. The NWS includes several connected seas, the largest of which is the North Sea with a total surface area of 575 000 km² (Lee, 1980). Biologically, the North Sea is one of the most productive regions in the world (Emeis et al., 2015). Due to high production rates, the North Sea fishing industry represents an important food and economic resource (Kerby et al., 2012). Fish production is limited by various factors, the most important of which are water temperature, and food availability (Carozza et al., 2019; Moore et al., 2013).

Different water bodies have been identified in the North Sea, based on hydrodynamic features such as water column depth and stratification (Tett et al., 2007), which affect phytoplankton structure and productivity and the biogeochemical cycling of carbon and nutrients (van Leeuwen et al., 2015). These 'ecohydrodynamic types' influence seasonal dynamics and succession of planktonic communities. In winter, gross community production (G) is limited by low solar radiation and net community production (N) is negative due to the dominance of ecosystem respiration (R). Intensive phytoplankton growth (usually dominated by diatoms) occurs during spring, when solar radiation increases (in terms of both intensity and time) and nutrient concentrations are high throughout the entire water column (Capuzzo et al., 2018). In areas with deeper water (>40 m), the timing and magnitude of spring blooms is influenced by the onset of stratification (Llope et al., 2009; Mészáros et al., 2021). Low levels of turbulence near the surface are required to keep fast sinking diatoms within the euphotic zone (van Haren et al., 1998). Spring blooms are important events for providing organic carbon for the rest of the food web in both pelagic and benthic environments (Peinert et al.,

1982; Painting and Forster, 2013). During summer, a combination of nutrient depletion and grazing pressure causes the cessation of the spring bloom and the succession of phytoplankton groups which occupy different ecological niches. In stratified regions, *G* was observed to peak at thermocline depths where solar radiation remains sufficient to support positive growth when combined with a weak flux of nutrients mixing up from deeper waters (Fernand et al., 2013). During autumn, storms and cooling can mix stratified open waters, reintroducing nutrients from deeper waters and triggering autumn blooms (Greenwood et al., 2010; Holt et al., 2012).

Direct measurements of primary production flux based on water samples in the North Sea are limited to disconnected time series stations. For example the Western Wadden Sea (Cadée and Hegeman, 2002), and the Oosterschelde estuary (Smaal et al., 2013) are sites where primary production rates are measured using *in-vitro* methodologies. Another example is represented by the time series located north of the outer edges of the Dogger Bank (Loveday et al., 2022). This site represents a 3 year long time series of high resolution glider data, which is part of the Alternative Framework to Assess Marine Ecosystem Functioning in Shelf Seas (AlterEco) project which involved, among others, measurements of net community production (Hull et al., 2021; Possenti et al., 2021). Most of the literature studying the interannual trends of primary production in the North Sea are based on changes in chlorophyll *a* concentration (*c*(Chl *a*)) and light attenuation (K_d) based on measurements of suspended particular matter (SPM). An example is given by Capuzzo et al. (2018), which reconstructed primary produciton trends in the southern and central North Sea with an empirical model based on ensamble of historical datasets of *c*(Chl *a*) and (K_d). Also Desmit et al. (2020), reconstructed primary production with an empirical model but this time *c*(Chl *a*) was associated to water pH and shown contrasting results to what was shown previously by Capuzzo et al. (2018). In situ datasets provided by time-series stations are sparse and often rise the questions if they are representative of wider regions. On the other hand remote sensing data are able to capture both spatial and temporal dynamics of primary production in surface waters (Alvera-Azcárate et al., 2021). Tilstone et al. (2023) used 21 years of satellite ocean colour data and provided, among other results, the North Sea basin-wide time series of surface net primary production (*P*). All these studies assessed primary production based on phytoplankton biomass accumulation given by

chlorophyll a rather than directly measuring photosynthetic flux. At present there is no comparable study based on flux rates that covers all the regions of the North Sea.

2.3 Aims

The overall aim of this study was to estimate surface net (*N*) and gross (*G*) community production across different zone of the North Sea in summer. Estimates for *N* were based on the *in-situ* measurements of biological oxygen saturation anomalies in water samples ($N(O_2/Ar)$; (Craig and Hayward, 1987)). Estimates of *G* were based on the triple oxygen isotope composition of oxygen dissolved in water ($G(^{17}O)$; (B. Luz and Barkan, 2000)). This work provides the first dataset for $N(O_2/Ar)$ and $G(^{17}O)$ in the North Sea.

2.4 Methods

2.4.1 Sampling strategy

A total of 52 stations were sampled across the North Sea using a CTD (Conductivity, Temperature and Depth) rosette and instrument package during the *RV Cefas Endeavour* Groundfish Survey (CEND12/19, 7 August to 5 September 2019; Figure 2), approximately 2 months before the end of the stratification period north of Dogger Bank and near the end of the stratified period in the Oyster Grounds (Greenwood et al. 2010; Queste et al., 2015). CTD casts were made twice a day, at around 03:00 and 18:00 local time (UTC+1). The location of these stations was assigned each day, taking account of the ground fish survey schedule, and weather conditions. The CTD was fitted with sensors for vertical profiling and a rosette with 12 10-L Niskin bottles for collecting water samples. In cases of rough weather conditions, discrete sampling was done using a single Niskin bottle attached to a wire and a messenger to fire the bottle at the chosen depths.

1.3.2. Sampling

At each station, vertical profiles of temperature, salinity, dissolved oxygen concentration ($c(O_2)$), turbidity and fluorescence were obtained during the CTD downcast. Temperature and salinity profiles were measured using SeaBird 911plus CTD sensors. Dissolved oxygen concentration profiles were determined using a Rinko III ARO-CAV optode attached to the CTD rosette. Turbidity was measured with a

Seapoint turbidity meter (Seapoint Inc., USA) also attached to the CTD. Triplicate water samples were collected into 125 ml borosilicate bottles via Tygon tubing attached to the Niskin bottles tap, and used for whole bottle Winkler titrations (Dickinson, 1996) to calibrate the Rinko optode. Winkler analyses were made every 7 days during the cruise. Titrations were performed using an automated *Sensoren Instrumente Systeme* dissolved oxygen analyser (SIS, Germany), with photometric end point detection (Williams and Jenkinson, 1982). Blank determination was performed between each new batch of Winkler titrations. The thiosulfate titration solution was calibrated against a KIO_3 standard at the beginning of the cruise (6 August 2019), and midway when the Endeavour docked at Aberdeen (20 August 2019).

Discrete water samples were collected in the surface mixed layer, bottom mixed layer and the deep chlorophyll maximum (as detected by the fluorometer during the downcast) using the Niskin bottles during retrieval of the CTD (i.e., the upcast).

The survey yielded a total of 110 bottle samples for triple oxygen isotopes and O_2/Ar ratios and 68 samples (201 including replicates) for Winkler titrations.

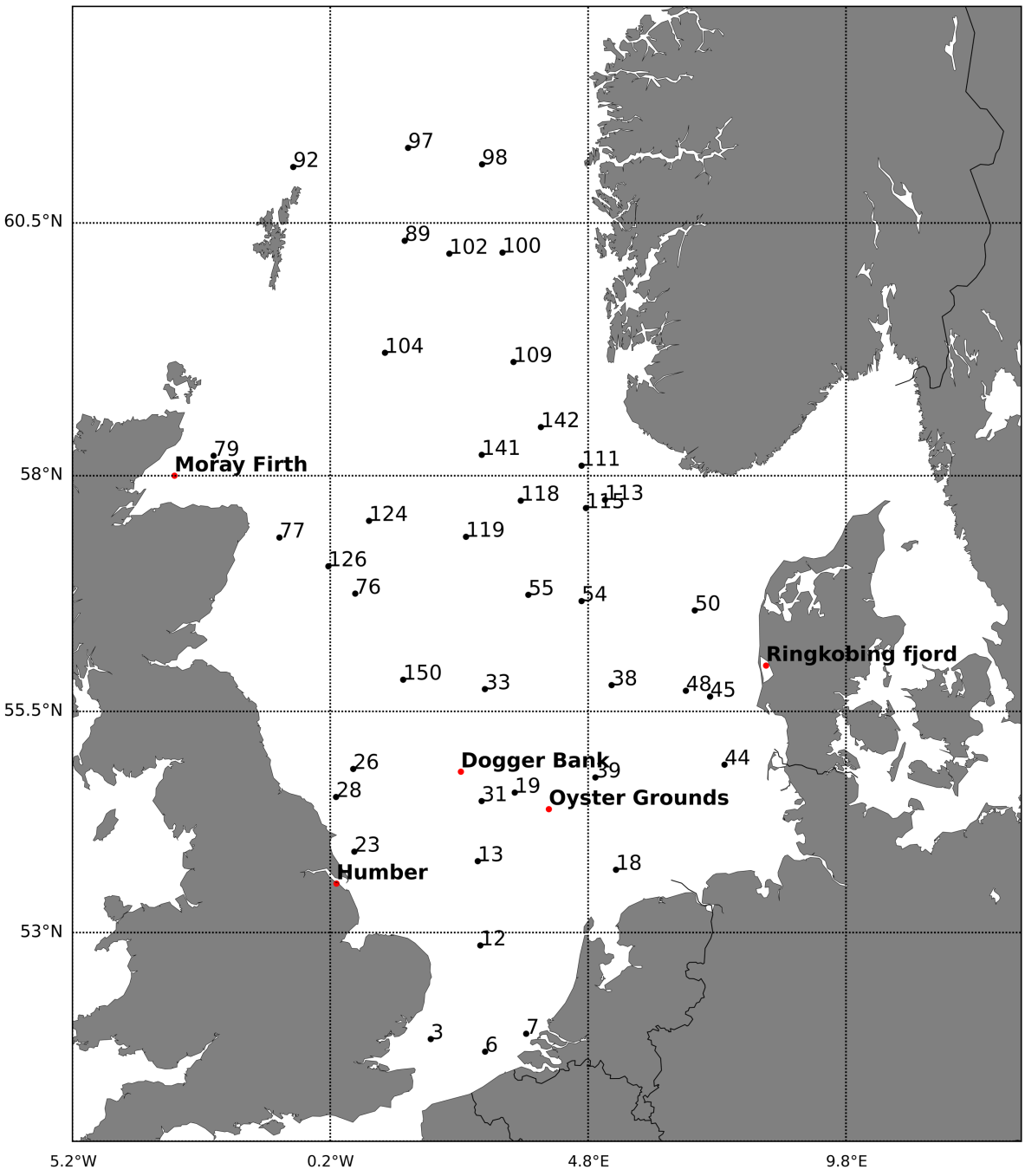

Figure 2: CEND12/19 sampling stations August and September 2019. The cruise started on 7 August 2019 (Station 3) and ended on 5 September 2019 (Station 150). Water samples were taken at 48 stations. Red dots represent landmarks frequently mentioned in the literature.

2.4.2 Experimental procedure

The analyses for O_2 isotopologues and O_2/Ar ratio in discrete water samples comprises three steps: 1) pre-cruise preparation of the sampling glass bottles. 2) collection of water samples from the Niskin bottles. 3) post-cruise gas extraction and purification via gas

chromatography and analyses via dual-inlet isotope ratio mass spectrometry (IRMS) (Figure 4). Pre-cruise preparation involved: calibration of the bottle volumes, application of 100 µl $HgCl_2$ saturated solution (dried in oven at 50 °C), and evacuation to a pressure equal to 5×10^{-6} mbar. Sample collection must avoid air contamination when collecting sea water from the Niskin bottles into the evacuated 330 ml glass bottles using Tygon tubing attached to the Niskin bottle tap. $HgCl_2$ stops all biological activity in the sample, preserving the *in situ* conditions encountered at the time of extraction (Emerson et al., 1991). Post cruise work tasks involved the extraction of gasses dissolved in the water samples using cold traps, the purification of the extracted gases (O_2 and Ar) gas from other gas species that can alter the end results (water vapour, CO_2 and N_2) via gas chromatography, and finally analysis of oxygen stable isotopes and oxygen/argon ratios via isotope ratio mass spectrometry. Measurements of the oxygen isotopic composition and the oxygen/argon ratio in samples and dry air standard gas was completed using a Thermo Finnigan MAT 253 IRMS. The oxygen isotopologues (*m*/*z* 32, 33, 34) and oxygen/argon ratios in the sample material were measured against a reference gas (4.7 % Ar in O_2). Dry air was used for calibration. All post-cruise laboratory work was done at the UEA Stable Isotope Laboratory and the methods are described in detail by Gloël (2012), González-Posada (2012), and Seguro Requejo (2017), based on Luz et al. (1999). The only difference from previous works at UEA is that in this investigation stable isotope analysis was done using MAT 253 rather than MAT 252 IRMS.

2.4.3 Calculations and calibrations

2.4.3.1 Calibration of the RINKO optode using discrete dissolved oxygen data

The calibration of the Rinko III Model ARO-CAV optode mounted on the CTD frame ("Rinko III sensor description," n.d.) was done using linear regression of the CTD optode data against the results of the Winkler titrations. Results showed that the Rinko III optode systematically underestimated $c(O_2)$ by (24±2) mmol m^{-3}. The raw optode concentrations were calibrated using the equation $c(O_2$; Rinko calibrated) = (1.045±0.011) $c(O_2$; Rinko raw) + (14.1±2.6) mmol dm^{-3} (Figure 3).

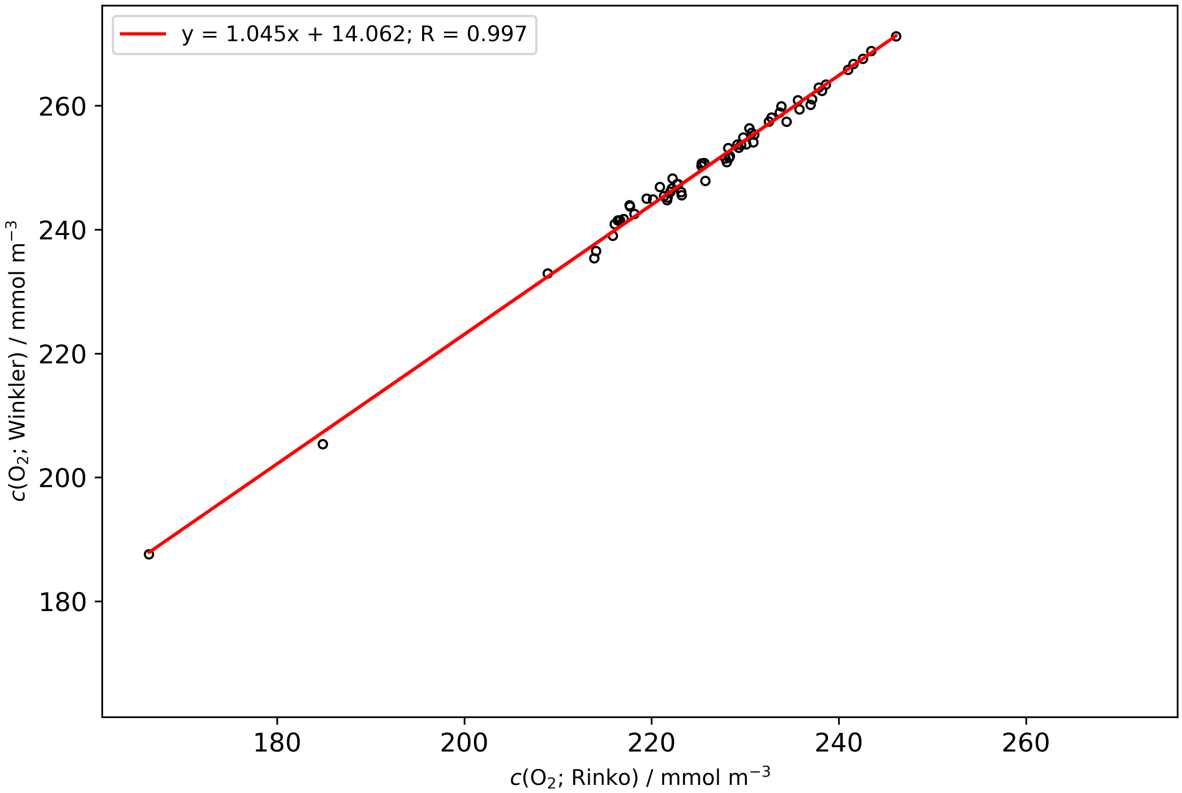

Figure 3: Linear regression between the dataset collected with the Rinko optode (abscissa) and the Winkler titration analysis (ordinates) gave $c(O_2;$ Winkler) = (1.045±0.011) $c(O_2;$ Rinko raw) + (14.1±2.6) mmol dm^{-3} (R^2 = 0.997).

Quality control and calibration steps included: 1) Removing upcast values from the raw CTD dataset because of discontinuities in the profile when the Niskin bottles were closed. Within the downcast dataset all data points with strong pressure inversions were removed (these were more prominent when the ship was moved by big swells). 2) Calculation of temperature/conductivity difference between primary and secondary respective sensors. 3) Calibration of oxygen optode data using Winkler data. 4) Saving new quality-controlled profile as netCDF file at 0.5 m resolution. Such tasks were performed using the R algorithm CTDQC (CTD quality control) developed by Dr Tom Hull (Cefas/UEA).

2.4.3.2Correction of $\delta(^{i}O)$ for dual-inlet pressure imbalance

The dual-inlet system of the IRMS aims to introduce the reference and the sample into the ion source at exactly the same flow rate. This procedure is automatised; however, perfect balancing is rarely achieved (Bender et al., 1994). This can be caused by a lack

of calibration of the bellows containing both reference and sample gas and generated while adjusting the bellow volume at the start of each analysis (Figure 4).

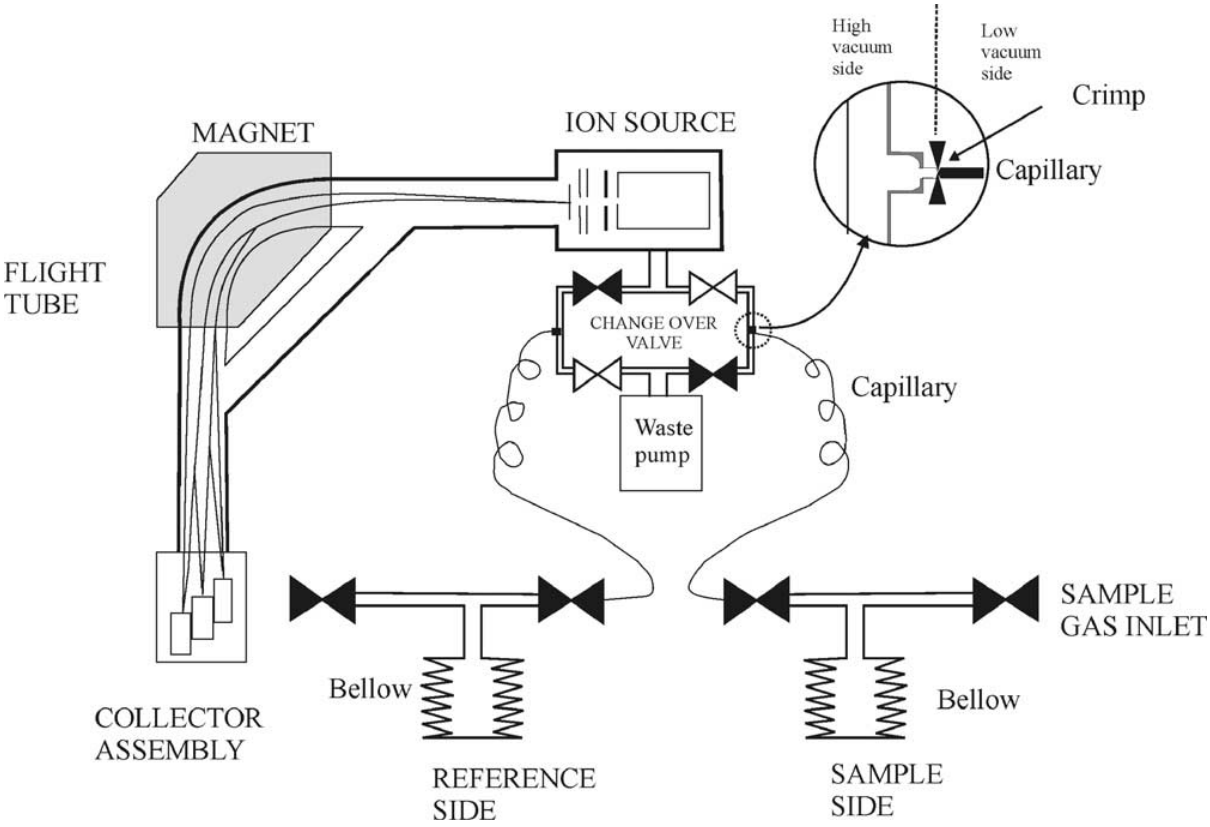

Figure 4: Illustration of a classic dual inlet mass spectrometer. White ribbons represent closed valves and black ribbons are open. From (Ghosh and Brand, 2003)

Therefore a correction, which considers the magnitude of dual inlet imbalance, is necessary to decrease this bias. To determine this correction factor, a test is run consisting of zero enrichment tests with manually adjusted bellow imbalances to vary the gas pressure of sample and reference bellows. The correction factor is obtained from the linear relationship of measured $\delta(^{i}\mathrm{O})$ against the difference between standard and sample voltages for m/z 32 ($\Delta U_{32} = U(32, \text{standard}) – U(32, \text{sample})$).

A total of 12 measurements were used to calculate correction for the imbalance test. Here the reference gas was set at fixed signal voltage (5 V) while changing the sample signal voltage ±0.25 V, in steps of 0.05 V. Imbalance corrected values for $\delta(^{18}\mathrm{O})$ and $\delta(^{17}\mathrm{O})$ were calculated as follows:

$$\delta(^{i}\mathrm{O};\ \text{imbalance-corrected}) = \delta(^{i}\mathrm{O};\ \text{uncorrected}) - m(^{i}\mathrm{O})\Delta U_{32} \qquad (5)$$

The slope m is derived by linear regression: $m(^{17}O) = (-4.0 \pm 1.4) \times 10^{-5}$ V^{-1} ($R^2 = 0.46$) and $m(^{18}O) = (3.3 \pm 0.6) \times 10^{-5}$ V^{-1} ($R^2 = 0.75$; Figure 5).

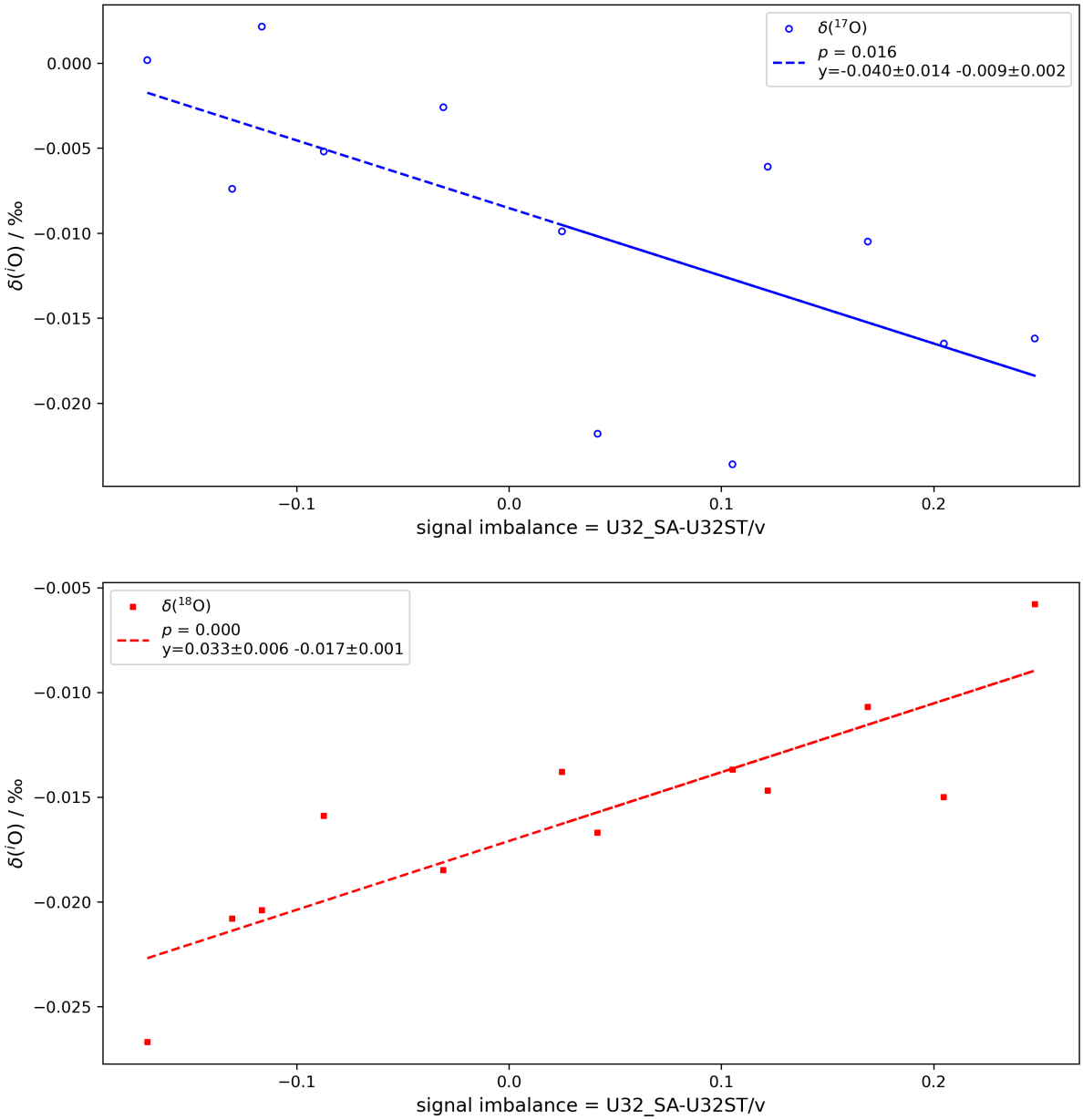

Figure 5: The linear regression analysis resulted from imbalance test of $\delta(^{17}O)$ and $\delta(^{18}O)$.

2.4.3.3Correction of $\delta(^{i}O)$ for N_2 interference

The separation line removes N_2 from the sample, yet there is a small amount of N_2 remaining after this process. N_2 contamination can affect both $\delta(^{18}O)$ and $\delta(^{17}O)$, presumably because N_2 interferes with the ionisation of O_2. Following Abe and Yoshida (2003), the N_2 correction factor was found by measuring the isotope delta of O_2-N_2 mixtures with seven different N_2 amount fractions. The resulting $\delta(^{i}O)$ values were then

plotted against the N_2 voltage difference (normalised with respect to the O_2 voltage) between reference and sample, $\Delta U(N_2/O_2)$, and a linear relation calculated. The N_2 amount fraction had negligible effects on $\delta(^{17}O)$ ($p = 0.42$) and $\delta(^{18}O)$ ($p = 0.17$; Figure 6). Therefore, no N_2 correction was applied.

The results from this investigation were unexpected because measurements using a different mass spectrometer (MAT 252) showed a linear increase of $\delta(^{17}O)$ with $\Delta U(N_2/O_2)$ (Gloël, 2012; González-Posada, 2012; Seguro Requejo, 2015; van der Meer, 2017), with regression slopes that did not vary much over time. It may be due to the specific ionisation conditions in the MAT 253 compared with the MAT 252, since source design and analyser geometry are the same for both instruments.

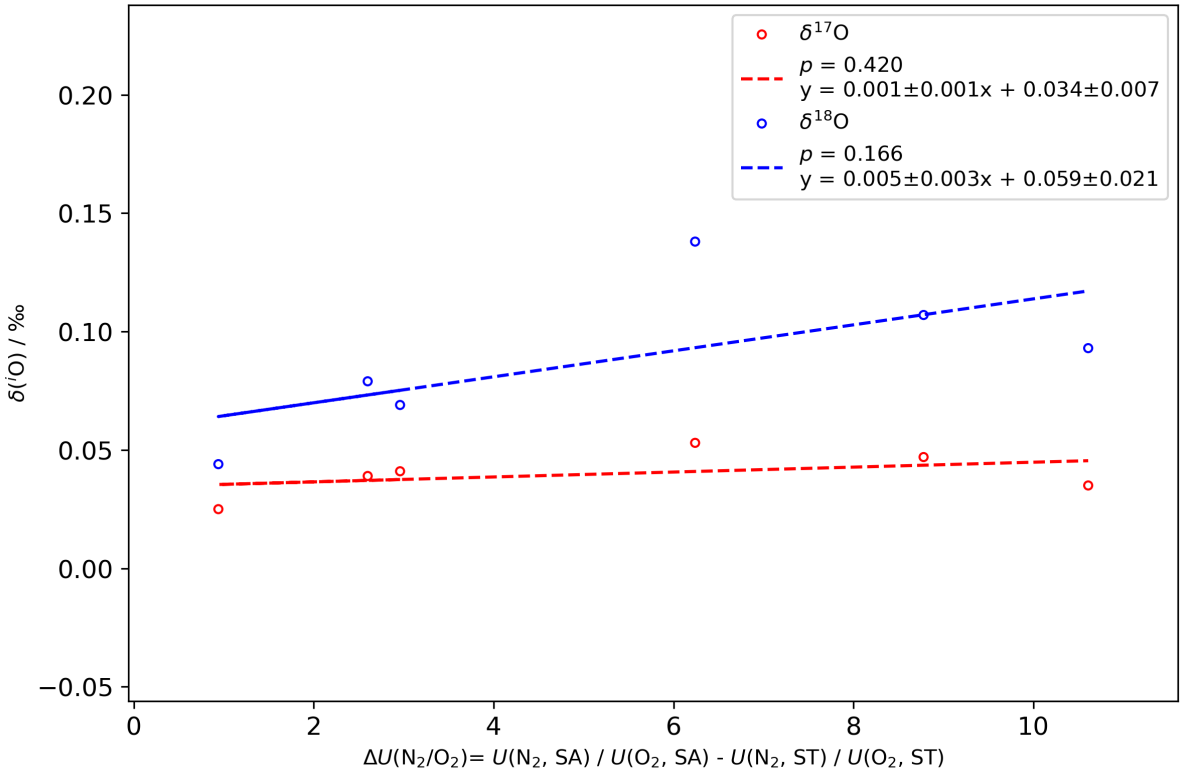

Figure 6: The linear regression analysis describing the effects of N_2 contamination in the ion chamber on $\delta(^{17}O)$ and $\delta(^{18}O)$.

2.4.4 O_2/Ar from IRMS discrete samples

The O_2/Ar ratios of the CEND12/19 discrete samples were measured and calculated from the so-called interfering mass intensities of O_2 (m/z 32) and Ar (m/z 40) measured by the MAT 253. The raw $\Delta(O_2/Ar)$ value was calculated with respect to the O_2/Ar working reference:

$$\Delta(\mathrm{O_2/Ar}, \text{measured}) = \frac{U(32, \text{sample})/U(40, \text{sample})}{U(32, \text{reference})/U(40, \text{reference})} - 1 \qquad (6)$$

A correction was then applied to correct for the partition of the gas between the headspace and the water phase inside the sample bottles (Seguro Requejo, 2017):

$$\Delta(\mathrm{O_2/Ar}, \text{partition-corrected}) = \frac{1 + \alpha(\mathrm{O_2})\frac{V_{\mathrm{WP}}}{V_{\mathrm{HS}}}}{1 + \alpha(\mathrm{Ar})\frac{V_{\mathrm{WP}}}{V_{\mathrm{HS}}}}[1 + \Delta(\mathrm{O_2/Ar}, \text{measured})] - 1 \qquad (7)$$

where α(X) are the Ostwald solubility coefficients for oxygen and argon ($\alpha(\mathrm{O_2})$ = 0.0258 and α(Ar) = 0.0284 at 24 °C and practical salinity S = 35). V_{WP} and V_{HS} are the gravimetrically determined volumes of the water phase and head space, respectively.

2.4.5 Dry air and water saturated air calibration for $\delta(^{i}\mathrm{O})$ and $\Delta(\mathrm{O_2/Ar})$

Dry air samples were purified and measured against working reference material in the same way as the samples. The results for dry air samples in this investigation (using MAT 253) were similar to those obtained in 2015 by Seguro (2017) using a MAT 252 IRMS (Table 1).

Table 1: Analyses of dry air against working reference in this study compared with results of Seguro (2017). 1 ‰ = 10^{-3}. 1 ppm = 10^{-6}.

	IRMS	$\delta(^{17}\mathrm{O})$/‰	$\delta(^{18}\mathrm{O})$/‰	$^{17}\Delta$/ppm	$\Delta(\mathrm{O_2/Ar})$/‰
This work	MAT 253	–0.45±0.04	–0.83±0.02	–25±11	130±2
Seguro (2017)	MAT 252	–0.49±0.03	–0.91±0.04	–24±10	130±1

Tropospheric air has a constant $\mathrm{O_2/Ar}$ amount ratio and is the preferred standard for dissolved oxygen isotope applications (Barkan and Luz, 2003). $\delta(^{i}\mathrm{O})$ and $\Delta(\mathrm{O_2/Ar})$ were converted to dry air as reference using the relationship:

$$\Delta(\text{sample/dry air}) = \frac{\Delta(\text{sample/working reference}) - \Delta(\text{dry air/working reference})}{1 + \Delta(\text{dry air/working reference})} \quad (8)$$

where Δ can stand for $\delta(^{17}\text{O})$, $\delta(^{18}\text{O})$ and $\Delta(\text{O}_2/\text{Ar})$.

Dry air calibration samples (DA) are processed through the same separation line as the gas extracted from water samples to ensure identical treatment.

Finally, $\Delta(\text{O}_2/\text{Ar})$ is expressed relative to air-saturated seawater:

$$\Delta(\text{O}_2/\text{Ar; vs. sat}) = [1 + \Delta(\text{O}_2/\text{Ar; vs. DA})]\frac{R(\text{O}_2/\text{Ar};\ \text{DA})}{R(\text{O}_2/\text{Ar};\ \text{sat})} - 1 \quad (9)$$

where $R(\text{O}_2/\text{Ar; DA})$ =22.43 is the ratio of the atmospheric O_2 and Ar amount fractions (Aoki et al., 2019) and $R(\text{O}_2/\text{Ar; sat})$ is the ratio of dissolved O_2 and Ar concentration at air saturation (20.38±0.02 for the range 10 to 20 ºC and S = 35±1).

2.4.6 Calculating $^{17}\Delta$ and production-rate / O_2 influx ratio g from IRMS discrete samples

The MAT 253 software returns results as $^{33}\delta$ and $^{34}\delta$ because the mass spectrometer measures the ion current ratios of molecules (m/z 32, 33 and 34). $^{33}\delta$ is the same as $\delta(^{17}\text{O})$ (for a stochastic isotope distribution). The correction from $^{34}\delta$ to $\delta(^{18}\text{O})$ is negligibly small (Kaiser and Röckmann, 2008). The measured triple oxygen isotope excess ($^{17}\Delta$) is defined as follows (Kaiser, 2011):

$$^{17}\Delta \equiv \delta(^{17}\text{O}); -0.5179\delta(^{18}\text{O}) \quad (10)$$

where 0.5179 is chosen to match $\gamma_R = {}^{17}\varepsilon_R/{}^{18}\varepsilon_R$, which is the ratio of respiratory isotopic fractionations.

Gross O_2 production in surface waters can be expressed as dimensionless $g = G / kc(\text{O}_2, \text{sat})$, where the denominator equals the oxygen influx across the air-sea interface:

$$g = \frac{(1 + {}^{17}\varepsilon_E)\frac{\delta({}^{17}O) - \delta_{sat}({}^{17}O)}{1 + \delta({}^{17}O)} - \gamma_R(1 + {}^{18}\varepsilon_E)\frac{\delta({}^{18}O) - \delta_{sat}({}^{18}O)}{1 + \delta({}^{18}O)} + \Delta(O_2)({}^{17}\varepsilon_E - \gamma_R\,{}^{17}\varepsilon_E)}{\frac{\delta_P({}^{17}O) - \delta({}^{17}O)}{1 + \delta({}^{17}O)} - \frac{\delta_P({}^{18}O) - \delta({}^{18}O)}{1 + \delta({}^{18}O)}} \quad (11)$$

where $\Delta(O_2)$ is the O_2 supersaturation, ${}^{17}\varepsilon_E$ and ${}^{18}\varepsilon_E$ are the kinetic fractionation of oxygen isotopes during sea-to-air evasion, $\gamma_R = {}^{17}\varepsilon_R/{}^{18}\varepsilon_R = 0.5179\pm0.0006$ represents the ratio of respiratory isotopic fractionation, $\delta({}^{17}O)$ and $\delta({}^{18}O)$ are the differences between the measured and air relative oxygen isotope ratios, $\delta_P({}^{17}O)$ and $\delta_P({}^{18}O)$ are the relative differences between photosynthetic and air O_2 isotopes (Kaiser, 2011; Kaiser & Abe, 2012). Unlike the equations of Luz and Barkan (2000) Eq. 11 does not involve approximations due to using ${}^{17}\Delta$ and unlike Prokopenko et al. (2011) Eq. 11 considers kinetic isotope fractionation during air-sea exchange.

2.4.7 Air-sea gas exchange, gas transfer velocity and wind speed

The gas transfer velocity of oxygen $k(O_2)$ (in m d^{-1}) is used for the estimation of N and G in surface waters from $\Delta(O_2/Ar)$, g, $\delta({}^{17}O)$ and $\delta({}^{18}O)$:

$$N = k(O_2)c(O_2, \text{sat})\,\Delta(O_2/Ar) \quad (12)$$

$$G = k(O_2)c(O_2, \text{sat})\,g \quad (13)$$

Where c refers to dissolved gas concentration, k to gas transfer velocity, and Δ to the excess in saturation anomaly. $k(O_2)$ is calculated from wind speeds at 10 m above sea level (U_{10}) and the Schmidt number Sc, a dimensionless number equal to the ratio of the kinematic viscosity of water and molecular diffusion coefficient of a given gas of interest. There are various gas transfer velocity parametrisations derived from several observational studies. In this study, the parameterisation of Nightingale et al. (2000), which is widely used and was derived from observations collected in the North Sea, was adopted:

$$k/(\text{m d}^{-1}) = 0.24\left(0.222\left(\frac{u_{10}}{\text{m s}^{-1}}\right)^2 + 0.333\frac{u_{10}}{\text{m s}^{-1}}\right)\sqrt{\frac{Sc}{660}} \quad (14)$$

The Schmidt number Sc was calculated using temperature-based parametrisations (Table 2):

$$Sc = A + B\frac{t}{°C} + C\left(\frac{t}{°C}\right)^2 + D\left(\frac{t}{°C}\right)^3 + E\left(\frac{t}{°C}\right)^4 \quad (15)$$

Table 2:Coefficients and check result (at 20 °C) for the Schmidt numbers of O_2 and Ar (Wanninkhof, 2014).

Gas	*A*	*B*	*C*	*D*	*E*	*Sc*(20 °C)
O_2	1920.4	−135.6	5.2122	−0.10939	0.00093777	568
Ar	2078.1	−146.74	5.6403	−0.11838	0.0010148	615

Weighted averages for gas transfer velocities $k(O_2, \text{weighted})$ retrospective to the sampling time are commonly used in the absence of time series data (Reuer et al., 2007; Seguro Requejo, 2017; Teeter et al., 2018). This calculation requires the O_2 residence time in the surface mixing layer (usually 2 weeks in coastal waters) as the averaging window of time (n = 2 weeks), while the weight coefficient (ω) represents the fraction of the water column ventilated at each time step (f) within n. An e-folding weighting scheme is adopted to assign more importance to the most recent wind speeds (Reuer et al., 2007; Teeter et al., 2018):

$$k(O_2, \text{weighted}) = \frac{\sum_{i=1}^{n} k_i \omega_i}{\sum_{i=1}^{n} \omega_i} \quad (16)$$

$$\omega_n = 1,\ \omega_i = \omega_{i+1}(1 - f_{i+1}) \quad (17)$$

$$f_i = \frac{k_i \Delta t}{z_{\text{mix}}},\ k_i \Delta t < z_{\text{mix}} \quad (18)$$

where n is the index of the most recent gas transfer velocity and equals the weighted period (in this study, $n = z_{\text{mix}} / k(O_2)$), Δt is the time resolution of the wind data (hourly; Teeter et al., 2018), i is the index number, k is the gas transfer velocity of oxygen, ω is the weighting coefficient at each time index i, f is the fraction of the mixed layer ventilated at each time index i and z_{mix} is the mixed layer depth. The weighting coefficient is most important for the most recent gas transfer velocities ($\omega_n = 1$) and less important for earlier gas transfer velocities.

Wind speed data was collected on the RV Cefas Endeavour using a MaxiMet GMX500 compact weather station located at about 16 m from the sea surface. Wind speeds were corrected to standard height of 10 m using the following expression (Hsu et al., 1994):

$$U_{10} = U_z \left(\frac{10}{z/\mathrm{m}}\right)^{0.11} \tag{19}$$

where U_z is the windspeed at measured height (z = 16 m). Data was collected continuously during the cruise and corrected for ship speed. Due to sensor malfunctioning, the wind speed dataset has a 17 day-gap from 22 August until 8 September (Figure 7).

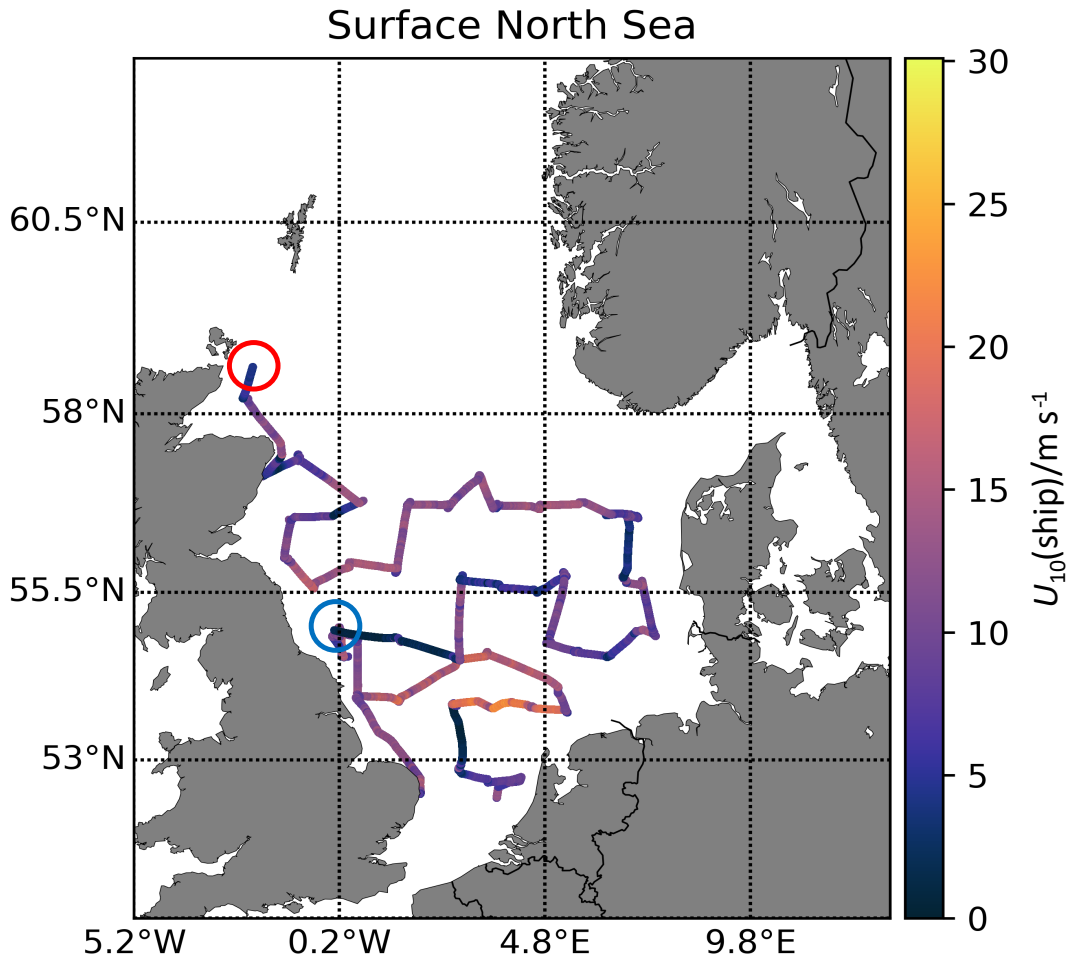

Figure 7: Wind speed measurements made during CEND1219. Gap in the data starting from the 22 August off the coasts of Shetland Islands (red circle) until 8 September on the way back to Lowestoft (blue circle).

Therefore, ERA5 reanalysis wind speeds were used instead to calculate air-sea flux interactions. The reanalysis data used in this study (ERA5) represents the fifth generation of the European Centre for Medium-Range Weather Forecasts (ECMWF). Reanalyses represents model hindcasts corrected with observational data. ERA5 outputs span from 1950 until present. ERA5 outputs are at hourly time resolution, and 31 km spatial resolution globally. Downloaded ERA5 analysis data contain instantaneous wind velocities at both *u* and *v* directions (Copernicus Climate Change Service (C3S), 2017) (Figure 8).

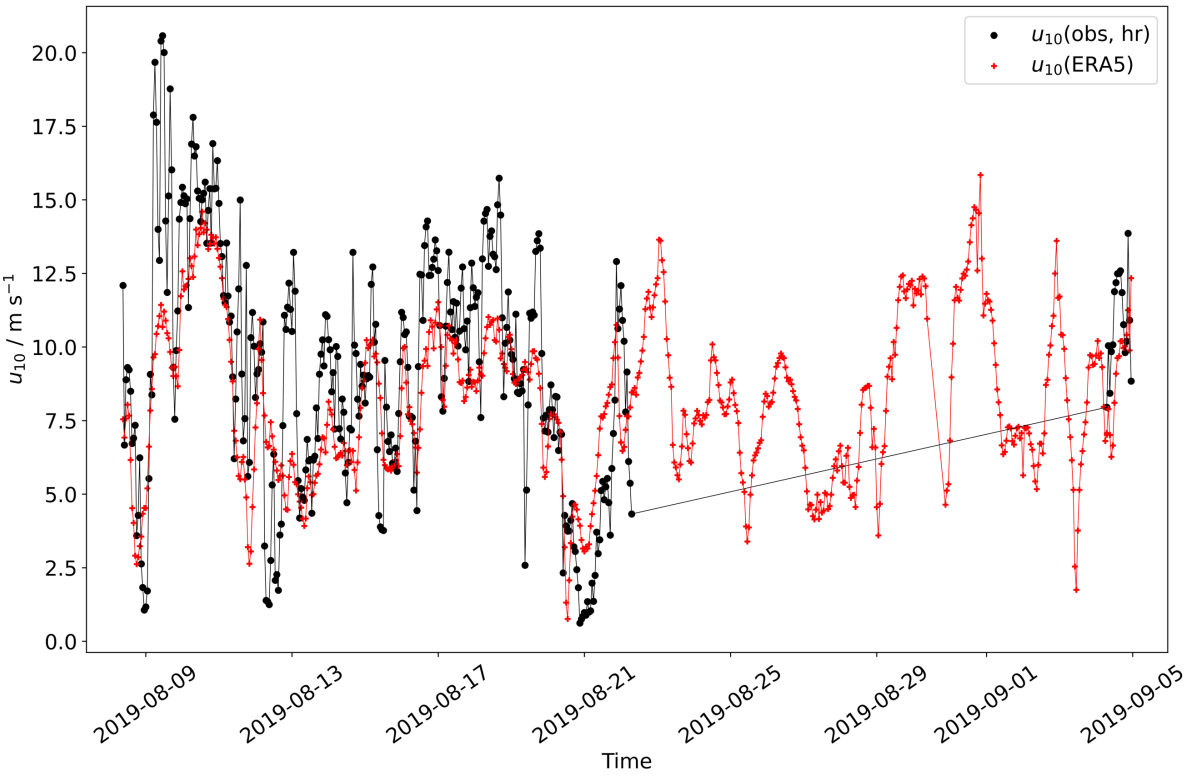

Figure 8: Comparison of ERA5 and ship observations along the time dimension: reference data (in black, uv10(ship, hourly mean)), ERA5 data extracted according to nearest neighbour matching approach (in red, uv10(ERA5)). ERA5 temporal resolution in hours.

Belmonte Rivas and Stoffelen (2019) assessed the quality of ERA5 global wind speed product using 2016 observations from the Advanced SCATterometer (ASCAT). Their results showed that globally ERA5 has a mean bias less than 0.3 m s^{-1} and a root mean squared error (RMSE) of about 2.5 m s^{-1}. Linear regression was used to compare ERA5 wind speeds with matching ship observations. Results showed that the ERA5 was underestimating observed windspeed maxima in the first half of the time series. This

resulted in a standard error that was 46 % greater than global averages, while the offset was 36 % bigger than global averages (Figure 9).

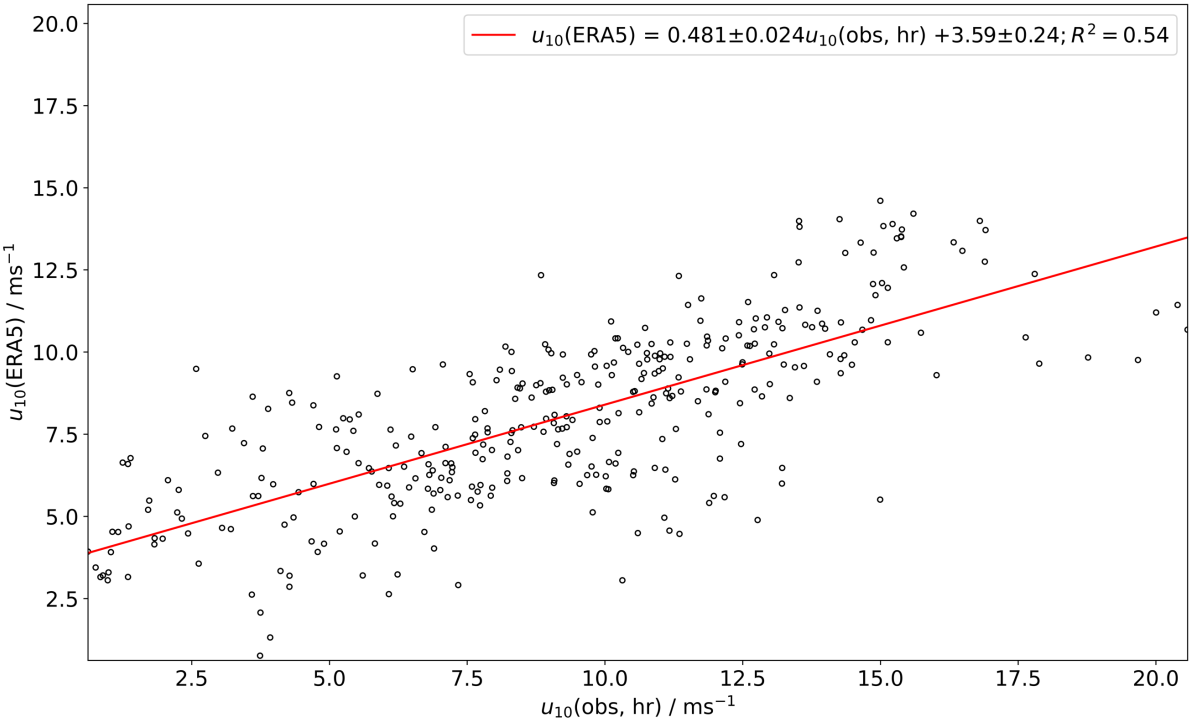

Figure 9: Linear regression analysis between wind speeds measured in this survey (u_{10}(obs, hr)) against ERA5 data (u_{10}(ERA5)). Fitted model (red line) equation is expressed in the legend.

2.5 Results

2.5.1 Temperature, salinity, and stratification:

Results for temperature (T), salinity (S), and oxygen concentrations ($c(O_2)$) at each CTD station (n = 38) were compared against the August means for the 1960–2014 period in the North Sea Biogeochemical Climatology (NSBC) (Hinrichs et al., 2017). This was done to provide an historical contextualization of this investigation's results. On average, surface waters were warmer than the NSBC August means (ΔT(mean surface) = (+2.33±0.75) °C), while bottom temperatures remained within historical variability (ΔT(mean bottom) = (+0.7±1.1) °C). This also suggested that in August 2019 the North Sea was thermally more stratified. The observed average surface temperature was (16±2) °C and ranged from 20 °C in the Strait of Dover (station 7) to 13 °C near Moray Firth in the north (station 79), significantly warmer than the NSBC August mean of

(14±2) °C. Observed average bottom temperature was (12±4) °C, ranging from 20 °C to 8 °C, in line with the NSBC mean of (11±3) °C (Figure 10).

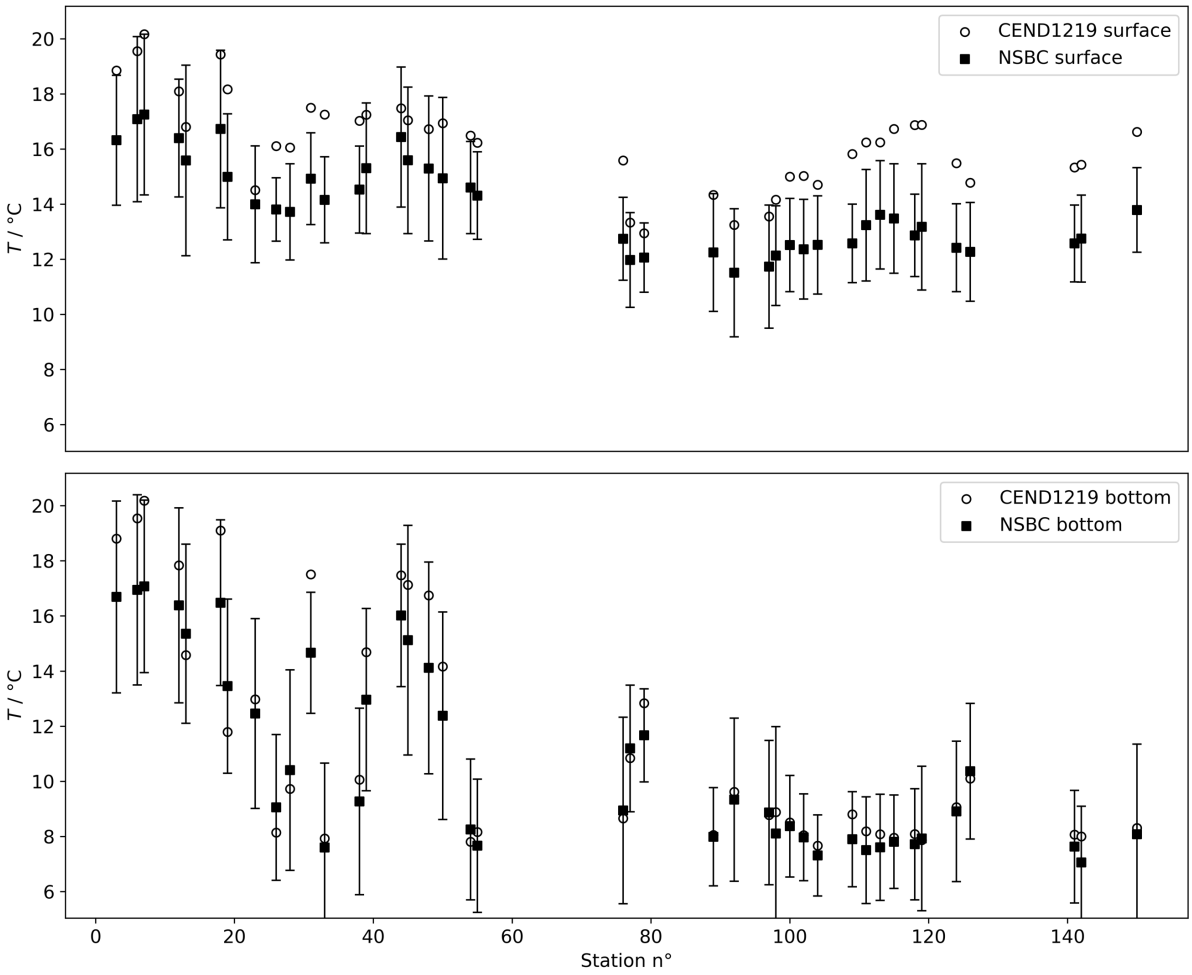

Figure 10:CEND1219 and North Sea Biogeochemical Climatology (NSBC) interpolated surface and bottom temperatures. NSBC values are mean and temporal standard deviations extracted for the time series from 1960 to 2014 (Hinrichs et al., 2017)

The mean observed salinity was 34.51±0.50 at the surface and 34.74±0.52 at the bottom. No significant difference between observed and NSBC salinity was found in either the surface (ΔS(mean surface) = 0.053±0.37) or bottom (ΔS(mean bottom) = 0.051±0.16) waters (Figure 11).

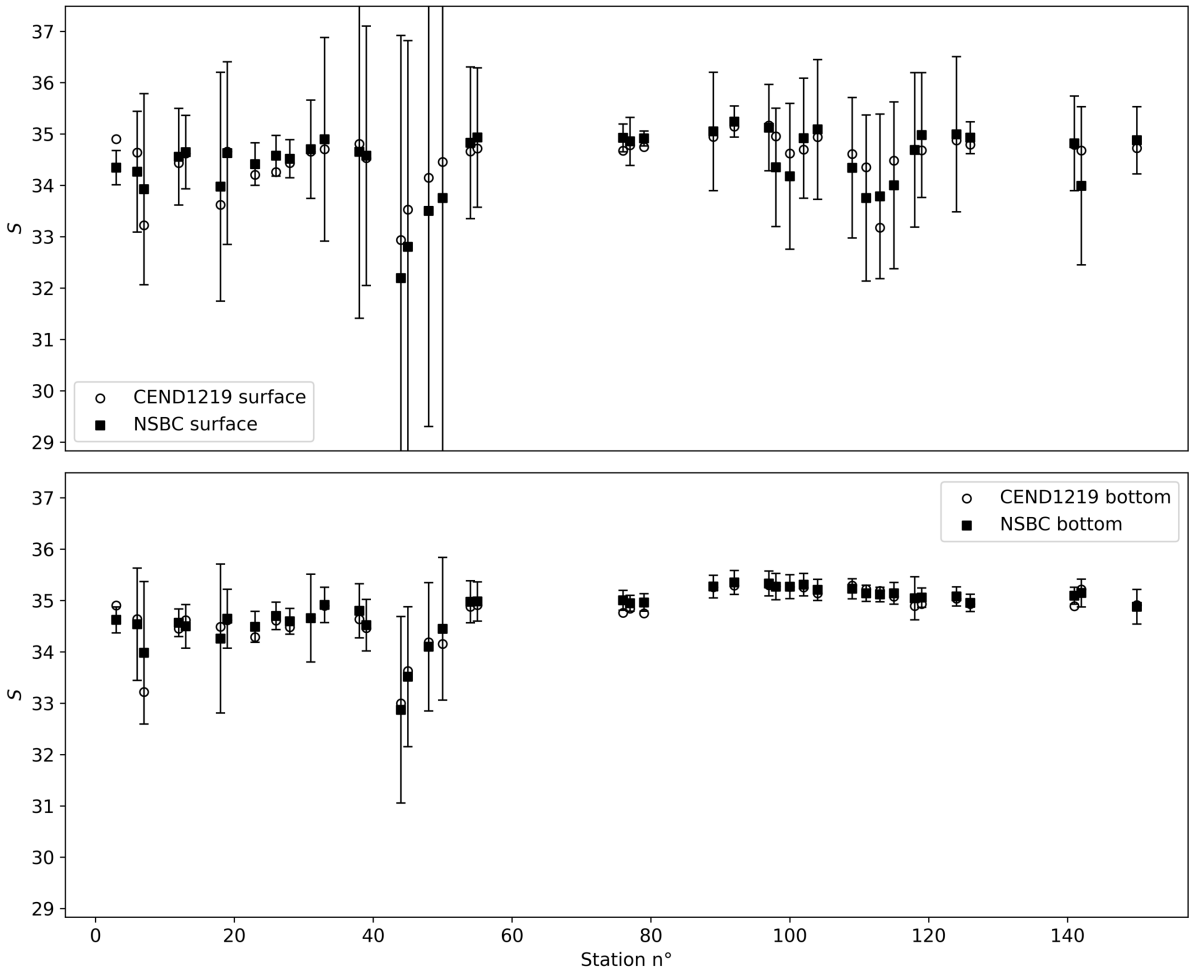

Figure 11: CEND1219 and North Sea Biogeochemical Climatology (NSBC) interpolated surface (top panel) and bottom (bot panel) salinity. NSBC mean (black squares) and temporal standard deviations (grey bands) extracted from a time series from 1960 to 2014 (Hinrichs et al., 2017)

The spatial distribution for temperature and salinity highlighted a clear division in the vertical stratification between stations south and north of Dogger Bank (55.5° N) (Figure 12). In the south, waters were fully mixed (Figure 13). Instead, in the central and northern North Sea were stratified. Here, the mixed layer depth was usually found at 30 m depth where the water column was deeper than 50 m (Figure 16). A thermocline also formed at stations south of Dogger Bank where the water was deeper than 30 m (Figure 14). The southern fully mixed waters were at 20 °C on average, but bottom water temperatures abruptly decreased to 6 °C north of 55.5° N (Figure 13). A comparison of the temperature and density differences between the bottom mixed layer (BML) and surface mixed layer (SML) indicated thermal stratification in the central North Sea, while stratification observed in front of the Skagerrak outflow was affected

by freshwater inputs (Figure 17). In general, bottom salinity was higher in open waters than near the coasts (Figure 12). Salinity minima were found in the Southern Bight (S = 32.5), in the German Bight (S = 33.0) and at the Skagerrak outflow (S = 32.5). The highest salinity was observed in the north-east (35.2). Salinity increased with depth especially near the Skagerrak outflow. Stations 109, 111, 113, and 115 (60.21° N, 2.11° E) showed a salinity reversal at the lower thermocline boundary (5 m: 34.6; 25 m: 34.0; 43 m: 35.3) (Figure 12 and Figure 15). In 109 all measured values around 30 m were disrupted by a lateral current.

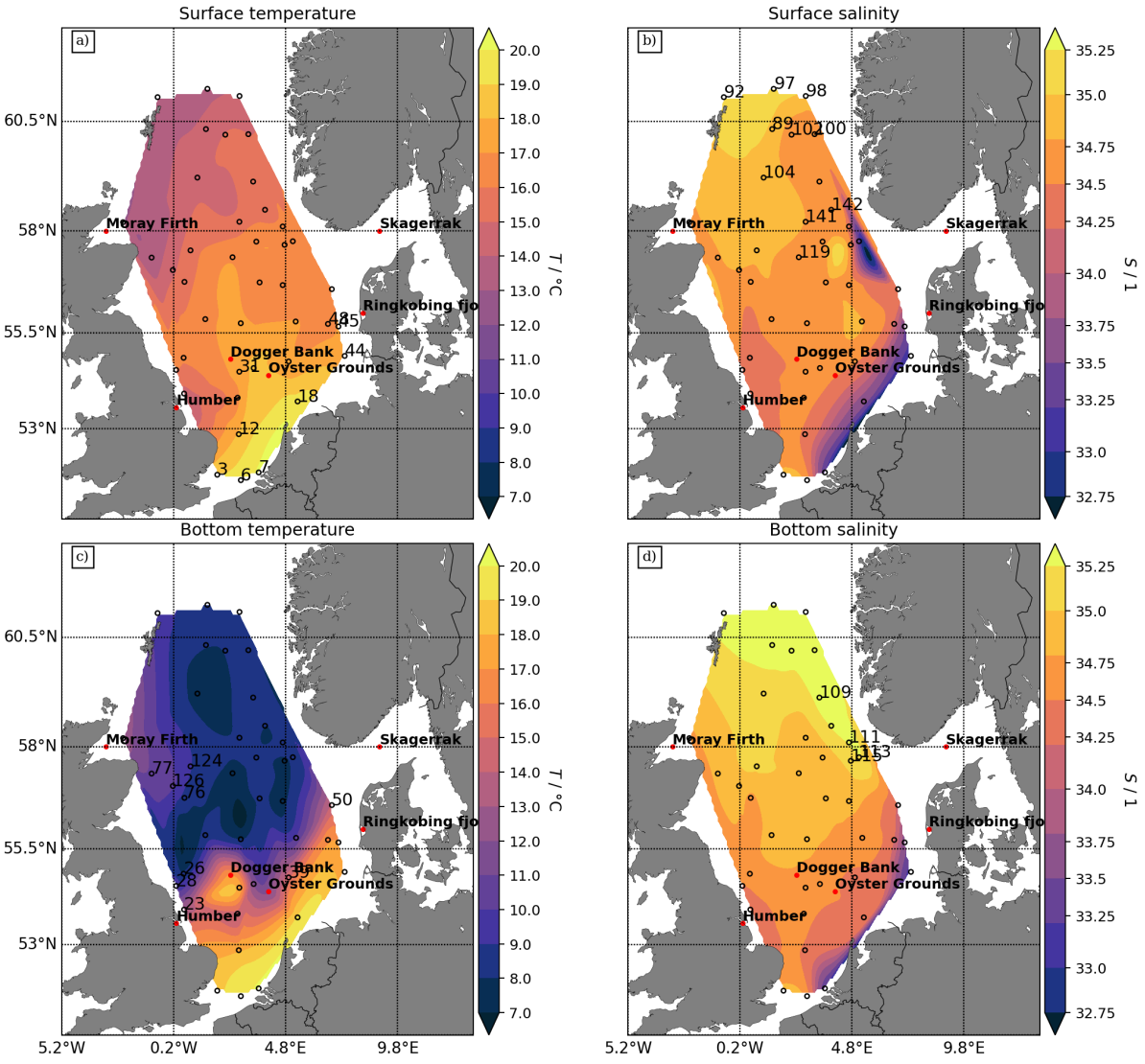

Figure 12:2D interpolations from CTD measurements of temperature (a and c) and salinity (b and d). Numbers refer to the station numbers.

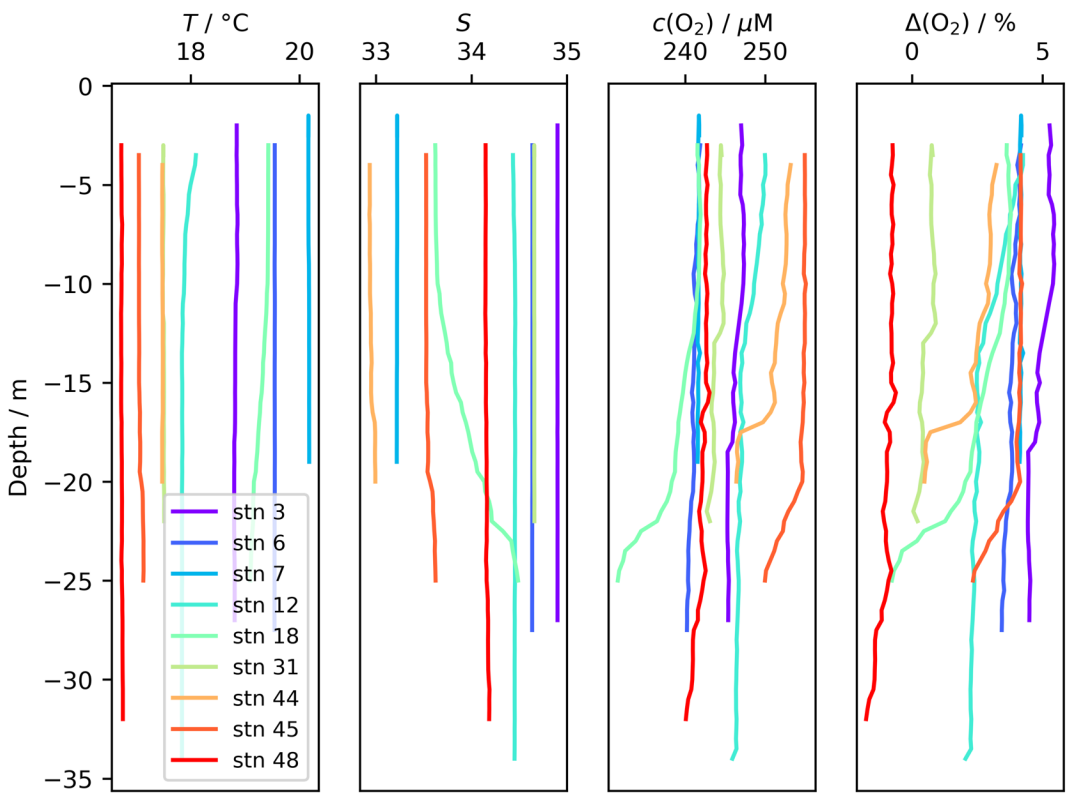

Figure 13: Examples of T, S, $c(O_2)$, $\Delta(O_2)$ profiles in the fully mixed area of the southern North Sea and off Scotland (station 79)

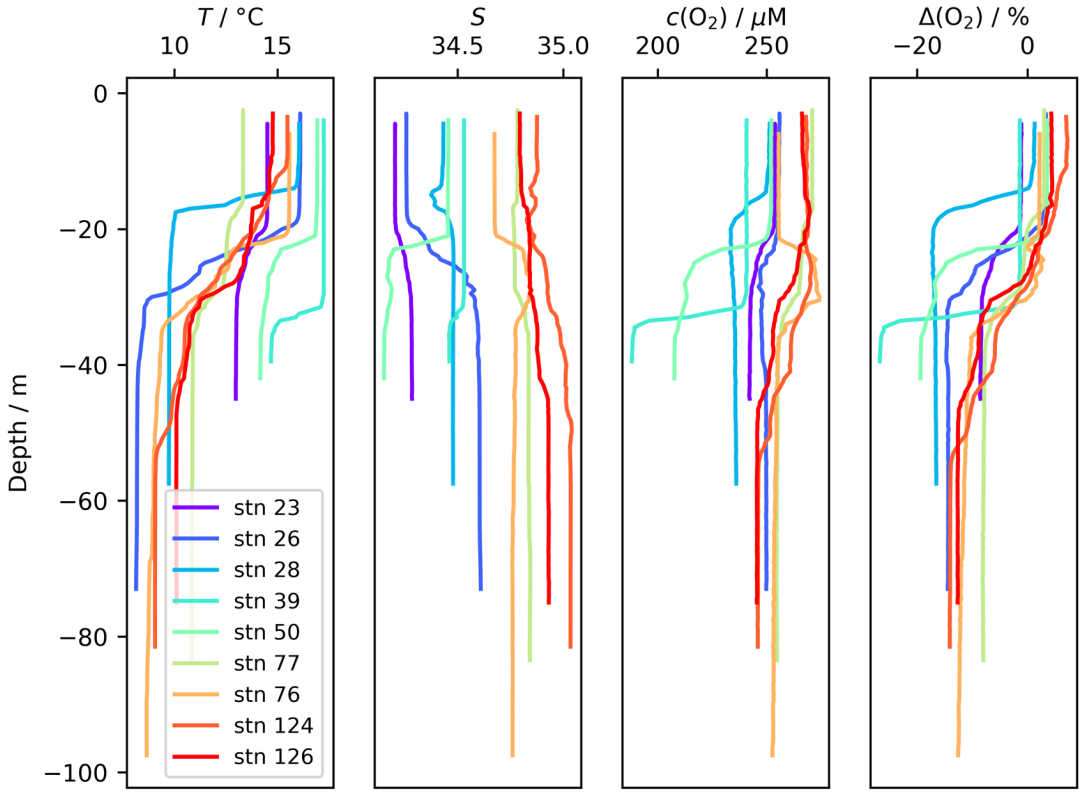

Figure 14: Examples of T, S, $c(O_2)$, $\Delta(O_2)$ profiles for the stratified areas in the southern North Sea with water columns deeper than 30 m. This group of stratified waters did not show a $c(O_2)$ maximum at thermocline depths.

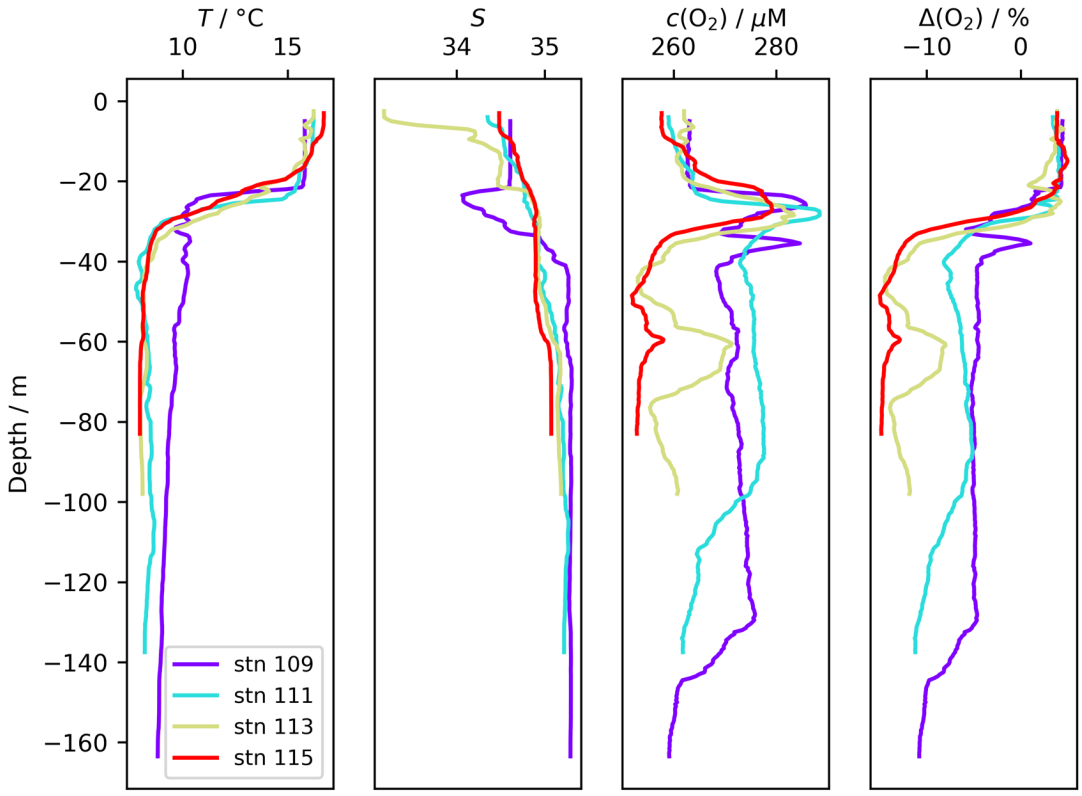

Figure 15: Examples of T, S, $c(O_2)$, $\Delta(O_2)$ profiles for the stratified areas in the southern North Sea with water columns deeper than 30 m. This group of stratified waters showed salinity increasing with depths a $c(O_2)$ maximum at thermocline depths.

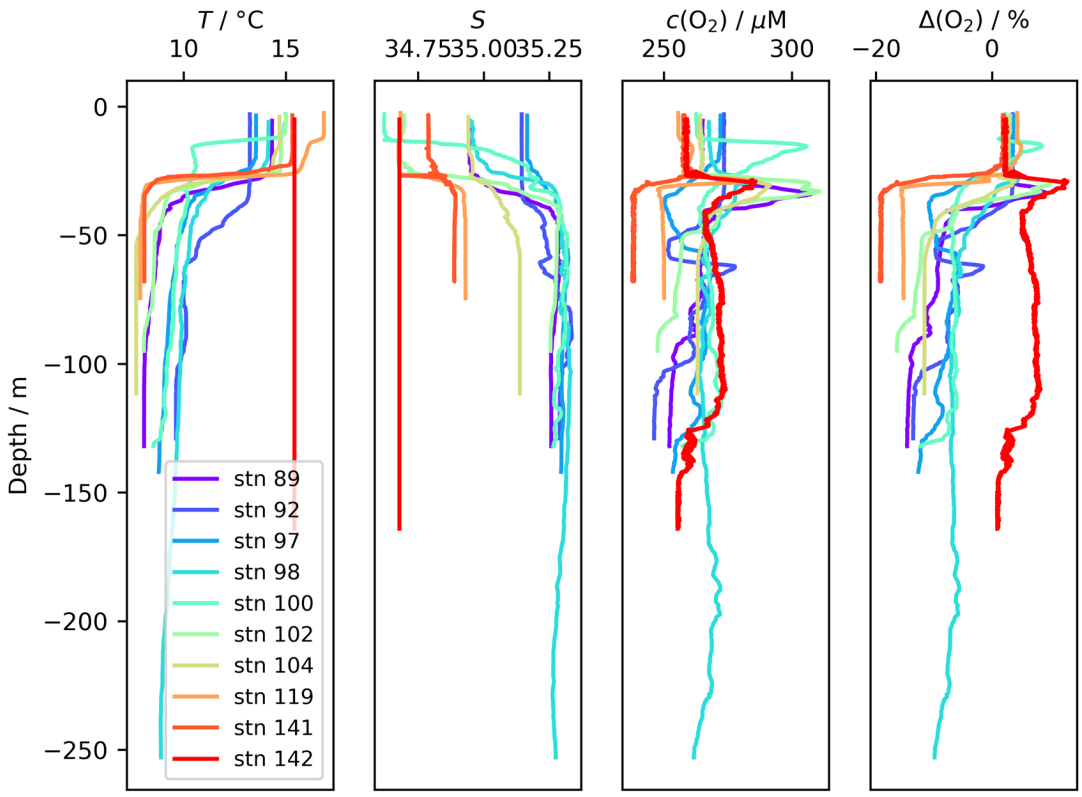

Figure 16: Examples of T, S, $c(O_2)$, $\Delta(O_2)$ profiles for the stratified waters in the central and northern North Sea. This group of stations were 50 to 250 m deep and showed a $c(O_2)$ maximum at thermocline depths.

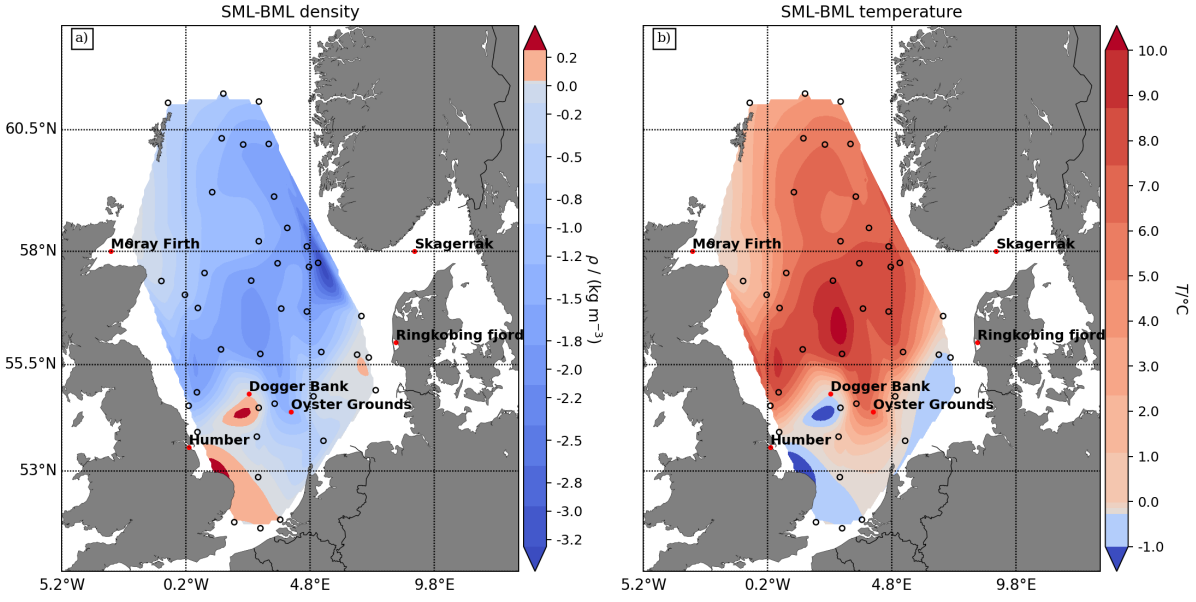

Figure 17: Stratification illustrated by the difference between surface mixed layer (SML) and bottom mixed layer (BML) in potential density (a) and temperature (b). Stratified areas were found to have high vertical temperature gradient and/or density gradient.

2.5.2 Dissolved oxygen concentration, supersaturation, and air-sea exchange:

Observed mean $c(O_2)$ was (260±10) mmol m^{-3} at the surface and (250±10) mmol m^{-3} at the bottom. Surface concentrations were insignificantly lower by (–4±14) mmol m^{-3} than the NSBC values. This difference was lower than the –9 mmol m^{-3} expected for the 2 °C warmer surface waters, indicating a higher average O_2 saturation than in the NSBC climatology. Bottom concentrations were also insignificantly lower by (–2±23) mmol m^{-3} than the NSBC, in line with the –3 mmol m^{-3} change expected for the on average 1 ºC warmer waters assuming solubility equilibrium (Figure 18).

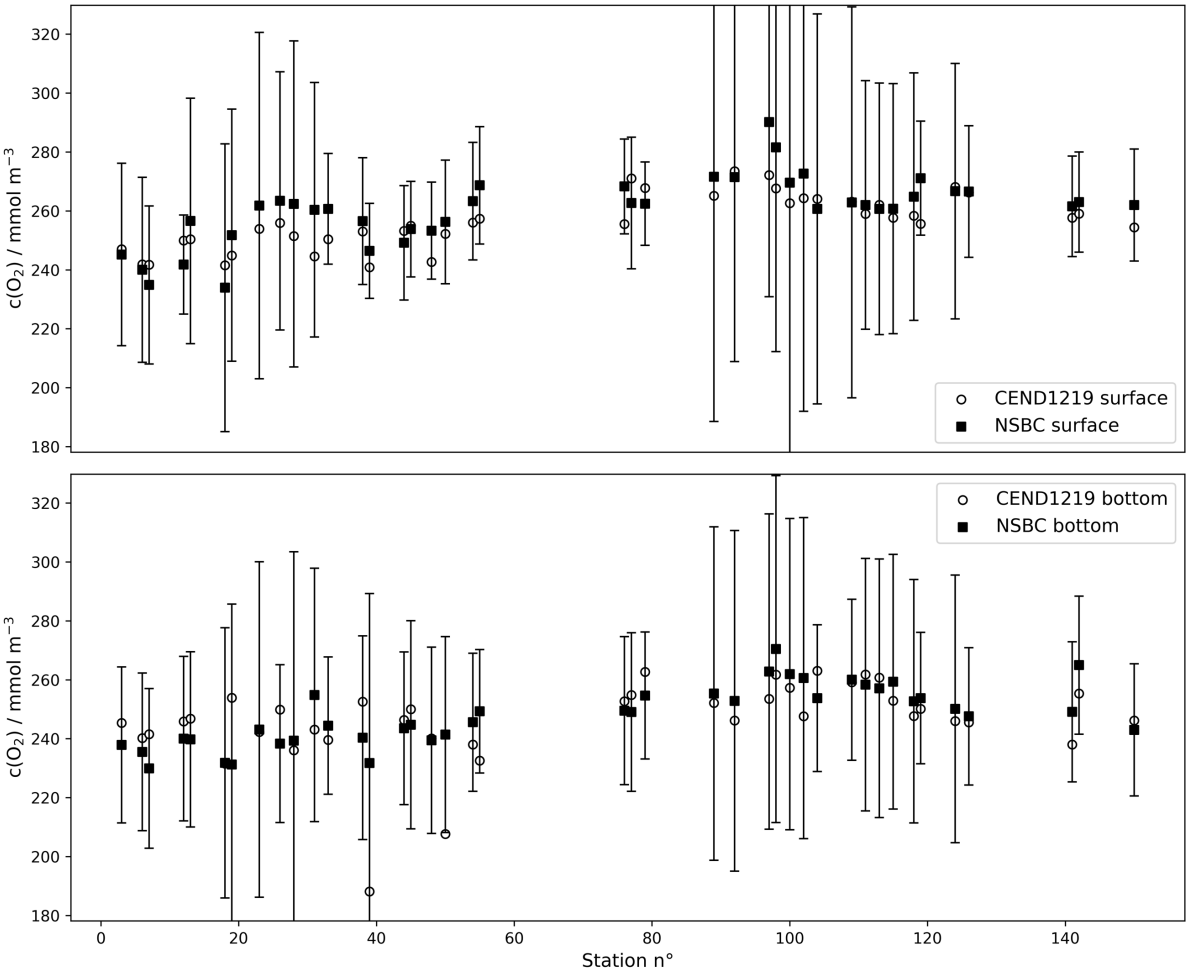

Figure 18: CEND1219 and North Sea Biogeochemical Climatology (NSBC) interpolated surface (top panel) and bottom (bot panel) waters dissolved oxygen concentration. NSBC mean (black squares) and temporal standard deviations (grey bands) extracted from a time series from 1960 to 2014 (Hinrichs et al., 2017)

The observed spatial distributions for $c(O_2)$ and $\Delta(O_2)$ are presented in Figure 19. Stratified regions were oxygen supersaturated at the surface (2.3±1.7) % and

undersaturated at bottom depths (–10±8) %. At the surface, dissolved oxygen concentrations increased northwards, following the temperature trend. Highest oxygen concentrations were found off the Shetland Islands (station 92; $c(O_2)$ = 266 mmol m^{-3}; $\Delta(O_2)$ = 2.7 %), and off Aberdeen (station 124; $c(O_2)$ = 261 mmol m^{-3}; $\Delta(O_2)$ = 6.0 %). Minimum values were found near Oyster Grounds (station 50, $c(O_2)$ = 235 mmol m^{-3}, $\Delta(O_2)$ = –2.1 %). At the bottom, the spatial gradient was less evident. A minimum was found near Oyster Grounds at station 39 ($c(O_2)$ = 183 mmol m^{-3}; $\Delta(O_2)$ = –27 %) (Figure 25). Oxygen concentration and supersaturation maxima for the whole series were found at thermocline depths (from 30 to 40 m) at almost all stratified stations north of Dogger Bank. Concentrations within the thermocline ranged between 280 and 300 mmol m^{-3} and supersaturations ranged between 8 and 10 %.

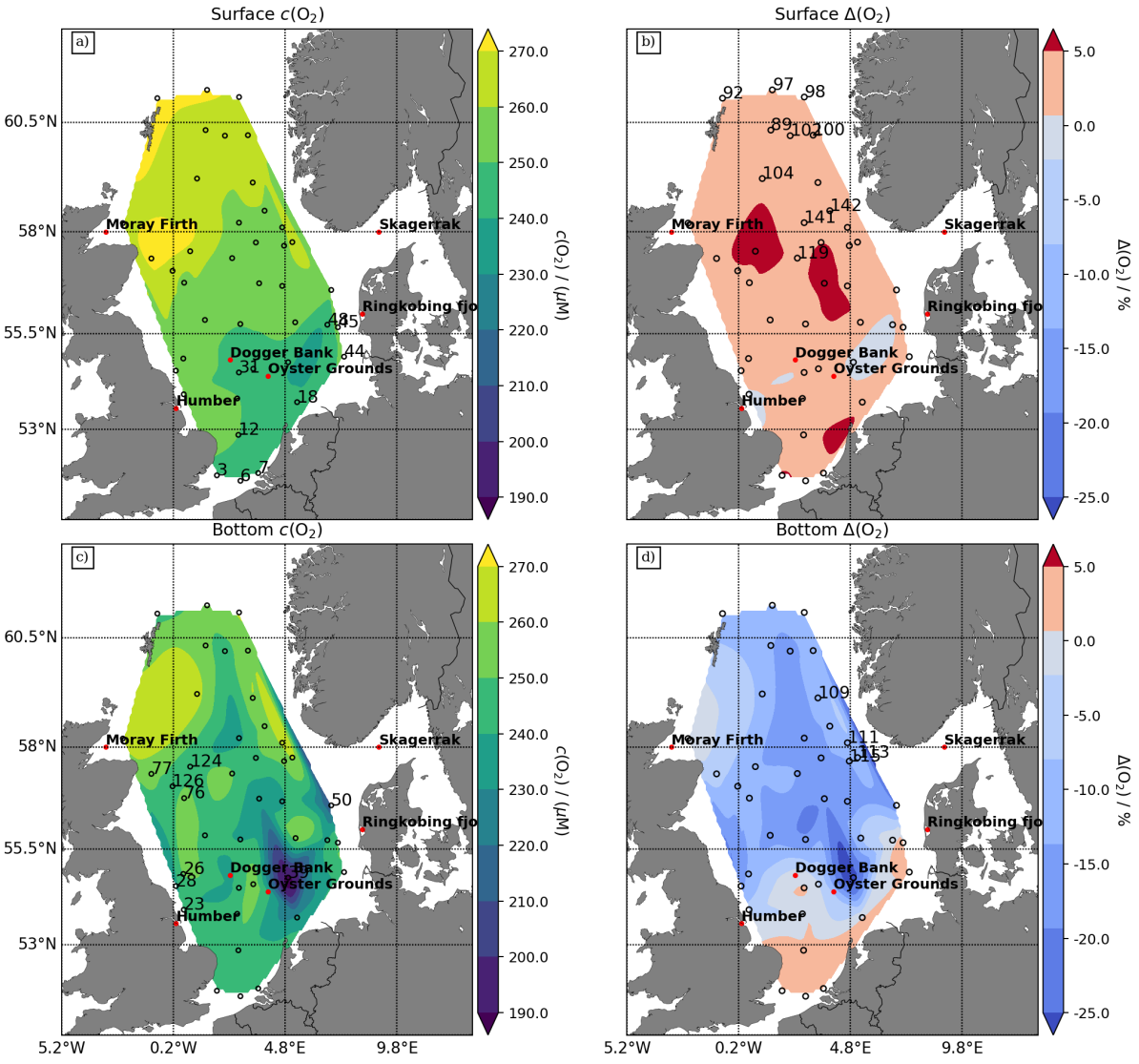

Figure 19: 2D interpolations from CTD sampling for dissolved oxygen concentrations (a and c) and supersaturation (b and d) measured at the surface mixed layer (a and b) and the bottom mixed layer (c and d). Numbers in a refer to the station numbers.

Calculated air-sea fluxes of oxygen, $F(O_2)$, are shown in Figure 20. During the sampling period, the observed surface waters were on average emitting oxygen by (13±16) mmol m^{-2} d^{-1} into the atmosphere. The areas off the river Humber estuary (UK), Moray Firth (UK) and stations closest the Ringkøbing Fjord (Denmark) were taking up oxygen from the atmosphere (–100, –18 and –38 mmol m^{-2} d^{-1}, respectively). Maximum oxygen fluxes ranged between 60 and 20 mmol m^{-2} d^{-1} at all open water stations where surface water was at its highest supersaturation (upper right panel in Figure 19 and Figure 20).

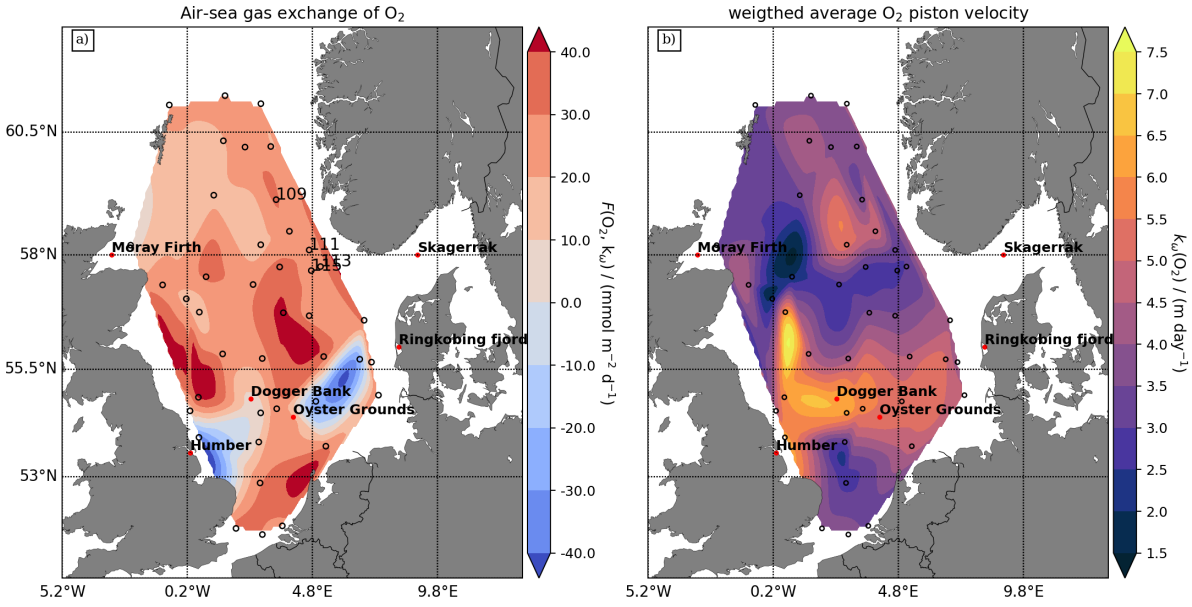

Figure 20:2D interpolations from discrete sampling of air-sea gas exchange of O_2 (left panel) and oxygen gas transfer velocity (right panel). Gas transfer velocities were inferred using ERA5 wind field. The omega sign represents the weighted average scheme described in eq. 14, 15, and 16. Negative $F(O_2)$ values correspond to O_2 uptake from the atmosphere.

2.5.3 Results from MAT 253 analyses: $\delta(^{17}O)$, $\delta(^{18}O)$, $^{17}\Delta$, $\Delta(O_2/Ar)$, g, $G(^{17}O)$, and $N(O_2/Ar)$

The measured oxygen isotope records relative to atmospheric dry air standard material showed high variability in surface waters (mean $\delta(^{18}O)$ = (0.4±0.4) ‰; mean $^{17}\Delta$ = (49±24) ppm (Figure 21). Southern North Sea $\delta(^{18}O)$ was (–0.4±0.2) ‰, significantly lower than for other sampled areas with (+0.5±0.2) ‰ (Figure 24). Waters just below

the surface mixed layer had maximum $\delta(^{18}O)$ values of 4.7 ‰ (Figure 21), with other local maxima in stratified waters near Dogger Bank. Samples below 100 m were characterised by low $\delta(^{18}O)$ variability, with a mean of (2.8±0.3) ‰. As expected, $\delta(^{18}O)$ and $\delta(^{17}O)$ were linearly correlated (slope: 0.5238±0.0016; intercept: 0.0554±0.0032 ‰; R^2= 0.999) (Figure 21).

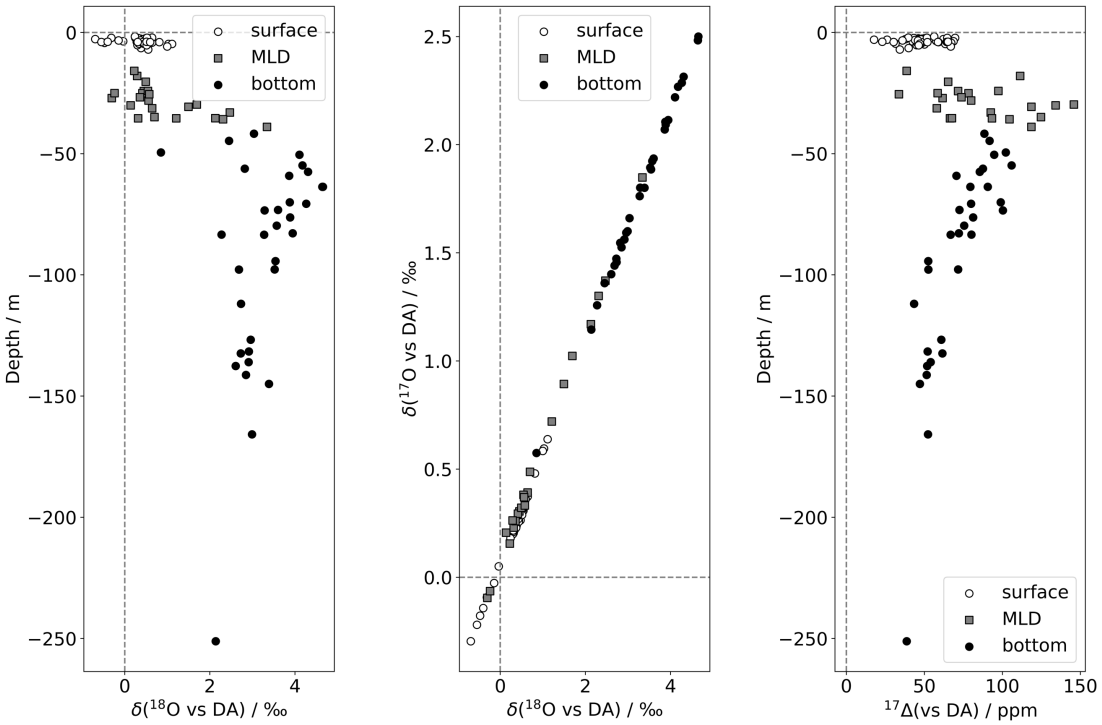

Figure 21: $\delta(^{18}O)$ and $^{17}\Delta$ vs sampling depth (left and right respectively), and $\delta(^{17}O)$ vs $\delta(^{18}O)$ (mid). Results are embedded with all corrections and calibrations explained in 1.3. Samples are divided into 3 depth groups: surface (0–10 m, in white), MLD (10–40 m, in grey), and bottom (40 m – seafloor, in black).

$^{17}\Delta$ (Figure 22) at the surface ranged between 18 and 80 ppm, with a mean of (49±12) ppm). At thermocline depths, $^{17}\Delta$ was higher and more variable than at the surface, with a mean of (87±29) ppm). $^{17}\Delta$ maxima were found just below the surface mixed layer in the central North Sea (Station 33: 146 ppm), off the Strait of Skagerrak (Station 111: 134 ppm) and off the Shetland archipelago (Station 89: 125 ppm).

The $\Delta(O_2/Ar)$ vertical distribution (Figure 22) almost mirrored $\delta(^{18}O)$ (Figure 21) since respiration at depth decreases the former and increases the latter quantity. Subsurface $\Delta(O_2/Ar)$ values ranged between –29.2 % and 2.5 % (mean: (–12±8) %). Average surface $\Delta(O_2/Ar)$ was (0.0±1.6) %. Subsurface maxima were found off Norway (Station

100: 2.5 %; Station 98: 2.0 %). Subsurface $\Delta(O_2/Ar)$ minima were found at 30 to 40 m all over the central North Sea.

Comparison between $\Delta(O_2/Ar)$ and $^{17}\Delta$ showed surface waters with high $^{17}\Delta$ (a sign of gross primary production) tended to atmospheric equilibrium for $\Delta(O_2/Ar)$ (a sign of absent net community production). At thermocline depths, $^{17}\Delta$ maxima coincided with $\Delta(O_2/Ar)$ undersaturation of (–5.1±7.1) % (Figure 23) because $^{17}\Delta$ is only negligibly affected by respiration.

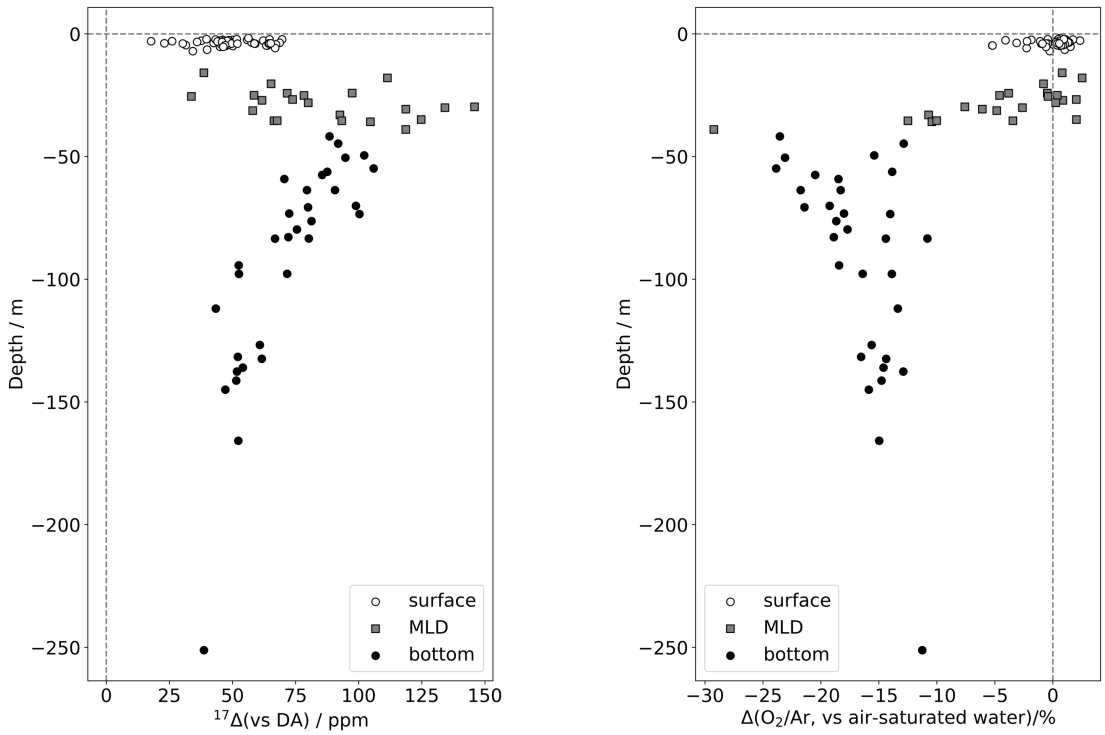

Figure 22: 17Δ and $\Delta(O_2/Ar)$ vs depth (left and right respectively. Samples are divided into 3 depth groups: surface (0–20 m, in white), MLD (20–40 m, in grey), and bottom (40 m – seafloor, in black).

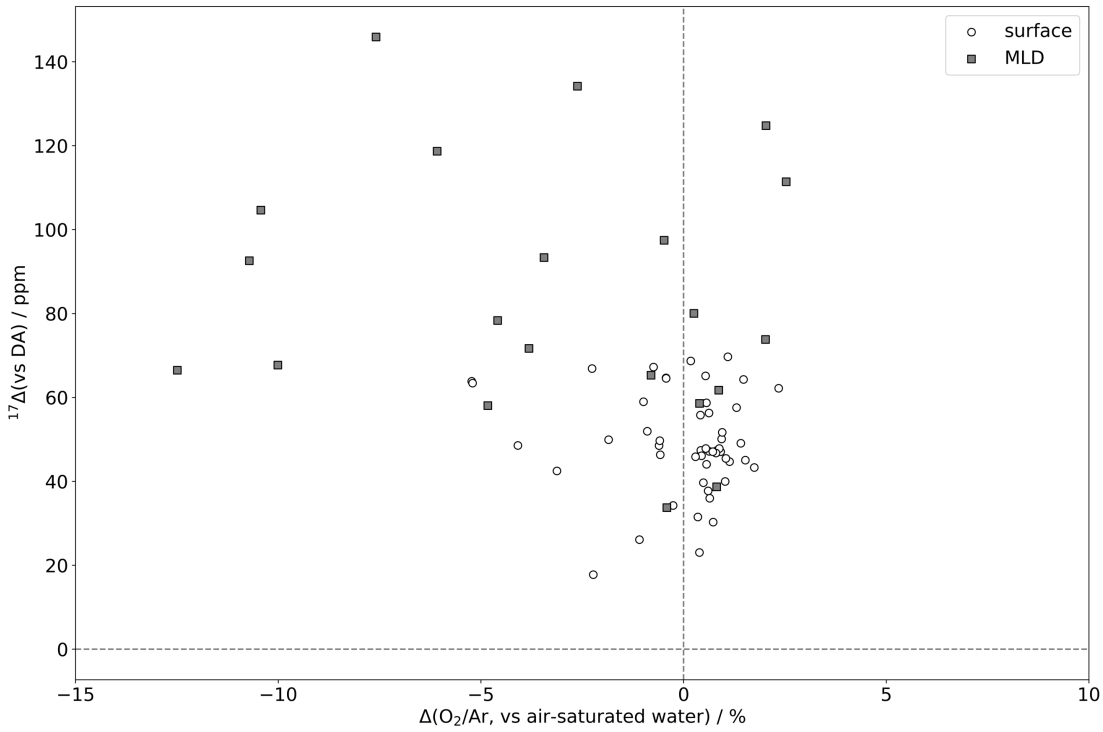

Figure 23: $\Delta(O_2/Ar)$ vs $^{17}\Delta$ for surface (white), and thermocline samples (grey).

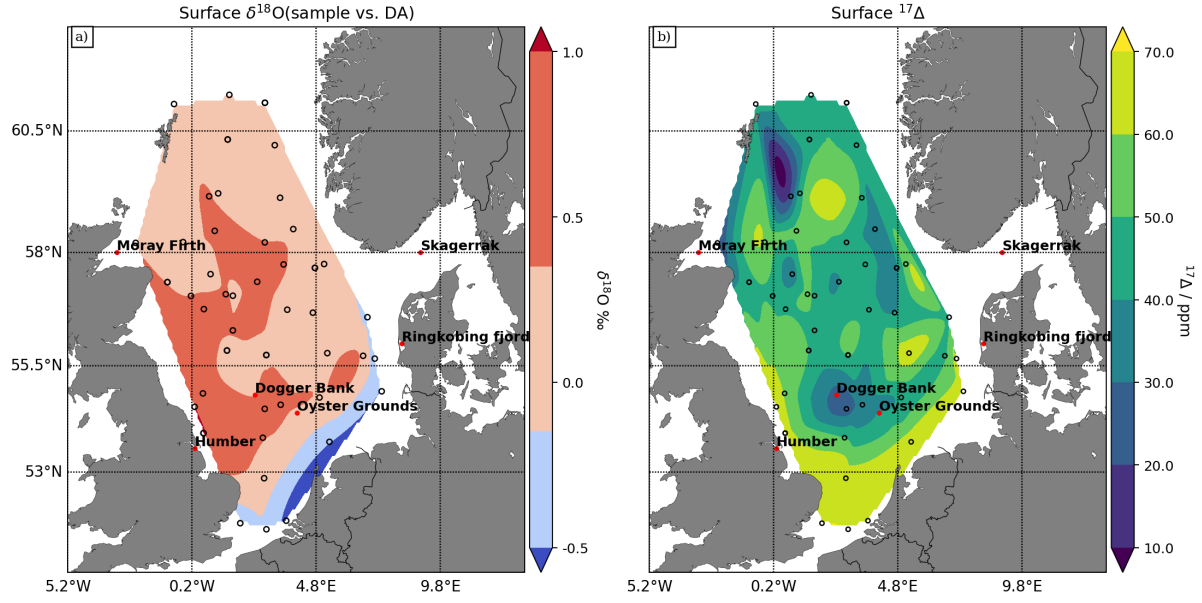

Figure 24: 2D interpolation from $\delta(^{18}O)$ and $^{17}\Delta$ surface values at each CTD station.

Figure 25 shows the geographic distribution of $\Delta(O_2/Ar)$, $^{17}\Delta$), $N(O_2/Ar)$ and $G(^{17}O)$ at surface. Average $\Delta(O_2/Ar)$ is (–0.1±1.7) %, and the derived $N(O_2/Ar)$ averaged (–3±16) mmol m^{-2} d^{-1}. Average $^{17}\Delta$ was (50±12) ppm and $G(^{17}O)$ was (300±150) mmol m^{-2} d^{-1}. Thus, total respiration (autotrophic and heterotrophic combined) was estimated to (300±160) mmol m^{-2} d^{-1}.

Highest $N(O_2/Ar)$ values were generally located in the eastern margin of the North Sea, e.g., in the Southern Bight (20 mmol m^{-2} d^{-1}), off Ringkøbing Fjord (18 mmol m^{-2} d^{-1}), and in the northernmost surface waters (22 mmol m^{-2} d^{-1}). Negative $N(O_2/Ar)$ was found prevalently between 52.5° N and 55.5° N, averaging (–29±21) mmol m^{-2} d^{-1}, and also in Moray Firth (–16 mmol m^{-2} d^{-1}).

$G(^{17}O)$ peaked off the coasts of UK, Belgium, and in the central North Sea within net heterotrophic waters. The most productive stations were located north of the Humber estuary (station 28: 476 mmol m^{-2} d^{-1}; station 26: 450 mmol m^{-2} d^{-1}; station 23: 433 mmol m^{-2} d^{-1}) and off Belgium (station 6: 425 mmol m^{-2} d^{-1}). Areas of low $G(^{17}O)$ were generally located in the central stratified open waters, except for the fully mixed waters in the Moray Firth (station 79: 39 mmol m^{-2} d^{-1}). The same stations were net heterotrophic (station 28: –80 mmol m^{-2} d^{-1}; station 26: –13 mmol m^{-2} d^{-1}; station 23: –79 mmol m^{-2} d^{-1}). No correlation was found between $N(O_2/Ar)$ and $G(^{17}O)$ for the whole dataset ($R^2 = 0.038$; $n = 35$). Subsampling the dataset according to water column hydrography gave slightly higher, but still weak correlations (fully mixed stations: $R^2 = 0.25$, $n = 9$; stratified stations: $R^2 = 0.20$, $n = 26$).

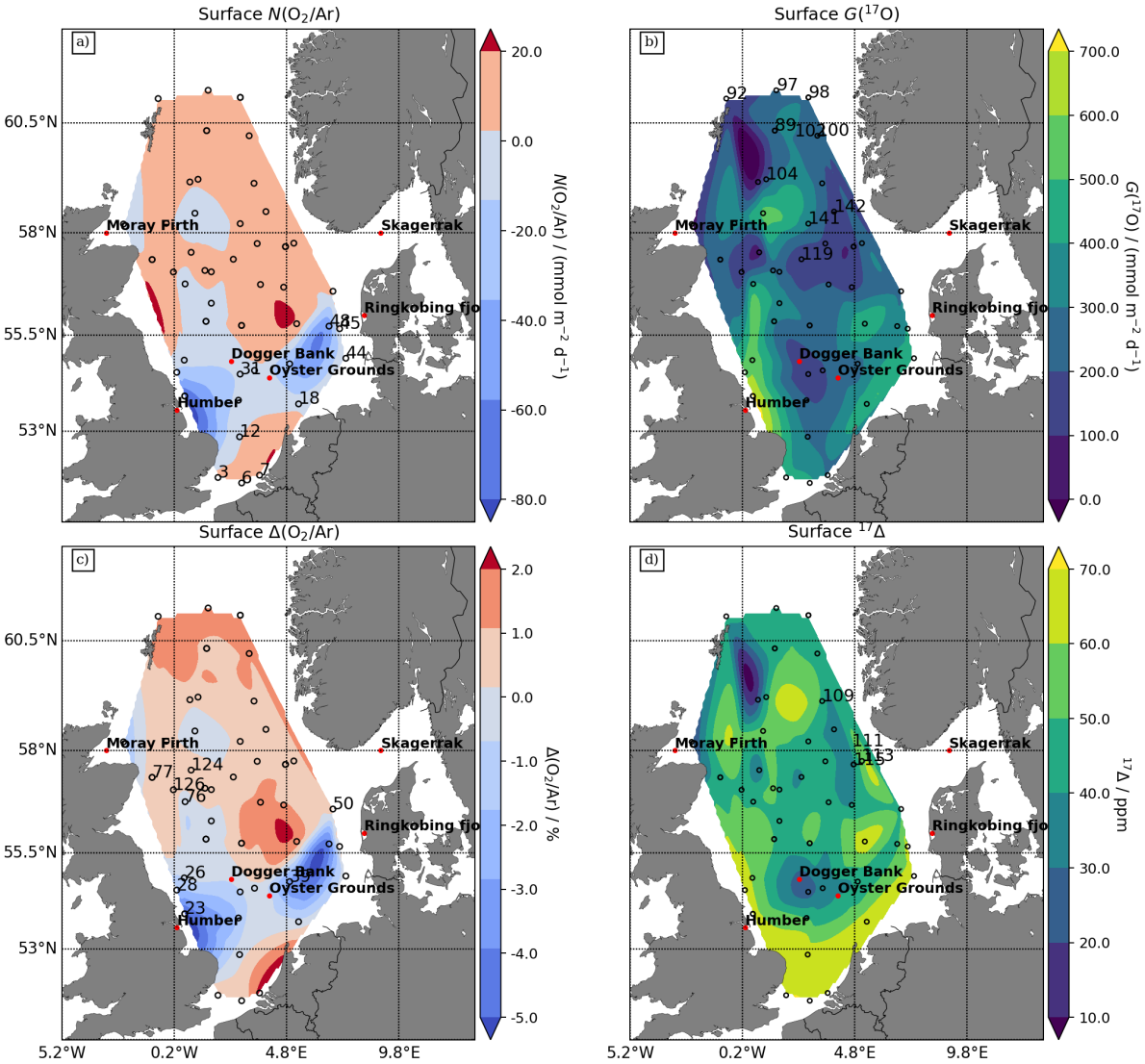

Figure 25:2D interpolation from triple oxygen isotopes and O_2 / Ar supersaturation measurements at each CTD station. Gross oxygen production (top right), net oxygen production (top left), triple oxygen isotope excess ($^{17}\Delta$) (bottom right), biological oxygen supersaturation (bottom left). Numbers in a refer to the station numbers included in Figure 13, Figure 14, and Figure 16.

2.6 Discussion

2.6.4 North Sea hydrography and oxygen cycling in late summer 2019

Temperature recorded from this study (August 2019) showed that SST was significantly warmer than the NSBC climatology (Hinrichs et al., 2017). This means that the North Sea surface waters were exceptionally warm. The North Atlantic surface

(0–10 m) warming is an ongoing non-linear trend with a steep increase (0.2–0.3 °C per decade) since 1975, which is superimposed on the multidecadal oscillatory mode also known as the Atlantic multidecadal oscillation (AMO) (Knight et al., 2006; Schlesinger and Ramankutty, 1994). Positive SST anomalies exceeding two standard deviations are not uncommon in adjacent sea basins (Gonzalez-Pola, et al., 2019), with the North Sea being an outstanding example in this case (Holt et al., 2016, 2010). Despite warmer surface temperatures, bottom mixed layer temperatures were slightly cooler, but within the standard deviation of the climatology. Bottom temperatures ranged from a maximum of 20 °C in the south to a minimum of 8 °C in the north with a sharp latitudinal temperature gradient in the central North Sea. This indicated a switch from southern fully mixed to northern stratified regions of the North Sea.

The spatial distribution highlighted three main hydrographic regimes: Stratification with vertical density and temperature gradients were observed in the central and northern North Sea, with differences between surface and bottom waters of up to 10 °C and 3.3 kg m^{-3}. The southern North Sea and Scottish coastal waters were fully mixed with little temperature and density difference between surface and bottom (0.5 °C and 0.3 kg m^{-3}). A vertical salinity gradient was observed at the Skagerrak outflow and the Norwegian Trench. Here, the haline stratification is stable throughout the year due to the outflow of Baltic brackish waters (Rodhe, 1996). The observed distribution is in agreement with the three physical regimes forced by tidal activity and bathymetry described by van Leeuwen et al. (2015) and Capuzzo et al. (2018). The observed thermohaline distribution was similar to an analogous survey in August 2010 (Queste et al. 2013) and in climatological data (Janssen et al., 1999).

The spatial distribution of oxygen saturations confirmed the three hydrographic regimes: fully mixed shallow waters where oxygen was supersaturated in the south; transition waters with high primary production (between coastal waters and Dogger Bank); stratified O_2-supersaturated waters with $c(O_2)$ maxima at thermocline depth (north of the Dogger Bank).

Seasonal stratification in the North Sea generally starts developing in late spring, decoupling the surface mixed layer from the bottom mixed layer, and lasts until autumn (Pingree and Griffiths, 1978; Janssen et al., 1999). An increase in stratification time can have either a positive or negative impact on regional primary production. A longer stratification time in the North Atlantic can decrease the net shelf edge influx of

nutrients, reducing primary production rates especially in the northern North Sea. At the same time, an increase in stratification time can prolong the annual growing season in areas that are not nutrient limited such as the stratified waters south of the Dogger Bank where nutrient flux is maintained by river input and photosynthesis can last until thermocline breakdown (Holt et al., 2010; Holt et al., 2012).

2.6.4.4 North Sea metabolic rates in late summer 2019

On average, the North Sea surface waters were in net metabolic balance with (–3±40) mmol m^{-2} d^{-1}. Overall, no statistically significant correlation was found between net oxygen production ($N(O_2/Ar)$) and gross oxygen production ($G(^{17}O)$) in surface waters. Higher, but still insignificant correlation was found when dividing the dataset into stratified and non-stratified stations. This suggests that biological oxygen production and loss by respiration were strongly coupled. Results also suggest that some of the production occurred below the surface in stratified areas. The discussion of metabolic rates is structured according to hydrographic regimes: fully mixed coastal waters, stratified waters in the south, and stratified waters in the central and northern North Sea, which include stratified waters influenced by Baltic outflow.

2.6.4.5 Fully mixed coastal waters

Fully mixed coastal waters showed great differences between the southern and northern North Sea. Southern stations off the Thames Estuary, Wadden Sea and German Bight were oxygen supersaturated ((3.5±0.5) %), highly productive ($G(^{17}O)$ = (360±110) mmol m^{-2} d^{-1}), and net heterotrophic ($N(O_2/Ar)$ = (–5±18) mmol m^{-2} d^{-1}). We followed (Seguro et al., 2019) method for converting $G(^{17}O)$ into carbon equivalents using photosynthetic quotient (1.32; (Laws, 1991)). According to Tilstone et al. (2023), our results for *G*, converted to C equivalents, of (3.1±0.9) g m^{-2} d^{-1} matched their August 90th percentile of (3.0±1.5) g m^{-2} d^{-1} for remote sensing-derived primary production.

A model study by Daewel and Schrum (2013), estimated high primary production rates in UK and southern European continental shelf coastal waters. The southern coastal waters were also seen to be highly turbid during the sampling period. These areas are constantly nutrient enriched given the discharge of major European rivers including the Scheldt, Maas, Rhine, Weser, and Elbe. Here, riverine nutrient inputs have historically fuelled enhanced primary production (Pätsch and Radach, 1997; Radach and Pätsch,

2007), also leading to the formation of harmful algal blooms (Cadée and Hegeman, 1986; Kraberg et al., 2019).

In contrast, Capuzzo et al. (2018) saw the southern fully mixed waters near continental coasts as one of the least productive areas of the North Sea. The basis of this argument is the effect of tidal forcing on resuspended particulate matter (SPM), which limits the penetration of solar radiation. In addition, strong tidal energy dissipation has a dilution effect on phytoplankton biomass, forcing primary producers into turbid and shaded portions of the water column (Zhao et al., 2019).

Both $G(^{17}O)$ and $N(O_2/Ar)$ estimates here do not take into account the effects of advection (Jonsson et al., 2013a; Kaiser, 2011). Given the observed local high turbidity and low gas transfer velocity (Figure 20), it is possible that the observed high $G(^{17}O)$ and $N(O_2/Ar)$ values were not of local origin, but advected from adjacent regions such as the English Channel. Warm Atlantic waters from the English Channel generally dominate the Southern Bight currents field (Winther and Johannessen, 2006). Such waters might have preserved $^{17}\Delta$ and $\Delta(O_2/Ar)$ signals from eutrophic waters of the north-eastern English Channel (e.g., Bay of Somme) (Desprez et al., 1992; Lefebvre et al., 2011). A recent study seems to support this hypothesis since it showed that mixing of oceanic and estuarine endmembers partially determines the concentrations of biologically active gases in the English Channel Costal waters (Sims et al., 2022). However, the timescales of advection in the eastern English channel (from hours to weeks, see Holt et al., 2010) are usually much slower than gas-exchange timescales (hours in fully mixed shallow waters) (Sims et al., 2022). Therefore, given the fact that all southernmost stations were fully mixed, it is more plausible to consider that gross and net production rates here estimated were of autochthonous origins.

2.6.4.6 Stratified waters in the western and eastern transition zones and the Oyster Grounds

Capuzzo et al. (2018) defined the eastern and the western 'transition' zones as among the most productive regions of the North Sea. The western zone is located between Humber Estuary and the western edge of Dogger Bank. The eastern zone is between the Ringkøbing Fjord and the eastern edge of Dogger Bank. Both zones showed the $G(^{17}O)$ across the entire study region: (500±90) mmol m^{-2} d^{-1} in the west, and (471±10) mmol m^{-2} d^{-1} in the east. Both zones were included within the *NW coasts* group in

Copernicus remote sensing dataset (Tilstone et al., 2023). Therefore, our results for G converted in carbon equivalents (west zone: (4.3±1.8) g m^{-2} d^{-1}; east zone: (4.0±2.0) g m^{-2} d^{-1}) exceeded the historical 90th monthly percentile for primary production by 32 %. This coincided with highly variable $N(O_2/Ar)$ values: The western zone was net heterotrophic ($N(O_2/Ar)$ = (–29±21) mmol m^{-2} d^{-1}), while the eastern zone was net autotrophic ($N(O_2/Ar)$ = (9±10) mmol m^{-2} d^{-1}). This suggested that despite the high $G(^{17}O)$, respiration was even higher in the western transition zone. Physical forcings such as tidal activity together with river runoff may explain the high $G(^{17}O)$ and heterogeneous $N(O_2/Ar)$. In the western transition zone, organic material and nutrient inputs discharged from the Humber can be traced up to 50 km away from the East Anglian coasts (Bristow et al., 2013) and thus to measured stations. Similarly, stations in the east were affected by Weser and Elbe river discharges (Große et al., 2017) and runoff from Danish fjords (Håkanson et al., 2007). High $G(^{17}O)$ could be fuelled by nutrient inputs coming from continental waters of the major rivers.

Model simulations showed that both areas are frontal systems and represent highly dynamic transitions from permanently stratified to seasonally stratified waters (Zhao et al., 2019). Frontal systems are often associated with high primary production, especially during late summer (Miller et al., 2015; Belkin et al., 2009; Le Fèvre, 1987). This is due to the injection of resuspended nutrients from the bottom into the nutrient depleted surface mixed layer, at neap tides. At the same time, the resuspension of particulate organic matter shades a smaller portion of the water column compared to shallow fully mixed coastal areas (Zhao et al., 2019). Due to variations in tidal energy and bathymetric morphology (Loder et al., 1994), the eastern and western transition zones are highly heterogenic.

Oxygen was undersaturated at all depths of station 39 near Oyster Grounds, likely due to intense respiration. This site was previously studied by Greenwood et al. (2010) and by Queste et al. (2013). Surface waters were net heterotrophic ($N(O_2/Ar)$ = –30 mmol m^{-2} d^{-1}), and $G(^{17}O)$ was lower than other areas south of the Dogger Bank (267 mmol m^{-2} d^{-1}). Also, $N(O_2/Ar)$ accounted for 99 % of calculated $F(O_2)$, which suggests that respiration was the dominant oxygen loss. Bottom water $c(O_2)$ and saturation anomaly were the lowest of the entire CEND1219 dataset (188 mmol m^{-3}, –27 % respectively). Similar saturations were observed in 2007–08 mooring data Greenwood et al., 2010),

in 2010 CTD casts (Queste et al., 2013) and the NSBC climatologies, suggesting that this is a site prone to intense oxygen loss by respiration.

In contrast to the areas in the southwest North Sea, the Moray Firth (Stn 79) and stations 76, 77, 124, and 126 showed low $G(^{17}O)$ (39 mmol m^{-2} d^{-1}), negative $N(O_2/Ar)$ of –16 mmol m^{-2} d^{-1}, near-zero surface $\Delta(O_2)$ and mild undersaturation at bottom depths with $\Delta(O_2)$ = –2.0 %. The low production rates encountered in this part of the North Sea was unexpected considering that North Atlantic waters are usually an important supply of nutrients into the North West European Shelf fuelling primary production (Brion et al., 2004; Vermaat et al., 2008). However, compared to the southern areas with riverine inputs, North Atlantic waters may still bring in fewer nutrients (Mathis et al., 2019). Reduced nutrient content in North Atlantic inflow waters could also be due to intense denitrification and primary production along-side the main influx at shelf break (Hydes et al., 2004). Nutrient data might help to verify the cause of low gross production in the northwest North Sea, but unfortunately, none were obtained during the cruise.

2.6.4.7 The stratified waters in the central and northern North Sea

The strong stratification observed in open waters north of Dogger Bank coincided with $N(O_2/Ar)$ = (10±6) mmol m^{-2} d^{-1} and $G(^{17}O)$ = (244±61) mmol m^{-2} d^{-1}. For seasonally stratified shelf waters it is often assumed that production at the end of summer is fuelled by remineralised nutrients (Falkowski and Raven, 2007). However, high new production can occur in subsurface waters, reaching rates on the order of spring bloom production (Sharples et al., 2001). In this region, bottom and the surface mixed layers were separated by a thick thermocline, given the deepening bathymetry with latitude. Stations located in the central and northern North Sea showed oxygen saturation maxima at thermocline depths, indicating that part of gross oxygen production probably occurred at the thermocline depths. This was confirmed by the $^{17}\Delta$ values, which were closer to the pure photosynthetic endmember values (250 ppm; Luz, 2000) at 30 m of depth ((125±11) ppm) than at the surface ((47±2) ppm). By the end of the growing season, regions of strong stratification are usually affected by steep vertical nutrient gradients. These are forced by photosynthetic consumption in the euphotic zone and by a weaker response to tidal forcing (Zhao et al., 2019). Queste et al. (2013) also associated thermocline oxygen maxima with deep chlorophyll maxima (DCM) in the

same region and in the same season (late August). This confirms that in late summer, DCMs are still a consistent and widespread feature of the northern North Sea at around 30 m of depth. DCMs in the northern North Sea were estimated to account for more than 50 % of summer water column production-rate in the northern north sea (Fernand et al., 2013).

While most of stratification observed in the northern North Sea can be attributed to thermal gradients, the eastern North Sea was stratified due to salinity gradients. The salinity reversal observed in stations 109, 111, 113, and 115 can be caused by lateral flow of surface freshwater currents coming from the Baltic flowing above denser North Sea waters (van Leeuwen et al., 2015). As for the rest of the northern North Sea, estimated $N(O_2/Ar)$ was mildly net autotrophic ((5.3±2.9) mmol m^{-2} d^{-1}) in this area and it was sustained by strong surface gross production flux ($G(^{17}O)$ = (202±58) mmol m^{-2} d^{-1}). According to model simulations, strong shelf edge currents can fuel substantial primary production rates during late summer, by resuspending deposited organic material (Bendtsen and Richardson, 2020).

Finally, stations in this area recorded $\delta(^{18}O)$ maxima at depths below photosynthetic activity. This is due to strong respiration readily consuming the newly formed organic material sinking down from thermocline depths.

2.7 Conclusions

The first North Sea basin wide measurements for net ($N(O_2/Ar)$) and gross ($G(^{17}O)$) oxygen production showed that surface waters were in balance during a particularly warm late summer in August 2019. Spatial distribution for both $N(O_2/Ar)$ and $G(^{17}O)$ signals varied largely between south and north and between stratified and non-stratified waters confirming that pelagic metabolism is strongly influenced by a multitude of drivers such as nutrient source, light availability, and hydrography. Elevated rates of gross production were seen in the fully mixed coastal areas in the south, confirming monthly averages shown from remote-sensing dataset. However, results from triple oxygen isotopes in this case should be interpreted carefully since they do not consider the effects of lateral transport. The “transition” zones were the most productive surface waters of the North Sea in August 2019, particularly off the East Anglian coast. Despite being the most productive, the transition zones were also net heterotrophic suggesting that respiration was higher than gross production. Finally, dominant net autotrophy was

observed at surface waters in the central and northern open waters but could have been biased by the effect of subsurface primary production, due to DCM formation, combined with vertical transport. The entrainment of $G(^{17}O)$ rich waters from below could result in overestimating G signals in the surface mixed layer. To correct bias from vertical and lateral transport non-steady state fluxes need to be integrated into $N(O_2/Ar)$ and $G(^{17}O)$ calculations (Seguro et al. 2021). This implies the collection of samples over time to establish time derivatives for all variables. Future investigation could integrate time series data to routine spatial measurements in targeted locations prone to advection (e.g., Southern Bight) and entrainment (e.g., north-eastern North Sea) to calculate the fluxes with adjacent waters. Alternatively, implementing $N(O_2/Ar)$ and $G(^{17}O)$ in marine ecosystem models coupled to a regional ocean model could be used to calculate advection and vertical transport.

To conclude, this study offers the first dataset of triple oxygen isotopes and oxygen/argon saturation anomalies in the North Sea. This has added new information on the distribution of late summer growth and remineralisation. In the future, this be used as in situ monitoring method for gross and net community production.

Chapter 3: Using the ERSEM model to determine best practice for net community production measurements at station L4, Western English Channel

3.1 Abstract

In marine systems, net community production (N) describes the net balance between gross primary production and total respiration. N can be inferred from coincident changes in the concentration of oxygen and argon in sea water $N(O_2/Ar)$. $N(O_2/Ar)$ is often equated with the biological flux of oxygen ($F_{bio}(O_2/Ar)$), defined as the fraction of the oxygen air-sea exchange flux that is a result of biological activity. However, this approach neglects the effect of mixing, and assumes the system is in a steady-state. In highly dynamic environments, such as shallow, tidally active shelf seas, this approximation may lead to large errors in the estimation of N.

We developed an Observing System Simulation Experiment (OSSE) to quantify the error associated with assuming $N = F_{bio}(O_2/Ar)$ in a shallow, tidally active shelf sea environment. This was achieved by adding argon (Ar) to the European Regional Sea Ecosystem Model (ERSEM) and running the model in 1D using the General Ocean Turbulence Model (GOTM), configured to simulate dynamics at the long-term ocean time-series site, Station L4, in the Western English Channel.

The model was validated against discrete O_2/Ar measurements at Station L4 for the years 2009 to 2010. $N(O_2/Ar)$ was then diagnosed from simulated oxygen and argon concentrations and compared with net community production calculated directly from simulated photosynthetic and respiratory fluxes (N(ERSEM)).

While considering typical measurement errors associated with the determination of oxygen and argon concentrations, we also determined the ideal sampling frequency at Station L4. A sampling frequency of one sample per 2 hours was determined to be optimal and would yield a factor of 10 improvement in the estimation of N when compared with the current weekly sampling protocol. Results showed that assuming N(ERSEM) = $F_{bio}(O_2/Ar)$, when sampling frequency matches Station L4 strategy, introduces a percentage error in the estimation N of up to 75 % compared to the error

in diagnosed $N(O_2/Ar)$. When setting the vertical integration to a depth horizon such as the mean annual euphotic depth at Station L4 (28 m), vertical mixing across the base of the euphotic zone is calculated to introduce a further error of between 15 % and 28 % of the total $N(O_2/Ar)$ flux during periods of high and low metabolic activity respectively. This error can be eliminated by integrating N over the full water column.

These results indicate the importance of accounting for non-steady-state conditions in dynamic shelf sea environments when using oxygen and argon concentrations to determine N. Although lateral transport has not been considered here, it is also likely to be an important factor, which could be investigated using 3D simulations. Quantitative net community production rates at L4 provide a direct estimate of carbon fluxes and may thus improve and advance the ERSEM model because they represent observations that are directly comparable to ERSEM parameters.

3.2 Introduction

The method for estimating pelagic net community production (N) in oxygen equivalents based on the ratio of oxygen and argon gas concentrations has received considerable attention in past decades. The basis of this method is derived from the fact that Ar is very similar to O_2 in respect to physical properties such as solubility and diffusivity and at the same time is totally inert to biological activity (Craig and Hayward, 1987). Ar is therefore used to isolate the biological O_2 saturation anomaly $\Delta(O_2/Ar)$. Over a sufficient time-scale N can be assumed in steady-state with air-sea flux of biological oxygen, thus N is estimated as the rate of air-sea exchange of biological O_2 $F_{bio}(O_2/Ar)$.

Although $F_{bio}(O_2/Ar)$ has been used widely as an estimation of N in open ocean environments (Cassar et al., 2009; Hamme et al., 2012; Kaiser et al., 2005), few studies have been carried out in shelf seas, where the steady-state assumption is less likely to hold. In northwest European shelf seas (NWESS) only three studies have used oxygen triple isotopes to estimate gross O_2 production (Gloël, 2012; Seguro et al., 2019; and this project). In August 2019, we estimated $F_{bio}(O_2/Ar)$ from hydrocasts across the North Sea on research cruise CEND1219 (See Chapter 2). However, samples were not repeated in time mandating the steady-state assumption. Seguro et al. (2019) reported on samples collected in 2015 along a repeat cruise track in the Celtic Sea and along the shelf edge, with time intervals of days to weeks between samples. Also, Gloël (2012) established a yearlong time series at Station L4 in 2009/10. Both datasets allowed the inclusion of changes in the oxygen triple isotope composition over time, not requiring the steady-state-assumption. In addition, both Gloël (2012) and Seguro et al. (2019) collected water samples at different depths. This allowed the effect of vertical diffusive mixing to be included in calculations of net biological O_2 balance, with the diffusive O_2 flux estimated across the base of the integration depth (taken to be the average euphotic depth). Combining the steady-state based estimate of $F_{bio}(O_2/Ar)$ with temporal changes (F_n) and vertical diffusive fluxes (F_v) of $\Delta(O_2/Ar)$ allowed Gloël (2012) and Seguro et al. (2019) to generate a more complete and therefore likely to be more accurate estimate of net O_2 production:

$$N = N(O_2/Ar) = F_{bio}(O_2/Ar) + F_n(O_2/Ar) + F_v(O_2/Ar) \qquad (20)$$

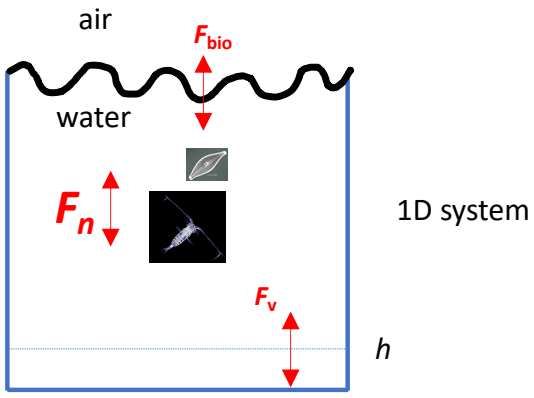

Figure 26: Schematic of the processes involved in eq. (20) where F_{bio} represents the air-sea flux term, F_n is the time disequilibrium term and F_v is the vertical diffusive flux.

Jonsson et al. (2013) and Teeter et al., (2018) used a box model to demonstrate that without information on temporal changes F_{bio} detects a weighted average of past productivity rates rather than an instantaneous value. However, these studies were based on simple box models with prescribed N and did not quantify the error of assuming $N = F_{bio}$ in a more realistic, spatially structured environment.

Past studies observed that upwelling in coastal and equatorial regions may lead to O_2/Ar undersaturation in surface waters, resulting in the misinterpretation of estimated $N(O_2/Ar)$ (Haskell et al., 2017). Meanwhile, Jonsson et al. (2013) used a biogeochemical ocean circulation model of the Southern Ocean to quantify the vertical exchange of biological oxygen across the base of the mixed layer, and to estimate the error derived from vertical transport and mixing when assuming that N is equal to the sea-to-air flux of biological oxygen (F_{bio}). Overall, they found that, excluding regions undersaturated in biological oxygen, F_{bio} was underestimating N by 5–15 % due to unaccounted for vertical transport and mixing. While this study was pertinent to oceanic waters, its relevance to shallow, dynamic shelf seas is unclear.

In this study, we used Observing System Simulation Experiments (OSSEs) to explore how much the different terms in Eq (20) contribute to $N(O_2/Ar)$ and how frequently they need to be measured. This was done using the time series at L4 Station collected by Gloël (2012) as case study.

3.3 Aims

The aim of this study was to evaluate the error in the estimation of $N(O_2/Ar)$ at Station L4 under the assumption of steady-state using models; and to investigate its dependence on the integration depth and sampling frequency. We formulated the following research questions:

Q1.) What is the magnitude of the error introduced by the approximation $N = F_{bio}(O_2/Ar)$ and how does this error vary over the seasonal cycle?

Q2). What is the magnitude of the error associated with the diffusive flux of oxygen and argon across the base of the integration depth in a dynamic turbulent water column such as L4, and is there a difference between seasons?

Q3.) What is the ideal sampling strategy for $N(O_2/Ar)$ at L4? Furthermore, does the ideal strategy match routine observations; and if not, what is the magnitude of the error when compared to the ideal sampling frequency?

This chapter aims to provide best practice for establishing regular base measurements of $N(O_2/Ar)$ in shelf sea applications and contextualising the already existing biological datasets such as L4 dataset with quantitative metabolic rate estimates.

3.4 Methods

In this section we provide a description of the different terms used to compute $N(O_2/Ar)$. Next, we describe the model system, the numerical method used to integrate the model forward in time, the L4 configuration, and the approach for evaluating the model's performance using *in-situ* data. Finally, we describe the method used to estimate $N(O_2/Ar)$, and to compare it with the value of N computed directly by ERSEM in the context of the three core research questions.

3.4.1 Study Area

Station L4 (50.25° N, 4.2167° W) is located 13 km south-southwest of Plymouth. The site is part of the WEC Observatory, a long running time series site where measures of plankton species composition were started in 1988 (Southward et al., 2004). Since 2000 the dataset has been extended to include CTD profiles and nutrient data, with samples collected on a weekly basis weather permitting. Since 2008 the station has included a moored buoy collecting meteorological data such as windspeed and direction,

atmospheric pressure, air temperature and solar radiation which are combined with the marine data such as temperature, salinity, fluorescence, turbidity, oxygen, and nutrient concentrations. The autonomous buoy collects data every hour before transmitting it back to Plymouth Marine Laboratory (PML) (Smyth et al., 2010). The L4 site has a depth of approximately 55 m and is seasonally stratified. It is also influenced by inputs from the Rivers Tamar and Plym. The growing season at L4 follows the onset seasonal stratification in the Spring, when net surface heating becomes positive; and ends in late September with the disruption of vertical stratification coinciding with net surface heating turning negative. Seasonal succession in planktonic groups is seen through time with a tendency toward decreasing size over the spring to summer transition, starting with the bigger diatoms at the onset of the growing season at the surface and ending with picophytoplankton at the bottom of the thermocline in late summer (Southward et al., 2004). This determines the formation of two major chlorophyll *a* concentration maxima across the growing season, one located at the surface (during spring and in some years in autumn) and the other located at the base of the thermocline during mid-summer (Smyth et al. 2010). Observations from L4 have been routinely used in the last decades for the development and validation of the European Regional Sea Ecosystem Model (ERSEM) (Butenschön et al., 2016).

3.4.2 The ERSEM-FABM-GOTM model

We configured 1D simulations for Station L4. To do so we used the European Regional Sea Ecosystem Model (ERSEM) (Butenschön et al., 2016) coupled to the 1D General Ocean Turbulence Model (GOTM) (Burchard et al., 1999) using the model coupler Framework for Aquatic Biogeochemical Model (FABM) (Bruggeman and Bolding, 2014). The ERSEM model was extended to include argon as a new tracer.

3.4.2.1The marine ecosystem model: ERSEM

The ERSEM model, described by Butenschön et al. (2016), is a marine ecosystem model for the lower trophic levels of the marine food web. The pelagic component of ERSEM includes 8 biological functional groups, including producers (4 groups), consumers (3 groups) and decomposers (1 group). The groups are distinguished by the size of organisms they represent and other significant biogeochemical traits (e.g., Si uptake in diatoms). Various forms of particulate and dissolved organic matter are included together with 4 nutrient state variables. The model also a description of pelagic

nitrification, which consumes oxygen. ERSEM explicitly represents five elements (C, O, N, P, and Si), which are cycled within the system by the biological functional groups, in fully dynamic stoichiometric ratios (except for mesozooplankton and benthic consumers, which have fixed stoichiometry). The equations describing the pelagic model are closed by horizontal boundary conditions describing the air-sea flux and surface fluxes across the sediment-water interface. In this investigation, lateral transport at all levels and vertical transport with the benthic system were excluded.

3.4.2.2 Argon

The argon concentration was added as a new state variable to ERSEM (Figure 1).

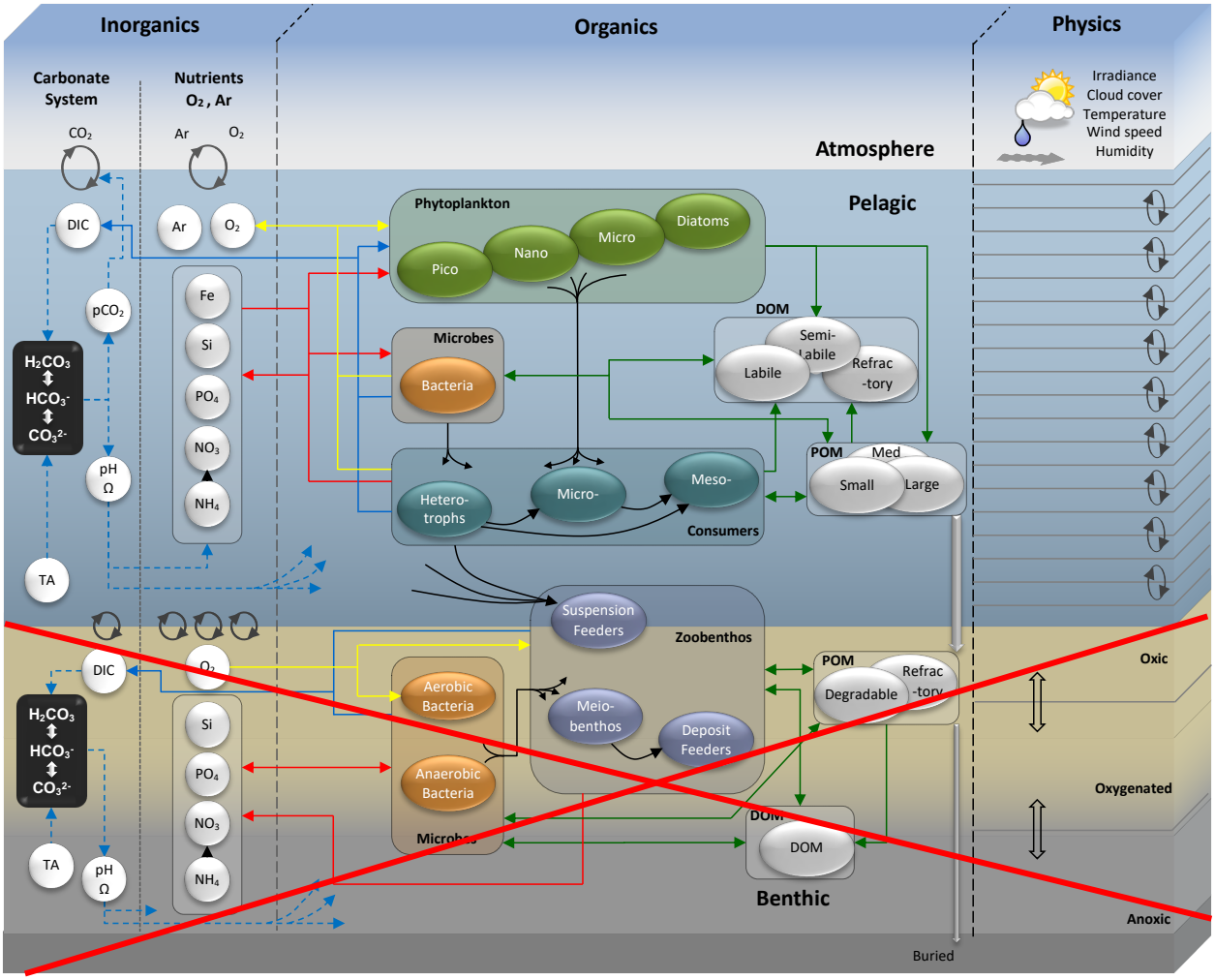

Figure 27: Schematic of the ERSEM-GOTM model setup showing all model dependencies between the inorganic and organic sub models (modified from Butenschön et al., 2016). This schematic also includes the addition of argon made in this study. Model code for argon is an analogue to the oxygen module. Internal physical transport is solved only in the vertical

directions by diapycnal diffusion (See validation section for more details). For this study, the benthic system was switched off (red cross) to decrease complexity and computing burden for online and post processing calculations.

The argon model includes parameterisations for air-sea gas exchange, and solubility changes as a function of temperature and salinity. The dependence of argon solubility on temperature and salinity was implemented using the polynomial equation of Hamme and Emerson (2004). Argon air-sea gas exchange was formulated as follows, with k parameterised as per Eq. (14).

$$F_{\mathrm{air-sea}}(\mathrm{Ar}) = k\big(c_{\mathrm{sat}}(\mathrm{Ar}) - c(\mathrm{Ar})\big) \tag{21}$$

In this study, the oxygen base model was also modified from the public version of ERSEM by implementing the parametrisation of $c_{sat}(O_2)$ described by (García and Gordon, 1992), which were also used by Gloël (2012).

3.4.2.3 Numerics

Coupled to the General Ocean Turbulence Model (GOTM; Burchard et al., 1999) and run in 1D, the GOTM-FABM-ERSEM model solves the equation:

$$\frac{\partial}{\partial t}c = \frac{\partial}{\partial z}K_{\mathrm{z}}\frac{\partial}{\partial z}c - w\frac{\partial}{\partial z}c + \frac{\partial}{\partial t}c\Big|_{\mathrm{bgc}} \tag{22}$$

where K_z is the vertical diffusivity ($m^2\ s^{-1}$), and w is the vertical velocity ($m\ s^{-1}$). The is advection-diffusion equation in 1D, modified to include biogeochemical sink and source terms. In all simulations presented here, we exclude the contribution of advection by setting $w = 0$. Approximate numerical solutions are generated by separating the contributions of transport and mixing, and biogeochemical sinks and sources. These changes are then merged to express the total rate of change of a state variable *c,* expressed as a concentration (Butenschön et al., 2012):

$$\frac{\partial c}{\partial t} = \frac{\partial c}{\partial t}\Big|_{\mathrm{trp}} + \frac{\partial c}{\partial t}\Big|_{\mathrm{bgc}} \tag{23}$$

Subscript "trp" represents the rate of change due to transport, and subscript "bgc" represents the rate of change due to biogeochemistry. The time discretisation used in

ERSEM-FABM-GOTM system is based on equidistant time steps, Δt (Butenschön et al., 2012):

$$c_{n+1} = c_n + \phi\left(\left.\frac{\partial c}{\partial t}\right|_{\text{trp}} + \left.\frac{\partial c}{\partial t}\right|_{\text{bgc}}, \Delta t\right) \tag{24}$$

where n is the discrete time index. c_n is the initial condition required by the integral operator ϕ to calculate the new values for c in the following time step (n+1). Here, Eq. (24) is solved using Operator Splitting (Strang, 1968). This coupling method separates the transport and biogeochemical components of Eq. (24) into two separate subsystems which are solved *sequentially* (Butenschön et al., 2012):

$$\gamma = c_n + \phi_{\text{trp}}\left(\left.\frac{\partial c}{\partial t}\right|_{\text{trp}}(c_n), \Delta t\right) \tag{25}$$

$$c_{n+1} = \gamma + \phi_{\text{bio}}\left(\left.\frac{\partial c}{\partial t}\right|_{\text{bgc}}(\gamma), \Delta t\right) \tag{26}$$

where γ represents the concentrations after transport and mixing has occurred. Such intermediate concentrations are not included in the simulation output file, but are needed to accurately compare the prognostic and diagnostic calculations of N. The solution to Eq. (25) requires the specification of boundary conditions for all tracers. Both oxygen and argon are exchanged across the air-sea interface. However, this is ignored in the integration of Eq. (25), where the air-sea interface is treated as an impermeable barrier using a Neuman boundary condition, with $\partial c/\partial z = 0$. The effect of air-sea exchange is instead folded into Eq. (26), where it is treated as an internal sink/source term within the surface layer.

Each state variable in ERSEM has its own rate equation (Butenschön et al., 2016). In the case of oxygen, the time rate of change of oxygen can be written as:

$$\left.\frac{\partial}{\partial t}c\right|_{\text{bgc}} = F_{\text{air-sea}} + G - R \tag{27}$$

$$F_{\text{air-sea}} = k\left(c_{\text{sat},0} - c_0\right) \tag{28}$$

ERSEM computes solutions for air-sea exchange and in the case of oxygen it also considers production by photosynthesis and respiration by phytoplankton, zooplankton

and bacteria (Eq. (27) and Eq. (28)). As air-sea gas exchange is only solved at the air-sea interface (subscript 0 in Eq. (28)), and is valid for the surface layer only (Butenschön et al., 2016).

In GOTM, the water column is divided into M (e.g., N = 100 at L4) layers of non-equal thickness $h(j)$ (Burchard et al., 1999):

$$h(j) = z(j) - z(j-1), j = 1, \dots, M \tag{29}$$

where j is the depth index and z(j) the depth variable. The discrete values for concentration quantities such as salinity S and oxygen concentration c represent a layer mean and are located at layer centres (j+1/2). Turbulence variables like vertical diffusivity of heat (K_z) are evaluated at layer interfaces (j+1). The layer indexing is organised in ascending order (bottom depths have lower indexing than surface depths) so that the layer interface below a layer centre has the same index and so that the total number of layer interfaces exceeds the total number of layer centres by 1. The sign convention for turbulent quantities is set that a positive flux is directed downwards, and a negative flux upwards (Burchard et al., 1999) (Figure 28).

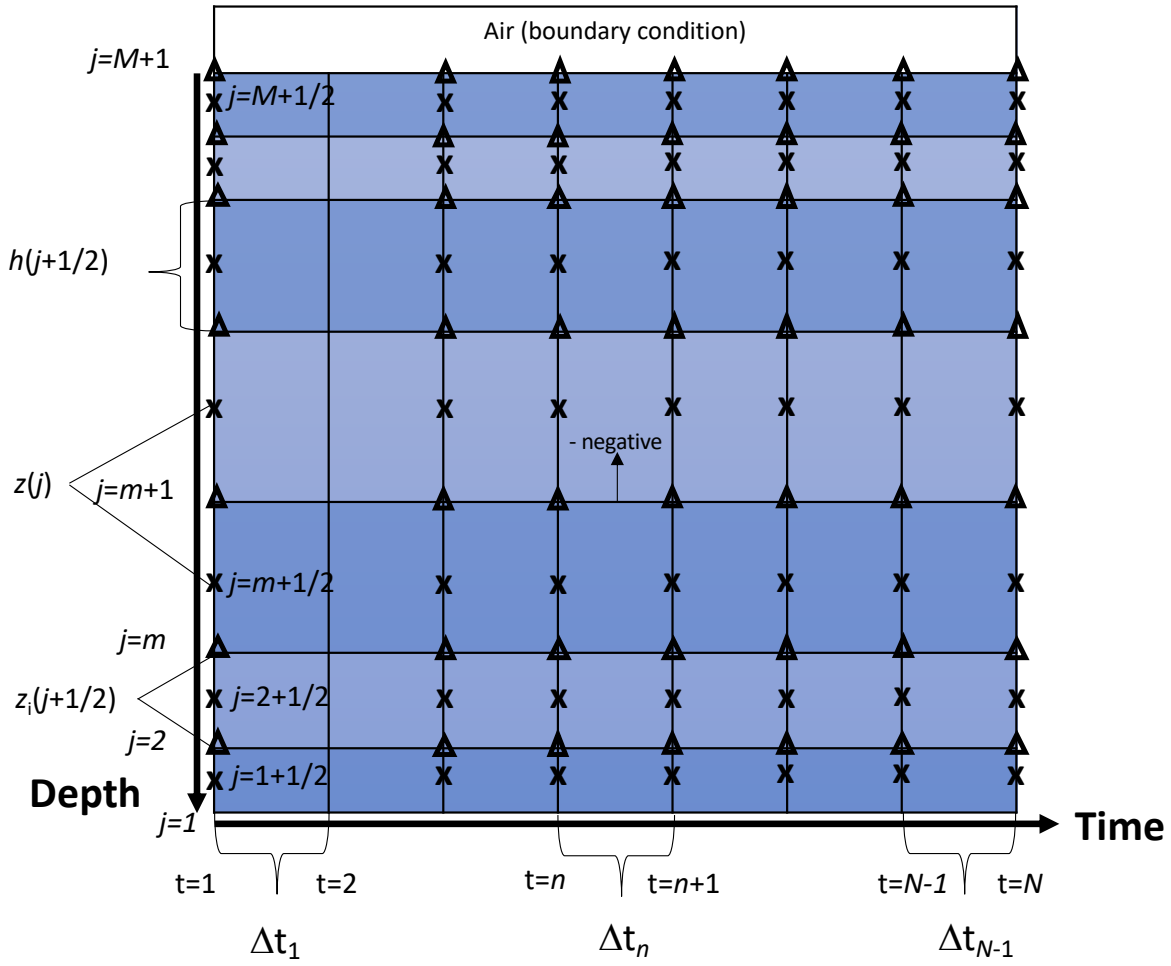

Figure 28: ERSEM-FABM-GOTM time and space organisation, discretisation, and sign convention. Time and space discretisation for concentration values are only affected by transport or by biogeochemistry and are represented in Eq. (24). Black triangles represent the time and space discretisation for vertical velocities. Black crosses represent the time and space discretisation for concentrations at the end of Operating Splitting integration which are returned in the simulation output file.

3.4.2.4 Simulation setups

All simulation runs were set to cover the period 2009–10 matching the period covered by $N(O_2/Ar)$ observations and using 2 years as model spin up starting from Jan 2007 to reach system equilibrium during the period covered in the results. The resolution for the model time step was set to 60 s and simulation results were saved as instantaneous values (i.e., without time averaging). The water column was broken up into 100 vertical σ-layers (Phillips, 1957). The thickness of vertical layers is uneven, with a zooming in applied at the bottom and surface. This method has the function to increase the

resolution in key portions of the water column (i.e., near to the surface and bottom interfaces; Figure 3).

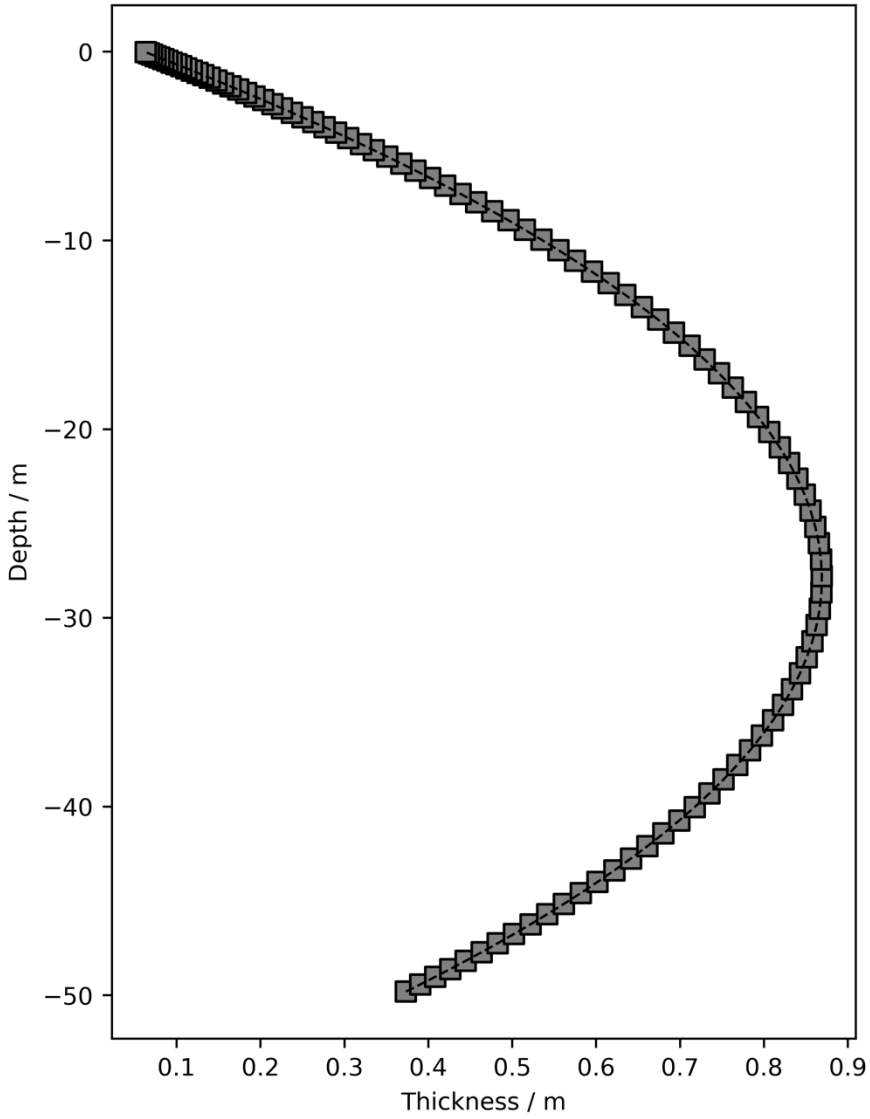

Figure 29: Vertical discretisation setup used in this investigation.

All site-specific forcing setups followed Powley et al. (2020) but adopting slight modifications to assist with achieving mass balance for dissolved oxygen and argon gas. Specifically, the model was run with a fixed sea surface elevation. The meteorological forcing data includes wind speeds, 2 m air temperature, 2 m dew point temperature, cloud cover, precipitation, and short-wave radiation extracted from ERA5 reanalysis data (which is set at a 0.25° × 0.25° resolution) (Copernicus Climate Change Service (C3S), 2017). The 1D model was relaxed toward observations for salinity and temperature profiles (Fishwick, 2018) using a restoring timescale of 1 month.

To simplify the model, the benthic system was switched off, meaning the only processes influencing tracer concentrations are those occurring in the water column. To do so all benthic biological activity (zoobenthos and benthic bacteria) and the related exchange of oxygen and dissolved inorganic carbon (DIC) across the sediment-water interface were switched off. In essence, the boundary condition at the seabed was limited to the flux of benthic dissolved organic matter, benthic particulate organic matter, benthic refractory matter, and benthic calcite. These are essential for the correct running of the pelagic model since they are coupled to the sinking and deposition of pelagic particulate organic material (POM) and pelagic calcite (Butenschön et al., 2016) (Figure 1).

3.4.3 Calculating *N* from the biological oxygen saturation anomaly

This section shows the formulations and explanation of the various terms composing Eq. (20). Major equations shown in this section were derived from the mass balance equations of dissolved oxygen and dissolved argon following algebraic manipulations shown in details by Gloël (2012).

3.4.3.1 $F_{bio}(O_2/Ar)$: the net air-sea gas exchange of biologically processed oxygen

The $F_{bio}(O_2/Ar)$ term represents the fraction of air-sea gas exchange that is made up of biological oxygen. The term has two components:

$$F_{bio}(O_2/Ar) = F_a + F_g \quad (30)$$

F_a represents the portion of biologically processed oxygen, expressed as the saturation anomaly ($\Delta(O_2/Ar)$), that is involved in air-sea gas exchange. F_a is a function of the wind speed, with higher wind speeds yielding higher fluxes across the air-sea interface:

$$F_a = k c_{sat}(O_2)\Delta(O_2/Ar) \quad (31)$$

Gloël (2012) and others calculate k using a weighted scheme (Reuer *et al.*, 2007) over the history of windspeeds prior to the sampling date. The size of the window is chosen to ensure that the weighted k value converges (i.e., over a multiple of the residence time of oxygen in the mixed layer). Previous works used fixed values, e.g., 60 days in open ocean waters (Reuer et al., 2007) or 30 days in coastal waters (Teeter et al., 2018).

However, such time windows are arbitrary and should not be taken as fixed values (Reuer et al., 2007). This averaging scheme requires the uses of historical data for windspeeds, e.g., from satellite scatterometer or reanalysis windspeed products.

Together, the product $c_{sat}(O_2)\Delta(O_2/Ar)$ represents the air-sea gradient of biological oxygen in the surface layer. In a simple mass balance relationship, with no physical exchange with other water masses, oxygen produced through photosynthesis in the surface mixed layer is lost to the atmosphere via air-sea gas exchange. At steady-state, the biological O_2 air-sea exchange flux ($F_{bio}(O_2/Ar)$) and N are equal (Kaiser et al., 2005). However, the assumption of steady-state never truly applies, as changes in physical factors such as water temperature, atmospheric pressure, and bubble effects influence gas exchange with the atmosphere. Using argon as an abiotic analogue for O_2 makes it possible to correct for these factors (Craig and Hayward, 1987) because O_2 and Ar share similar physical properties (Table 3).

Table 3: Effects of air injection and temperature changes on N_2, Ar, and O_2 saturation anomalies, together with supersaturation in mixing due to the nonlinear temperature-dependence of the saturation concentration. Where row 4 represents the products of Bunsen solubility coefficients and molecular diffusion coefficients in sea water at 22°C. The effects on oxygen and argon are almost identical (extracted from Craig and Hayward, 1987)

Process	N_2	O_2	Ar
Air injection (1 ml kg^{-1})	7.67 %	3.75 %	3.42 %
$\Delta T = 1$ °C	1.79 %	2.00 %	2.01 %
Mixing (10 °C + 20 °C)	0.86 %	0.98 %	0.94 %
$(\beta D)_i/(\beta D)_{Ar}$ (22 °C)	0.38	0.90	1

The biological component of the oxygen saturation anomaly can be isolated from the physical component using the argon saturation anomaly as follows (Craig and Hayward, 1987):

$$\Delta(O_2/Ar) = \frac{c_w/c'_w}{c_{sat}/c'_{sat}} - 1 \qquad (32)$$

c and c’ stand for the O_2 and Ar concentrations, respectively. The index "w" refers to the water sample; and the index "sat" to air-saturated water at the temperature and salinity of the sample.

The F_g term from Eq. (30) represents the difference in the physical properties of oxygen and argon gas during air-sea gas exchange. Although the two gases share very similar diffusivity and solubility properties, they are not identical to one another (Table 3). These discrepancies are accounted for using the equation:

$$F_g = kc_{sat}(s_0 - \Delta(O_2/Ar))\left(1 - \sqrt{\frac{Sc}{Sc'}}\frac{1 + \overline{\Delta(O_2/Ar)}}{1 + \Delta(O_2/Ar)}\right) \quad (33)$$

Sc and *Sc*’ are the Schmidt number for oxygen and argon respectively, and s_0 represents the oxygen saturation anomaly at the surface:

$$s = \frac{c}{c_{sat}} - 1 \quad (34)$$

Terms including an overbar represent depth-averaged values.

3.4.3.2 $F_n(O_2/Ar)$: the change in the biological oxygen saturation anomaly over time

The term $F_n(O_2/Ar)$ represents the change in time of biological oxygen:

$$F_n(O_2/Ar) = h\left(\frac{dc}{dt} - \frac{c}{c'}\frac{dc'}{dt}\right) \quad (35)$$

h represents the vertical layer thickness. This term requires a time series of simultaneous measurements of dissolved oxygen and argon concentrations through the water column so the time derivatives can be evaluated. This term is usually omitted in studies of $N(O_2/Ar)$ along cruise transects, which are not repeated over time (e.g., Teeter et al., 2018); or approximated for transects where there is a long time interval in-between repeat samples (e.g., Seguro et al., 2018). Without this information, $N(O_2/Ar)$ can only be calculated for the surface mixed layer assuming steady-state.

3.4.3.3 $F_v(O_2/Ar)$: the diffusion of biological oxygen across the integration depth z_{int}

The term $F_v(O_2/Ar)$ in Eq. (20) represents the vertical diffusive mixing and is a function of the vertical gradient of O_2 and Ar, and the vertical diffusivity (K_z), where all terms are taken and calculated at the integration depth (z_{int}):

$$F_{\mathrm{v}}(\mathrm{O_2/Ar}) = K_z\left(\frac{\mathrm{d}c}{\mathrm{d}z} - \frac{c}{c'}\frac{\mathrm{d}c'}{\mathrm{d}z}\right) \tag{36}$$

3.4.4 Post processing calculations for $N(O_2/Ar)$ and N(ERSEM) from model output

This section shows the post-processing calculations used to obtain $N(O_2/Ar)$. $N(O_2/Ar)$ was compared with the target value calculated directly from simulated photosynthetic and respiratory fluxes N(ERSEM). The aim of this task was to assure mass conservation within post-processing calculations. $N(O_2/Ar)$ was calculated using the results of the prognostic model ERSEM-FABM-GOTM for dissolved oxygen and argon concentrations. The different terms composing Eq. (20) were computed at different points of the water column. The term $F_{bio}(O_2/Ar)$ was calculated using values of the surface layer ($j=M$). The term representing vertical diffusion flux, $F_v(O_2/Ar)$, was calculated at the chosen integration depth (z_{int}), The time disequilibrium term, F_n, was calculated for every depth level and then summed. Combined, these yield

$$N(\mathrm{O_2/Ar}) = F_{\mathrm{bio}}(j = M) + F_{\mathrm{v}}(j = j(z_{\mathrm{int}})) + \sum_{k=j(z_{\mathrm{int}})}^{M} F_{\mathrm{n}}(k), \tag{37}$$

In sections 3.4.4.1 to 3.4.4.3, we describe how each term in Eq. (37) was calculated. $N(O_2/Ar)$ performance was compared against the difference between gross photosynthetic production and total respiration from ERSEM, N(ERSEM):

$$N(\mathrm{ERSEM}) = \sum_{k=j(z_{\mathrm{int}})}^{M} Q_{\mathrm{P}}h(k)g(k) - \sum_{k=j(z_{int})}^{M} Q_{\mathrm{R}}h(k)r(k), \tag{38}$$

The terms g and r are the gross production and respiration rates. Both g and r are expressed in carbon equivalents (mg m^{-3} d^{-1}) and need to be converted to oxygen equivalents (mmol m^{-3} d^{-1}). This was done using the conversion factors Q_P (0.11 mol g^{-1}) and Q_R (0.1 mol g^{-1}), which combine the photosynthetic (1.32 mol mol^{-1}; Laws, 1991) and respiratory quotients (1.2 mol mol^{-1}; Mayzaud et al., 2005) and molar mass of carbon (12 g mol^{-1}). Differences between $N(O_2/Ar)$ and N(ERSEM) were quantified using the root mean square difference (Δ_{RMS}):

$$\Delta_{\mathrm{RMS}} N = \sqrt[2]{\overline{e(N)^2}} \tag{39}$$

Where:

$$e(N) \; = \; N(\mathrm{ERSEM}) - \; N(\mathrm{O_2/Ar}). \tag{40}$$

Quantitative $N(O_2/Ar)$ performance over multiple (n) years was also expressed using the coefficient of determination (R^2):

$$R^2 = 1 - \frac{\sum_k e(N)^2}{\sum_k \left(N_k(\mathrm{ERSEM}) - \overline{N}(\mathrm{ERSEM})\right)^2} \tag{41}$$

$$\overline{N}(\mathrm{ERSEM}) = \frac{1}{n}\sum_{k=1}^{n} N_k(\mathrm{ERSEM}) \tag{42}$$

3.4.4.1 $F_{bio}(O_2/Ar)$: the air-sea gas exchange component

The air-sea gas exchange term $F_{bio}(O_2/Ar)$ was calculated as per Eq. (30) using concentrations for layer $j = M$ (surface).

The operator-splitting method (Strang, 1968) was included in post-processing calculations to isolate the biogeochemical concentrations at the surface level and achieve a close match between the air-sea flux calculated in post-processing and the analogue flux simulated in ERSEM.

When $F_{bio}(O_2/Ar)$ is calculated from values taken at sampling intervals Δt greater than the simulation time step, we integrate production over the residence time of oxygen in the portion of the water column included in the integration depth (z_{mix}). To do this, we

account for wind speed prior to sampling through the piston velocity using the weighted average scheme shown in chapter 2 section 2.4.7.

3.4.4.2 $F_n(O_2/Ar)$: the time disequilibrium term

$F_n(O_2/Ar)$ was defined at all depth levels as follows:

$$F_n(O_2/Ar)(j) = h(j)\left(\frac{dc(j)}{dt} - \frac{c(j)}{c'(j)}\frac{dc'(j)}{dt}\right), \quad (43)$$

A finite difference approximation was used to evaluate the time derivative in the F_n term.

3.4.4.3 $F_v(O_2/Ar)$: the vertical diffusive mixing term

The vertical diffusivity flux $F_v(O_2/Ar)$ was defined at the interface layer matching the integration depth, i.e., $j_{int} = j(z = z_{int})$:

In practice, the vertical gradient in the numerator was calculated using the python

$$F_v(O_2/Ar)(j_{int}) = K_z(j_{int})\left(\frac{dc(j_{int})}{dz} - \frac{c(j_{int})}{c'(j_{int})}\frac{dc'(j_{int})}{dz}\right). \quad (44)$$

function *numpy gradient*, which returns second order central differences (Harris et al., 2020).

3.4.4.4 Model evaluation against observations

Results from ERSEM-FABM-GOTM simulations at L4, including the variables T, S, $c(O_2)$, $c(Ar)$, $\Delta(O_2)$, $\Delta(Ar)$ and $\Delta(O_2/Ar)$ were compared against observational dataset from Gloël (2012). Evaluation was performed qualitatively as time series comparisons between model and observed data (Figures 6–12). Furthermore, evaluation was performed quantitatively using robust statistics. Median-based instead of mean based-statistics are here used to limit the significance of observational outliers during the evaluation process (Daszykowski et al., 2007). Robust statistics are summarised in target diagrams (Figure 5) built using normalised unbiased median absolute error $\widetilde{|u|}_n$ on the abscissa, normalised median bias $\tilde{e}_n$ on the ordinate axis and the spearman rank correlation coefficient (ρ_s, colour coded) (modified from Jolliff et al., 2009):

$$\widetilde{|u|}_{\mathrm{n}} = \frac{\widetilde{|u|}}{Q_{\mathrm{observed}}} \tag{45}$$

$$\tilde{e}_{\mathrm{n}} = \frac{\tilde{e}}{Q_{\mathrm{observed}}} \tag{46}$$

$$Q = Q_3 - Q_1 \tag{47}$$

where the individual error is defined as

$$e = X_{\mathrm{predicted}} - X_{\mathrm{observed}} \tag{48}$$

And the individual unbiased error as:

$$u = e - \tilde{e} \tag{49}$$

Here, when individual error (e) and individual unbiased error (u) fall towards the 0 value it means that the model successfully predicts the observations. $X_{\mathrm{predicted}}$ and X_{observed} are respectively the model and observation values matched in time and space. The tilde as overbar represents the median and the vertical bars represents absolute values. Q is the interquartile range calculated as the difference between the third and the first quartiles (Q_1 and Q_3 respectively). $\widetilde{|u|}_{\mathrm{n}}$ represents the unbiased error or random error and the sign indicates whether the model Q is larger (positive) or smaller (negative) than the observations Q. $\tilde{e}_{\mathrm{n}}$ provides a relative measure whether the magnitude of the model median consistently over or underestimates the matched observations. Both estimators are symmetric to each other since are both normalised against the interquartile range of the observed values. The correlation coefficient (color-coded) was also included using the non-parametric spearman rank correlation coefficient (ρ_s) and graphically represented as colour code in the target diagram (Figure 5). Results for model evaluation are presented in section 3.5.1.

3.4.5 Experimental procedure

This section describes the methods adopted to tackle the experimental questions described in section 3.3.

3.4.5.1 Q1: uncertainties derived from steady-state assumption

Error expressed in $\Delta_{RMS}N$ was used to compare the uncertainties of steady-state (N(ERSEM) = $F_{bio}(O_2/Ar)$). with non-steady-state assumption (N(ERSEM) = $N(O_2/Ar)$). This experiment was repeated two times including 5 days during the spring bloom and 5 days during winter. The experiment was repeated using two sampling intervals: the first using a sampling interval that matches the model time step (Δt = 60 s), the second that uses a sampling interval of 7 days (reflecting the routine sampling strategy at Station L4 (Gloël, 2012)). Both N(ERSEM) and $N(O_2/Ar)$ were integrated over the full water column. This removed the error associated with $F_v(O_2/Ar)$. Results are presented in section 3.5.3.

3.4.5.2 Q2: $N(O_2/Ar)$ sensitivity to integration depth in shallow dynamic waters such as L4

$N(O_2/Ar)$ was calculated using three different integration depths: at 2 m, at the annual mean euphotic depth (28 m), and full column (50 m) over 2-year-long simulation run. Euphotic depth was calculated as the depth where photosynthetic available radiation (PAR) was 1 % of its surface value. The annual mean euphotic depth was calculated excluding night-time hours. Monthly statistics for $F_{bio}(O_2/Ar)$, $F_n(O_2/Ar)$ and $F_v(O_2/Ar)$ terms were used to assess their sensitivity when changing the integration depth. Monthly statistics included the median ($\tilde{x}$) set as the box internal horizontal line, 1st and 3rd quartiles (Q_1 and Q_3) as the box edges, and 5th and 95th percentiles (P_5 and P_{95}) set as the box whiskers. Box plots were calculated after binning the dataset every 1 month to provide information on the monthly change in $F_v(O_2/Ar)$ vs total $N(O_2/Ar)$ at the three different integration depths. Results are presented as box plots in section 3.5.4.

3.4.5.3 Q3: Determination of the optimal sampling interval

To address Q3, the optimal sampling interval along the time dimension was calculated over a 5 year-long simulation (2010–2015). $N(O_2/Ar)$ was calculated after subsampling the simulation results at increasing sampling intervals ($N_{\Delta t}(O_2/Ar)$), where Δt was set at 1 min, 10 min, 30 min, 1 day, 2 days, 4 days, 1 week, 10 days, 2 weeks, and 1 month. The time intervals were arbitrarily selected among the possible divisors of the total amount of the simulation time steps. Calculations for $N_{\Delta t}(O_2/Ar)$ were then repeated using oxygen concentrations affected by relative experimental error ($N_{\Delta t,noise}(O_2/Ar)$).

The relative experimental error used in this experiment matched the sampling error reported in Gloël (2012) for the L4 dataset (σ = 0.03 %). To simulate the effects of random error in model simulations a normally distributed random error ε_c was added to $c(O_2)$ used to calculate $N_{\Delta t,\mathrm{noise}}(O_2/Ar)$ as follows:

$$c_{\mathrm{noise}}(O_2) = c(O_2)(1 + \varepsilon_c), \tag{50}$$

Both $N_{\Delta t}(O_2/Ar)$ and $N_{\Delta t,\mathrm{noise}}(O_2/Ar)$ were compared against a stepwise average of N(ERSEM) where the averaged window was set equal to Δt ($N_{\Delta t}$(ERSEM)), using full water column integrations (50 m). The optimal sampling interval was selected using Δ_{RMS} and R^2 (indicating correlation between target and prediction) as quantitative metrics of evaluation. Differences in Δ_{RMS}N and R^2 between control and experimental runs isolate the effects of experimental noise. Results are presented in section as histograms and time series analysis in section 3.5.5.

3.5 Results

3.5.1 Model evaluation against observed dataset at L4

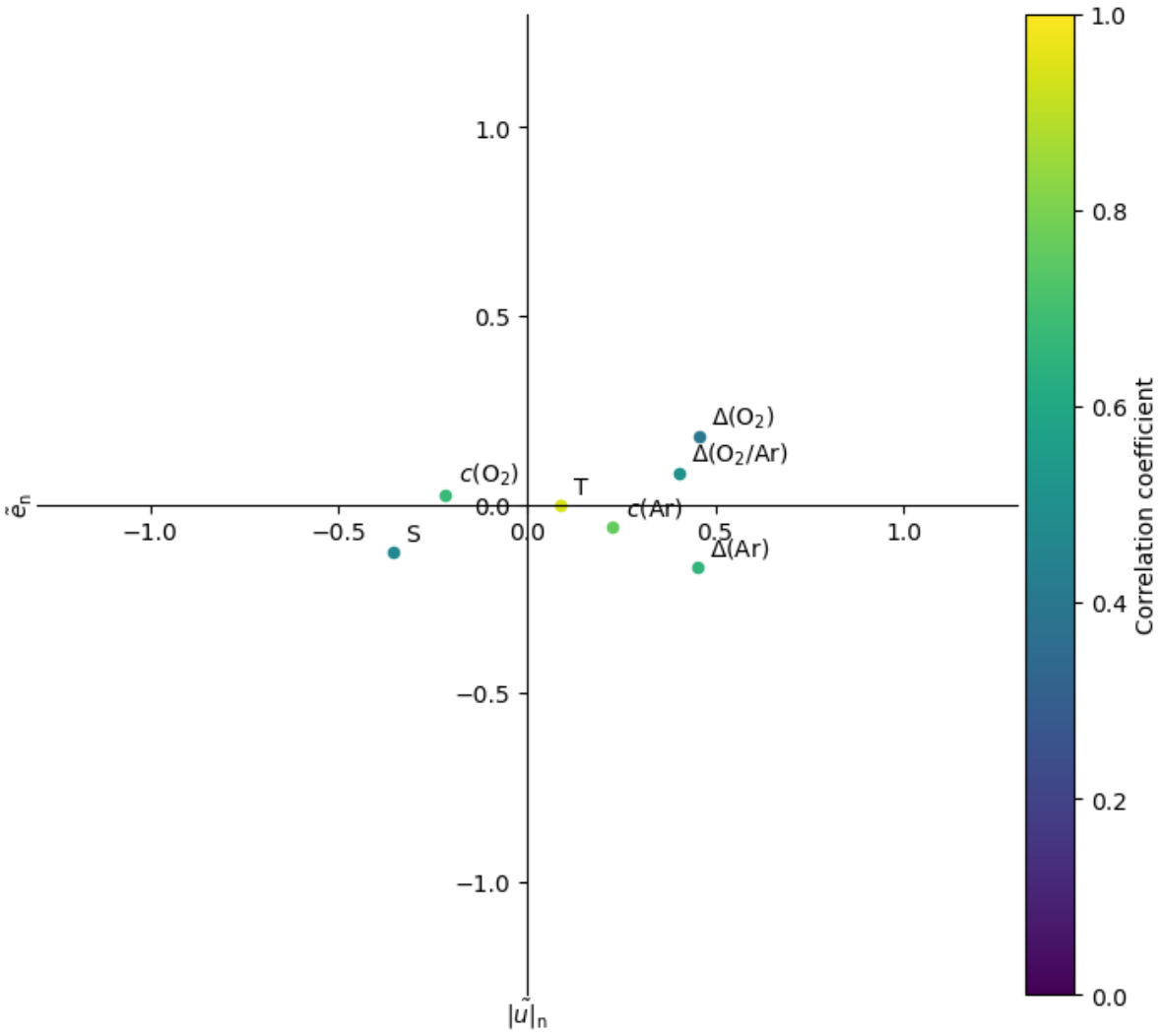

Figure 30: Robust target diagram representing overall model performance compared to observed data for temperature (*T*), salinity (*S*), oxygen concentration $c(O_2)$, argon concentration c(Ar), oxygen saturation anomaly $\Delta(O_2)$, argon saturation anomaly Δ(Ar) and biological oxygen saturation anomaly ($\Delta(O_2/Ar)$. $\widetilde{|u|}_n$ represents the normalised unbiased median absolute error. $\tilde{e}_n$represents the normalised median bias. The colour code reflects the correlation coefficient between model and observation. Full description in section 3.4.4.4.

Overall, the model simulation had good performance in predicting temperatures measured at the 4 depths (2 m, 10 m, 25 m, 50 m) used by Gloël (2012) (ρ_s = 0.94, $\widetilde{|u|}_n$ = 0.09, $\tilde{e}_n = -3.2 \times 10^{-3}$; Figure 30). The model was restored to temperature profiles with a one month restoring time scale, which was used to ensure that the model stayed

within reasonable bounds. Despite this the model appears to have a warm bias at surface in the summer – Autumn 2010, and a slight cold bias in deeper waters (Figure 31). This perhaps points to a problem with enhanced stratification where heat is not penetrating down to deeper waters. The model is also missing to lateral advection, which could also be responsible for resulted bias on temperature field.

In general, the salinity field was well represented by the model especially at subsurface depths, however predictions at surface suffered considerable bias ($\rho_s = 0.47$, $|\widetilde{u}|_n = 0.35$, $\tilde{e}_n = -0.12$) (Figure 30, and Figure 32). Salinity was overestimated at surface throughout most of the times series. It is most likely that L4 station was under the influence of westerly and southerly winds in the winter months transporting low salinity waters coming from the Tamar Estuary and Plymouth Sound that usually occur in the area (Uncles et al., 2020). As the model was in 1D it was deficient to represent lateral transport.

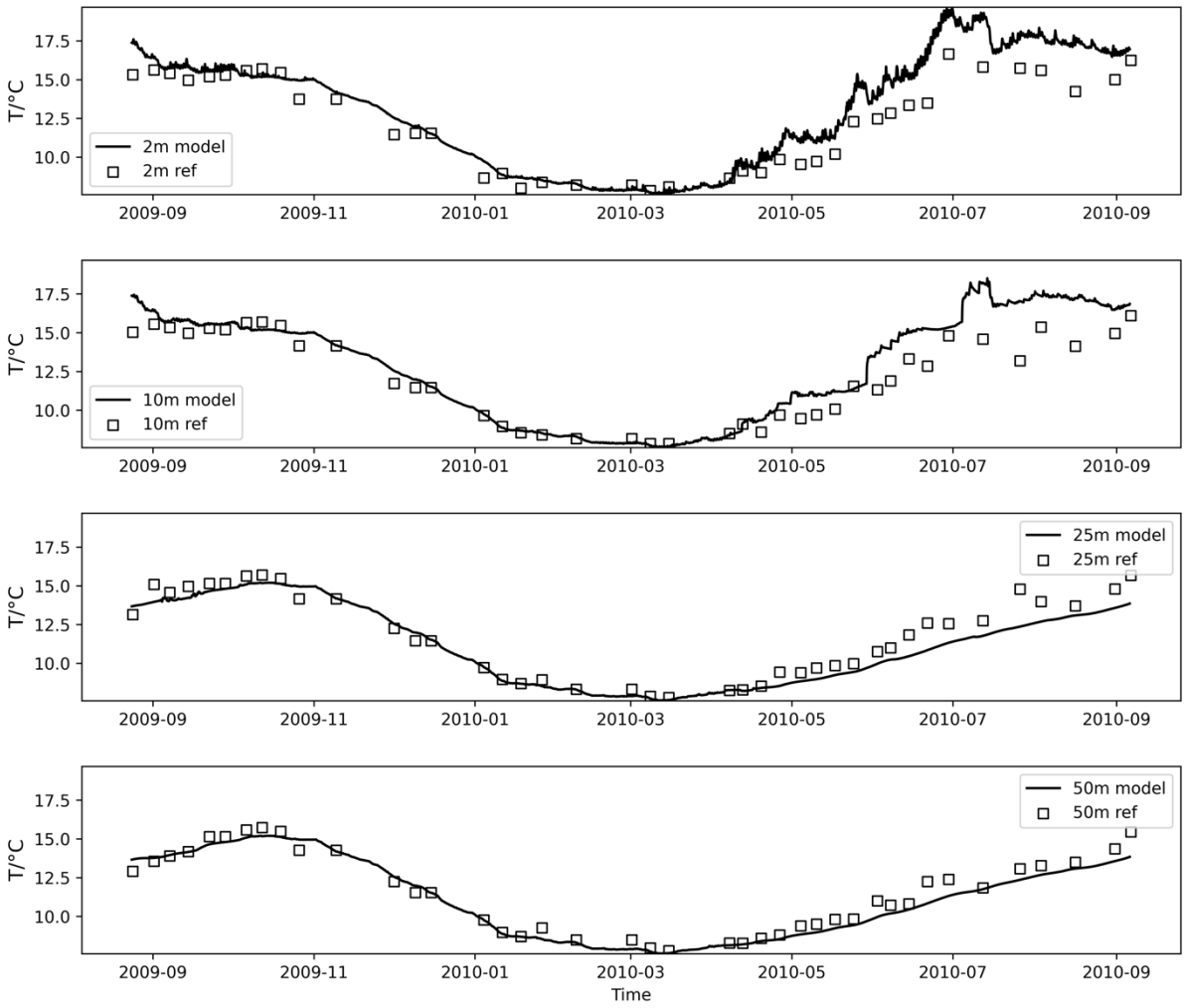

Figure 31: Modelled temperature (T) (solid line), compared with observations (white squares) collected by Gloël (2012), at 2 m, 10 m, 25 m, 50 m depth.

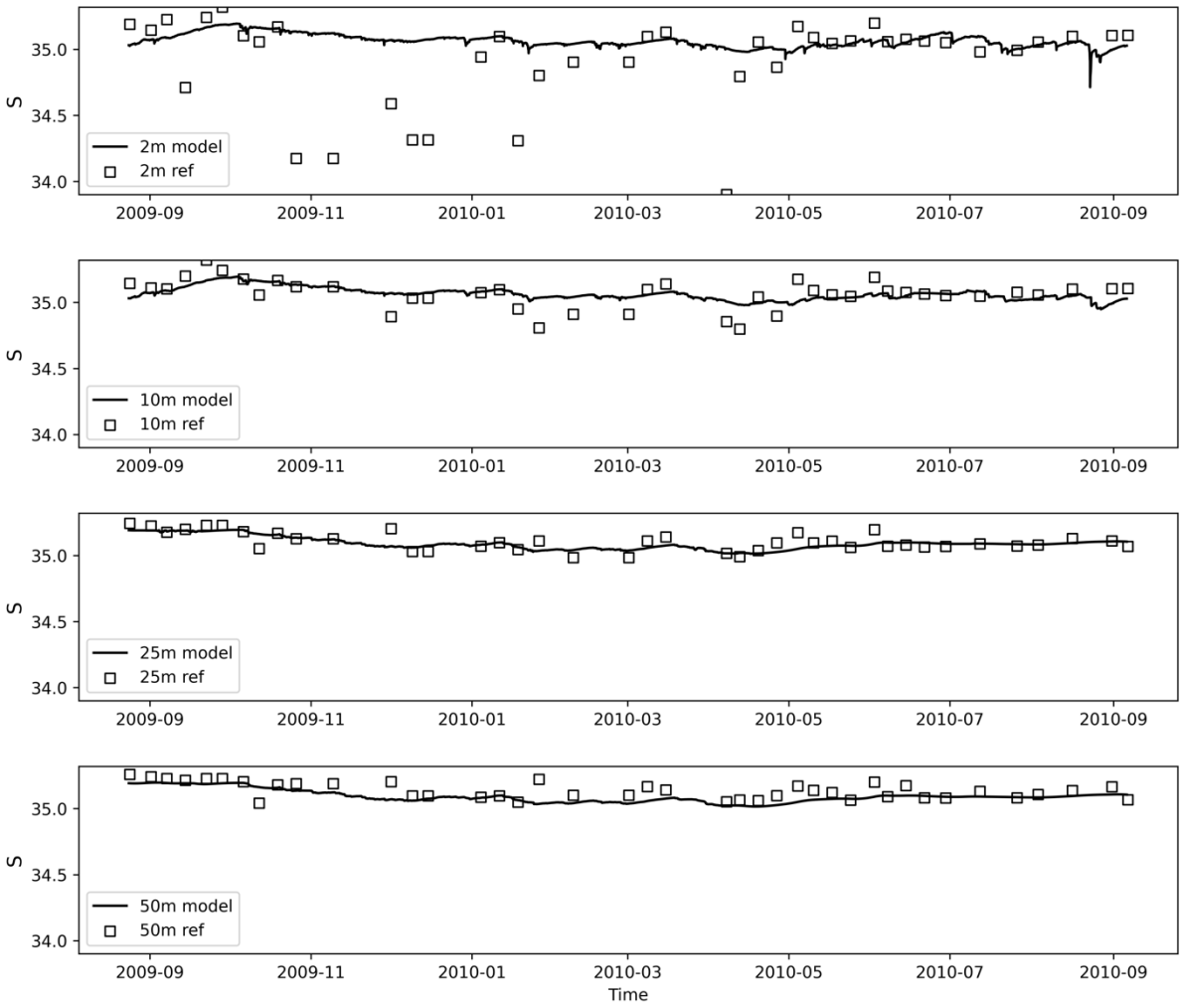

Figure 32: Modelled salinity (S) (solid line), compared with observations (white squares) collected by Gloël (2012), at 2 m, 10 m, 25 m, 50 m depth.

Simulations outputs for $c(O_2)$ exhibited a low overall bias and were well correlated with observed values. As shown in Figure 30, the model $c(O_2)$ interquartile range was smaller than the observations, which impacted the absolute error ($\rho_s = 0.70$, $|\widetilde{u}|_n = 0.19$, $\tilde{e}_n = 2.2 \times 10^{-5}$). Simulation results for 2 m and 10 m capture observed trends, although concentrations are higher than observed during the summer of 2009, and the peak in surface $c(O_2)$ following the spring bloom of 2010 is overestimated (Figure 33). Furthermore, model $c(O_2)$ shows that concentrations in surface waters (2 m and 10 m) are higher than those at deeper depths (25 m and 50 m) – a difference that is less marked in the observations (Figure 33). Higher than expected model $c(O_2)$ values were predicted at bottom depths, especially in the summer and autumn of 2010, when the simulated temperature field was also lower than observed. This could be an artefact of the model which tends to overestimate the strength of stratification in autumn 2010 as

compared to 2009 (Figure 33); the absence of lateral transport; or respiration rates being lower than observed. Model performance for c(Ar) (ρ_s = 0.76, $|\widetilde{u}|_n$ = 0.22, $\tilde{e}_n$= 3.2 × 10^{-3}) (Figure 30) was found to be like for $c(O_2)$. Overall good performance at all depths from September 2009 until mid-June 2010 was observed, after which the model outputs start diverging from observations, with marked differences between the surface and deeper waters observed (Figure 34). Argon gas is inert to biological activity therefore this divergence from observations cannot be attributed to biological processes (e.g., the exclusions of benthic system dynamics). Thus, these differences reflect physical processes, which likely include a solubility effect for Ar, given that surface temperatures were higher in the model in the summer of 2010. Model performance was lower for oxygen, argon, and biological oxygen saturation anomalies compared to the respective concentrations: $\Delta(O_2)$ (ρ_s = 0.44, $|\widetilde{u}|_n$ = 0.41, $\tilde{e}_n$ = 0.1), and Δ(Ar) (ρ_s = 0.65, $|\widetilde{u}|_n$ = 0.45, $\tilde{e}_n$ = –0.17), $\Delta(O_2/Ar)$ (ρ_s = 0.55, $|\widetilde{u}|_n$ = 0.29, $\tilde{e}_n$ = 8.1 × 10^{-2}) (Figure 30). As for $c(O_2)$, the simulated $\Delta(O_2)$ and $\Delta(O_2/Ar)$ were found to be overestimating 2010 April maxima which coincides with the onset of the spring bloom at L4 (Smyth et al., 2010). Furthermore, predictors for $\Delta(O_2)$, Δ(Ar) and $\Delta(O_2/Ar)$ overestimated summer 2010 vertical changes that are not observed in the reference data (Figure 34, Figure 35 and Figure 36 respectively).

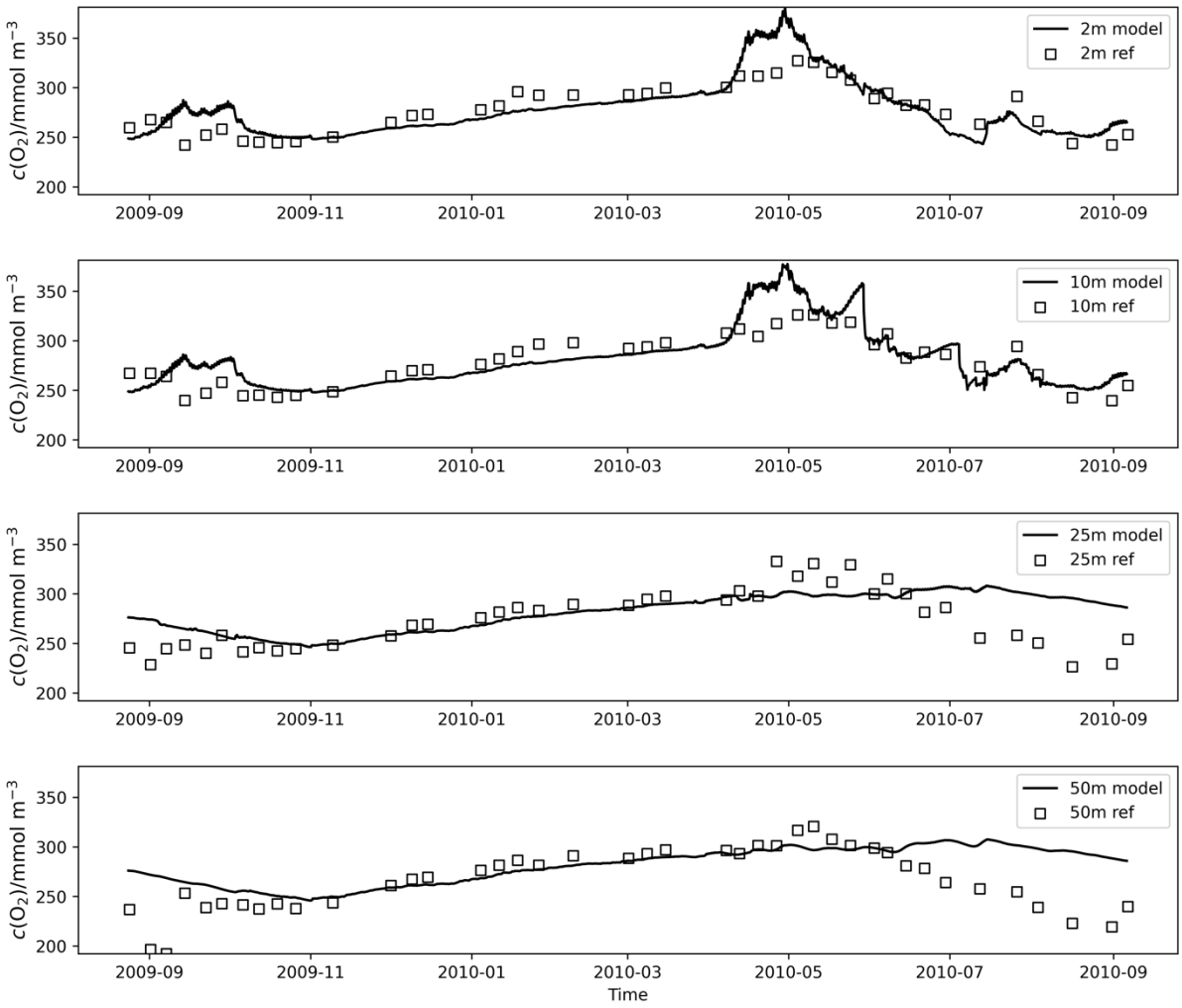

Figure 33: Modelled oxygen concentration ($c(O_2)$ (solid line), compared with observations (white squares) collected by Gloël (2012), at 2 m, 10 m, 25 m, 50 m depth.

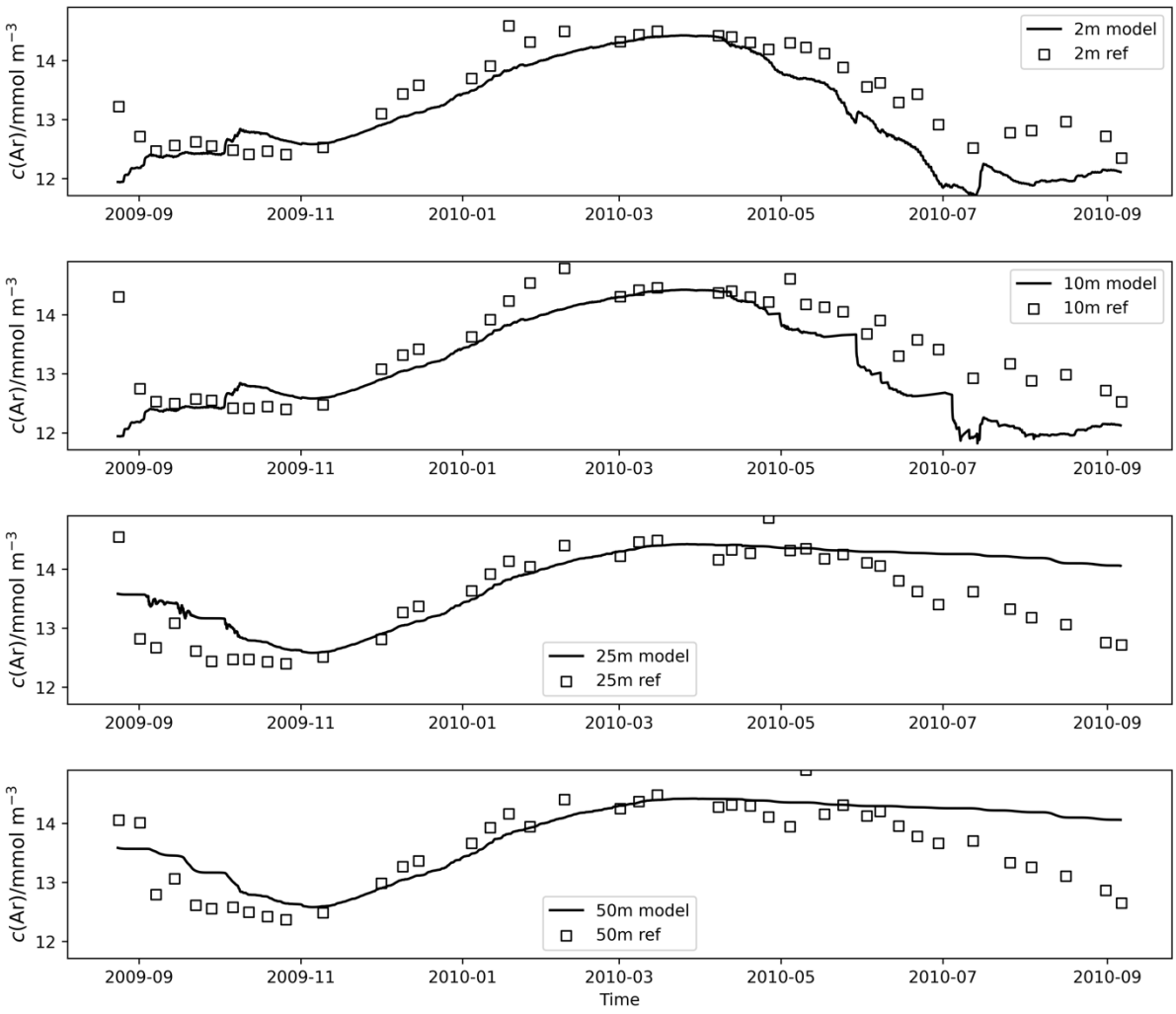

Figure 34: Modelled argon concentration (*c*(Ar)) (solid line), compared with observations (white squares) collected by Gloël (2012), at 2 m, 10 m, 25 m, 50 m depth.

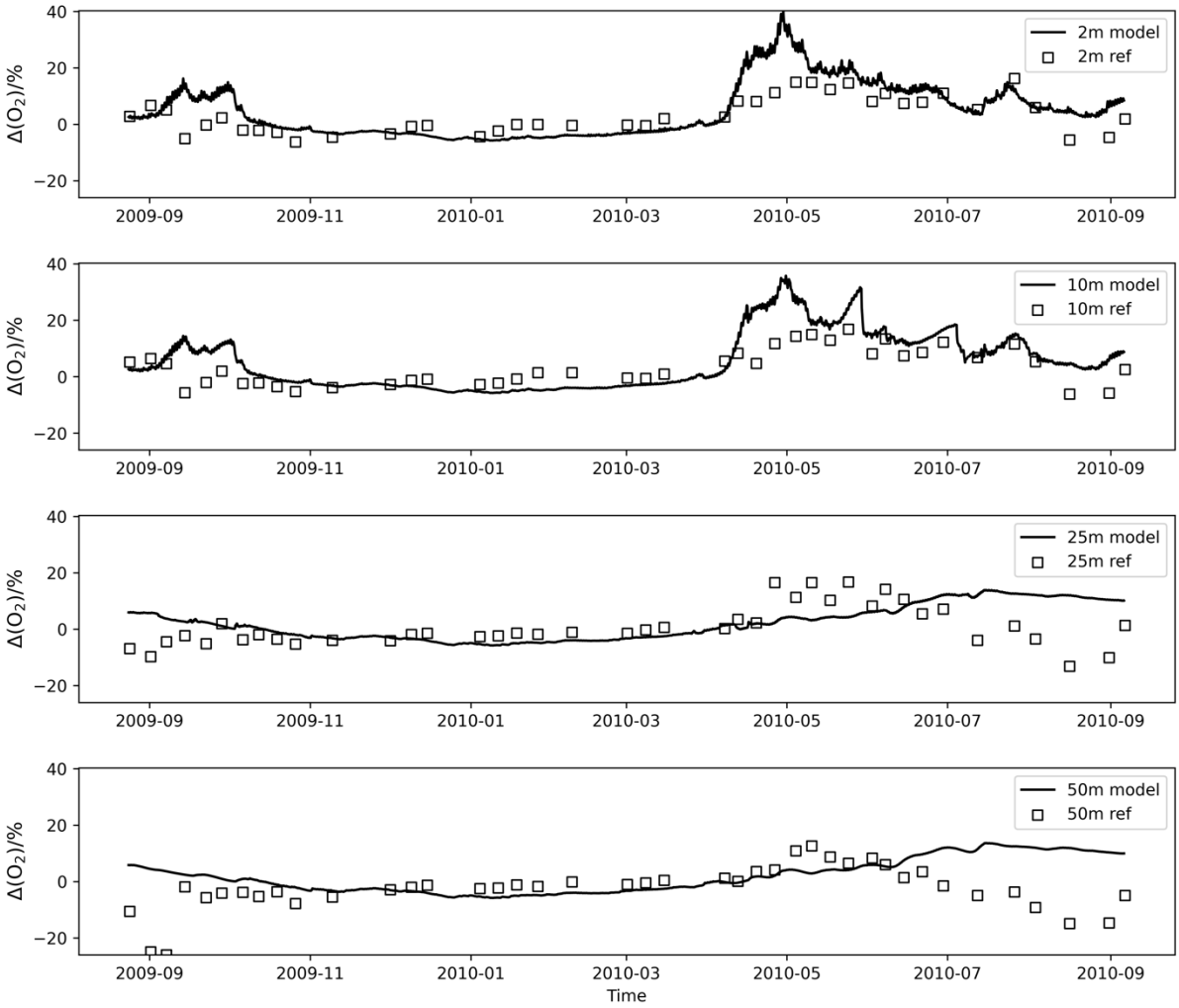

Figure 35: Modelled oxygen saturation anomaly ($\Delta(O_2)$) (solid line), compared with observations (white squares) collected by Gloël (2012), at 2 m, 10 m, 25 m, 50 m depth.

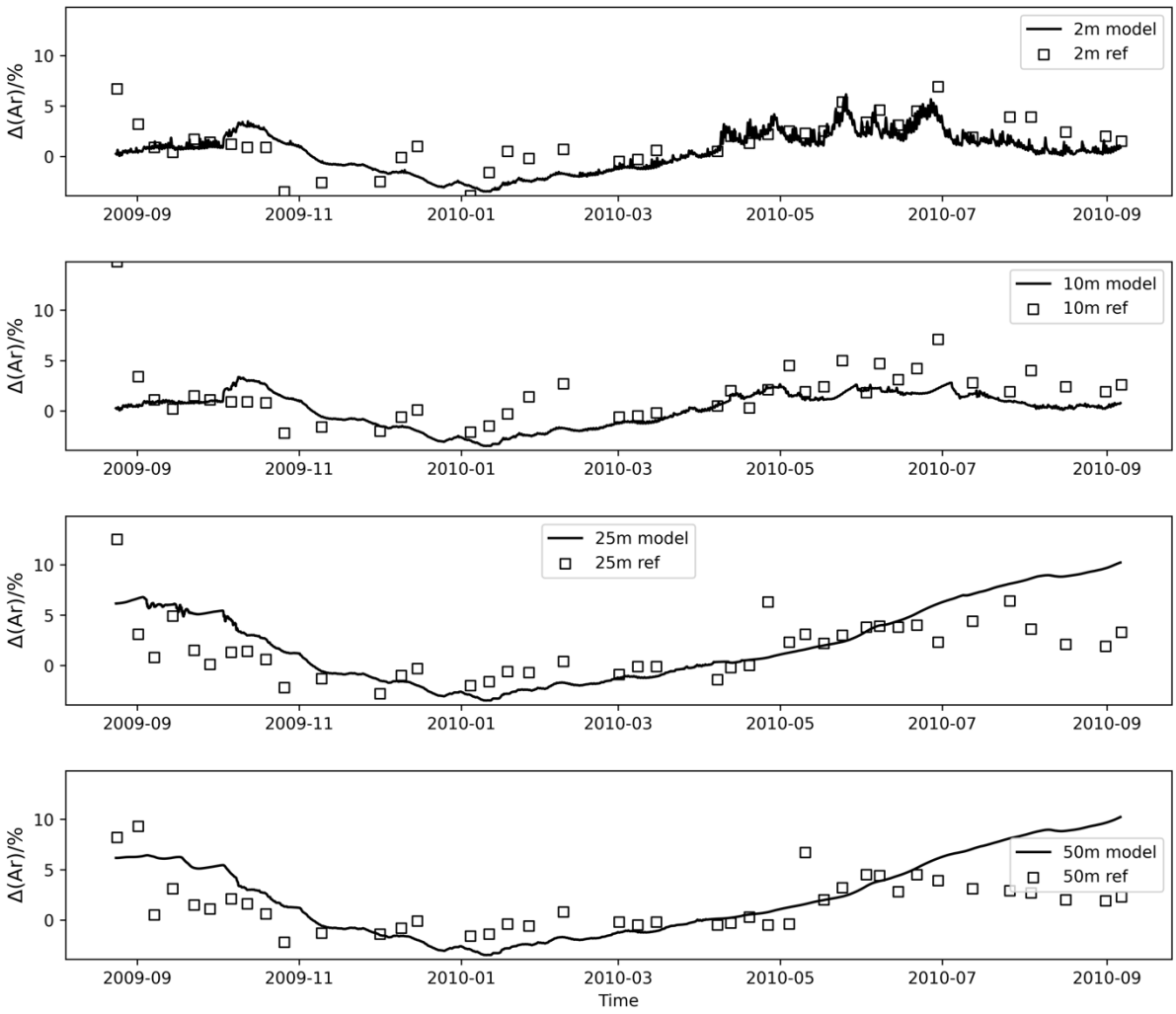

Figure 36: Modelled argon saturation anomaly (Δ(Ar)) (solid line), compared with observations (white squares) collected by Gloël (2012), at 2 m, 10 m, 25 m, 50 m depth.

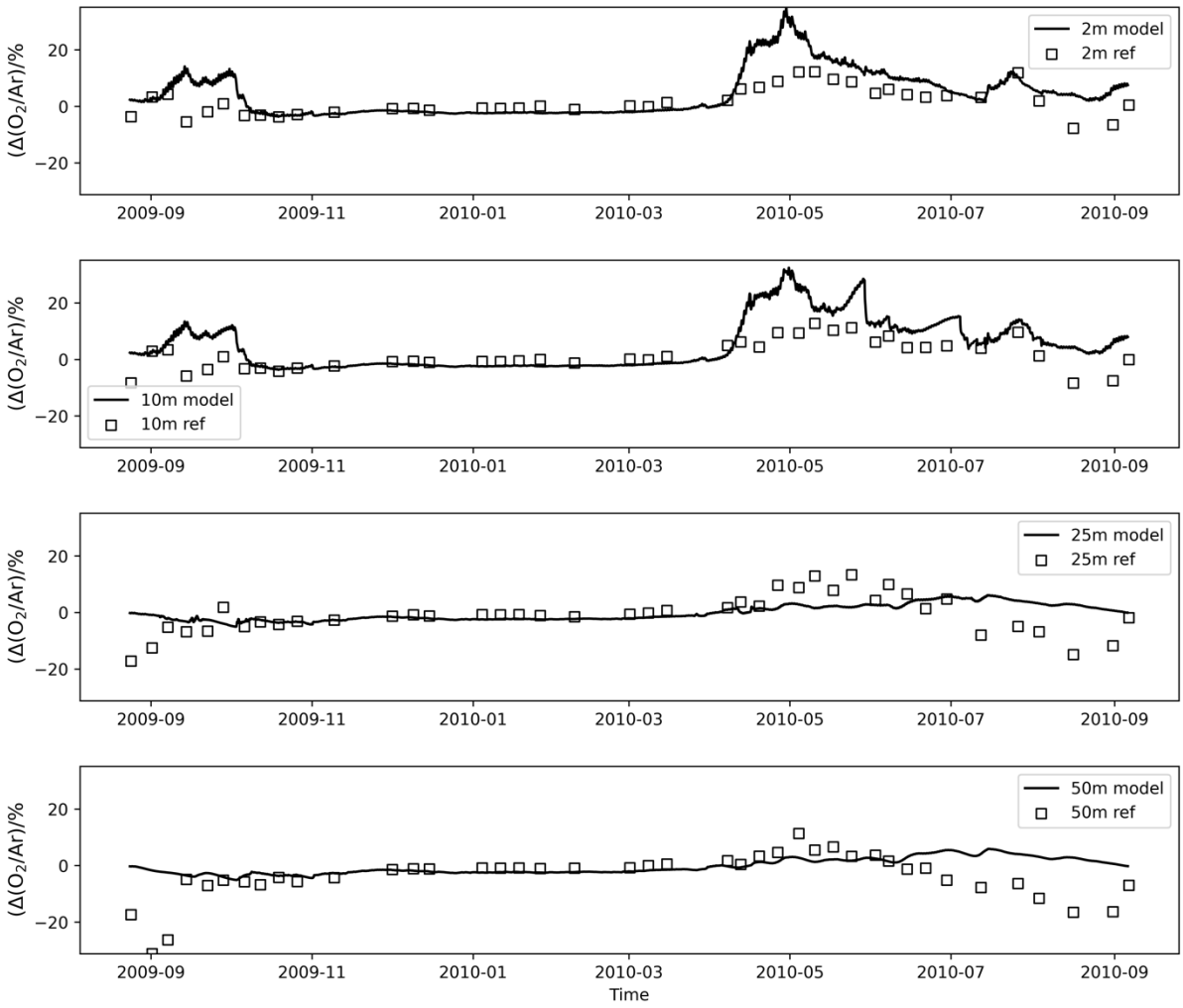

Figure 37: Modelled biological oxygen saturation anomaly ($\Delta(O_2/Ar)$) (solid line), compared with observations (white squares) collected by Gloël (2012), at 2 m, 10 m, 25 m, 50 m depth.

3.5.2 Evaluating the diagnostic model ($N(O_2/Ar)$) in post processing calculations: N(ERSEM) vs $N(O_2/Ar)$

Overall $N(O_2/Ar)$ quasi-perfectly replicated net metabolism in oxygen equivalents simulated in ERSEM-GOTM (ρ_s = 0.99, $\widetilde{|u|}_n = 7.1 \times 10^{-4}$, $\tilde{e}_n = -1.3 \times 10^{-4}$). Small residual differences are attributed to numerical artefacts, in particular arising in periods of higher productivity ($\Delta_{RMS}N(10\text{ m}) = 0.03$ mmol m^{-2} d^{-1}) (Figure 38). This error is generated by three factors: 1) incorrect representation of the diagnostic model in $N(O_2/Ar)$ equations, 2) incorrect representation of ERSEM-FABM-GOTM numerics in post processing calculations, and 3) incorrect representation of the coupling scheme between GOTM and ERSEM. The operator splitting method (Eq. (24)) need to be accounted before calculating biogeochemical processes. We here used the state of the

system (γ calculated in Eq. (25)) following the diffusion step to compute air-sea fluxes, as this matches what is done in ERSEM. Importantly, there is a half time step mismatch between diagnostic and state variables in the ERSEM-FABM-GOTM results file. Therefore, all variables used for calculations need to be sliced accordingly to not introduce a time-dependent systematic error in $N(O_2/Ar)$. This time dependent error was introduced when calculating time differentiations in post processing which did not completely represent the more complex calculations used online by the model in ERSEM-FABM-GOTM. Despite such residual differences were not fully corrected the diagnostic model performance was satisfy actory considering its purpose in the experiments.

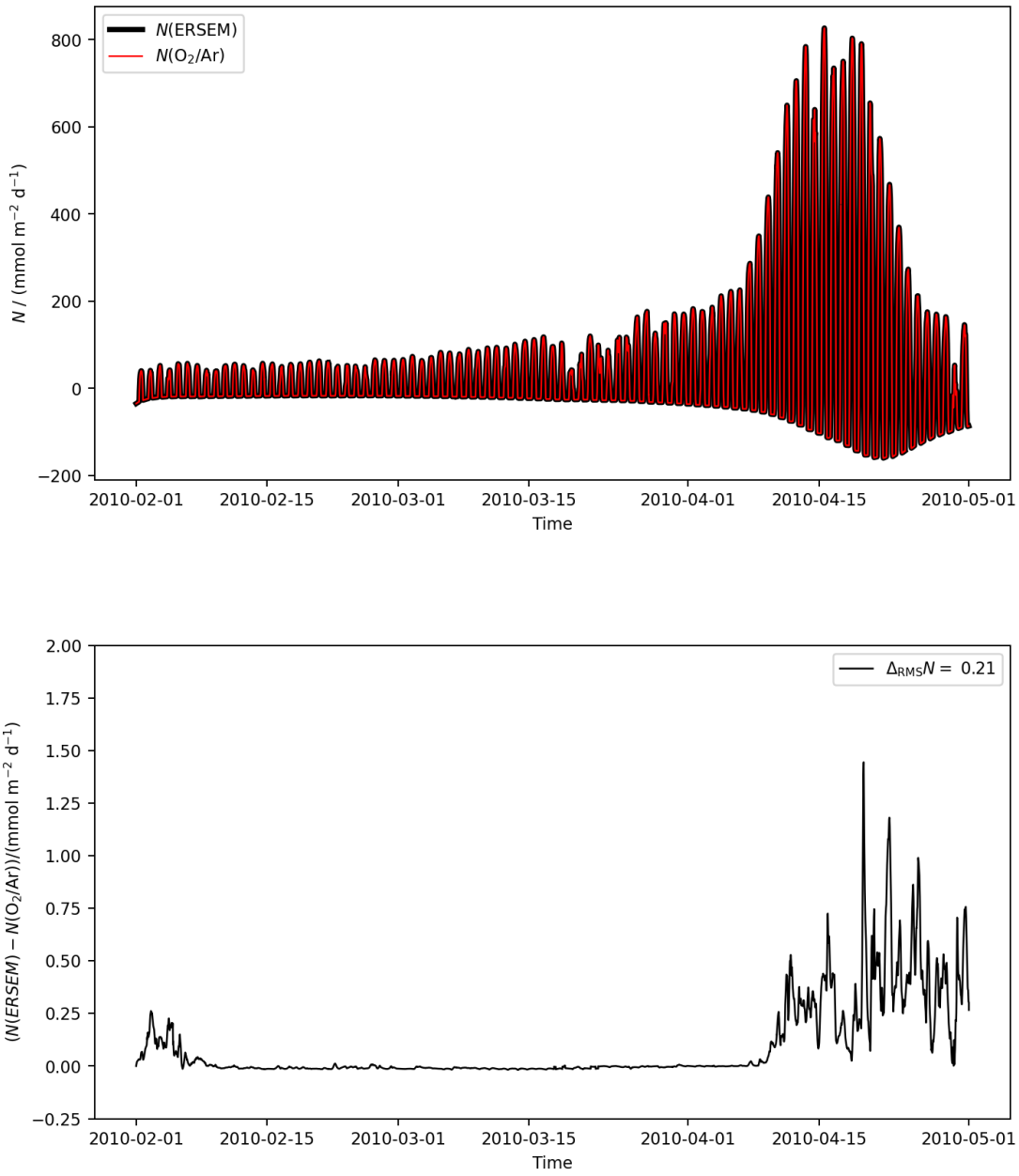

Figure 38: Plot comparing N(ERSEM) (thick black line) to $N(O_2/Ar)$ (red line) when both use an integration depth set at 10 m (top panel). The lower panel shows a residual plot using $N(O_2/Ar)$ as predictor and N(ERSEM) as reference including $\Delta_{RMS}(N)$ as $N(O_2/Ar)$ error estimate.

3.5.3 Q1: uncertainties derived from steady-state assumption

Results here quantify the error when assuming N is in steady-state (N(ERSEM) = $F_{bio}(O_2/Ar)$) in shelf sea waters such as those found at L4. The resulting error caused by steady-state assumption was compared against the underlying error described in the previous section (N(ERSEM) = $N(O_2/Ar)$). Differences between the two errors isolates

error caused by the steady-state assumption. In both cases net community production was calculated by integrating over the full water column in order to include the whole pelagic system and to remove the effects of vertical diffusion, which isolates the importance of the non-steady-state term $F_n(O_2/Ar)$. The error is expressed as a root mean squared difference calculated using $N(O_2/Ar)$ or $F_{bio}(O_2/Ar)$ as predictors and N(ERSEM) as the reference value. The same experiment is repeated showing the results in two contrasting scenarios: during the growing season in spring and summer (where the signal from biology dominates over physical transport) and during the winter season (*vice versa*). To give context, results are compared with main biological and physical forcings affecting net oxygen production in the two seasonal scenarios.

3.5.3.4 Assuming steady-state during the growing season

During the selected scenario (late April 2010) at L4 (n = 7200), the water column was net autotrophic ($N(O_2/Ar)$ = (120±280) mmol m^{-2} d^{-1}) (Figure 39e) and dominated by the photoautotrophic nano- and pico-plankton size classes in ERSEM (Figure 39c and Figure 39d). Oxygen consumed through respiration integrated over same period is shown in Figure 39d ($R(O_2)$ = (166±32) mmol m^{-2} d^{-1}), and was about half of the oxygen produced in the same period (Figure 39c: $G(O_2)$ = (290±310) mmol m^{-2} d^{-1}) establishing a net autotrophic community structure. Comparing net oxygen production flux predicted at all depths prognostically by ERSEM-GOTM (Figure 39b: N(ERSEM) = (1.2±4.3) mmol m^{-2} d^{-1}) to photosynthetic active radiation (Figure 39a: I(PAR) = (23.4±56.4) W m^{-2}) shows that the simulated timing, intensity, and depth of daytime production is influenced by the penetration of short-wave radiation down through the water column. As an example, the timing and intensity of mid-day $G(O_2)$ maxima coincides with the peak intensity and penetration of shortwave radiation.

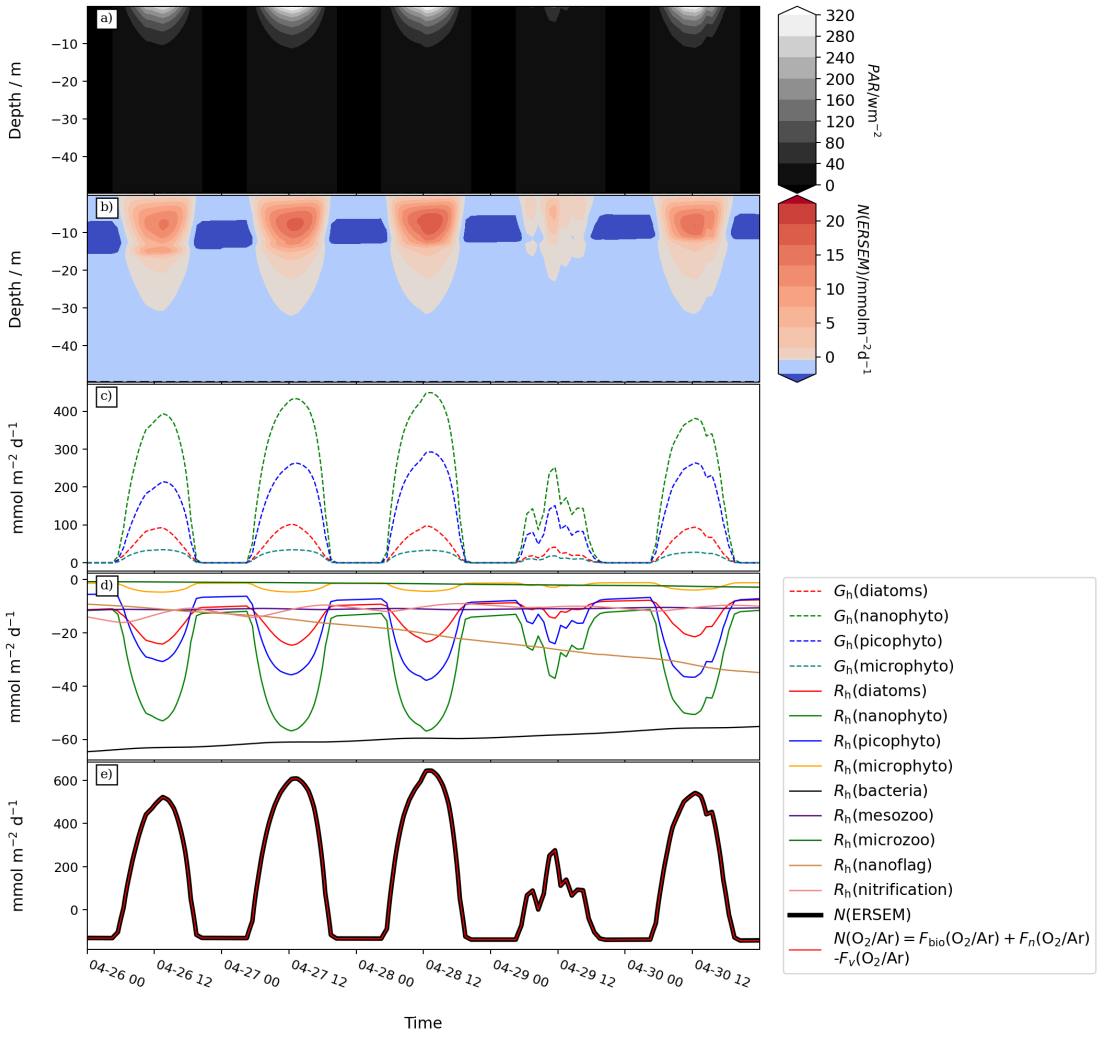

Figure 39: In this plot $N(O_2/Ar)$ and N(ERSEM) (e) integrated over the full water column (dashed black line in a and B), during late spring bloom 2010, are compared to photosynthetic active radiation (a), non-integrated net oxygen production (b) and integrated net primary production ($NPP = G - R$(autotrophic)) (c) and heterotrophic respiration (d). Integration depth (black dashed line in a and b) is set at 50m.

In this scenario, O_2 was supersaturated (Figure 40a: $c(O_2)$ = (330±33) mmol m^{-3}). At 16 m of depth, a sharp O_2 gradient divided surface waters from the rest (Figure 40a). Biological oxygen was on average supersaturated (Figure 40b: ($\Delta(O_2/Ar)$ = (15±13) %) with surface waters being the most enriched in biological oxygen. Vertical diffusivity (Figure 40c: K_z = ($10^{-3.2\pm1.6}$ m^2 s^{-1}) was found to be stronger below 30 m of depth and above 5 m of depth. While the variability in K_z calculated below 30 m of depth was cyclical (2 peaks per day at the start and at the end of each day), variability in the topmost part of the water column was found to be more episodic. K_z was found at minima in between 5 and 30 m of depth (Figure 40c). Wind forcing (Figure 40d: u_{10} =

(4.3±1.8) m s^{-1}) drives turbulent mixing in the surface, resulting in a downward transfer of energy and momentum. At the same time K_z below 30 m of depth is strongly affected by cyclical horizontal velocity peaks representing tidal forcing. These results into an upward transfer of energy and momentum. In ERSEM-FABM-GOTM system internal horizontal velocities are fully parametrised given the 1D vertical only nature of the model. The K_z minima found in between 5–30 m of depth results because the effects of wind stress and tidal forcing does not penetrate to the middle of the water column.

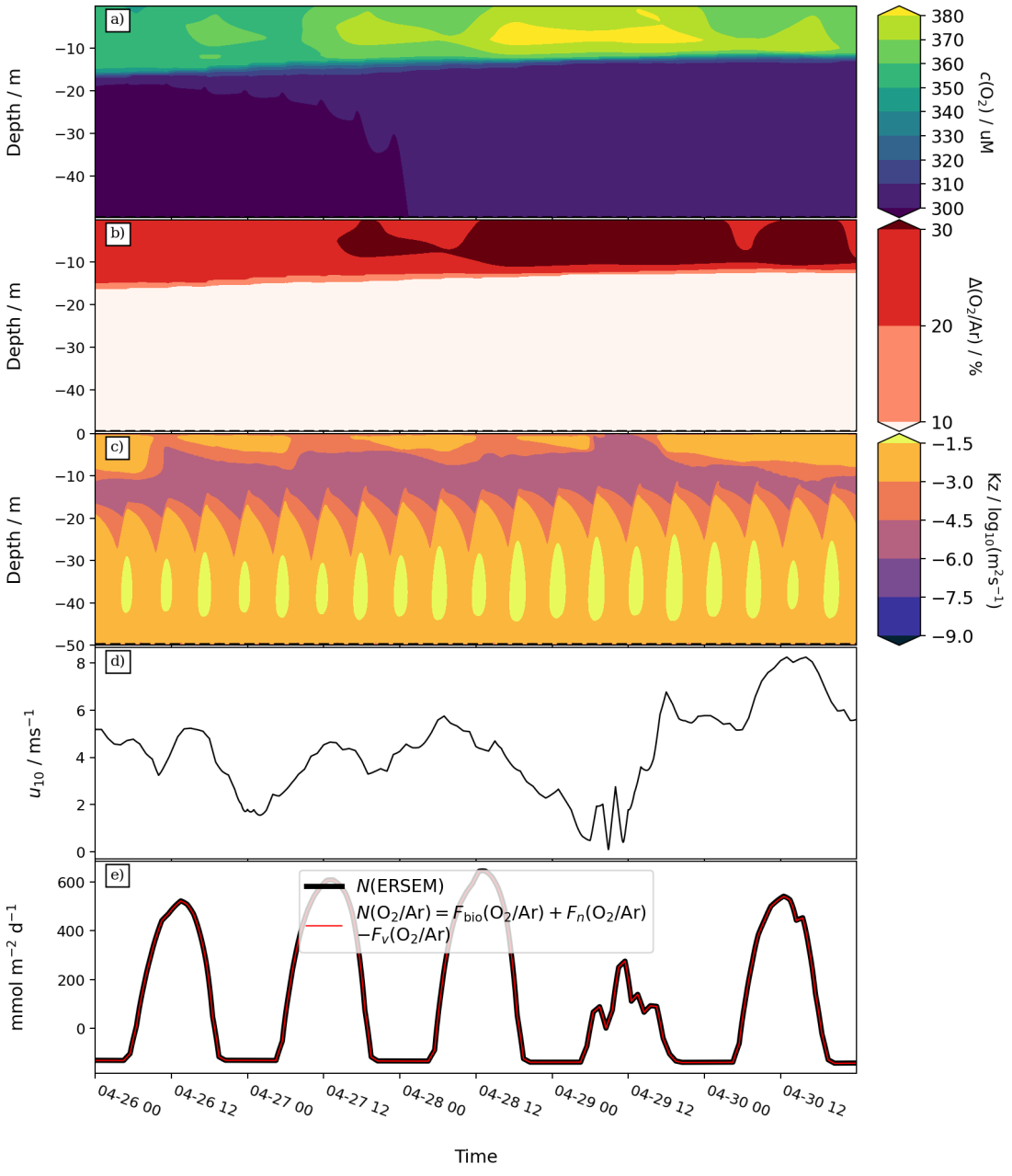

Figure 40: In this plot N(O$_2$/Ar) and N(ERSEM) (e), during late spring bloom 2010, are compared to 3 forcing variables representing windspeeds (a), vertical turbulent diffusivity (c)

and the oxygen saturation anomaly driven by net metabolism (b). Integration depth (black dashed lines in a, b, and c) is set at 50 m.

Figure 41 shows the error that arises if N is assumed to be in steady-state during the sea spring bloom. Here, integrations are performed over the whole water column, thus removing the effects of vertical diffusivity on inferred $N(O_2/Ar)$ (Figure 41c agrees with Figure 41b). Results show that neglecting the non-steady-state term $F_n(O_2/Ar)$ in the calculation of $N(O_2/Ar)$ completely decouples it from N(ERSEM), increasing the estimated error by three orders of magnitude (Figure 41b: $\Delta_{RMS}N = 270$ mmol m^{-2} d^{-1}). As shown in Figure 41d and Figure 41a, when the sampling interval matches the simulation time step (a measurement per minute in this case) the time disequilibrium term $F_n(O_2/Ar)$ dictates the $N(O_2/Ar)$ performance in representing day and night variability. The air-sea gas exchange term $F_{bio}(O_2/Ar)$ taken alone represents a time average of N.

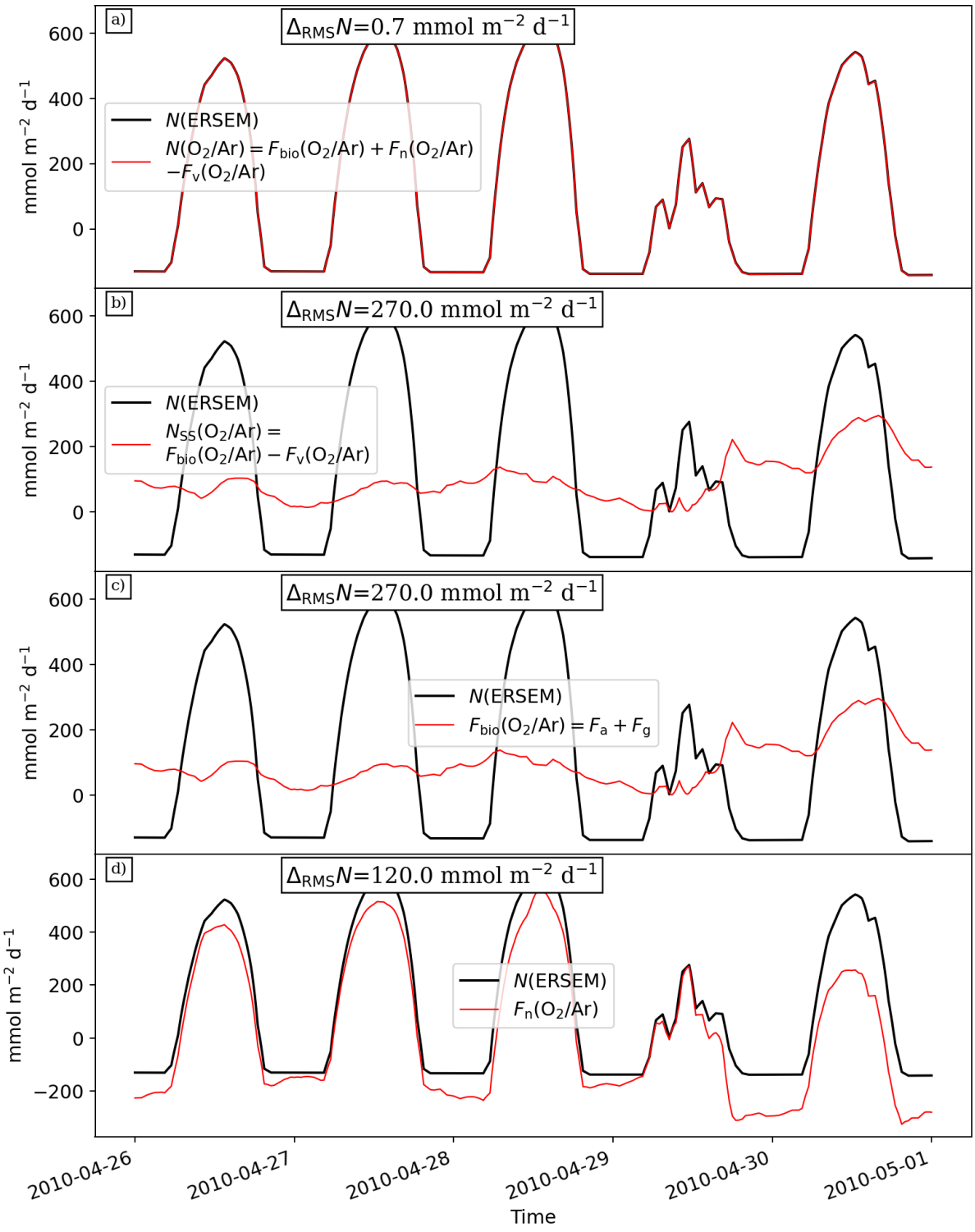

Figure 41: Diagnostic model performance (red) vs its target value (black) during the late spring bloom 2010 at L4. Diagnostic models are namely: in (a) the full non-steady-state (N(ERSEM) = $N(O_2/Ar)$), in (b) assuming steady-state (N(ERSEM) = $F_{bio}(O_2/Ar)$ - $F_v(O_2/Ar)$), In (c) assuming steady-state with no influence from diffusive flux (N(ERSEM) = $F_{bio}(O_2/Ar)$), and in (d) non-steady-state omitting air sea gas exchange and diffusive flux (N(ERSEM) = $F_n(O_2/Ar)$). Integration depth was set at 50 m (not shown).

3.5.3.5 Assuming *N* in steady-state during winter

During the selected scenario (Dec 2009) at L4 (n = 7200), the ERSEM-GOTM model predicted low biological metabolic activity (Figure 42e: $N(O_2/Ar) = -1.5 \times 10^5$ mmol m^{-2} d^{-1}) dominated by a net heterotrophic community composed of bacteria and to a lesser extent nano- and pico-phytoplankton groups (Figure 42c and Figure 42d). During this scenario photosynthetic active radiation (Figure 42a: $I(PAR) = (5.2 \pm 15.0)$ W m^{-2}) is limited compared to the growing season hindering gross oxygen production (Figure 16c: $G(O_2) = 5 \times 10^4$ mmol m^{-2} d^{-1}) and indirectly consumption (oxygen consumption is driven by biomass and temperature), which was found to be four times stronger than production during the selected period (Figure 42d: $R(O_2) = 2 \times 10^5$ mmol m^{-2} d^{-1}).

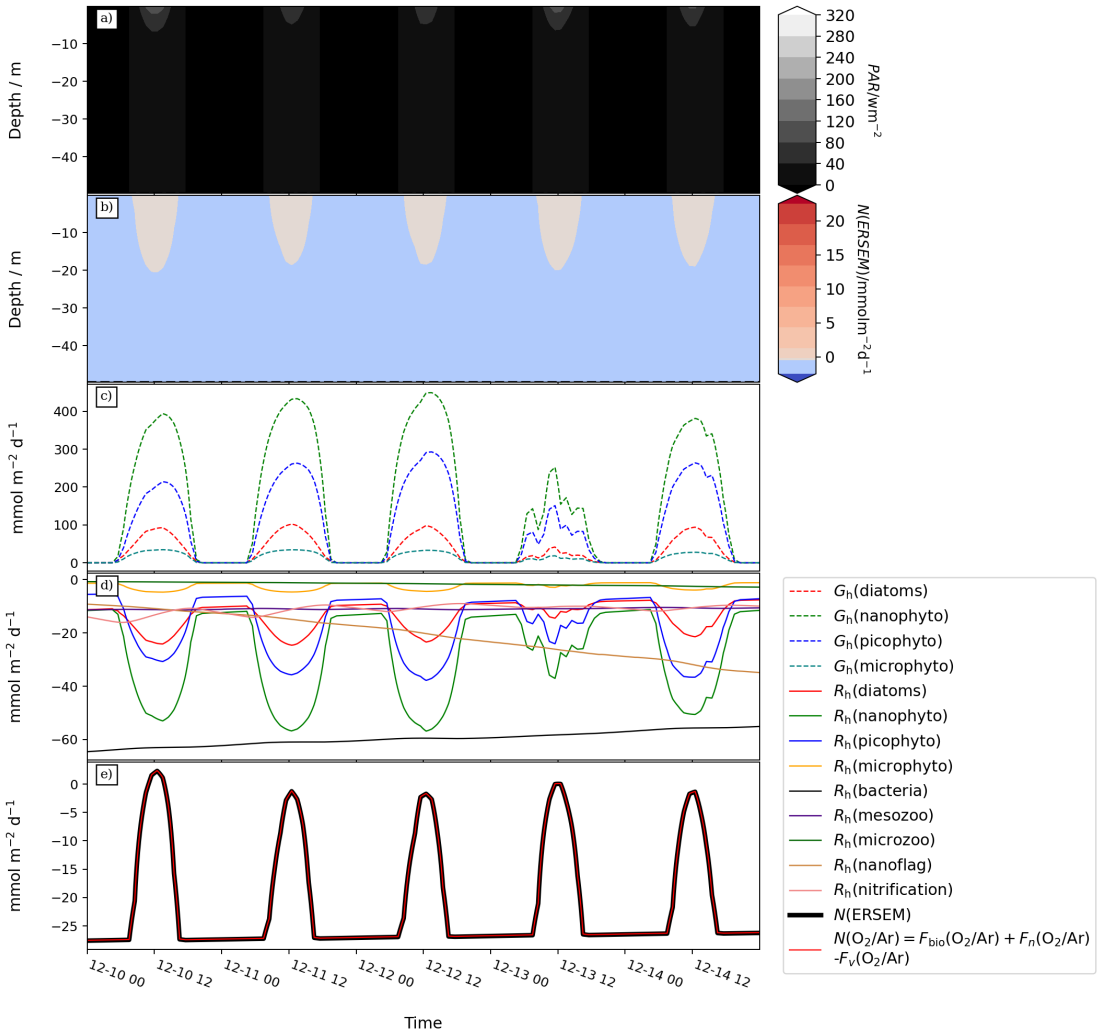

Figure 42: In this plot *N*(O2/Ar) and *N*(ERSEM) (e) integrated over the full water column (dashed black line in a and b), during spring bloom 2010, are compared to photosynthetic active radiation (a), net oxygen production (b) and primary production G_h (c) and respiration R_h (d). Integration depth (black dashed line in a and b) is set at 50 m.

During winter, wind speeds were on average stronger and more constant than during spring (Figure 43d: (7.0±2.6) m s^{-1}) and force the water column to be fully mixed expressed by high vertical turbulent diffusivity (Figure 43c: $K_h = 10^{-1.9\pm2.6}$ m^2 s^{-1}). This together with low net heterotrophic activity (see above) causes oxygen concentrations to be almost constant and undersaturated in time and space (Figure 43a: $c(O_2)$ = (261.5±0.4) mmol m^{-3}), where the dominance of respiration forces negative $\Delta(O_2/Ar)$ across the whole period (Figure 18b: $\Delta(O_2/Ar)$ = (–1.9±0.05) %).

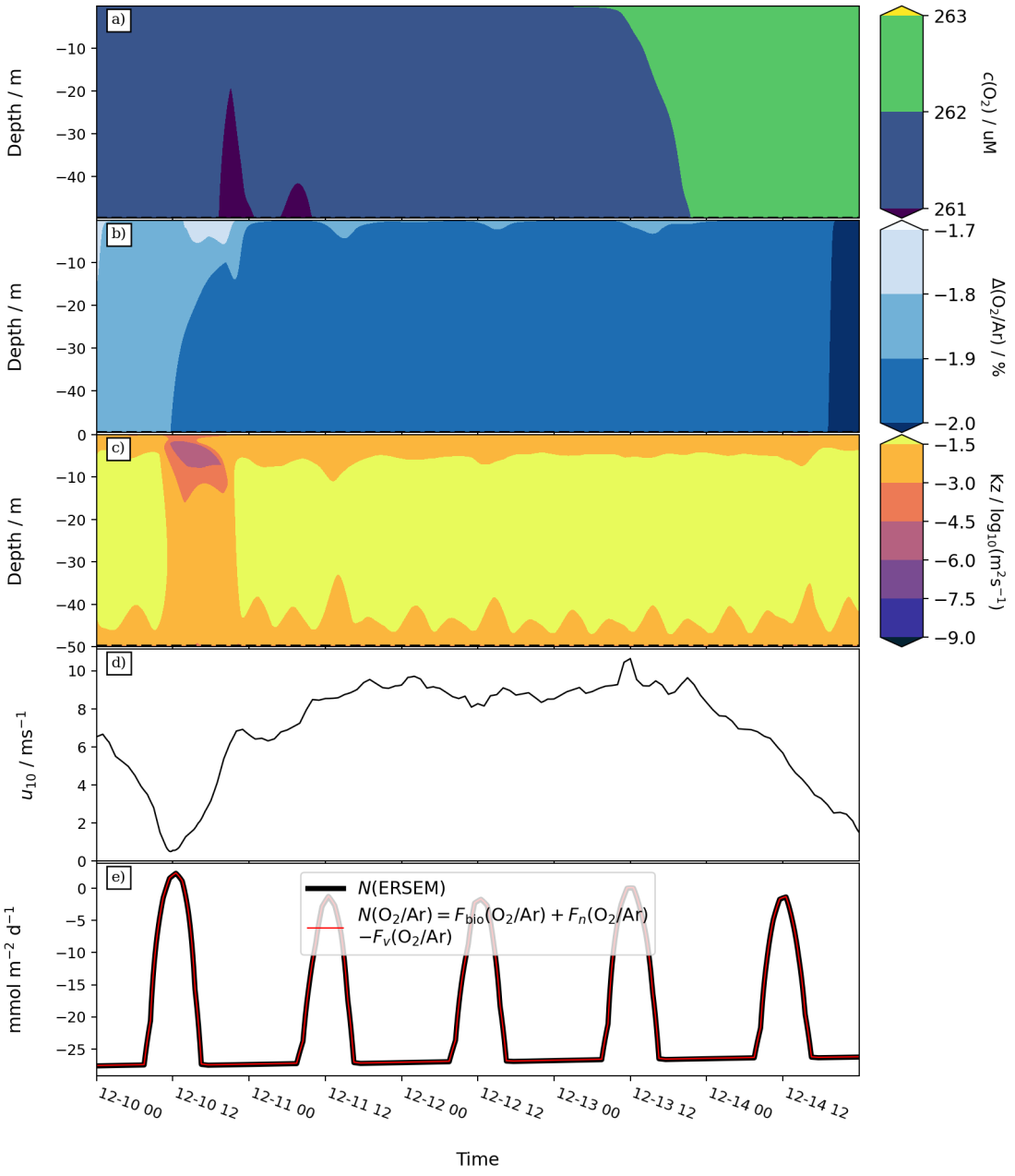

Figure 43: In this plot $N(O_2/Ar)$ and N(ERSEM) (e), during winter 2010, are compared to 3 forcing variables representing windspeeds (a), vertical diffusivity (c) and the oxygen

saturation anomaly driven by net metabolism (b). Integration depth (black dashed lines in a, b, and c) is set at 50 m.

Figure 44 shows that under these conditions, $F_{bio}(O_2/Ar)$ has a higher impact on model performance (Figure 44d: $\Delta_{RMS}N$ = 17 mmol m^{-2} d^{-1}) than $F_n(O_2/Ar)$ (Figure 44b: $\Delta_{RMS}N$ = 13 mmol m^{-2} d^{-1}).

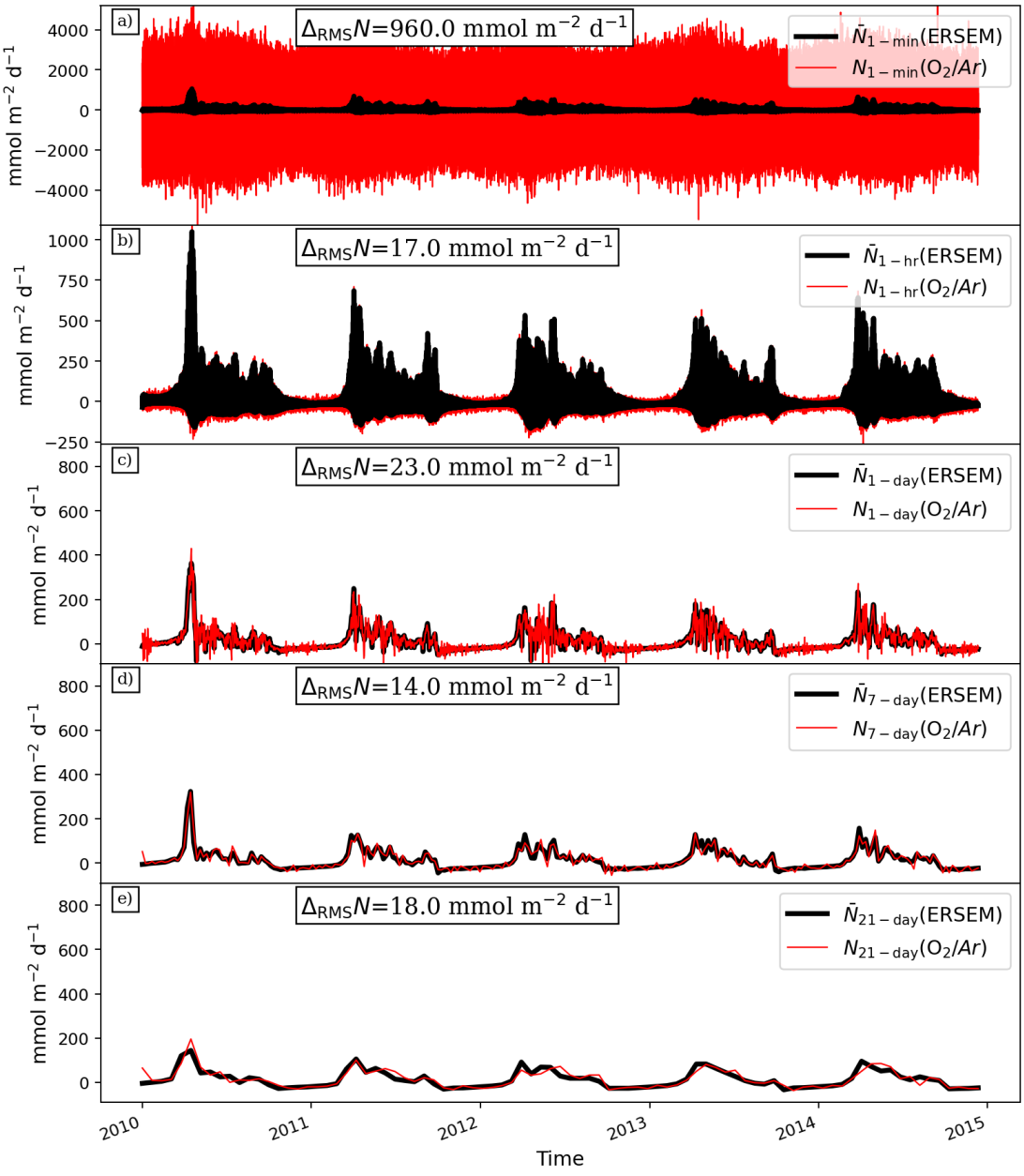

Figure 44: Diagnostic model performance (red) vs its target value (black) during winter 2009 at L4. Diagnostic models are namely: in (a) the full non-steady-state (N(ERSEM) = $N(O_2/Ar)$), in (b) assuming steady-state (N(ERSEM) = $F_{bio}(O_2/Ar)$ - $F_v(O_2/Ar)$), In (c) assuming steady-state with no influence from diffusive flux (N(ERSEM) = $F_{bio}(O_2/Ar)$), and

in (d) non-steady-state omitting air sea gas exchange and diffusive flux (N(ERSEM) = F_n). Integration depth was set at 50 m (not shown).

3.5.3.6Assuming steady-state at coarser sampling frequency

Figure 45 is like Figure 41, but for a sampling interval of 7 days (matching the ship-based sampling strategy for L4) and the time series covers 2 years (from 2009-01-01 to 2010-12-31). The discrepancy between the steady-state and non-steady-state results is still present but becomes less evident. Overall, not including the time disequilibrium term ($F_n(O_2/Ar)$) implies a +75 % uncertainty which is much less than what was shown at a sampling interval of 1 minute (Figure 41 and Figure 44). Omitting $F_n(O_2/Ar)$ from calculations results in wrong predictions of the onset and the duration of the spring bloom at L4. This result suggests that the steady-state assumption is less problematic for longer sampling interval. However, the selected sampling interval (7 days) was not sufficiently long to achieve steady-state.

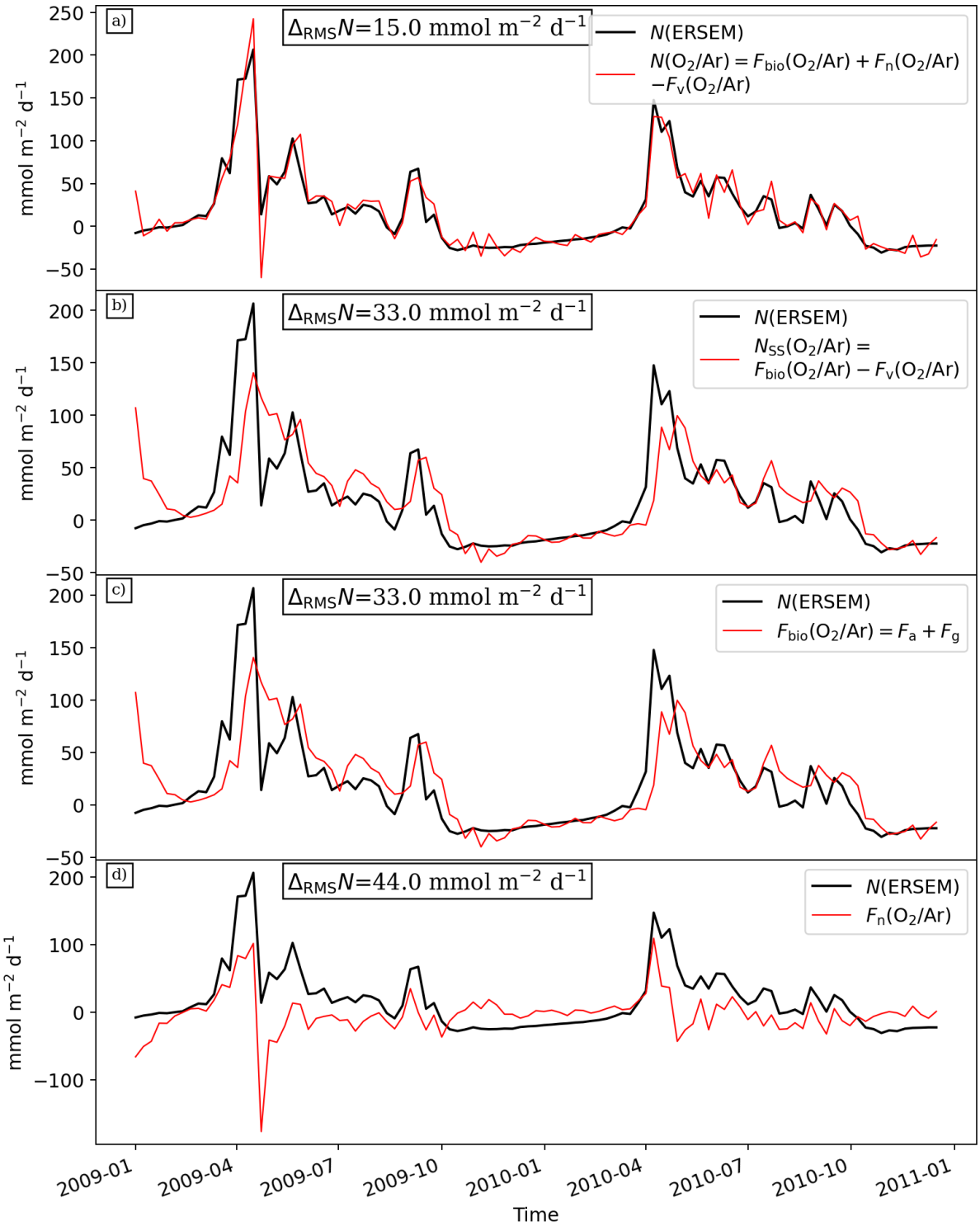

Figure 45: Diagnostic model performance (red) vs its target value (black) from spring bloom until summer 2010 at L4. Diagnostic models are namely: in (a) the full non-steady-state (N(ERSEM) = $N(O_2/Ar)$), in (b) assuming steady-state (N(ERSEM) = $F_{bio} - F_v$), In (c) assuming steady-state with no influence from diffusive flux (N(ERSEM) = F_{bio}), and in (d) non-steady-state omitting air sea gas exchange and diffusive flux (N(ERSEM) = F_n).

Integration depth was set at 50 m (not shown). Sampling intervals are 7 days long. N(ERSEM) is averaged at each sampling interval using the values of the previous week.

3.5.4 Q2: $N(O_2/Ar)$ sensitivity to integration depth in shallow dynamic waters such as L4.

The sensitivity of $N(O_2/Ar)$ and its composing terms was quantified using three different integration depths: surface mixed layer (2 m), euphotic depth (28 m), and full water column (50 m). The euphotic depth varies with time but was taken here as the mean depth where I(PAR) drops below 1 % of the surface value, and across the whole length of the simulation at simulation time resolution. Results are summarised as box plots, built using the monthly statistics described in section 3.4.5.2.

Results indicate that at L4, when water samples are taken near to the surface the inferred $N(O_2/Ar)$ can be one order of magnitude smaller than the total pelagic net community production (Table 4). When z_{int} was set at euphotic depth, the results for the third quartile and the 95th percentile were similar if not identical to $N(O_2/Ar)$ integrating the full water column. In contrast, results for the 1st quartile and 5th percentile were slightly overestimated (Table 4). These differences between integration depths follow from the pelagic distribution of functional groups across the water column where all gross oxygen production occurs in the upper 28 m of the water column while a substantial part of respiration occurs below the euphotic depth (Table 4 and Figure 46b and Figure 46c).

Table 4: Summary statistics for the overall net oxygen production from oxygen argon ratios ($N(O_2/Ar)$). z_{int} is the integration depth.

N/(mmol m^{-2} d^{-1})						
	z_{int}/m	P_5	Q_1	P_{50}	Q_3	P_{95}
$N(O_2/Ar)$	2	−5±4	−3±2	3±6	14±16	30±37
	28	−51±35	−37±23	2±28	91±99	187±179
	50	−69±41	−53±28	−13±25	79±97	174±173

The relevance of each term in Eq. (20) was also investigated: First, the diagnostic model minimises error associated the time disequilibrium term ($F_n(O_2/Ar)$) and it needs to include estimates of the vertical diffusive flux ($F_v(O_2/Ar)$) when z_{int} = 2 m. For z_{int} = 2 m, $F_{bio}(O_2/Ar)$ and $F_v(O_2/Ar)$ dominate $N(O_2/Ar)$ throughout most of the year (Figure 46; Table 5). However, the time disequilibrium term ($F_n(O_2/Ar)$) explained for most of $G(^{17}O)$, especially at the onset of the growing season during the spring bloom (April: $\tilde{F}_n(O_2/Ar)$ = –3 mmol m^{-2} d^{-1}; P_5 = –52 mmol m^{-2} d^{-1}; P_{95} = 89 mmol m^{-2} d^{-1}). This result highlights the importance of including estimates of vertical diffusivity when estimating $N(O_2/Ar)$ for the surface mixed layer only (Figure 46a; Table 5). Second, to minimise the error associated to neglecting $F_v(O_2/Ar)$, the diagnostic model should be integrated over the whole water column, however measurements need to be repeated in time to account for $F_n(O_2/Ar)$. When z_{int} was set at sub mixed layer integration depths the time disequilibrium term $F_n(O_2/Ar)$ represents much of the $N(O_2/Ar)$ flux during months of high pelagic metabolic activity. In winter $F_n(O_2/Ar)$ has the same influence as air-sea gas exchange term and the vertical diffusive flux. Here the influence of $F_v(O_2/Ar)$ was only shown using 28 m integration depth since K_z = 0 m^2 s^{-1} when h was set at 50 m of depth). Finally integrating at a depth horizon matching the average euphotic depth requires accurate measurements in both space and time and no term should be neglected (Figure 46b and Figure 46c).

Table 5: Summary statistics for the terms composing $N(O_2/Ar)$. z_{int}: integration depth.

F/(mmol m^{-2} d^{-1})				
Flux name	z_{int}/m	P_5	P_{50}	P_{95}
$F_{bio}(O_2/Ar)$ growing season	2 m	5±3	37±19	111±70
$F_n(O_2/Ar)$ growing season	2 m	–22±18	–3±2	30±30
	28 m	–180±89	–37±11	240±140
	50 m	–178±87	–43±15	240±140
$F_v(O_2/Ar)$ growing season	2 m	0.5±1.5	26±13	91±52
	28 m	–55±29	–7±4	–0.4±0.2
	50 m	0	0	0
$F_{bio}(O_2/Ar)$ winter	2 m	–40±16	–9±12	30±38
$F_n(O_2/Ar)$ winter	2 m	–7±7	–0.5±1	7±5
	28 m	–53±43	–6±6	55±49
	50 m	–40±30	–8.7±5.6	6±15
$F_v(O_2/Ar)$ winter	2 m	–40± 17	–10±12	24±36
	28 m	–53±43	–6±6	55±49
	50 m	0	0	0

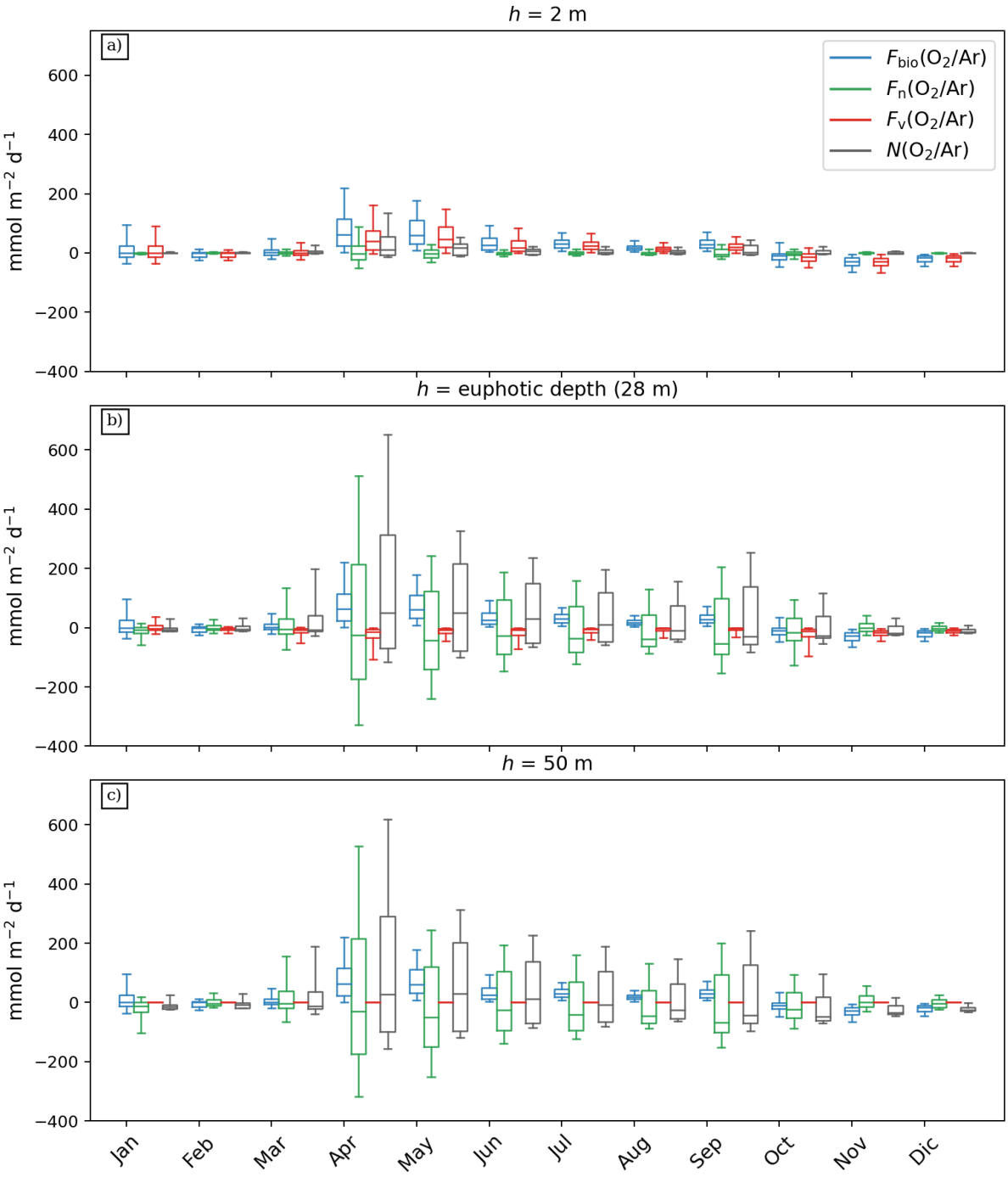

Figure 46: Month-by-month box model for $N(O_2/Ar)$ (in grey) and its constituent terms such as air-sea flux ($F_{bio}(O_2/Ar)$ in blue), vertical diffusivity ($F_v(O_2/Ar)$ in red) and time disequilibrium ($F_n(O_2/Ar)$ in green). Terms statistics through each month are compared to one another under three different integration depth scenarios such as surface depths (z_{int} = 2 m in panel a), euphotic zone (28 m in panel b) and integrating full water column (50 m in panel c). Where each box represents 5 statistics: the lower whisker cap is set to the 5th percentile, the lower box interface represents the 1st quartile, the inner horizontal line is the median, the upper limit of the box is the 3rd quartile, and the upper whisker cap is the 95th percentile.

3.5.5 Q3: $N(O_2/Ar)$ model sensitivity to the sampling interval and sampling error.

Figure 47 shows that the $N(O_2/Ar)$ calculated from discrete samples coarser than the model resolution ($N_{\Delta t}(O_2/Ar)$) represent N(ERSEM) averaged in time ($\overline{N}_{\Delta t}$(ERSEM)). Comparing results between different resolutions (Figure 44) it was shown that the higher the sampling interval the greater the calculated root mean squared difference ($\Delta_{RMS}N$). The greatest $\Delta_{RMS}N$ increase occurs when switching from sampling intervals of minutes to hours (+190 %) and hours to days (+120 %) compared to coarser sampling intervals. This result seems to suggest that having a finer resolution in the measurements would produce better results.

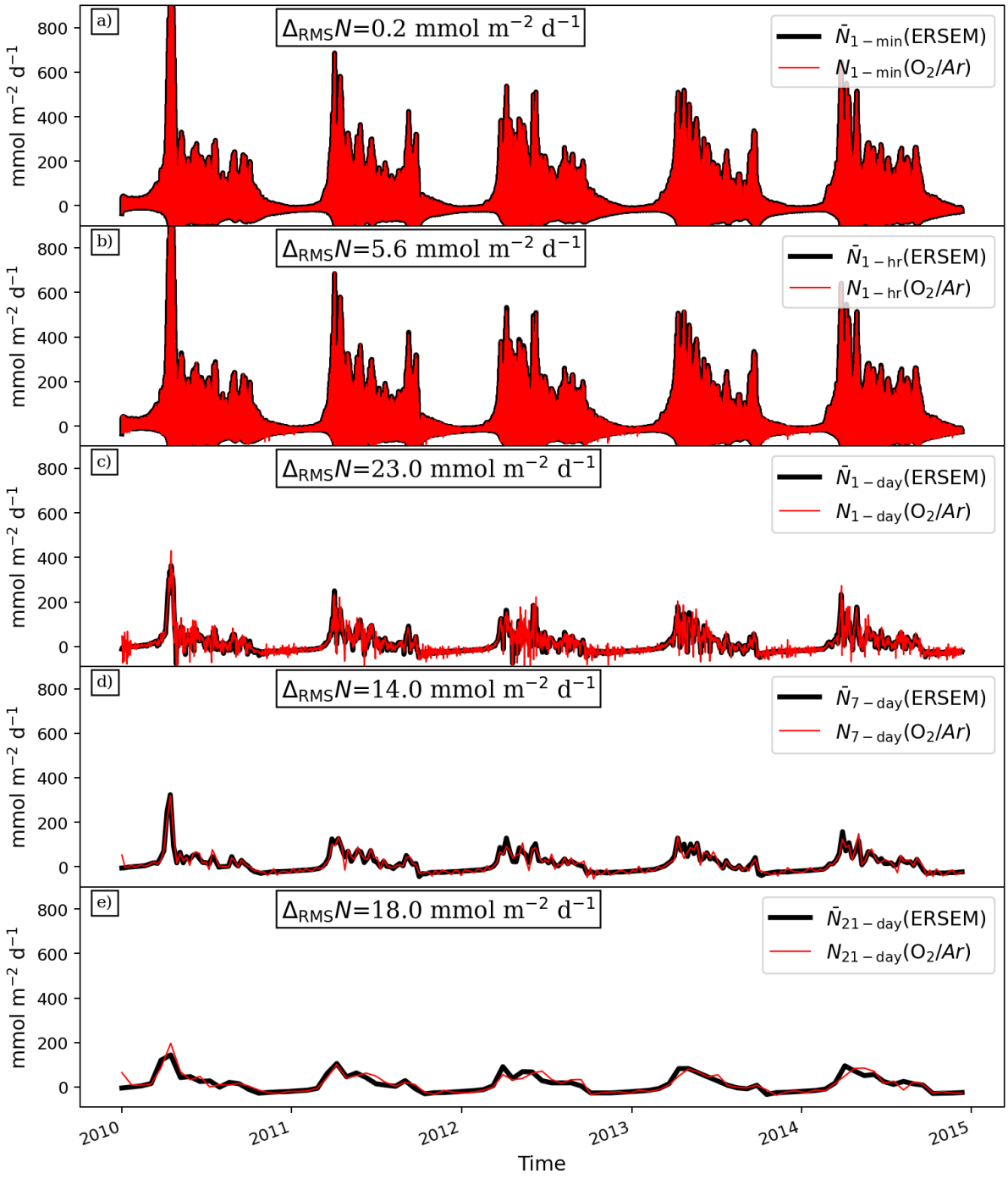

Figure 47: Direct timeseries comparison between time averaged N(ERSEM) ($\bar{N}_{\Delta t}$(ERSEM)) and N(O_2/Ar) calculated from subsampled at various intervals ($N_{\Delta t}$(O_2/Ar)) : every minute (n = 2630880), hour (n = 43848), day (n = 1827), week (n = 261) and 21 days (n= 87). Sampling resolutions coarser than 1 hour are taken at 10:00 am representing the time when L4 is routinely sampled. Performance of $N_{\Delta t}$(O_2/Ar) in predicting $\bar{N}_{\Delta t}$(ERSEM) is quantified as root mean squared difference $\Delta_{RMS}N$..

The sampling error reported in Gloël (2012) for the L4 dataset (σ = 0.03 %) was added to $c(O_2)$ as described in section 3.4.5.2. Results showed that the estimates of net community production calculated from sampling intervals smaller than 1 per day $N_{\Delta t}(O_2/Ar)$ were the most affected by experimental error while sampling intervals coarser than 1 per day had lower accuracy (Figure 48). The result suggests that there could be an optimum sampling interval for L4 station of the order of hours and days.

The optimum sampling strategy was then tested by increasing the number of sampling intervals and quantifying their predictive power using $\Delta_{RMS}N$ and the correlation coefficient (R^2). Estimates with sampling error were compared against estimates without sampling error (acting as control). Among the tested sampling strategies, calculations for $N_{\Delta t}(O_2/Ar)$ using a sampling interval of 2 hours produced the best predictions of net community production (Figure 49). In $N_{2\text{-}hr}(O_2/Ar)$ the performance of calculations unaffected by the sampling error are worse than calculations based on shorter sampling intervals (see grey bars in Figure 24); however, its analogue affected by sampling error best performed the other diagnostic models (See black bars in Figure 49).

We further investigated if there is a different optimal sampling interval for each season. Results showed that sampling once every 2 hours is the best strategy to in all seasons within the 5 years long simulation (Figure 50). All seasons showed the same results as in Figure 49 except for winter, in which the optimum sampling interval was 3 hours. In winter overall correlation coefficient and error was lower in all sampling frequencies after the introduction of the experimental error.

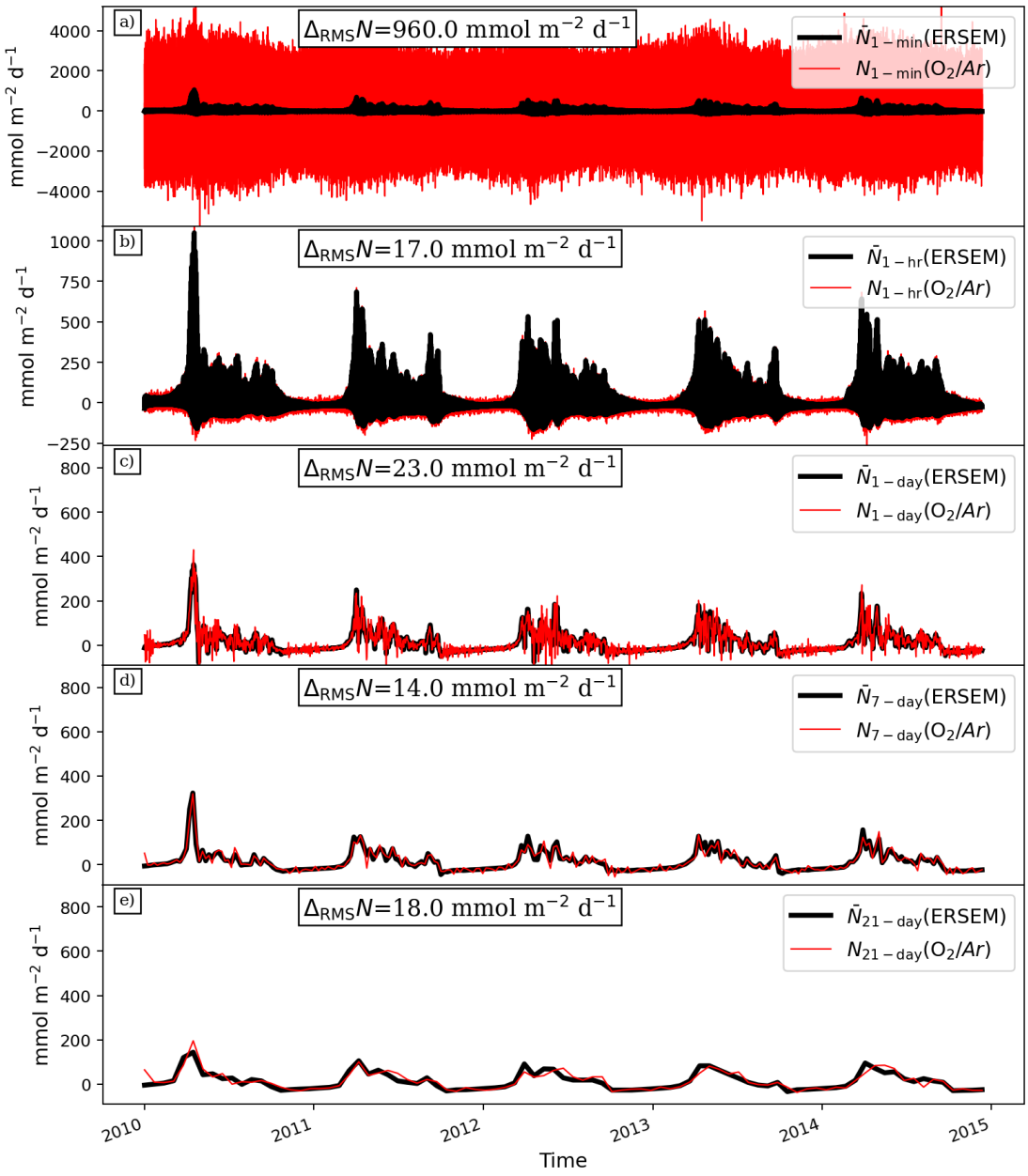

Figure 48: Direct timeseries comparison between time averaged N(ERSEM) ($\bar{N}_{\Delta t}$(ERSEM)) and N(O$_2$/Ar) calculated using from subsampled at various intervals ($N_{\Delta t}$(O$_2$/Ar)). Performance of $N_{\Delta t}$(O$_2$/Ar) in predicting $\bar{N}_{\Delta t}$(ERSEM) is quantified as root mean squared difference ($\Delta_{RMS}N$). Oxygen concentrations used to calculate $N_{\Delta t}$(O$_2$/Ar) are affected by relative sampling error with normal distribution (σ =0.03 %).

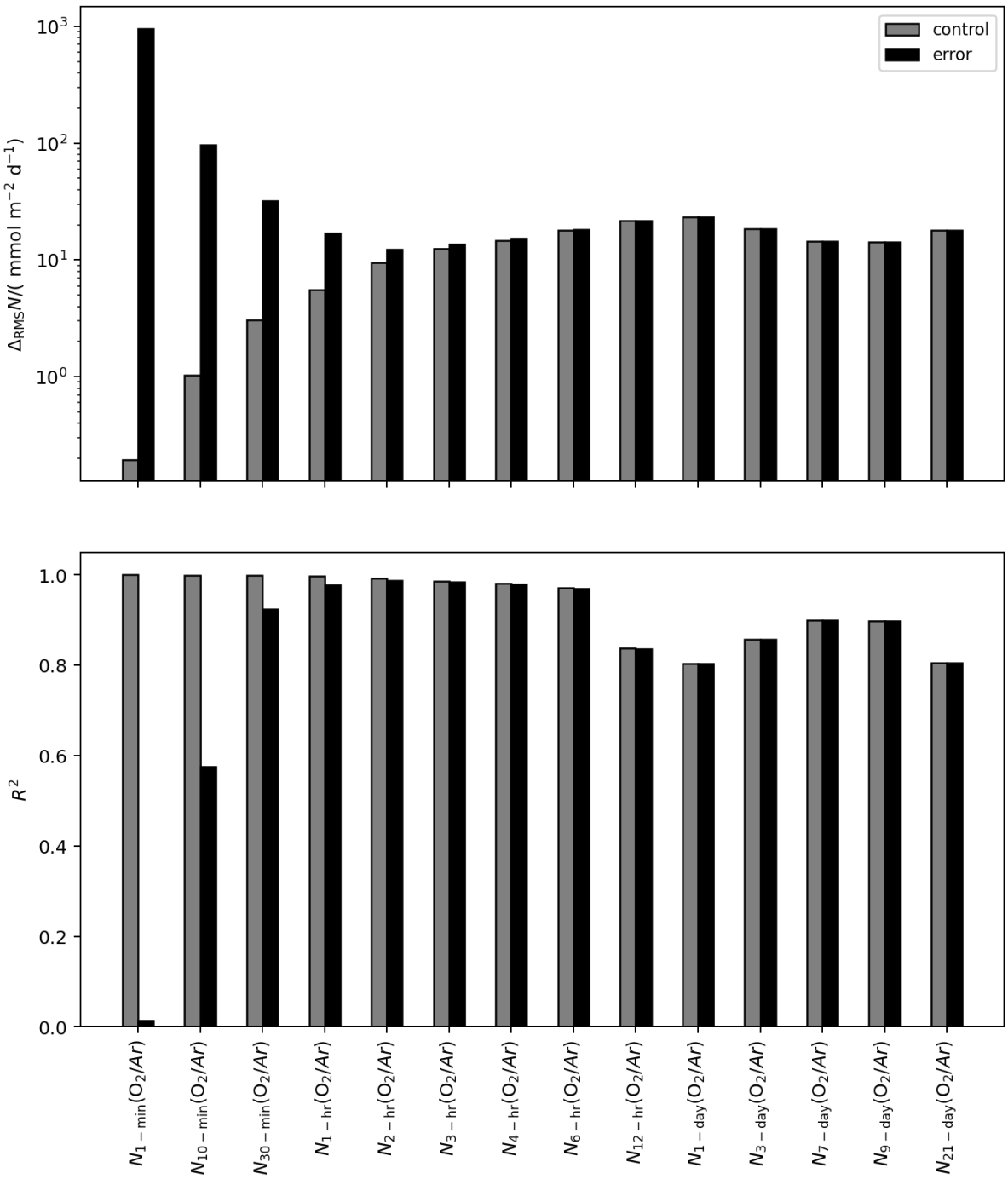

Figure 49: $\Delta_{RMS}(N)$ (above) and R^2 (below) against increasing sampling frequency at L4 over 5 years (from 01/01/2010 to 01/01/2015). Where results in black are calculated using oxygen concentrations affected by relative sampling error with normal distribution (σ = 0.03 %).

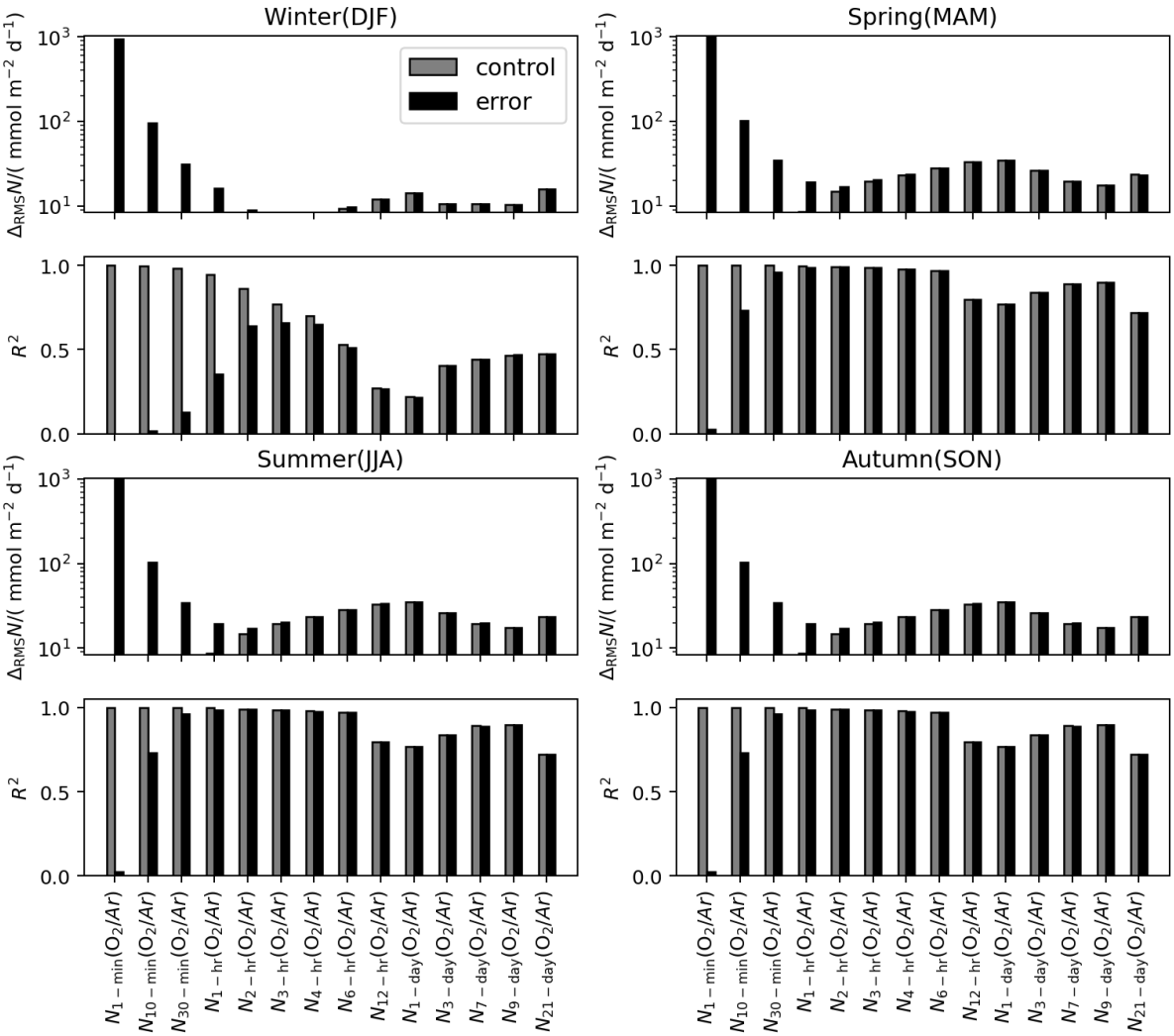

Figure 50: Seasonal ideal sampling strategy. $\Delta_{RMS}N$ (above) and R^2 (below) against increasing sampling intervals at L4 over 5 years (from 01/01/2010 to 02/01/2015) after dataset being reorganised according to the four different seasons. Where results in black are calculated with sampling experimental error was added to $c(O_2)$.

A final sensitivity test on sampling intervals was made to address why higher sampling resolutions are particularly affected by the experimental error. To do so the calculations used to produce Figure 41, which provided a detailed breakdown for $N(O_2/Ar)$ at the highest possible time resolution, was repeated but this time using values affected by experimental error (Figure 51). The error observed in high sampling frequencies comes solely from the calculations of the disequilibrium term $F_n(O_2/Ar)$ (Figure 51).

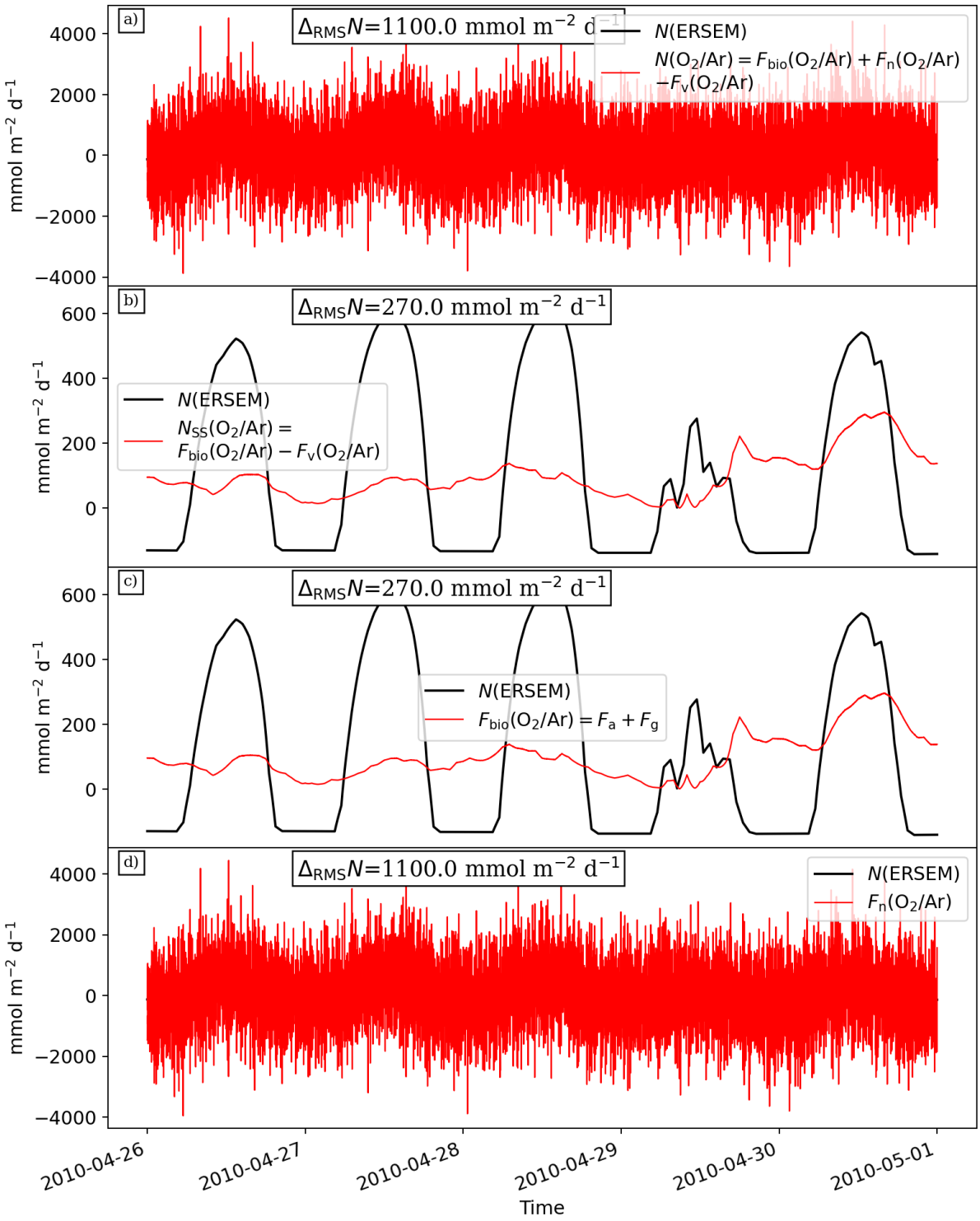

Figure 51: Diagnostic model performance affected by experimental error (red) vs its target value (black) during the late spring bloom 2010 at L4. Diagnostic models are namely: in (a) the full non-steady-state (N(ERSEM) = N(O_2/Ar)), in (b) assuming steady-state (N(ERSEM) = F_{bio}(O_2/Ar) - F_v(O_2/Ar)), In (c) assuming steady-state with no influence from diffusive flux (N(ERSEM) = F_{bio}(O_2/Ar)), and in (d) non-steady-state omitting air sea gas exchange and diffusive flux (N(ERSEM) = F_n(O_2/Ar)). Integration depth was set at 50 m (not shown).

3.6 Discussion

3.6.1 Q1: uncertainties derived from steady-state assumption

This study has found that for shelf sea applications, the steady-state assumption should be avoided by repeating sampling stations in time. This allows the time disequilibrium term $F_n(O_2/Ar)$ to be inferred $N(O_2/Ar)$. If $N(O_2/Ar)$ is in steady-state over time intervals that match sampling frequency used by Gloël (2012) would introduce a 75 % error during periods of high metabolic activity ($N(O_2/Ar)$ = (124.1±276.2) mmol m^{-2} d^{-1}) at Station L4. In Gloël (2012) it was reported no significant difference in the results between net community production flux calculated assuming steady-state (i.e., $F_n(O_2/Ar) = 0$) and non-steady-state (i.e., $F_n(O_2/Ar) \neq 0$). However, results here were based on a direct comparison against a target known quantity (N(ERSEM)) and clearly showed significant underestimations, especially during periods of high metabolic activity such as the spring bloom (Gloël, 2012). The omission of the time disequilibrium term in the calculation of $N(O_2/Ar)$ results in the underestimation of episodes of high production rates such as the spring bloom. Furthermore, not including $F_n(O_2/Ar)$ results in the misprediction of the timing and the duration of such events. This result agrees with a modelling study based on a box model (Jonsson et al., 2013). In both this work and Jonsson et al. (2013) omitting $F_n(O_2/Ar)$ results in a time lag between the production of oxygen by photosynthesis and its detection by $N(O_2/Ar)$ (Figure 16). Jonsson et al. (2013) suggested that steady-state $N(O_2/Ar)$ rather than a real-time estimate is a much closer estimate of N(ERSEM) averaged over the past residence time. Similarly to Jonsson et al. (2013), Teeter et al. (2018) demonstrated that when $N(O_2/Ar) = F_a(O_2/Ar)$ alone (named *bioflux* in both Jonsson et al. 2013, and Teeter et al. 2018) it approximates the exponentially weighted N(ERSEM) over a sampling window of about 1 month (representing the mean O_2 residence time in shallow waters). The omission of $F_n(O_2/Ar)$ causes a 6 % decrease of prediction error during periods of low metabolic rates ($N(O_2/Ar)$ = (–20.6±9.7) mmol m^{-2} d^{-1}). This suggests that on seasonal time scales the relevance of $F_n(O_2/Ar)$ is dependent on biological rates.

3.6.2 Q2: $N(O_2/Ar)$ sensitivity to integration depth in shallow dynamic waters such as L4.

The relative contribution of vertical transport, when integration depth was set at the euphotic depth, represented a substantial proportion of $N(O_2/Ar)$ in both high ((15.0±15.0) %) and low ((28.1±10.6) %,) periods of metabolic activity. Unfortunately, the influence of the diffusion term was not calculated by Gloël 2012 therefore direct comparisons to L4 data are not possible. However, vertical diffusivity contributions to $N(O_2/Ar)$ resulted here were found much higher than what observed in the Celtic Sea (Seguro et al., 2018) (there reported as 6.8 %) when the integration depth was set to match the mixed layer depth. Results not accounting for vertical diffusive mixing will lead to under- or overestimations, depending on the sign of the transport flux. For example, if thermocline waters are significantly undersaturated compared to the mixed layer the vertical transport (due to deepening of the mixed layer depth and/or diffusivity across the mixed layer depth) would dilute mixed layer O_2 concentrations and finally decrease its exchange to the atmosphere. As a result of vertical transport $N(O_2/Ar)$ can significantly deviate from its target value N(ERSEM). Studies in regions characterised by strong vertical mixing such as coastal areas (Giesbrecht et al., 2012; Hamme and Emerson, 2006; Haskell and Fleming, 2018; Izett et al., 2018; Jonsson et al., 2013), discussed that $N(O_2/Ar)$ can be overestimated by shoaling waters that are supersaturated of biological oxygen when the integration depth used for calculations is set above the deep chlorophyll maxima (e.g., Cassar et al., 2007; Giesbrecht et al., 2012; Reuer et al., 2007).

3.6.3 Q3: $N(O_2/Ar)$ model sensitivity to sampling intervals and sampling error.

In the last section results indicated that in shallow coastal waters such as L4 it is preferable to use sampling intervals of 2 hours. This time resolution was the least affected by systematic and random error. Here systematic error is referred as the difference between $N(O_2/Ar)$ and N(ERSEM) introduced by increasing sampling time frequency without prescribed random error ($\sigma = 0.03$ %). The time disequilibrium term $F_n(O_2/Ar)$ was responsible for high predicting error resulting from sampling intervals of high resolution. The root mean squared difference $\Delta_{RMS}N$ shown in Fig 24b and Fig 15b were almost identical while all the other panels containing the disequilibrium term resulted dominated by random error. The disequilibrium term is particularly affected

by random error because it constituted by time derivative calculation resulting in sharp gradients along the time axis. Furthermore, since the term is multiplied by the integration depth z_{int}, integrating the whole water column proportionally increases the effects of sampling error to $F_n(O_2/Ar)$.

This result indicates that changing the sampling strategy used in Gloël (2012) (weekly samples) to a sample per hour, would have decreased the predicting error by 1 order of magnitude and the correlation to N(ERSEM) would have improved by a factor of 3. The hourly resolution is, however, impractical for the methodology used by Gloël (2012) which involves analysing oxygen and argon supersaturations from water samples collected from hydrocasts (See Chapter 2 methods for $N(O_2/Ar)$ analysis). Finally, the results indicate that the integration depth should avoid oxygen vertical gradients given the high sensitivity of derivatives of oxygen concentrations affected by random noise. Therefore, integrating the full water column would bring the double benefit of having the full quantitative estimate of L4 pelagic metabolic rates and diminished uncertainties caused by sampling error.

3.7 Conclusions

This study highlighted that assuming $N(O_2/Ar)$ is in steady-state in dynamic systems such as shelf seas may cause up to 75 % error to predicted values. The steady-state assumption implies severe underestimations during periods of high metabolic activity and overestimations in periods of low metabolic activity. Vertical mixing, when the integration depth was set at the euphotic depth, represented a significative proportion of $N(O_2/Ar)$ in both high ((15.0±15.0) %) and low ((28.1±10.6) %,) periods of metabolic activity. This was found to be a much higher contribution than what previous studies observed in the Celtic Sea in 2018. Given the shallow nature of coastal shelf sea waters integrating the full water column can represent a valid option to avoid uncertainties related to vertical diffusive mixing. Finally, the ideal sampling frequency for dissolved oxygen and argon concentrations at station L4 would be a sample per 2 hours. Coarser resolutions are affected by an overall drop in model performance inferring net community production. Higher resolutions are dominated by the experimental error. The non-steady-state term $F_n(O_2/Ar)$, which is a function of depth and temporal gradient, was most sensitive to random error at high resolutions. Hourly scale variability data for $N(O_2/Ar)$ could be successfully collected using a membrane

inlet mass spectrometer (MIMS) (Kaiser *et al*., 2005) installed on the sampling station at L4 (Smyth et al., 2010). Setups for MIMS equipment for shelf sea applications was described in Seguro et al. (2019).

Given the 1D nature of ERSEM-FABM-GOTM simulations the contributions for lateral transport were not addressed in this experiment. However, past studies discussed the importance of lateral transport affecting $N(O_2/Ar)$ and how in some geographical areas affected by strong currents such as the Southern Ocean, lateral transport accounts for most of the $N(O_2/Ar)$ flux (Jonsson et al., 2013a). Therefore, future work could implement this experiment into 3D model simulations by coupling ERSEM to the Nucleus for European Modelling of the Ocean (NEMO) (following Skákala et al., 2018) and setting the simulation run for the whole Western English Channel. This could help quantifying the effects of lateral transport in shallow dynamic waters such as shelf seas, including L4. This also might help explaining how representative are L4 measurements of net community production over the Western English Channel region.

Chapter 4: Using the ERSEM model to simulate gross production with oxygen triple isotopes at L4, Western English Channel

4.1 Abstract

Gross production (G) refers to the rate of total organic carbon production by oxygenic photoautotrophs. As organic carbon is produced, oxygen is released to the environment as a product of photosynthesis. G can be calculated from the simultaneous measurement of the three oxygen isotopologues dissolved in sea water, $G(^{17}O)$. While the oxygen triple isotope-method has been widely used in the open ocean, it is less common in dynamic and tidally mixed shelf sea environments, where assumptions regarding steady-state dynamics are less likely to hold. Although corrections for non-steady-state dynamics can be made, these require a time series of observations which is not always available. Furthermore, it remains uncertain at what frequency observations should be made to account for non-steady-state dynamics, and thus minimise the error in the associated calculation of $G(^{17}O)$.

To help answer these questions and to determine a set of best practices for the calculation of $G(^{17}O)$ in shelf-sea environments, we configured an Observing System Simulation Experiment (OSSE) to reproduce conditions at Station L4 in the Western English Channel. Considering typical measurement errors associated with the determination of oxygen isotope concentrations, we determined the ideal sampling frequency at Station L4 to be weekly. Compared with assuming steady-state, the error in diagnosed $G(^{17}O)$ is 53 % lower when considering week-to-week changes. Moreover, when steady-state was assumed, the timing and magnitude of production peaks during the spring bloom were found to be in error relative to the exact values.

In addition, we used an OSSE to investigate the impact of phytoplankton species-specific isotope effects in photosynthesis on diagnosed $G(^{17}O)$. We found that neglecting these isotope effects can cause a small systematic overestimate of $G(^{17}O)$, rising to up to +50 % during the spring bloom at L4.

Taken together, these results can be used to design observational studies aimed at determining $G(^{17}O)$ in dynamic shelf-sea environments like Station L4.

4.2 Introduction

Shelf seas play a fundamental role in the global carbon cycle. Through oxygenic photosynthesis, organisms convert inorganic carbon dissolved in sea water to energy-rich organic carbon, producing oxygen as a co-product. Gross oxygen production (G) refers to the total amount of oxygen per unit area that is released into the environment by all primary producers.

Over the past 20 years, G has been estimated from the simultaneous measurement of the three-oxygen stable isotopologues $^{16}O^{16}O$, $^{16}O^{17}O$ and $^{16}O^{18}O$ dissolved in surface seawater (Luz and Barkan, 2000 ; Kaiser, 2011). The basis of this method is derived from the fact the isotopic composition of O_2 in the atmosphere differs from that of photosynthetic O_2. Stratospheric photochemical reactions transfer more ^{17}O out of O_2 than expected from the fraction of ^{18}O transferred by a mass-dependent process. This relatively ^{17}O-depleted stratospheric air mixes with the troposphere. In contrast, oxygen isotope effects during photosynthesis and respiration follow mass-dependent isotope fractionation laws. Thus, the mass balance of oxygen triple isotopes in surface waters is determined by the rates of air-sea gas exchange, photosynthesis and respiration. Using a steady-state approach like that used for the calculation of net community production rates (Chapter 3), the rate of air-sea exchange can be determined from wind-speed based gas exchange parameterisations. In addition, the fact that the relative fractionations in $^{17}O/^{16}O$ and $^{18}O/^{16}O$ during respiration is tightly constrained can be exploited to separate photosynthesis and respiration, resulting in a biogeochemical estimate of the photosynthetic O_2 production rate, designated $F_{bio}(^{17}O)$.

$F_{bio}(^{17}O)$ is routinely measured together with $F_{bio}(O_2/Ar)$ (Juranek and Quay, 2013). Just as $F_{bio}(O_2/Ar)$, $F_{bio}(^{17}O)$ has been rarely used in topographically complex, tidally mixed shelf seas where the assumption of steady state is less likely to hold when compared with less dynamic, open ocean environments.

In northwest European shelf seas (NWESS) only three studies have used oxygen triple isotopes to estimate gross O_2 production (Gloël, 2012; Seguro et al., 2019; and this project). The present project did not include measurements repeated in time, mandating the steady-state approach used in Chapter 2. However, Seguro et al. (2019) reported on samples collected in 2015 along a repeat cruise track in the Celtic Sea and along the

shelf edge, with time intervals of days to weeks between samples. Also, Gloël (2012) established a yearlong time series at Station L4 in 2009/10. Both datasets allowed the inclusion of changes in the oxygen triple isotope composition over time, not requiring the steady-state-assumption.

In addition, both Gloël (2012) and Seguro et al. (2019) collected water samples at different depths. This allowed the effect of vertical diffusive mixing to be included in calculations of photosynthetic O_2 production, with the diffusive O_2 flux estimated across the base of the integration depth (taken to be the average euphotic depth).

Combining the steady-state based estimate of $F_{bio}(^{17}O)$ with temporal changes ($F_n(^{17}O)$) and vertical diffusive fluxes ($F_v(^{17}O)$) of oxygen triple isotopologues allowed Gloël (2012) and Seguro et al. (2019) to generate a more complete and therefore likely to be more accurate estimate of gross O_2 production:

$$G = G(^{17}O) = F_{bio}(^{17}O) + F_n(^{17}O) + F_v(^{17}O) \quad (51)$$

In a previous modelling study, oxygen isotopes were added to a one-dimensional mixed layer model to assess the error associated with neglecting vertical mixing in $G(^{17}O)$ calculations at the Bermuda Atlantic Time-series (BATS) and Hawaii Ocean Time-series (HOT) sites (Nicholson et al., 2012). In their experiment, neglecting vertical transport resulted in the largest source of error, accounting for an overestimate of G between 60 % and 80 %. Vertical mixing becomes an important term when a mass of water that is rich in photosynthetic oxygen shoals from below the integration depth (which in Nicholson et al. 2012 was set to be the depth of the surface mixed layer, z_{mix}), causing overestimates of G. This usually occurs in periods when the primary producers form a deep chlorophyll maximum below z_{mix}. While this study was pertinent to oceanic waters, its relevance to shallow, dynamic shelf seas is unclear.

In this chapter, we will explore how much the different terms in Eq. (51) contribute to $G(^{17}O)$ and how frequently they need to be measured. For this purpose, Observing System Simulation Experiments (OSSEs) will be run using the one-dimensional GOTM model coupled to the ERSEM ecosystem model.

The calculation of $F_{bio}(^{17}O)$ requires the isotopic composition of photosynthetic O_2. In the past, the $^{18}O/^{16}O$ fractionation during photosynthesis ($^{18}\varepsilon_P$) was considered to be small and photosynthetic oxygen was thought to have the same isotopic composition as

the source water (Guy et al., 1993). For example, $^{18}\varepsilon_P$ was found to be 0.62 ‰ (Guy et al., 1993) for *Phaeodactylum tricornutum* and 0.5 ‰ for *Synechocystis* (Helman et al., 2005).

However, a separate study based on flask cultures found considerably higher $^{18}\varepsilon_P$ for several autotrophs including *Nannochloropsis oculata* (2.85 ‰) and *Chlamydomonas reinhardtii* (7.04 ‰) (Eisenstadt et al., 2010). Isotopic fractionation was suggested to occur during oxygen consumption reactions (e.g., photoreduction, and photorespiration) during photosynthesis (Eisenstadt et al., 2010). This study not only demonstrated $^{18}\varepsilon_P >> 0$, but also showed that the relationship between $^{17}\varepsilon_P$ and $^{18}\varepsilon_P$ varied between species.

Variations in the latter relationship have been suggested to cause variations of up to 30 % in $G(^{17}O)$ estimates (Kaiser and Abe, 2012). Most of the studies using $G(^{17}O)$ have made no consider this issue and assumed no isotopic fractionation (e.g., Hendricks et al., 2004; Luz and Barkan, 2005; Stanley et al., 2010). Other studies use the average ε_P of Eisenstadt et al. (2010) (e.g., Kaiser, 2011; Luz and Barkan, 2011; Nicholson et al., 2012; Prokopenko et al., 2011).

An additional focus of this chapter is therefore a quantitative estimate of the error in $G(^{17}O)$ caused by potential variations in the isotopic composition of the photosynthetic endmembers, again using OSSEs with the GOTM-ERSEM model combination.

4.3 Aims

The main aim of this Chapter is to use models to quantify uncertainties associated with the estimate of pelagic gross production from simultaneous measurements of the three isotopologues of oxygen in a shallow, dynamic shelf sea setting. The following research questions were addressed:

Q1.) What is the error introduced by assuming that $G(^{17}O)$ is in steady-state at L4?

Q2). What is the relative contribution of the diffusive flux to estimates of gross oxygen production in a dynamic turbulent water column such as L4?

Q3.) What is the ideal temporal sampling strategy for establishing a $G(^{17}O)$ time series at L4? Does the ideal strategy match routine observations; and if not, how much error is introduced when compared to the ideal sampling frequency?

Q4). What is the effect on $^{17}\Delta$ of primary producers that have distinct photosynthetic oxygen isotope fractionation effects? Further, what is the effect on $G(^{17}O)$?

4.4 Methods

In this section we describe the oxygen isotope fractionation scheme which was added to ERSEM. Further, we describe the diagnostic model used to estimate $G(^{17}O)$ from ERSEM outputs, and the method used to compare it with the value of G computed directly by ERSEM. These methods are described in the context of the four core research questions that were addressed in the study.

4.4.1 The ERSEM-FABM-GOTM model

We configured a 1D model simulation for Station L4 in the Western English Channel. We used the European Regional Sea Ecosystem Model (ERSEM) (Butenschön et al., 2016) coupled to the 1D General Ocean Turbulence Model (GOTM) (Burchard et al., 1999) using the Framework for Aquatic Biogeochemical Models (FABM) (Bruggeman and Bolding, 2014) coupling framework. A description of the numerical integration scheme and the simulation set up for Station L4 can be found in Chapter 3.

4.4.2 Notations and definitions in isotopic calculations:

The abundance of an oxygen isotope is commonly expressed using delta notation:

$$\delta(^{i}\mathrm{O}) = \frac{r_{\mathrm{sample}}(^{i}\mathrm{O}/^{16}\mathrm{O})}{r_{\mathrm{standard}}(^{i}\mathrm{O}/^{16}\mathrm{O})} - 1 \tag{52}$$

where the term r represents the isotope ratio defined as:

$$r(^{i}\mathrm{O}/^{16}\mathrm{O}) = \frac{n(^{i}\mathrm{O})}{n(^{16}\mathrm{O})} \tag{53}$$

where n is the amount of the substance and the superscript i can be either 17 or 18. $\delta(^{i}\mathrm{O})$ may be abbreviated as $^{i}\delta$ (Kaiser, 2011).

The isotopic fractionation factor is defined as:

$$^{i}\alpha(\mathrm{A/B}) = \frac{r_{\mathrm{A}}(^{i}\mathrm{O}/^{16}\mathrm{O})}{r_{\mathrm{B}}(^{i}\mathrm{O}/^{16}\mathrm{O})} = \frac{1 + {}^{i}\delta_{\mathrm{A}}}{1 + {}^{i}\delta_{\mathrm{B}}} \tag{54}$$

The isotopic fractionation ε is defined as

$$^{i}\epsilon = {}^{i}\alpha - 1 \quad (55)$$

The relationship between $^{17}O/^{16}O$ and $^{18}O/^{16}O$ is expressed as:

$$\gamma = \frac{^{17}\epsilon}{^{18}\epsilon} \quad (56)$$

Specifically, the ratio of isotopic fractionations during respiration is $\gamma_R = 0.5179 \pm 0.0006$ (Luz and Barkan, 2005).

Many different mathematical expressions exist for expressing the relationships between $\delta(^{17}O)$ and $\delta(^{18}O)$, with different advantages, as reviewed by Kaiser (2011). Here, the ^{17}O isotope excess, $^{17}\Delta$, was defined using a linear relationship with a coefficient $\kappa = \gamma_R = 0.5179$, i.e., equal to the ratio of respiration isotopic fractionations, following Kaiser (2011):

$$^{17}\Delta = \delta\left(^{17}O\right) - \kappa\delta\left(^{18}O\right) \quad (57)$$

Since $^{17}\Delta$ depends on the chosen mathematical relationship and coefficients in its definitions, it is most useful to illustrate variations between $\delta(^{17}O)$ and $\delta(^{18}O)$ for presentational purposes, rather than for quantitative calculations.

For this reason, we also use the dual-delta method of Kaiser (2011) to calculate $F_{bio}(^{17}O)$ and $G(^{17}O)$ from $\delta(^{17}O)$ and $\delta(^{18}O)$ directly rather than approximations using the ^{17}O excess ($^{17}\Delta$).

4.4.3 Adding Oxygen isotopes ^{16}O, ^{17}O and ^{18}O to ERSEM

ERSEM has a modular code structure, which has been built using Objective Orientated design principles. Each state variable has its own base model, which is implemented in separate source files. Similar state variables (e.g., different phytoplankton groups) share the same source code, but are distinguished by parameter values and switches which are specified in the run configuration file. In this study, the oxygen base model represented the most abundant oxygen isotope (^{16}O). In ERSEM, the oxygen model includes parameterisations for air-sea gas exchange and solubility changes as a function of temperature and salinity. The dependence of oxygen solubility on temperature and salinity was updated relative to the published model, with a new scheme implemented

using the polynomial equation given by (García and Gordon, 1992) for the coefficients based on Benson and Krause 1984.

Oxygen air-sea gas exchange (F_{as}) was calculated as follows:

$$F_{as} = k\left(c_{sat,0} - c_0\right), \tag{58}$$

Where k is the O_2-specific gas exchange coefficient, c_0 is the surface water O_2 concentration and $c_{sat,0}$ is the O_2 air-saturation concentration for surface water temperature and salinity.

The oxygen isotopes ^{17}O and ^{18}O were added as new state variables to ERSEM. Isotope fractionation can occur during gas exchange at the air-sea interface and during photosynthesis and respiration. Support for the two new state variables representing ^{17}O and ^{18}O was implemented into ERSEM's original source file for oxygen (*oxygen.F90*). Fractionation during air-sea gas exchange was explicitly accounted for. Fractionation during photosynthesis and autotrophic respiration was inserted into ERSEM's source file primary producers (*primary_producers.F90*). Finally, oxygen fractionation during heterotrophic respiration was implemented in three separate files: *bacteria.F90, mesozooplankton.F90, and microzooplankton.F90* (Figure 52). The model was run without the benthic system.

Fractionation during air-sea gas exchange:

During air-sea gas exchange, fractionation occurs due to kinetic ($^i\alpha_E$: O_2 evasion) and equilibrium fractionation ($^i\alpha_{eq}$):

$$^iF_{as} = -^i\alpha_E k(^i\alpha_{eq} c_{sat,0} - c_0) \tag{59}$$

where $^iF_{as}$ is the air-sea flux for ^{17}O (i = 17) and ^{18}O (i = 18). $^{18}\alpha_E$ is equal to 0.9972 (Knox et al., 1992), while $^{18}\alpha_{eq}$ is a function of temperature according to Benson et al. (1979):

$$^{18}\alpha_{eq} = 1 + {}^{18}\alpha_{sat} = e^{7.2951\times10^{-4}+0.42696\,K/T} \tag{60}$$

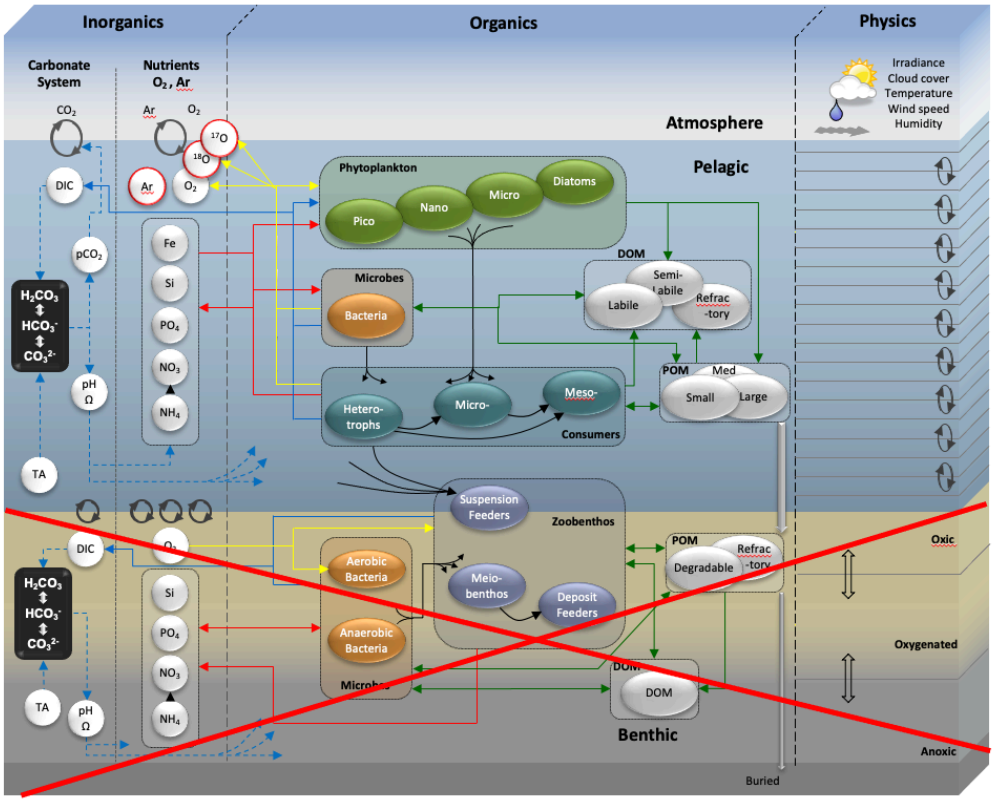

Figure 52: Schematic of the ERSEM-GOTM model setup showing all model dependencies between the inorganic and organic sub models (modified from Butenschön et al., 2016). This schematic also includes the addition of oxygen isotopes ^{17}O and ^{18}O made in this study. Internal physical transport is solved only in the vertical directions by diapycnal diffusion (See validation section for more details). For this study, the benthic system was switched off (red cross) to decrease complexity and computing burden for online and post-processing calculations.

Equilibrium fractionation for ^{17}O was calculated as a function of $^{18}\alpha_{eq}$ (Benson and Krause, 1984) and $^{17}\Delta_{sat}$ (Luz and Barkan, 2009):

$$^{17}\alpha_{eq} = 1 + {}^{17}\alpha_{sat} = e^{7.2951\times10^{-4}+0.42696\ \mathrm{K}/T+{}^{17}\Delta_{sat}} \quad (61)$$

where

$$^{17}\Delta_{sat}/\mathrm{ppm} = 0.5871t/^{\circ}\mathrm{C} + 1.798 \quad (62)$$

Finally, $^{17}O/^{16}O$ fractionation during O_2 evasion was calculated as a function of $^{18}\alpha_E$, $^{18}\alpha_{eq}$, and $^{17}\alpha_E$, assuming a mass-dependent relationship with coefficient 0.516 (Kaiser and Abe, 2012):

$$^{17}\alpha_{\mathrm{E}} = \frac{(^{18}\alpha_{\mathrm{eq}}\,^{18}\alpha_{\mathrm{E}})^{0.516}}{^{17}\alpha_{\mathrm{eq}}} \tag{63}$$

4.4.3.1 Fractionation during biological processes:

In ERSEM, biological sources and sinks of O_2 are expressed as concentration changes over time. The isotopic fractionations for respiration and production were implemented as follows:

$$\frac{\mathrm{d}c_{\mathrm{bio}}}{\mathrm{d}t} = Q_{\mathrm{P}}g - Q_{\mathrm{R}}r \tag{64}$$

$$\frac{\mathrm{d}\,^{i}c_{\mathrm{bio}}}{\mathrm{d}t} = Q_{\mathrm{P}}\left(1 + {}^{i}\delta_{\mathrm{P}}\right)g - Q_{\mathrm{R}}\frac{^{i}c}{c}\left(1 + {}^{i}\varepsilon_{R}\right)r \tag{65}$$

where the left-hand side represents the change of biological ^{16}O, ^{17}O and ^{18}O concentration over time. The terms g and r are the gross production and respiration rates. Both g and r are expressed in carbon equivalents (mg m^{-3} d^{-1}) and need to be converted to oxygen equivalents (mmol m^{-3} d^{-1}). This was done using the conversion factors Q_P (0.11 mol g^{-1}) and Q_R (0.1 mol g^{-1}), which combine the photosynthetic (1.32 mol mol^{-1}; Laws, 1991) and respiratory quotients (1.2 mol mol^{-1}; Mayzaud et al., 2005) and molar mass of carbon (12 g mol^{-1}). Eq. (65) includes the photosynthetic endmember ${}^{i}\delta_P$, while r is multiplied by the isotope ratio of dissolved O2 (${}^{i}c/c$), and the fractionation factor during respiration ($1+{}^{i}\varepsilon_R$) (Kaiser, 2011).

Combining the equations for air-sea gas exchange and biological processes for all three isotopes and assuming steady-state gives as solution the gross oxygen production rate $F_{\mathrm{bio}}(^{17}O)$ as per the dual-delta method of Kaiser (2011):

$$F_{\mathrm{bio}}(^{17}\mathrm{O}) = kc_{\mathrm{sat},0}\frac{\begin{array}{c}(1 + {}^{17}\epsilon_{\mathrm{E}})\dfrac{{}^{17}\delta - {}^{17}\delta_{\mathrm{sat}}}{1 + {}^{17}\delta} - \gamma_{\mathrm{R}}(1 + {}^{18}\epsilon_{\mathrm{E}})\dfrac{{}^{18}\delta - {}^{18}\delta_{\mathrm{sat}}}{1 + {}^{18}\delta} \\ + \left(\dfrac{c}{c_{\mathrm{sat},0}} - 1\right)({}^{17}\epsilon_{\mathrm{E}} - \gamma_{\mathrm{R}}\,{}^{18}\epsilon_{\mathrm{E}})\end{array}}{\dfrac{{}^{17}\delta_{\mathrm{P}} - {}^{17}\delta}{1 + {}^{17}\delta} - \gamma_{\mathrm{R}}\dfrac{{}^{18}\delta_{\mathrm{P}} - {}^{18}\delta}{1 + {}^{18}\delta}} \tag{66}$$

4.4.3.2 Contribution of temporal changes in isotopic composition to $G(^{17}O)$:

Kaiser (2011) also provided the formulation for the time disequilibrium term (F_n) which is required when estimating G under non-steady-state conditions ($d\delta/dt \neq 0$):

$$F_n(^{17}O) = \frac{hc\dfrac{d\ln\dfrac{1+{}^{17}\delta}{(1+{}^{18}\delta)^{\gamma_R}}}{dt}}{\dfrac{{}^{17}\delta_P - {}^{17}\delta}{1+{}^{17}\delta} - \gamma_R\dfrac{{}^{18}\delta_P - {}^{18}\delta}{1+{}^{18}\delta}} \quad (67)$$

where h represents the layer thickness and c the O_2 concentration therein.

4.4.3.3 Contribution of vertical diffusive mixing to $G(^{17}O)$:

Finally, the term $F_v(^{17}O)$ in Eq. (51) represents vertical diffusive mixing as a function of the vertical gradient of $\delta(^{17}O)$ and $\delta(^{18}O)$ and the vertical diffusivity (K_z), where all terms are taken and calculated at the integration depth (z_{int}).

$$F_v(^{17}O) = \frac{K_z c\dfrac{d\ln\dfrac{1+{}^{17}\delta}{(1+{}^{18}\delta)^{\gamma_R}}}{dz}}{\dfrac{{}^{17}\delta_P - {}^{17}\delta}{1+{}^{17}\delta} - \gamma_R\dfrac{{}^{18}\delta_P - {}^{18}\delta}{1+{}^{18}\delta}} \quad (68)$$

4.4.4 Post-processing calculations for G(ERSEM) and diagnosing $G(^{17}O)$ from model output

This section details the methods used in post-processing calculations to obtain $G(^{17}O)$, which is compared with the target value calculated directly from simulated photosynthetic fluxes G(ERSEM).

$G(^{17}O)$ was calculated using the results of the prognostic model (ERSEM-FABM-GOTM) for dissolved triple oxygen isotopes concentrations. The different terms in Eq. (51) were computed at different points in the water column. $F_{bio}(^{17}O)$ was calculated using values for the surface layer (i.e., $j = M$, where j is the layer index in a model configuration with M vertical layers). In GOTM, vertical indexing is organised so that the sediment-water interface layer has an index of 0. In the L4 configuration, the water column was dividing into 100 layers of uneven thickness (see Chapter 3).

The term representing vertical diffusion flux, $F_v(^{17}O)$, was calculated at the chosen integration depth (z_{int}), The time disequilibrium term, $F_n(^{17}O)$, was calculated for every depth level and then summed. Combined, this yields:

$$G(^{17}O) = F_{bio}(^{17}O)(j = M) + F_v(^{17}O)(j = j(z_{int})) + \sum_{k=j(z_{int})}^{M} F_n(^{17}O)(k) \quad (69)$$

In sections 3.4.4.1 to 3.4.4.3, we describe how each term in Eq. (69) was calculated.

$G(^{17}O)$ performance was compared with total gross production from ERSEM, G(ERSEM). G(ERSEM) was calculated by integrating g in equation (64) over depth:

$$G(\text{ERSEM}) = \sum_{k=j(z_{int})}^{M} Q_P h(k) g(k) \quad (70)$$

where h is the thickness of layer j. Differences between $G(^{17}O)$ and G(ERSEM) were quantified using the root mean square difference (Δ_{RMS}):

$$\Delta_{RMS} G = \sqrt[2]{\overline{e(G)^2}} \quad (71)$$

where

$$e(G) = G(\text{ERSEM}) - G(^{17}O) \quad (72)$$

$\Delta_{RMS} G$ provides a quantitative measure of the error in $G(^{17}O)$ compared with the target value G(ERSEM). A drawback of this statistic is that it does not indicate whether $G(^{17}O)$ is positively or negatively biased.

Quantitative $G(^{17}O)$ performance over multiple (n) years was also expressed using the coefficient of determination (R^2):

$$R^2 = 1 - \frac{\sum_k e(G)^2}{\sum_k \left(G_k(\text{ERSEM}) - \bar{G}(\text{ERSEM})\right)^2} \quad (73)$$

$$\bar{G}(\text{ERSEM}) = \frac{1}{n} \sum_{k=1}^{n} G_k(\text{ERSEM}) \quad (74)$$

4.4.4.1 $F_{bio}(^{17}O)$: the air-sea gas exchange component

The air-sea gas exchange term $F_{bio}(^{17}O)$ was calculated as per equation (66) using concentrations and δ values for layer $j = M$ (surface).

The operator-splitting method (Strang, 1968) was included in post-processing calculations to isolate the biogeochemical concentrations at the surface level and achieve a close match between the air-sea flux calculated in post-processing and the analogue flux simulated in ERSEM. When $F_{bio}(^{17}O)$ is calculated from values taken at sampling intervals Δt greater than the simulation time step, we adopted the weighting scheme for piston velocity explained in detail in Chapter 2.

4.4.4.2 $F_n(^{17}O)$: the time disequilibrium term

$F_n(^{17}O)$ was defined at all depth levels as follows:

$$F_n(^{17}O)(j) = \frac{h(j)c(j)\dfrac{\mathrm{dln}\dfrac{1+{}^{17}\delta(j)}{(1+{}^{18}\delta(j))^{\gamma_R}}}{\mathrm{d}t}}{\dfrac{{}^{17}\delta_P(j)-{}^{17}\delta(j)}{1+{}^{17}\delta(j)}-\gamma_R\dfrac{{}^{18}\delta_P(j)-{}^{18}\delta(j)}{1+{}^{18}\delta(j)}} \tag{75}$$

A finite difference approximation was used to evaluate the time derivative in the F_n term.

4.4.4.3 $F_v(^{17}O)$: the vertical diffusive mixing term

The vertical diffusivity flux $F_v(^{17}O)$ was defined at the interface layer matching the integration depth, i.e., $j_{int} = j(z = z_{int})$:

$$F_v(^{17}O) = \frac{K_z(j_{int})c(j_{int})\dfrac{\mathrm{dln}\dfrac{1+{}^{17}\delta(j_{int})}{(1+{}^{18}\delta(j_{int}))^{\gamma_R}}}{\mathrm{d}z}}{\dfrac{{}^{17}\delta_P(j_{int})-{}^{17}\delta(j_{int})}{1+{}^{17}\delta(j_{int})}-\gamma_R\dfrac{{}^{18}\delta_P(j_{int})-{}^{18}\delta(j_{int})}{1+{}^{18}\delta(j_{int})}} \tag{76}$$

In practice, the vertical gradient in the numerator was calculated using the python function *numpy gradient*, which returns second order central differences (Harris et al., 2020).

4.4.5 Experimental procedure

We used the following procedure to address the aims of the study:

4.4.5.1 Q1: uncertainties derived from steady-state assumption at L4

Uncertainties derived from the steady-state assumption were quantified following the same experimental procedure detailed in chapter 3 section 3.4.5.1. This involved comparing the error expressed in $\Delta_{\mathrm{RMS}}G$ when assuming steady-state conditions (G(ERSEM) = $F_{\mathrm{bio}}(^{17}\mathrm{O})$) with calculations that account for non-steady-state conditions (G(ERSEM) = $G(^{17}\mathrm{O})$). The experiment was repeated using two sampling intervals: the first using a sampling interval that matches the model time step (Δt = 60 s), the second that uses a sampling interval of 7 days (reflecting the routine sampling strategy at Station L4 (Gloël, 2012)). Both G(ERSEM) and $G(^{17}\mathrm{O})$ are integrating over the whole water column to remove the error associated with the vertical diffusive flux ($F_{\mathrm{v}}(^{17}\mathrm{O})$). Results are presented in section 4.5.2.

4.4.5.2 Q2: $G(^{17}\mathrm{O})$ sensitivity to the integration depth at L4

This experiment followed the same procedure described in chapter 3 section 3.5.3. This involved calculating $G(^{17}\mathrm{O})$ with three different integration depths (2 m, 28 m and 50 m) and calculating monthly statistics for the $F_{\mathrm{bio}}(^{17}\mathrm{O})$, $F_{\mathrm{n}}(^{17}\mathrm{O})$ and $F_{\mathrm{v}}(^{17}\mathrm{O})$ terms. Monthly statistics include the median ($\tilde{x}$), 1st and 3rd quartiles (P_{25} and P_{75}) and 5th and 95th percentiles (P_5 and P_{95}). Results are presented as box plot in section 4.7.2.

4.4.5.3 Q3: Determination of the optimal sampling interval

The optimal sampling interval was determined by configuring a set of experiments based on 5-year-long simulations (2010–15) at L4. $G(^{17}\mathrm{O})$ was calculated after subsampling the simulation results at increasing sampling intervals ($G_{\Delta t}(^{17}\mathrm{O})$) where Δt = 1 min, 10 min, 30 min, 1 day, 2 days, 4 days, 1 week, 10 days, 2 weeks, and 1 month. The time intervals were arbitrarily selected among the possible divisors of the total number of simulation time steps. The calculation was then repeated using oxygen isotope concentrations affected by experimental error. Here, $G(^{17}\mathrm{O})$ was evaluated using a time average of G(ERSEM) over the intervals listed above. Results were evaluated using Δ_{RMS} and the coefficient of determination (R^2) before and after adding experimental error to evaluate the ideal sampling frequency in time at Station L4.

The standard error was introduced to model simulation results for the three-oxygen isotopes as follows, using uncertainty estimates of Gloël (2012) and Seguro et al. (2019). First, normally distributed noise with standard deviation $\sigma(c)$ = 0.03 % was added to all three concentrations:

$$c_{\text{noise},1}\left(^{i}\text{O}\right) = c(^{i}\text{O})(1 + \sigma_c) \tag{77}$$

In the second step, a relative error with $\sigma(\delta)$ = 0.1 ‰ standard deviation was added for $c(^{18}\text{O})$, with the error for $c(^{17}\text{O})$ being correlated via the respiration fractionation coefficient γ_{R}:

$$c_{\text{noise},2}\left(^{18}\text{O}\right) = c_{\text{noise},1}\left(^{18}\text{O}\right)(1 + \sigma(\delta)) \tag{78}$$

$$c_{\text{noise},2}\left(^{17}\text{O}\right) = c_{\text{noise},1}\left(^{17}\text{O}\right)(1 + \gamma_{\text{R}}\sigma(\delta)) \tag{79}$$

Finally in the last step, noise with $\sigma(^{17}\Delta)$ = 7 ppm standard deviation was added to $c(^{17}\text{O})$:

$$c_{\text{noise},3}\left(^{17}\text{O}\right) = c_{\text{noise},2}\left(^{17}\text{O}\right)(1 + \sigma(^{17}\Delta)) \tag{80}$$

Figure 53 shows the effect of experimental error on c, $\delta(^{i}\text{O})$, and $^{17}\Delta$ in comparison to the original values. Results are presented in section 4.5.3.

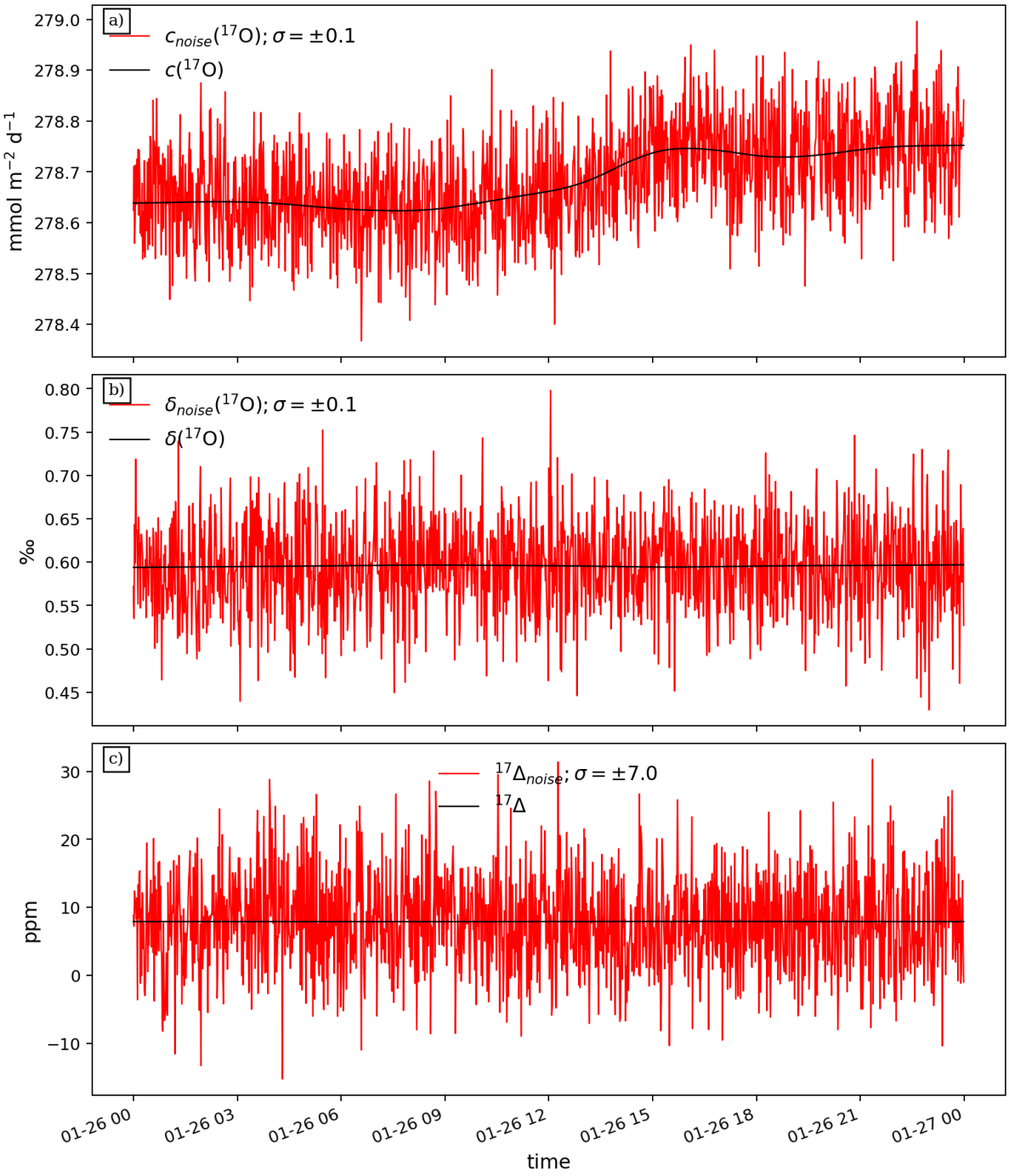

Figure 53: Application of experimental error to oxygen concentrations showing the effects on concentrations (a), δ values (b) and $^{17}\Delta$(c). In each panel "clean" values (black) are compared against the values with calculated experimental error (red).

4.4.5.4 Q4: uncertainty derived from oxygen fractionation during photosynthesis

In the fourth experiment, three distinct simulations were prepared. In exp 1 (control), all photoautotrophic groups were assigned the same photosynthetic oxygen end

members (control: $\delta(^{17}O)_P$ = –12.107 ‰ and $\delta(^{18}O)_P$ = –23.647 ‰) which represents the oxygen isotope ratios in VSMOW (Kaiser and Abe, 2012; Table 3, row 7). In exp 2, diatoms were assigned different photosynthetic end member values ($\delta(^{17}O)_P$ = –9.821 ‰ and $\delta(^{18}O)_P$ = –19.326 ‰ from Kaiser and Abe, 2012) while the other three phytoplankton groups had VSMOW values. In exp 3, all ERSEM photosynthetic functional groups had different photosynthetic end member values that assigned to ERSEM functional groups based on their cell diameter (Table 1, as per Table 3 rows 7 to 7e found in Kaiser and Abe, 2012 pp. 2925)

Table 6: Isotopic composition of photosynthetic O_2 assigned to ERSEM functional groups following Kaiser and Abe (2012) used for exp 2 (diatoms only) and exp 3 (all groups)

Functional groups	Species name	$\delta_P(^{17}O)$/‰	$\delta_P(^{18}O)$/‰	$^{17}\Delta_P$/ppm
Control	VSMOW	–12.107	–23.647	140
P1 diatoms	*Phaeodactylum tricornutum*	–9.821	–19.326	188
P2 nanophytoplankton	*Emiliania huxleyi*	–9.094	–17.971	213
P3 picophytoplankton	*Nannochloropsis oculata*	–10.629	–20.865	177
P4 microphytoplankton	*Chlamydomonas reinhardtii*	–8.498	–16.774	189

The first experiment aimed to estimate the error if all photoautotrophic groups have $\delta_P(^{17}O)$ and $\delta_P(^{18}O)$ equal to VSMOW values. This was tested by calculating $^{17}\Delta$ from exp 1 and comparing the results against the $^{17}\Delta$ from exp 2. $\Delta_{RMS}G$ quantified the error caused when assuming that $\delta(^{17}O)_P$ and $\delta(^{18}O)_P$ match VSMOW values using the results of the control simulation run ($G_{exp1}(^{17}O)$), from the simulation which has diatoms having different $\delta_P(^{17}O)$ and $\delta_P(^{18}O)$ values ($G_{exp2}(^{17}O)$); and finally, from the simulation reflecting all end members values shown in Table 6 ($G_{exp3}(^{17}O)$). Results are presented as a mixture of Hovmöller and timeseries plots in section 4.6.4.

4.5 Results

4.5.1 Diagnostic model performance

We tested the diagnostic model by verifying $G(^{17}O)$ matched G(ERSEM) (Figure 54). Figure 54c shows the predicted annual time series of $^{17}\Delta$ and demonstrates that triple oxygen isotopologues were successfully included in ERSEM for the first time. In the mixed layer, $^{17}\Delta$ maximum values usually match production peaks suggesting that most of the biogenic oxygen is readily released to the atmosphere (see Figure 54b). Below the mixed layer, $^{17}\Delta$ accumulates during the growing season, showing the portion of biogenic oxygen not lost to the atmosphere slowly accumulates within the bottom mixed layer during stratification until autumn when the signal is lost, coinciding with the breakdown of stratification and ventilation (Figure 54c). Figure 54b and e (in red) represent the post-processing calculations inferring $G(^{17}O)$ integrated over every depth layer and over the full water column respectively. Both figures show that $G(^{17}O)$ correctly predicts G(ERSEM).

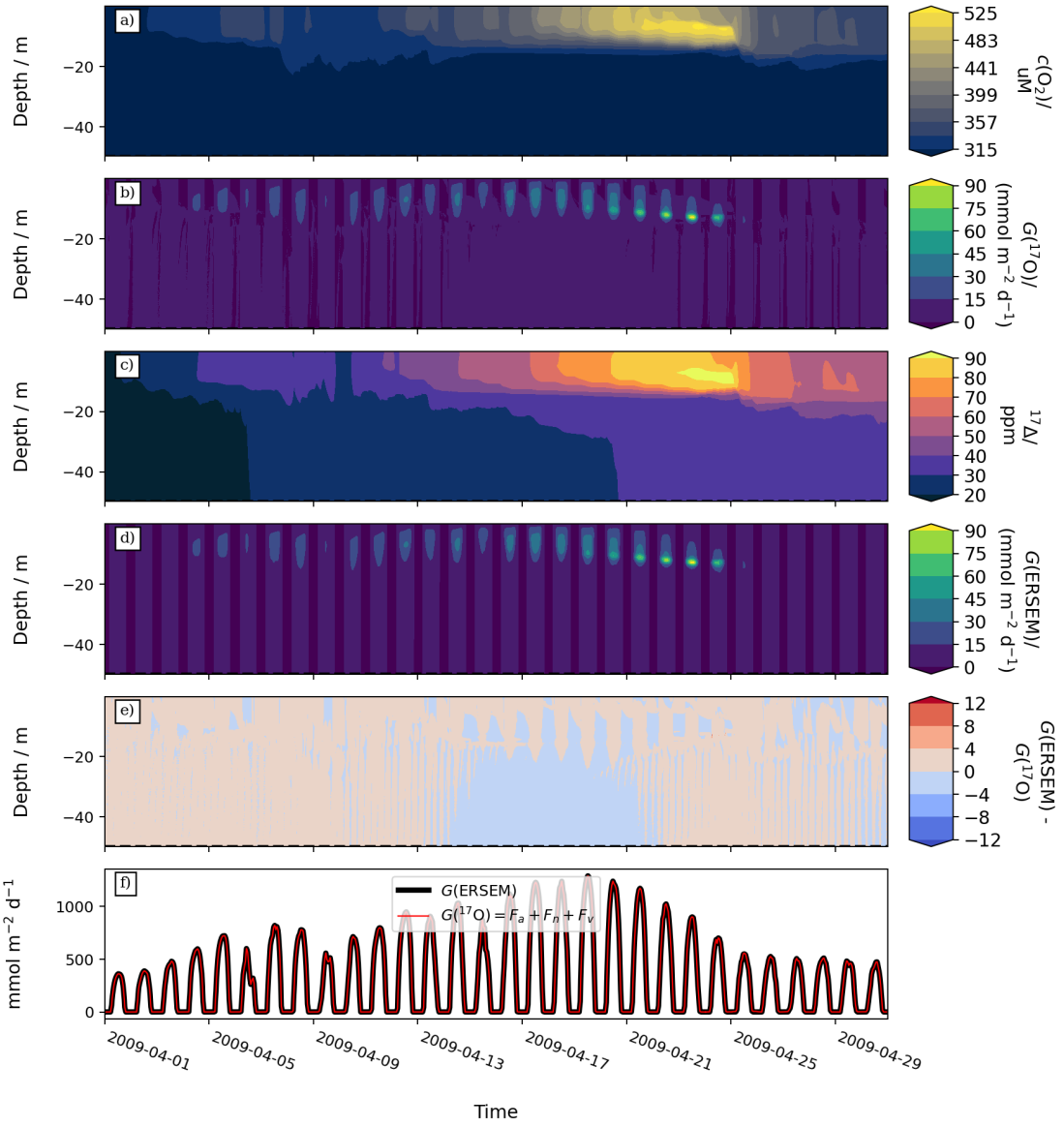

Figure 54: Diagnostic model performance overview. a) oxygen 16 concentrations in all depth layers. b) diagnostic model for gross oxygen production flux calculated in each depth layer. c) Triple isotope excess defined in Kaiser and Abe 2012 calculated at all depth layers. d) Prognostic model outputs for gross oxygen production (mmol m^{-3} d^{-1}) multiplied by layer thickness (m) to match diagnostic model units (mmol m^{-2} d^{-1}). e) difference between diagnostic (G(ERSEM)) and prognostic ($G(^{17}O)$) models. f) a comparison between diagnostic (G(ERSEM)) and prognostic ($G(^{17}O)$) models depth integrations.

There was a residual error (0.7 mmol m^{-2} d^{-1}), which was small relative to the magnitude of the fluxes (about 0.1 %). This is to be expected given the post-processing calculations rely on the evaluation of spatial and temporal gradients from discrete sets of data points. For example, there is a discrepancy between the forward differencing approximation used to calculate $F_n(^{17}O)$ and the numerical time integration technique

adopted by ERSEM-FABM-GOTM, which includes the operator-splitting method. For the purpose of this experiment, a 0.1 % residual error was accepted.

4.5.2 Q1: uncertainties derived from steady-state assumption at L4

Figure 55 shows what happens when assuming steady-state during the spring bloom and using a sampling interval that matches the model time step (Δt = 60 s). Results show that removing the disequilibrium term $F_n(^{17}O)$ increases the prediction error by three orders of magnitude (Figure 55b: $\Delta_{RMS}G$ = 270 mmol m^{-2} d^{-1}; n = 7200). The disequilibrium term $F_n(^{17}O)$ taken alone was more representative of G(ERSEM) (Figure 55d: $\Delta_{RMS}G$ = 210 mmol m^{-2} d^{-1}) than $F_{bio}(^{17}O)$ on its own (Figure 55c: $\Delta_{RMS}G$ = 290 mmol m^{-2} d^{-1}). From the timeseries plots, it is possible to distinguish the effects that $F_{bio}(^{17}O)$ and $F_n(^{17}O)$ have on the diagnostic model. While $F_{bio}(^{17}O)$ averages the overall gross oxygen production, $F_n(^{17}O)$ provides information on the day and night cycle. However, the two need to be added to avoid a systematic underestimation of the actual gross production.

Figure 56 is like Figure 55, but for a sampling interval of 7 days (matching the ship-based sampling strategy for L4) and the time series covers almost 2 years (from 2009-01-01 to 2010-10-07). Results show that at coarser sampling intervals there was a 53 % increase in the prediction error between $G(^{17}O)$ and $G_{SS}(^{17}O)$ (Figure 56a and b). The increase in prediction error was substantially smaller than in Figure 55. This result suggests that the steady-state assumption is less problematic for longer sampling interval. However, the selected sampling interval (7 days) was not sufficiently long to achieve steady-state. Across the selected time series $G_{SS}(^{17}O)$ mostly failed to predict the timing and magnitude of G(ERSEM) during both spring blooms, and at the end of 2009. The time lag between $G_{SS}(^{17}O)$ and G(ERSEM) is most evident in the 2009 spring bloom where the magnitude was well represented; however, the timing of the peak and onset of the spring bloom was 2 weeks later than that seen in G(ERSEM) (Figure 56b and c). Instead, $G_{SS}(^{17}O)$ almost missed the 2010 spring bloom. Furthermore, during autumn 2009, $F_{bio}(^{17}O)$ (and thus $G_{SS}(^{17}O)$) detected a production peak of 310 mmol m^{-2} d^{-1} (almost 50 % of the 2009 spring bloom). However, this was an artefact of the diagnostic model which overestimated G(ERSEM) by two orders of magnitude (Figure 56b and c).

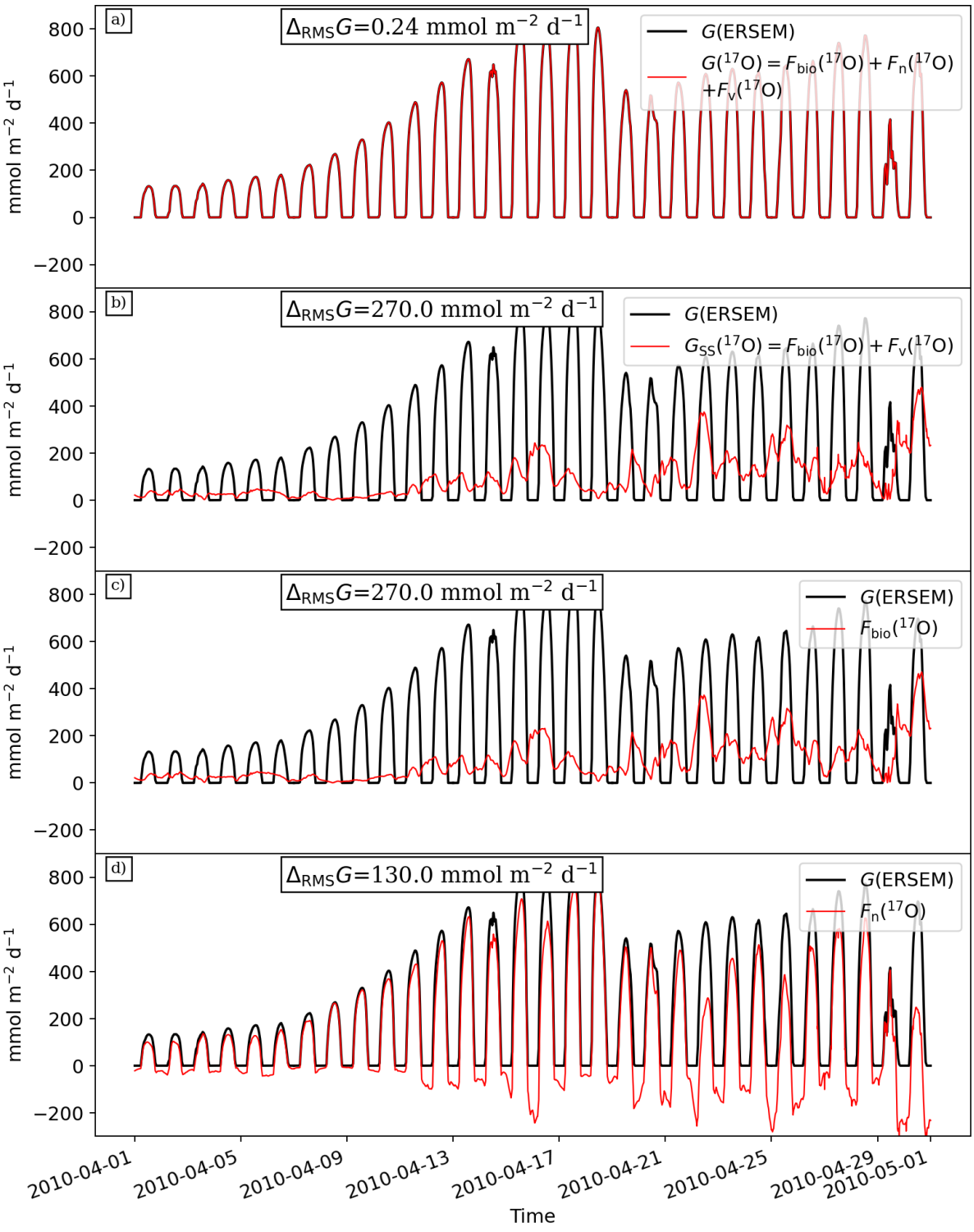

Figure 55: Diagnostic model performance (red) vs its target value (black) during the 2010 spring bloom at L4. Diagnostic models are namely the full non-steady-state G(^{17}O) (a), G(^{17}O) assuming steady-state (b), G(^{17}O) non-steady-state omitting diffusion (c), and G(^{17}O) non-steady-state omitting air sea gas exchange (d). Integration depth is set at 50 m.

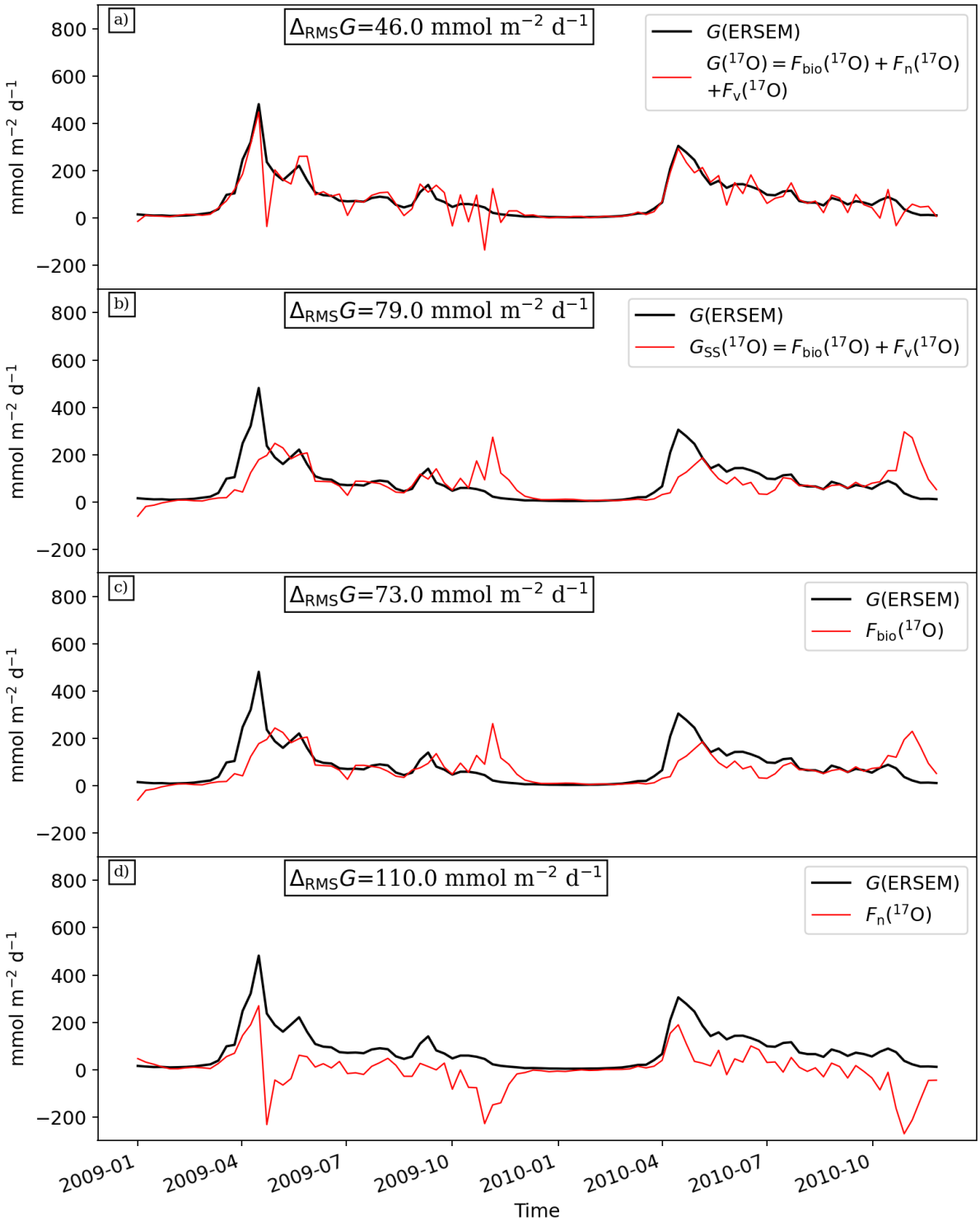

Figure 56: Diagnostic model performance (red) vs its target value (black) from 2009-01-01 to 2010-10-07 at L4. Diagnostic models are namely the full non-steady-state G(^{17}O) (a), G(^{17}O) assuming steady-state (b), G(^{17}O) non-steady-state omitting diffusion (c), and G(^{17}O) non-steady-state omitting air sea gas exchange (d). Integration depth is set at 50 m.

4.5.3 Q2: Influence of integration depth on $G(^{17}O)$ at L4

In this section the relative contribution of all terms composing $G(^{17}O)$ were quantified using three different integration depths (z_{int}): near surface (2 m), the average depth of the euphotic zone (28 m), and full water column (50 m). The euphotic depth varies with time but was taken as the mean depth where PAR is at 1 % of surface values.

Results indicate that surface mixed layer $G(^{17}O)$ (z_{int} = 2 m: median $\tilde{G}(^{17}O)$ = (6.4±8.2) mmol m^{-2} d^{-1}) can be one order of magnitude smaller than total production (z_{int} = 50 m: $\tilde{G}(^{17}O)$ = (40±52) mmol m^{-2} d^{-1}) (Table 7). As expected due to light availability, results for z_{int} = 28 m were similar to those for z_{int} = 50 m (Table 7). This also shows that that the use of a constant euphotic depth only caused negligible errors.

Table 7: Summary statistics for $G(^{17}O)$. h is the integration depth, P_5 and P_{95} are the 5th and 95th percentiles, P_{25} and P_{75} are the 1st and 3rd quartiles, and P_{50} represents the median.

$G(^{17}O)$/(mmol m^{-2} d^{-1})					
z_{int}/m	P_5	P_{25}	P_{50}	P_{75}	P_{95}
2	0.011±0.014	0.18±0.21	6.4±8.2	19±22	37±46
28	0.011±0.014	0.21±0.25	39±50	140±140	250±240
50	0.011±0.014	0.21±0.25	40±52	150±140	250±240

The relevance of each term in Eq. (51) was also investigated: To minimise the bias associated neglecting $F_v(^{17}O)$, the diagnostic model should be integrated over the whole water column. For z_{int} = 28 m and 50 m, $F_n(^{17}O)$ dominates over $F_{bio}(^{17}O)$ and $F_v(^{17}O)$, especially during the growing season. For z_{int} = 2 m, F_{bio} and $F_v(^{17}O)$ dominate $G(^{17}O)$ both during highly productive periods (April to September) and winter (Figure 57; Table 8). This highlights the importance of including $F_v(^{17}O)$ when estimating $G(^{17}O)$ for z_{int} = 2 m. Results also show that omitting $F_n(^{17}O)$ has a minor impact for most of the year with the exception of the spring bloom (April: $\tilde{F}_n(^{17}O)$ = 0.5 mmol m^{-2} d^{-1}; P_5 = –63 mmol m^{-2} d^{-1}; P_{95} = 106 mmol m^{-2} d^{-1}) (Figure 57a).

Table 8: Summary statistics for the terms composing $G(^{17}O)$. z_{int} is the integration depth, P_5 and P_{95} are the 5th and 95th percentiles, P_{25} and P_{75} are the 1st and 3rd quartiles, and P_{50} represents the median.

F/(mmol m^{-2} d^{-1})						
Flux name	z_{int}/m	P_5	P_{25}	P_{50}	P_{75}	P_{95}
$F_{bio}(^{17}O)$ growing season	2 m	13±17	30±23	56±41	100±79	184±143
$F_n(^{17}O)$ growing season	2 m	–24±21	–9±6	–1±2	9±11	32±37
	28 m	–210±120	–86±35	–20±13	120±96	300±210
	50 m	–180±96	–70±29	–6±23	150±100	330±220
$F_v(^{17}O)$ growing season	2 m	–210±100	–110±53	–59±25	–29±11	–4±4
	28 m	–3±9	4±3	10±5	23±14	64±44
	50 m	0	0	0	0	0
$F_{bio}(^{17}O)$ winter	2 m	-1.2±22	18±25	36±43	68±81	135±153
$F_n(^{17}O)$ winter	2 m	–8±7	–3±3	–1±1	11±2	37±8
	28 m	–97±110	–37±45	–16±21	12±19	80±66
	50 m	–140±170	–62±80	–27±36	7±25	74±71
$F_v(^{17}O)$ winter	2 m	–130±150	–63±77	–33±39	–15±23	3.4±21
	28 m	–68±105	–16±28	–4.9±12	1.6±7	20±16
	50 m	0	0	0	0	0

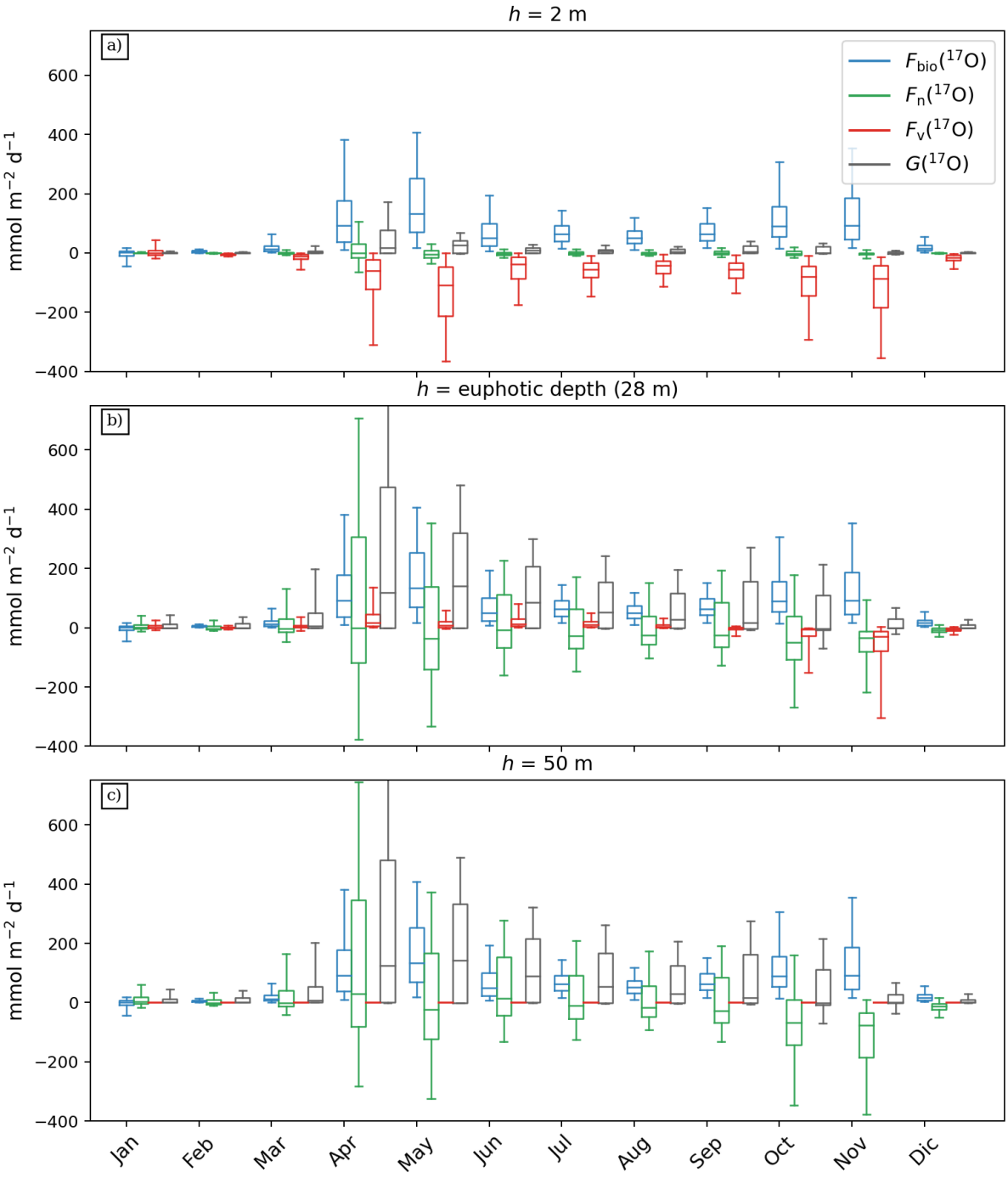

Figure 57: Month-by-month box model for $G(^{17}O)$ (in grey) and its constituent terms such as air-sea flux ($F_{bio}(^{17}O)$ in blue), vertical diffusivity ($F_v(^{17}O)$ in red) and time disequilibrium ($F_n(^{17}O)$ in green). Terms statistics through each month are compared to one another under three different integration depth scenarios such as surface depths (z_{int} = 2 m in panel a), euphotic zone (28 m in panel b) and integrating full water column (50 m in panel c). Where each box represents 5 statistics: the lower whisker cap is set to the 5th percentile, the lower box interface represents the 1st quartile, the inner horizontal line is the median, the upper limit of the box is the 3rd quartile, and the upper whisker cap is the 95th percentile.

4.5.4 Q3: Determination of the optimal sampling interval

The optimum sampling interval for $G(^{17}O)$ at L4 was investigated using a multiannual run (2010–15). The optimal sampling interval for L4 station was identified by calculating $G(^{17}O)$ from oxygen concentrations and isotope deltas with added simulated experimental noise (see 4.4.5.3). This was done by comparing a control run and an experimental run. In the control run, $G(^{17}O)$ was calculated using oxygen concentrations unaffected by noise, using different sampling intervals ($G_{\Delta t}(^{17}O)$). $G_{\Delta t}(^{17}O)$ performance was then tested against full time-resolution G(ERSEM) averaged over time (Figure 58). The same calculations were carried out for the experimental run with added noise. The diagnostic model performance was evaluated according to $\Delta_{RMS}G$ and R^2 metrics (4.4.4). Differences in $\Delta_{RMS}G$ and R^2 between control and experimental runs isolate the effects of experimental noise.

Figure 58 shows that prediction error increases with increasing sampling intervals. $\Delta_{RMS}G$ increased by 2 orders of magnitude by increasing sampling intervals from the simulation time step (Δt = 60 s) to Δt = 60 min (Figure 58a and b). The error then increased by a factor of 3 moving from Δt = 1 h to 24 h (Figure 58b and c) and increased further up to the coarsest resolution here tested (Δt = 21 d) where $\Delta_{RMS}G$ was 2 orders of magnitude higher than for Δt = 1 min (Figure 58e). In contrast, results from the experimental run indicate that sampling intervals that are the close to the simulation time step are greatly affected by measurement error (Figure 59). This suggests that the ideal sampling resolution is Δt = 7 d (Figure 59d).

The optimum sampling interval was then tested by increasing the number of sampling intervals and quantifying their performance using $\Delta_{RMS}G$ and R^2. Results showed that samples for triple oxygen isotopes should be taken once every 9 days at L4 after accounting for experimental random error (Figure 60). The effects of sampling error on $\Delta_{RMS}G$, which is represented by the difference between control and experimental run, decays against sampling interval down to a sample per day and then it plateaus until sample per month (Figure 60). Sampling every 9 days then best performs the rest of the sampling intervals since it has a better correlation coefficient (R^2).

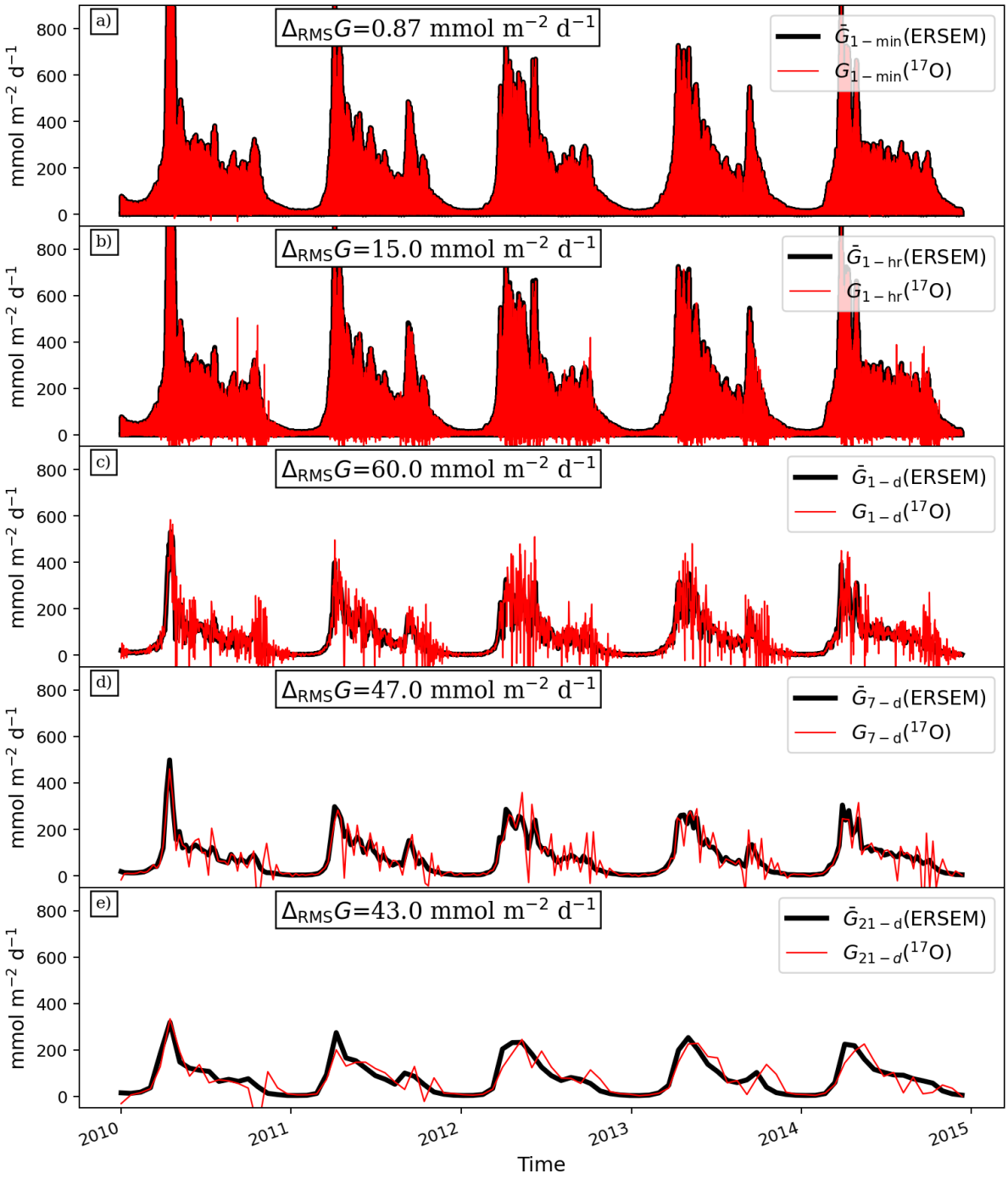

Figure 58: Control run unaffected by experimental error. Direct timeseries comparison between G(ERSEM) and $G(^{17}O)$ over 5 years at different sampling intervals: namely per minute (a, n 2632320) per hour (b, n = 43872) per day (c, n = 1828), per week (d, n = 261) and every 21 days (e, n= 87). For sampling resolutions coarser than 1 h, values are taken at 10:00 am representing the time when L4 is routinely sampled. Model performance for $G(^{17}O)$ is quantified as root mean squared difference ($\Delta_{RMS}G$).

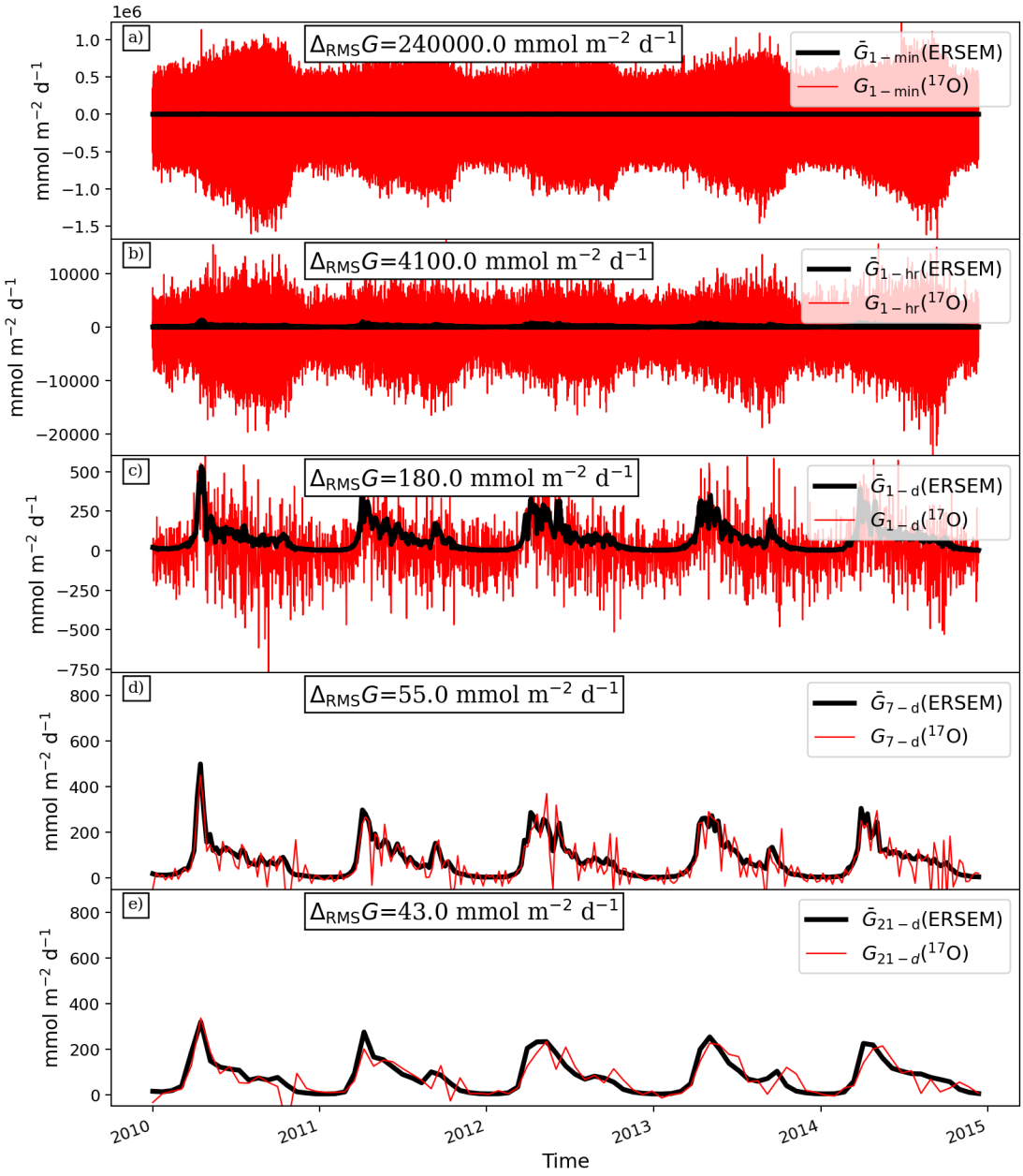

Figure 59: Experimental run using oxygen concentrations affected by experimental error. Direct timeseries comparison between G(ERSEM) and $G(^{17}O)$ over 5 years at different sampling intervals: namely per minute (a, n = 2632320) per hour (b, n = 43872) per day (c, n = 1828), per week (d, n = 261) and every 21 days (e, n = 87). For sampling resolutions coarser than 1 h, values are taken at 10:00 am representing the time when L4 is routinely sampled. Model performance for $G(^{17}O)$ is quantified as root mean squared difference ($\Delta_{RMS}G$).

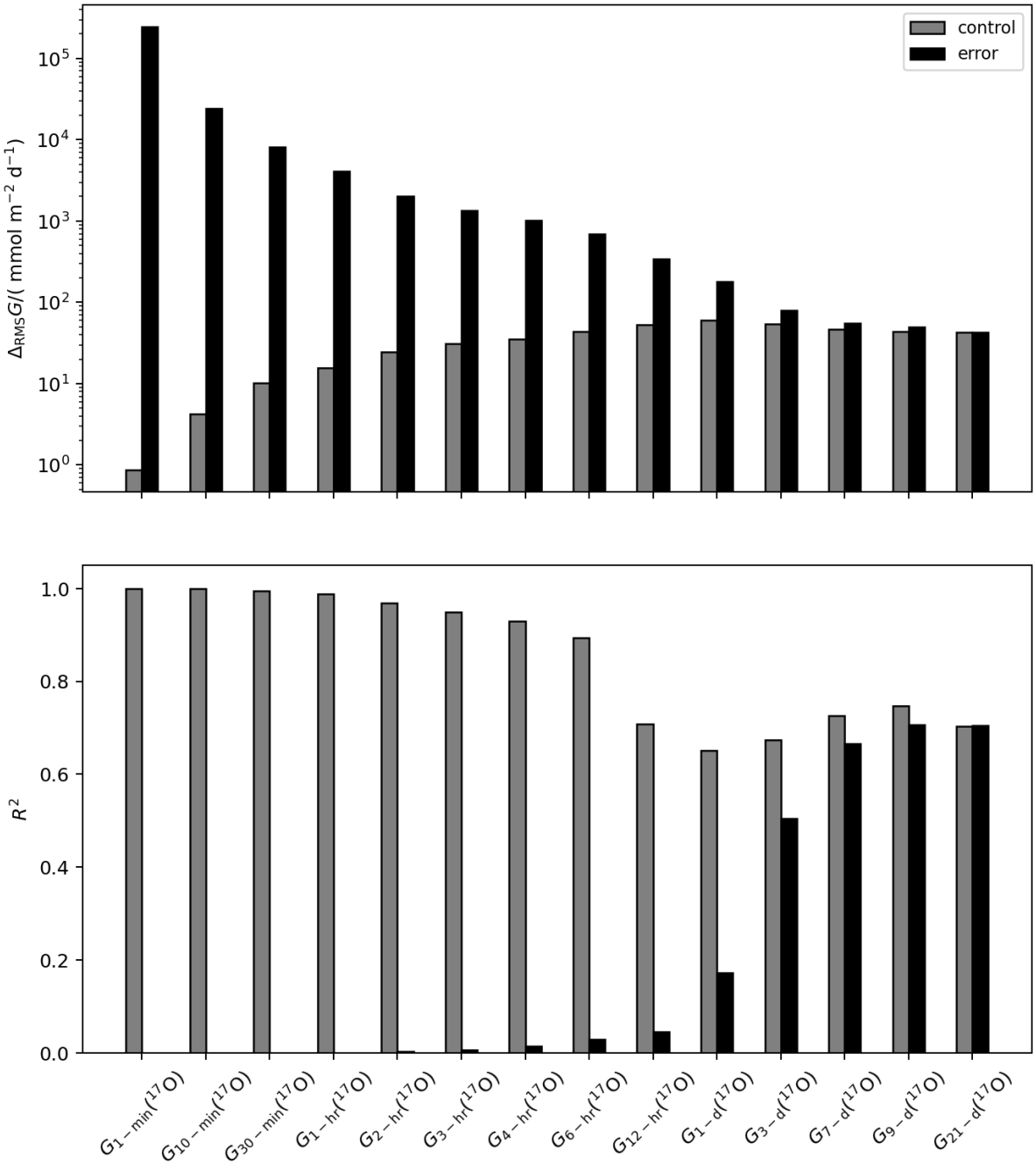

Figure 60: predicted $G(^{17}O)$ $\Delta_{RMS}G$ (above) and R^2 (below) against increasing sampling frequency at L4 over 1 year (from 01/01/2010 to 25/12/2014). Where results in black are calculated with sampling experimental error was added to $c(^{i}O_2)$. Add more resolutions in between daily and weekly.

We further investigated if there is a different optimal sampling interval for each season. This involved dividing the data according to the four different seasons winter (December, January, February), spring (March, April, May), summer (June, July, August), and autumn (September, October, November). Results showed that sampling

once per week remains as the best strategy to be adopted in all seasons within the 5 years long simulation (Figure 61). All seasons showed the same results apart from winter, for which R^2 was lower at all sampling frequencies after the introduction of the experimental error.

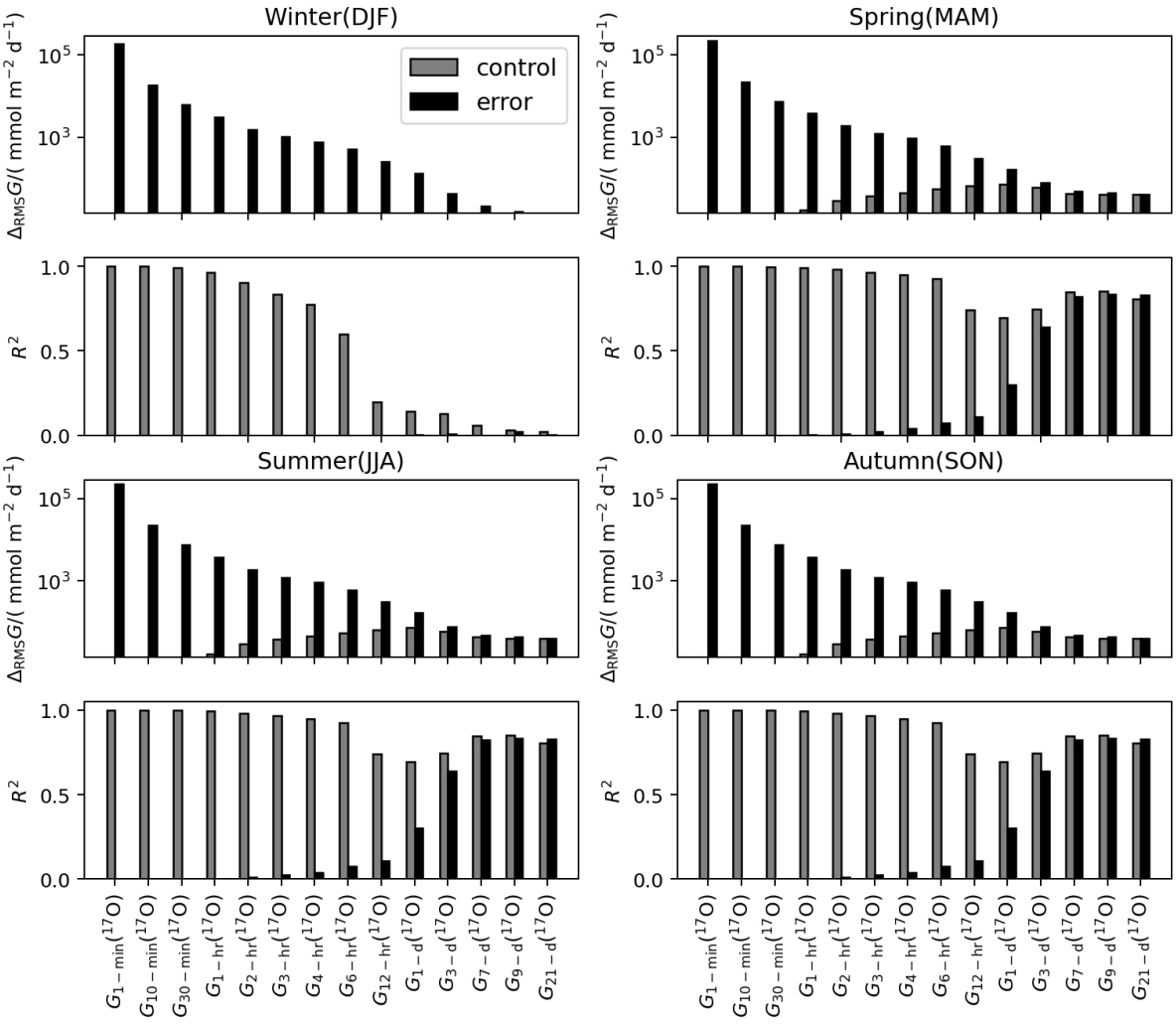

Figure 61: Seasonal ideal sampling strategy. Predicted $G(^{17}O)$ $\Delta_{RMS}G$ (above) and R^2 (below) against increasing sampling frequency at L4 over 1 year (from 01/01/2010 to 25/12/2014) after dataset being reorganised according to the four different seasons. Where results in black are calculated with sampling experimental error was added to $c(^{i}O_2)$.

A final test addressed why sampling intervals closest to the simulation time step are particularly affected by the experimental error. To do so, Figure 55 was replotted for values affected by experimental error. It showed that the error observed in high sampling frequencies comes from the calculation of the disequilibrium term $F_n(^{17}O)$ (Figure 62).

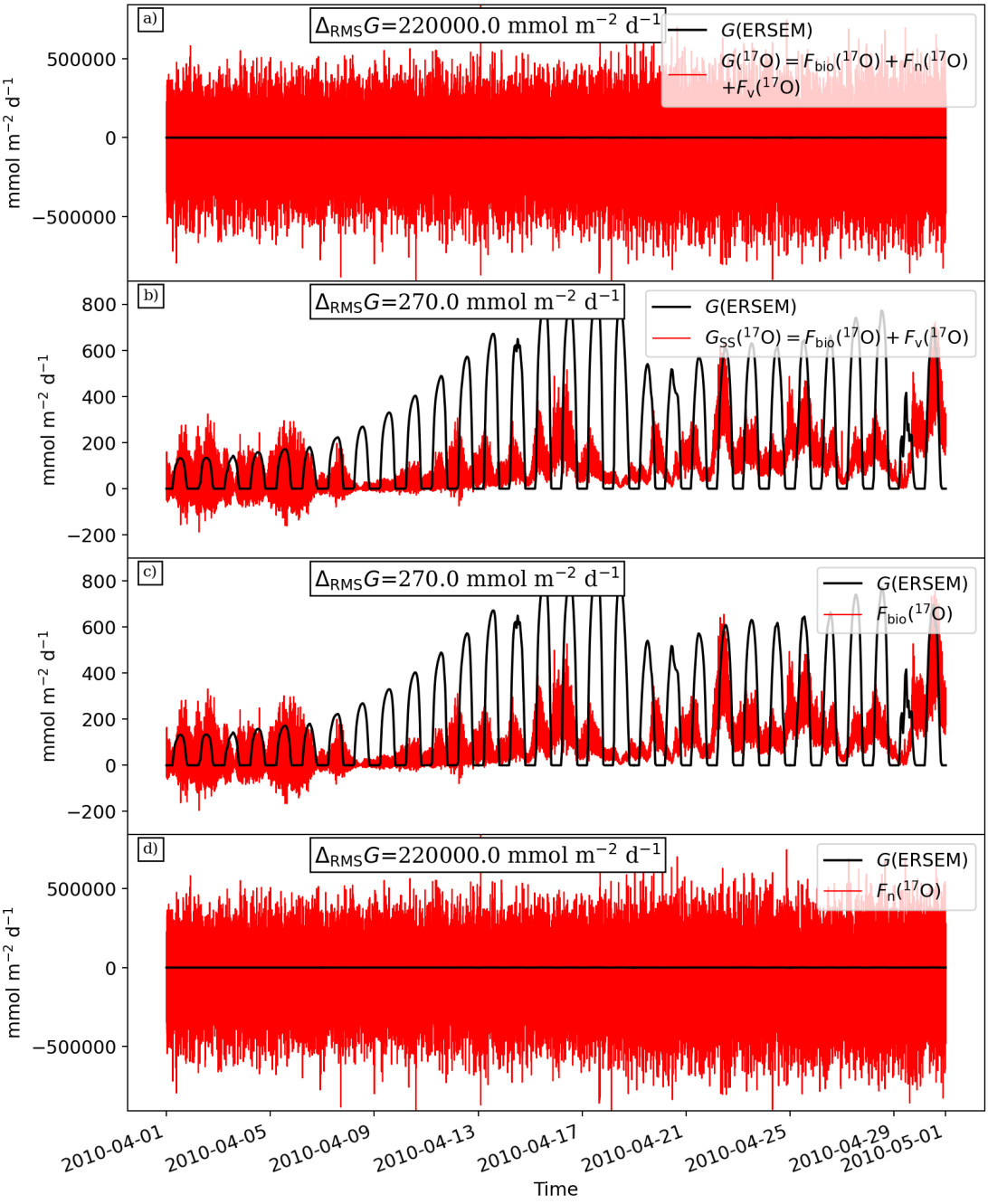

Figure 62: Effects of experimental error on the three terms composing the diagnostic model $G(^{17}O)$. Diagnostic models are namely the full non-steady-state $G(^{17}O)$ (a), $G(^{17}O)$ assuming steady-state (b), $G(^{17}O)$ non-steady-state omitting diffusion (c), and $G(^{17}O)$ non-steady-state omitting air-sea gas exchange (d). Integration depth is set at 50m (not shown), and sampling resolution is set at Δt = 60 s.

4.5.5 Q4: Uncertainty derived from oxygen fractionation during photosynthesis

This experiment involved a control run (exp1) with all functional groups having photosynthetic endmembers values corresponding to VSMOW, with $^{17}\Delta_P$ = 140 ppm

(Table 6); whereas in experimental run exp2, $\delta(^{17}O)_P$ = –9.821 ‰ and $\delta(^{18}O)_P$ = –19.326 ‰, corresponding to $^{17}\Delta_P$ = 188 ppm was assigned to diatoms. The resulting $^{17}\Delta$(exp2) values were to +2 to +10 ppm higher than $^{17}\Delta$(exp1) (Figure 63c), with the offset displaying a seasonal cycle following diatom gross production (Figure 63c and e). This highlighted that the prediction error was higher in 2010 when diatoms were more abundant (Figure 63e) and specifically during mid to late summer when the $^{17}\Delta$ signal was located below the mixed layer depth (Figure 63d).

Focussing on the spring bloom 2010, exp2 gave a diagnosed $G(^{17}O)$ value +35 mmol m^{-2} d^{-1} higher for exp2 than for exp1 (Figure 64a to c). Peaks in $G_{exp2}(^{17}O)$ overestimates are most evident in the second week past the onset of stratification (10 m on average during mid-day, Figure 64d) coinciding with the period when diatoms are the most abundant group (Figure 64e). Such an offset can lead to a substantial systematic overestimate (up to +300 mmol m^{-2} d^{-1}) of the actual gross oxygen production when values are integrated over the whole water column (Figure 64f; blue line), which caused $\Delta_{RMS}G$ to increase by 2 orders of magnitude when compared to $G_{exp1}(^{17}O)$.

A third $G(^{17}O)$ estimate was calculated using values form the simulation results where every functional group has a distinctive fractionation factor during photosynthesis ($(G_{exp3}(^{17}O))$, see 4.5.5). Results showed that, when all functional groups had different $\delta_P(^{17}O)$ and $\delta_P(^{18}O)$ $\Delta_{RMS}G_{exp3}(^{17}O)$ resulted in 73 % higher than $\Delta_{RMS}G_{exp1}(^{17}O)$ (Figure 65f).

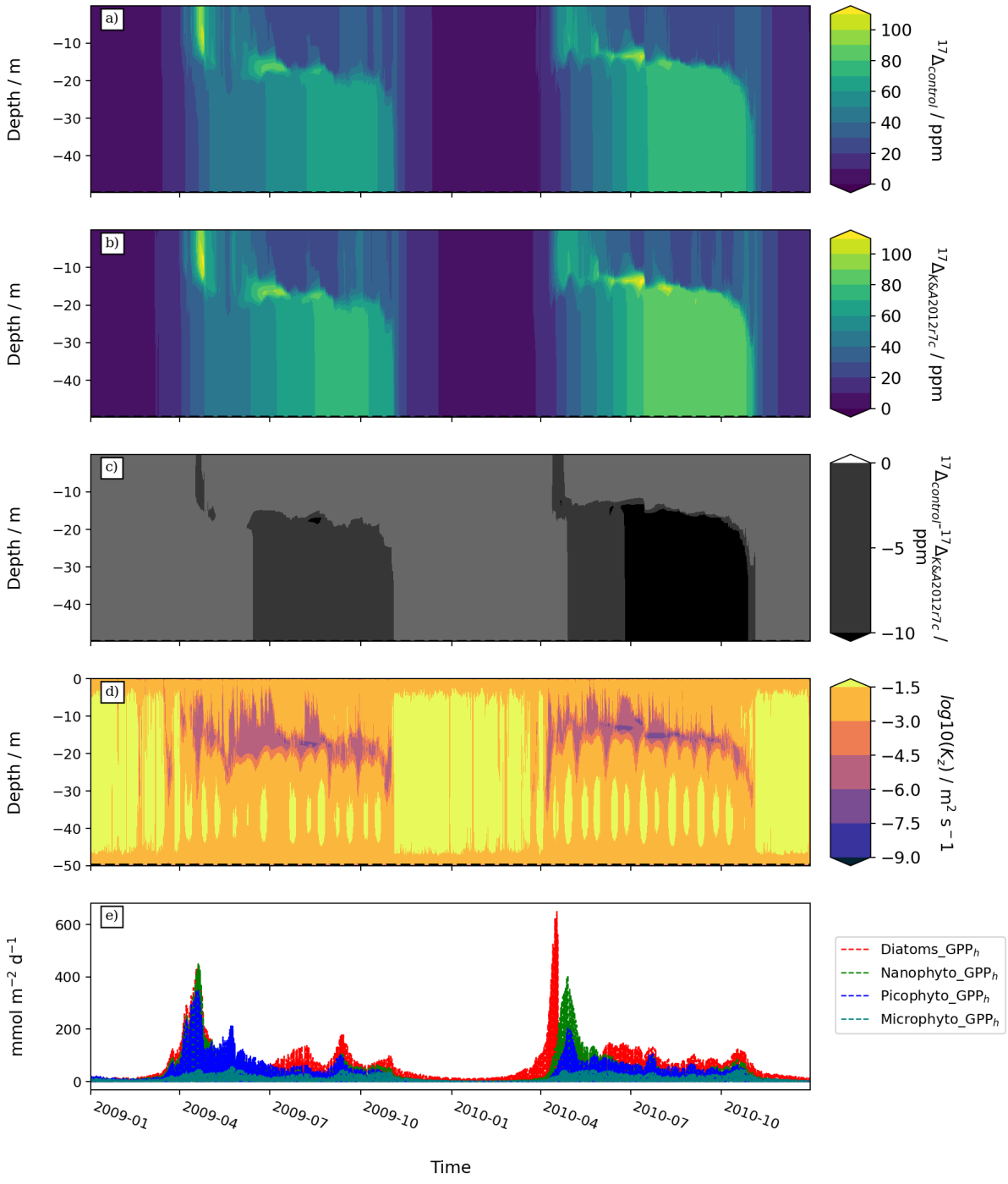

Figure 63: Effects of group specific $^{i}\delta_P$ values on modelled $^{17}\Delta$. a) $^{17}\Delta$ calculated using VSMOW as photosynthetic endmember for all functional groups ($^{17}\Delta_P$ = 140 ppm; Table 6). b) $^{17}\Delta$ calculated using $^{17}\Delta_P$ = 188 ppm and $^{17}\Delta_P$ = 140 ppm for the other groups (Table 6). c) Difference between a) and b). d) Vertical diffusivity of heat in $\log_{10}$ scale. e) Group-specific gross production integrated over the whole water column.

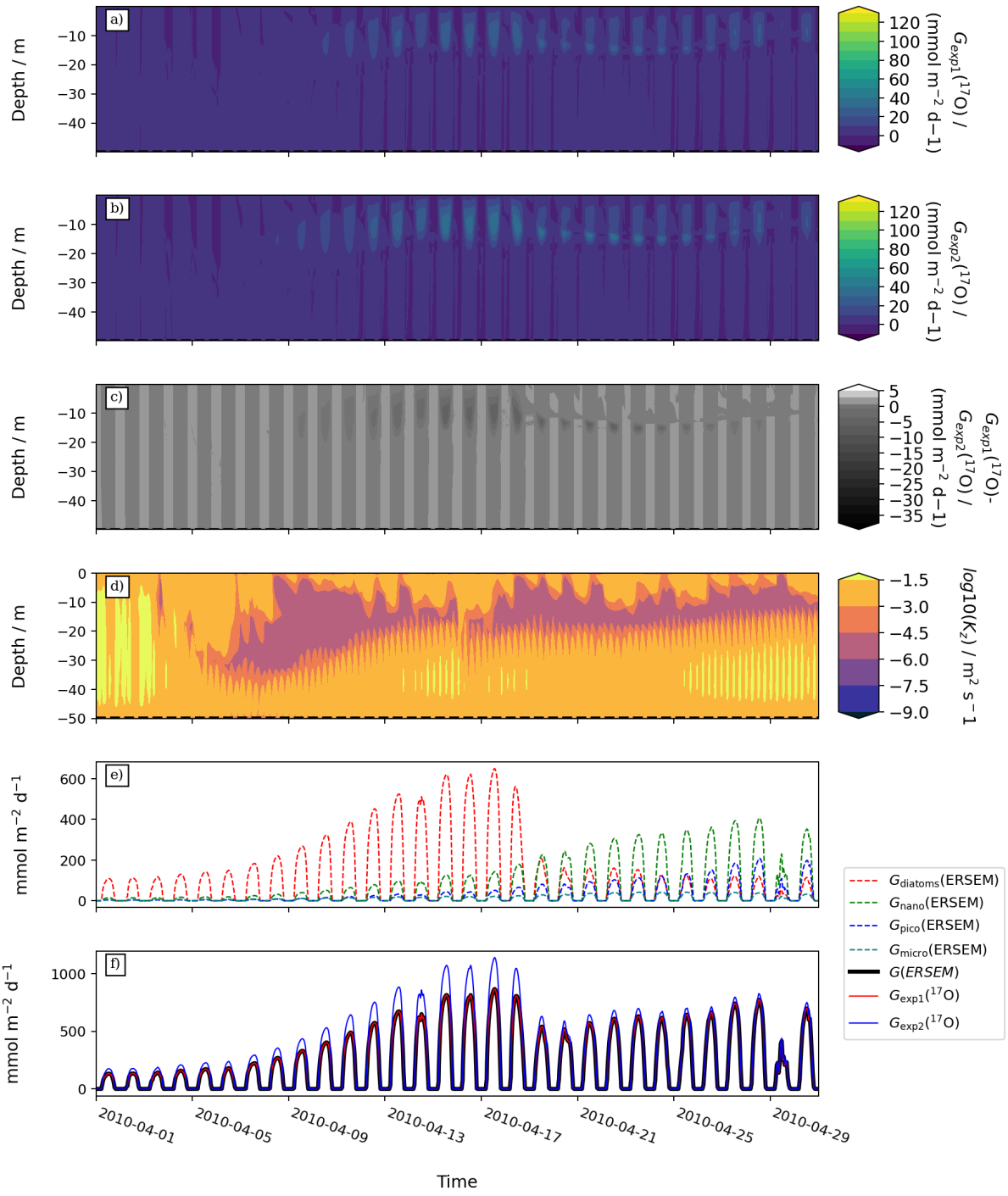

Figure 64: Effects of group specific $\delta_P(^iO)$ values on modelled $^{17}\Delta$. a) $^{17}\Delta$ calculated using VSMOW as photosynthetic endmember for all functional groups ($^{17}\Delta_P$ = 140 ppm; Table 6). b) $^{17}\Delta$ calculated using $^{17}\Delta_P$ = 188 ppm and $^{17}\Delta_P$ = 140 ppm for the other groups (Table 6). c) Difference between a) and b). d) Vertical diffusivity of heat in $\log_{10}$ scale. e) Group-specific gross production integrated over the whole water column. f) Target values for gross oxygen production G(ERSEM) (black) compared against $G_{exp1}(^{17}O)$ (red), and $G_{exp2}(^{17}O)$ (blue).

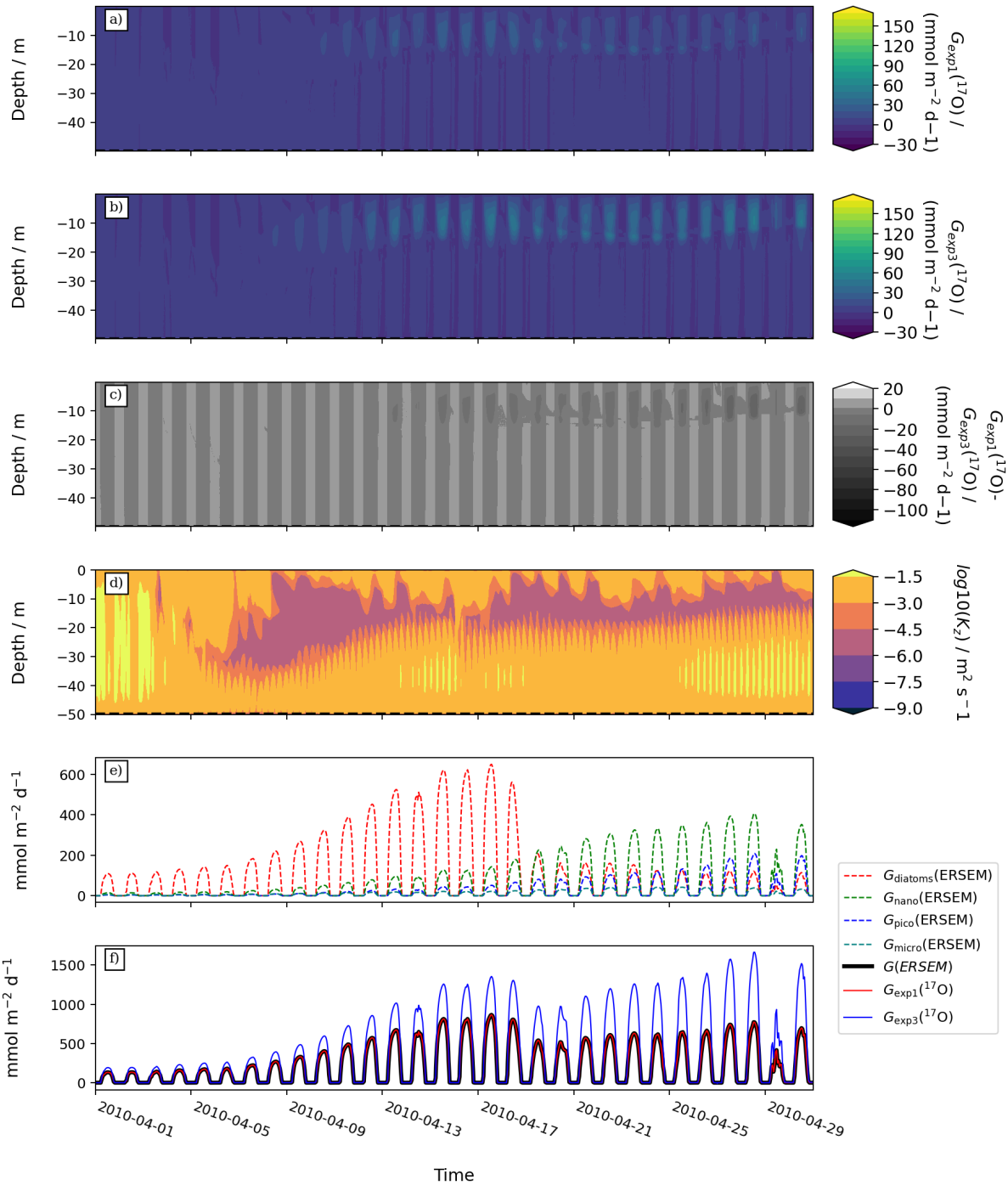

Figure 65: Effects of group specific $\delta_P(^iO)$ values on modelled $^{17}\Delta$. a) $^{17}\Delta$ calculated using VSMOW as photosynthetic endmember for all functional groups ($^{17}\Delta_P$ = 140 ppm; Table 6). b) $^{17}\Delta$ calculated using species-specific $^{17}\Delta_P$ values for four different phytoplankton function groups (Table 6). c) Difference between a) and b). d) Vertical diffusivity of heat in $\log_{10}$ scale. e) Group-specific gross production integrated over the whole water column. f) Target values for gross oxygen production G(ERSEM) (black) compared against $G_{exp1}(^{17}O)$ (red), and $G_{exp3}(^{17}O)$ (blue).

4.6 Discussion

4.6.1 Q1: Uncertainties derived from steady-state assumption at L4

In the first experiment we showed that the $G_{SS}(^{17}O)$ error was 2 orders of magnitude higher than $G(^{17}O)$ when the sampling time interval matched the simulation time step. Instead, when the sampling was set to 7 days, matching the sampling strategy adopted by Gloël, (2012), $G_{SS}(^{17}O)$ error was 53 % higher than $G(^{17}O)$. This result demonstrated that a sampling interval of 7 days does not fully integrate the timescale of air-sea gas exchange and that the time disequilibrium term $F_n(^{17}O)$ is required for gross oxygen production estimates.

Results also showed that gross production influences dissolved oxygen isotope ratios over varying time scales depending on the physical state of the water column where samples are taken. Results for $G_{SS}(^{17}O)$ particularly struggle to detect the onset, duration and magnitude of spring blooms which in some cases go undetected (e.g., spring 2010). Nicholson et al. (2014) showed that the omission of the time disequilibrium leads to an underestimation of G during spring blooms and an overestimate during summer. Our results confirm this and show that the bias may vary in different years and the diagnosed spring peak may be delayed with respect to actual values (Figure 55d). This confirms what was shown in the previous chapter with $N(O_2/Ar)$, i.e., that there is always a time lag between the peak in the prognostic and diagnostic production rates.

Nicholson et al. (2014) showed that $G_{SS}(^{17}O)$ overestimates G by 62 % in autumn. Our results confirm this overestimate at the end of the growing season. This error coincides with the breakdown of stratification and associated full water column ventilation. As shown in Figure 54c, $^{17}\Delta$ is conserved if isolated form air-sea gas exchange. This means that during a growing season coinciding with strong stratification, the isotope effect of gross production accumulates in bottom waters (at least in a one-dimensional system). Then, when bottom waters are ventilated at the end of stratification, the tracer signature is lost to the atmosphere resulting in a $G_{SS}(^{17}O)$ peak, which could lead to confounding interpretations. If sampling intervals are taken at timescale shorter than the oxygen residence time, this effect is buffered by the $F_n(^{17}O)$ term (Figure 56d).

4.6.2 Q2: $G(^{17}O)$ sensitivity to integration depth in shallow dynamic waters such as L4

When calculating $G(^{17}O)$ in temperate shelf seas, two physical environments need to be taken into consideration: the surface and the bottom mixed layers. In the surface layer, the isotopic composition of oxygen is primarily affected by production, vertical diffusivity, and air-sea gas exchange on a time scale of weeks. This is particularly true during the spring bloom at the surface when most of the $^{17}\Delta$ signal is readily lost to the atmosphere or penetrates below into the forming thermocline instead of accumulating within the surface mixed layer (Figure 54c). $F_n(^{17}O)$ is a function of integration depth (z_{int}) and time disequilibrium ($d\delta(^iO)/dt$); therefore, it only plays a marginal role when z_{int} = 2 m (Figure 57a). Therefore, measurements along cruise tracks inferring $G_{SS}(^{17}O)$ can achieve good results If vertical diffusivity can be estimated together with the vertical gradients of $\delta(^{17}O)$ and $\delta(^{18}O)$ crossing a shallow integration depth (Figure 57a).

In the bottom mixed layer, $^{17}\Delta$ increases when photosynthesis is still active but isolated from ventilation. The euphotic depth was on average at 28 m, deeper than the surface mixed layer depth (15 m). Therefore, $^{17}\Delta$ increased in the bottom mixed layer across the growing season, leading to overestimates of $G(^{17}O)$ in autumn as discussed in the previous section. The autumn bias, which is a consequence of the change in the physical state of the water column, can be corrected with accurate measurements of vertical diffusivity if the integration depth is set to represent the surface mixed layer. A disadvantage of this strategy is that vertical diffusivity is notoriously difficult to measure and often parametrised (Seguro et al., 2019). Another disadvantage of integrating the surface waters is that they only carry 16 % of the total pelagic gross oxygen production (Table 7). Instead, if integration depth includes the euphotic depth or more the autumn bias can be corrected with the time disequilibrium term (Figure 57c), but this requires a measurement time-series.

4.6.3 Q3: Determination of the optimal sampling interval

The sensitivity test on sampling frequency along time dimension showed that the ideal sampling resolution for $G(^{17}O)$ at L4 (once a week) is coarser than the ideal sampling strategy for $N(O_2/Ar)$ reported in the previous chapter (once a day). In this case, samples taken every week were least affected by noise due to measurement uncertainty. As in Chapter 3, the term that suffered most from noise was $F_n(^{17}O)$. Values of $\Delta_{RMS}G$ in

Figure 62b and Figure 55b were almost identical while all other panels containing $F_n(^{17}O)$ were dominated by random error. $F_n(^{17}O)$ is particularly affected by random error because it includes a time derivative resulting in sharp gradients along the time axis. Such calculation is done using $\delta(^{i}O)$ values which suffer from experimental error more than concentrations resulting in even sharper time gradients than seen in chapter 3. This result suggests that estimates of $G(^{17}O)$ can be easily included into the weekly monitoring programme taking place at L4 station (Smyth et al., 2010).

4.6.4 Q4: Uncertainty originating from oxygen fractionation during photosynthesis

The last set of experiments results indicated that assuming homogeneity in photosynthetic end members ($\delta_P(^{i}O)$) when calculating $G(^{17}O)$ can result in overestimates of gross oxygen production up to +300 mmol m^{-2} d^{-1} (Figure 64f and Figure 65f). This was also highlighted by $^{17}\Delta$, showing systematic overestimates within the thermocline from spring to autumn (up to +10 ppm).

Using species-specific photosynthetic oxygen isotope fractionation in $G(^{17}O)$ calculations was not addressed here, and this has the potential to be explored in future works. Luz and Barkan (2011) recommend using $\delta_P(^{17}O) = -10.126$ and $\delta_P(^{18}O) = -20.014$ to achieve proper estimates of gross oxygen production. Such values were derived as the average of $\delta_P(^{i}O)$ from three datasets (Helman et al., 2005; Eisenstadt et al., 2010; Barkan and Luz, 2011). The same approach was used in several subsequent studies (Hamme et al., 2012; Nicholson et al., 2012; Juranek and Quay, 2013; Stanley et al., 2015; Manning et al., 2017; Li et al., 2022). However, most of the literature seems to ignore is that the values were calculated from flask cultures (therefore suffering the bottle effect) and using certain species that are not very representative of marine functional groups (e.g., *Synechocystis* used to represent cyanobacteria is a fresh water species that acts differently if cultivated in seawater; Iijima et al., 2015), or present very peculiar phenotypic plasticity (e.g., *Phaeodactylum tricornutum* used to represent all diatoms is the only species that can grow in the absence of silicon; Chuang et al., 2014). At present there is scarcity of observational studies involving marine species-specific fractionation during photosynthesis, and given the substantial error associated with $G(^{17}O)$, these are essential for better estimates of gross production, which – in

combination with marine ecosystem models – can increase our understanding of pelagic metabolic rates within complex dynamic systems such as shelf seas.

4.7 Conclusions

In conclusion, this study shows for the first time the implementation of oxygen triple isotopologue scheme within the ERSEM model.

4.7.1 Q1: Uncertainties derived from steady-state assumption at L4

Using an observing simulation system experiment (OSSE) this study represents a guideline for the establishment of a time series station, in dynamic temperate shelf sea waters, measuring the three oxygen isotopologues as proxy for gross oxygen production ($G(^{17}O)$). This work was done at L4 station in the Western English Channel as case study. The main results showed that the establishment of a discrete sampling strategy will allow the calculation of $G(^{17}O)$ as non-steady-state flux reducing the prediction error by 53 %.

4.7.2 Q2: $G(^{17}O)$ sensitivity to integration depth in shallow dynamic waters such as L4

Sampling should take into consideration the integration of the whole water column instead of the surface mixed layer on contrary to what is done in open ocean applications. This sampling strategy will greatly avoid substantial systematic error represented by the contribution of vertical transport flux ($F_v(^{17}O)$), which is notoriously difficult to measure, often parametrised and has major impact at turbulent depths.

4.7.3 Q3: Determination of the optimal sampling interval

Results shown that at the selection of sampling intervals has significant impact to $G(^{17}O)$ error and ideal sampling interval needs to consider sampling error. In the case of L4, samples should be ideally taken once per week, after applying random error to oxygen concentrations for the three isotopologues. This sampling frequency matches the ongoing sampling routine being place at L4 station facilitating the inclusion of $G(^{17}O)$ method. $G(^{17}O)$ calculated with this sampling strategy, however, suffers overestimates in autumn associated to the end of stratification time and full water column turnover.

4.7.4 Q4: Uncertainty originating from oxygen fractionation during photosynthesis

$G(^{17}O)$ estimates need to take into consideration the photosynthetic fractionation of oxygen isotopes since assuming no fractionation during photosynthesis and wrong parametrisation can cause substantial error in $G(^{17}O)$. Luz and Barkan (2011) recommend using $\delta_P(^{17}O) = -10.126$ and $\delta_P(^{18}O) = -20.014$ to achieve proper estimates of gross oxygen production, representing the average of all $\delta_P(^{i}O)$ ever observed and published so far. However, such values are based on *in vitro* cultures of non-marine phytoplankton in certain cases and thus could not be representative for shelf sea applications.

4.7.5 Future remarks

From our study we were unable to assess the influence of lateral transport given the 1D nature of ERSEM-FABM-GOTM. L4 is considerably affected by lateral transport (Smyth et al., 2010) and thus it important to investigate the importance of advection to $^{17}\Delta$ and $G(^{17}O)$ especially in autumn, which according to our results, is a period that usually lead to substantial overestimates. This can be achieved by coupling our version of ERSEM, which includes the triple oxygen isotope scheme, to a physical regional model that solves transport in the horizontal direction (3D) at high resolution such as the Nucleus for European Modelling of the Ocean (NEMO) (Skákala et al., 2018).

Finally, L4 station holds a long-lasting time series of phytoplankton species succession and at present, there is a lack of observations for species specific photosynthetic isotopic fractionations representative of temperate marine shelf seas in general and L4 specifically. Future work at L4 station has the potential to improve the accuracy of $G(^{17}O)$ by considering phytoplankton community structure with species-specific $\delta_P(^{17}O)$ and $\delta_P(^{18}O)$ values.

Chapter 5: Conclusions and future work

The overall aim of this thesis was to address gaps in the knowledge of shelf-sea pelagic net (N) and gross (G) community production. This aim was split into two specific objectives:

1) To generate the first dataset of dissolved triple oxygen isotopes ($^{17}\Delta$) and oxygen-to-argon saturation anomaly ($\Delta(O_2/Ar)$) measurements as a proxy for net ($N(O_2/Ar)$) and gross ($G(^{17}O)$) oxygen production across the North Sea

2) To use an ecosystem model to investigate the robustness of $N(O_2/Ar)$ and $G(^{17}O)$ estimates in a shelf sea environment with respect to simplifying assumptions.

5.1 Measurements of pelagic net metabolic rates in the North Sea during late summer 2019

$N(O_2/Ar)$ and $G(^{17}O)$ were estimated from waters samples collected across the North Sea during the *RV Cefas Endeavour* Groundfish Survey (CEND12/19, 7 August to 5 September 2019). This provided the first dataset of triple oxygen isotopes and oxygen/argon saturation anomalies in the North Sea and added new information on the distribution of late summer production and remineralisation.

5.1.1 Research questions and summary of the results

What is the net metabolic state (producing, consuming, or in balance) in the North Sea surface waters during late summer?

> Overall, surface waters were in metabolic balance during a particularly warm late summer in August 2019 ($N_{SS}(O_2/Ar)$ = (–3±40) mmol m^{-2} d^{-1}).

Do net and gross community production change with latitude?

> The spatial distribution for both $N_{SS}(O_2/Ar)$ and $G_{SS}(^{17}O)$ varied from south to north and between stratified and non-stratified waters.
>
> Southern stations off the Thames Estuary, Wadden Sea and German Bight were O_2-supersaturated ((3.5±0.5) %), highly productive ($G_{SS}(^{17}O)$ = (360±110) mmol m^{-2} d^{-1}), and net heterotrophic ($N_{SS}(O_2/Ar)$ = –5±18) mmol m^{-2} d^{-1}).
>
> The central North Sea showed the highest $G_{SS}(^{17}O)$: (500±90) mmol m^{-2} d^{-1} in the west, and (471±10) mmol m^{-2} d^{-1} in the east. Deep chlorophyll *a* maxima

were not encountered in this region suggesting that the observed production rates were representative of the overall water column (bearing in mind that all estimates neglect lateral transport).

Net autotrophy was observed in the northern North Sea ($N_{SS}(O_2/Ar)$ = (10±6) mmol m^{-2} d^{-1}). The associated gross production $G_{SS}(^{17}O)$ = 244±61 mmol m^{-2} d^{-1}) is most likely an overestimate due to shoaling of high-$^{17}\Delta$ waters.

What is the net metabolic balance in the most productive area of the North Sea?

The $G_{SS}(^{17}O)$ maxima found in the central North Sea coincided with highly variable $N_{SS}(O_2/Ar)$ values: The western zone was net heterotrophic ($N_{SS}(O_2/Ar)$ = (–29±21) mmol m^{-2} d^{-1}), while the eastern zone was net autotrophic ($N_{SS}(O_2/Ar)$ = (9±10) mmol m^{-2} d^{-1}). This suggested that – with $G_{SS}(^{17}O)$ being similar in the west and east – respiration was even higher in the west, especially close to the Humber Estuary. This could possibly be due to remineralisation of organic material resuspended from the seabed.

5.1.2 Future work

Future investigation could integrate time series data to routine spatial measurements in targeted locations prone to advection (e.g., Southern Bight) and entrainment (e.g., north-eastern North Sea) to calculate the fluxes from adjacent waters. Alternatively, implementing $N(O_2/Ar)$ and $G(^{17}O)$ in marine ecosystem models coupled to a regional ocean model could be used to calculate advection and vertical transport.

5.2 Using the ERSEM model to determine best practice for net and gross community production measurements at station L4, Western English Channel

Using an observing simulation system experiment (OSSE), this study represents a guideline for the establishment of a time series station, in dynamic temperate shelf sea waters, for measuring $N(O_2/Ar)$ and $G(^{17}O)$. This work was done at L4 station in the Western English Channel as case study.

5.2.3 Research questions and summary of the results

What is the relative error for $N(O_2/Ar)$ and $G(^{17}O)$ resulting from the steady-state assumption at Station L4?

The main results showed that the establishment of a discrete sampling strategy will allow the calculation of $G(^{17}O)$ and $N(O_2/Ar)$ as non-steady-state flux reducing the prediction error by 53 % and 75 %, respectively. When steady-state was assumed, the timing and magnitude of production peaks during the spring bloom were found to be in error relative to the exact values.

What is the $N(O_2/Ar)$ and $G(^{17}O)$ sensitivity to integration depth in shallow dynamic waters such as L4?

Sampling should take into consideration the integration of the whole water column instead of the surface mixed layer on contrary to what is done in open ocean applications. This sampling strategy will greatly avoid substantial systematic error represented by the contribution of vertical transport flux (F_v), which is notoriously difficult to measure, often parametrised and has major impact at turbulent depths.

What is the optimal sampling frequency for establishing a $N(O_2/Ar)$ and $G(^{17}O)$ time-series at Station L4?

Changing the sampling strategy used by Gloël (2012) (weekly samples) to hourly would have decreased the predicting error by 1 order of magnitude and the correlation to N(ERSEM) would have improved by a factor of 3. Hourly scale variability data for $N(O_2/Ar)$ could be successfully collected by installing a membrane inlet mass spectrometer (MIMS) (Kaiser *et al*., 2005) at L4 (Smyth et al., 2010). A MIMS setup for shelf sea applications was described by Seguro et al. (2019).

The chosen sampling interval has a significant impact on $G(^{17}O)$ and the ideal sampling interval needs to consider experimental measurement error. Bearing the influence of the latter in mind, samples should ideally be taken every 9 days. This sampling frequency is similar to the ongoing sampling routine at station L4 (7 days), facilitating the inclusion of the $G(^{17}O)$ method. When steady-state is assumed with this sampling strategy, $G_{SS}(^{17}O)$ suffers overestimates in autumn associated with the end of stratification and full water column turnover.

What is the relative error in $G(^{17}O)$ derived from varying oxygen isotope fractionation during photosynthesis?

$G(^{17}O)$ estimates need to take into consideration the photosynthetic fractionation of oxygen isotopes since assuming no fractionation during photosynthesis and wrong parametrisation can cause substantial error in $G(^{17}O)$. Luz and Barkan (2011) recommend using $\delta_P(^{17}O) = -10.126$ and $\delta_P(^{18}O) = -20.014$ to achieve proper estimates of gross oxygen production, representing the average of all $\delta_P(^{i}O)$ ever observed and published so far. However, such values are based on *in vitro* cultures of non-marine phytoplankton in certain cases and may not be representative of shelf sea communities.

5.2.4 Future work

Our study was unable to assess the influence of lateral transport given the 1-D nature of ERSEM-FABM-GOTM. L4 is considerably affected by lateral transport (Smyth et al., 2010) and thus it important to investigate the role of advection for $^{17}\Delta$, $G(^{17}O)$, and $N(O_2/Ar)$, especially in autumn, which according to our results, is a period that usually displays substantial $G(^{17}O)$ overestimates. This can be achieved by coupling our version of ERSEM, which includes the triple oxygen isotope and argon schemes, to a physical regional model that solves transport in the horizontal direction (3-D) at high resolution such as the Nucleus for European Modelling of the Ocean (NEMO) (Skákala et al., 2018).

Finally, L4 station holds a long-lasting time series of phytoplankton species succession, but at present, there is a lack of species-specific photosynthetic isotopic fractionations representative of temperate marine shelf seas in general and L4 specifically. Future work at L4 station has the potential to greatly improve accuracy of $G(^{17}O)$ estimates if phytoplankton community characterisations are associated with measurements of $\delta_P(^{17}O)$ and $\delta_P(^{18}O)$.

References

Alvera-Azcárate, A., Van der Zande, D., Barth, A., Troupin, C., Martin, S., Beckers, J.-M., 2021. Analysis of 23 Years of Daily Cloud-Free Chlorophyll and Suspended Particulate Matter in the Greater North Sea. Front. Mar. Sci. 8, 707632. https://doi.org/10.3389/fmars.2021.707632

Aoki, N., Ishidoya, S., Matsumoto, N., Watanabe, T., Shimosaka, T., Murayama, S., 2019. Preparation of primary standard mixtures for atmospheric oxygen measurements with less than 1 μmol mol−1 uncertainty for oxygen molar fractions. Atmospheric Meas. Tech. 12, 2631–2646. https://doi.org/10.5194/amt-12-2631-2019

Barkan, E., Luz, B., 2011. The relationships among the three stable isotopes of oxygen in air, seawater and marine photosynthesis. Rapid Commun. Mass Spectrom. 25, 2367–2369. https://doi.org/10.1002/rcm.5125

Bastardie, F., Brown, E.J., Andonegi, E., Arthur, R., Beukhof, E., Depestele, J., Döring, R., Eigaard, O.R., García-Barón, I., Llope, M., Mendes, H., Piet, G., Reid, D., 2021. A Review Characterizing 25 Ecosystem Challenges to Be Addressed by an Ecosystem Approach to Fisheries Management in Europe. Front. Mar. Sci. 7, 629186. https://doi.org/10.3389/fmars.2020.629186

Bean, T.P., Greenwood, N., Beckett, R., Biermann, L., Bignell, J.P., Brant, J.L., Copp, G.H., Devlin, M.J., Dye, S., Feist, S.W., Fernand, L., Foden, D., Hyder, K., Jenkins, C.M., van der Kooij, J., Kröger, S., Kupschus, S., Leech, C., Leonard, K.S., Lynam, C.P., Lyons, B.P., Maes, T., Nicolaus, E.E.M., Malcolm, S.J., McIlwaine, P., Merchant, N.D., Paltriguera, L., Pearce, D.J., Pitois, S.G., Stebbing, P.D., Townhill, B., Ware, S., Williams, O., Righton, D., 2017. A Review of the Tools Used for Marine Monitoring in the UK: Combining Historic and Contemporary Methods with Modeling and Socioeconomics to Fulfill Legislative Needs and Scientific Ambitions. Front. Mar. Sci. 4, 263. https://doi.org/10.3389/fmars.2017.00263

Belkin, I.M., Cornillon, P.C., Sherman, K., 2009. Fronts in Large Marine Ecosystems. Prog. Oceanogr. 81, 223–236. https://doi.org/10.1016/j.pocean.2009.04.015

Belmonte Rivas, M., Stoffelen, A., 2019. Characterizing ERA-Interim and ERA5 surface wind biases using ASCAT. Ocean Sci. 15, 831–852. https://doi.org/10.5194/os-15-831-2019

Bender, M., Grande, K., Johnson, K., Marra, J., Williams, P.J.L.B., Sieburth, J., Pilson, M., Langdon, C., Hitchcock, G., Orchardo, J., Hunt, C., Donaghay, P., Heinemann, K., 1987. A comparison of four methods for determining planktonic community production. Limnol. Oceanogr. https://doi.org/10.4319/lo.1987.32.5.1085

Bendtsen, J., Richardson, K., 2020. New production across the shelf-edge in the northeastern North Sea during the stratified summer period. J. Mar. Syst. 211, 103414. https://doi.org/10.1016/j.jmarsys.2020.103414

Benson, B.B., Krause, D., 1984. The concentration and isotopic fractionation of oxygen dissolved in freshwater and seawater in equilibrium with the

atmosphere1: Oxygen solubility in seawater. Limnol. Oceanogr. 29, 620–632. https://doi.org/10.4319/lo.1984.29.3.0620

Benson, B.B., Krause, D., Peterson, M.A., 1979. The solubility and isotopic fractionation of gases in dilute aqueous solution. I. Oxygen. J. Solut. Chem. 8, 655–690. https://doi.org/10.1007/BF01033696

Boyes, S.J., Elliott, M., 2014. Marine legislation – The ultimate 'horrendogram': International law, European directives & national implementation. Mar. Pollut. Bull. 86, 39–47. https://doi.org/10.1016/j.marpolbul.2014.06.055

Brion, N., Baeyens, W., De Galan, S., Elskens, M., Laane, R.W.P.M., 2004. The North Sea: source or sink for nitrogen and phosphorus to the Atlantic Ocean? Biogeochemistry 68, 277–296. https://doi.org/10.1023/B:BIOG.0000031041.38663.aa

Bristow, L.A., Jickells, T.D., Weston, K., Marca-Bell, A., Parker, R., Andrews, J.E., 2013. Tracing estuarine organic matter sources into the southern North Sea using C and N isotopic signatures. Biogeochemistry 113, 9–22. https://doi.org/10.1007/s10533-012-9758-4

Bruggeman, J., Bolding, K., 2014. A general framework for aquatic biogeochemical models. Environ. Model. Softw. 61, 249–265. https://doi.org/10.1016/j.envsoft.2014.04.002

Burchard, H., Bolding, K., Ruiz-Villarreal, M., 1999. GOTM, a general ocean turbulence model. Theory, implementation and test cases.

Bushinsky, S.M., Emerson, S., 2015. Marine biological production from in situ oxygen measurements on a profiling float in the subarctic Pacific Ocean. Glob. Biogeochem. Cycles 29, 2050–2060. https://doi.org/10.1002/2015GB005251

Butenschön, M., Clark, J., Aldridge, J.N., Allen, J.I., Artioli, Y., Blackford, J., Bruggeman, J., Cazenave, P., Ciavatta, S., Kay, S., Lessin, G., van Leeuwen, S., van der Molen, J., de Mora, L., Polimene, L., Sailley, S., Stephens, N., Torres, R., 2016. ERSEM 15.06: a generic model for marine biogeochemistry and the ecosystem dynamics of the lower trophic levels. Geosci. Model Dev. 9, 1293–1339. https://doi.org/10.5194/gmd-9-1293-2016

Butenschön, M., Zavatarelli, M., Vichi, M., 2012. Sensitivity of a marine coupled physical biogeochemical model to time resolution, integration scheme and time splitting method. Ocean Model. 52–53, 36–53. https://doi.org/10.1016/j.ocemod.2012.04.008

Cadée, G.C., Hegeman, J., 2002. Phytoplankton in the Marsdiep at the end of the 20th century; 30 years monitoring biomass, primary production, and Phaeocystis blooms. J. Sea Res. 48, 97–110. https://doi.org/10.1016/S1385-1101(02)00161-2

Cadée, G.C., Hegeman, J., 1986. Seasonal and annual variation in phaeocystis pouchetii (haptophyceae) in the westernmost inlet of the Wadden Sea during the 1973 to 1985 period. Neth. J. Sea Res. 20, 29–36. https://doi.org/10.1016/0077-7579(86)90058-X

Capuzzo, E., Lynam, C.P., Barry, J., Stephens, D., Forster, R.M., Greenwood, N., McQuatters-Gollop, A., Silva, T., van Leeuwen, S.M., Engelhard, G.H., 2018.

A decline in primary production in the North Sea over 25 years, associated with reductions in zooplankton abundance and fish stock recruitment. Glob. Change Biol. 24, e352–e364. https://doi.org/10.1111/gcb.13916

Carozza, D.A., Bianchi, D., Galbraith, E.D., 2019. Metabolic impacts of climate change on marine ecosystems: Implications for fish communities and fisheries. Glob. Ecol. Biogeogr. 28, 158–169. https://doi.org/10.1111/geb.12832

Cassar, N., Barnett, B.A., Bender, M.L., Kaiser, J., Hamme, R.C., Tilbrook, B., 2009. Continuous high-frequency dissolved O 2/Ar Measurements by Equilibrator Inlet Mass Spectrometry. Anal. Chem. https://doi.org/10.1021/ac802300u

Cassar, N., Nicholson, D., Khatiwala, S., Cliff, E., 2021. Decomposing the Oxygen Signal in the Ocean Interior: Beyond Decomposing Organic Matter. Geophys. Res. Lett. 48. https://doi.org/10.1029/2021GL092621

Chuang, C.-Y., Santschi, P.H., Jiang, Y., Ho, Y.-F., Quigg, A., Guo, L., Ayranov, M., Schumann, D., 2014. Important role of biomolecules from diatoms in the scavenging of particle-reactive radionuclides of thorium, protactinium, lead, polonium, and beryllium in the ocean: A case study with *Phaeodactylum tricornutum*. Limnol. Oceanogr. 59, 1256–1266. https://doi.org/10.4319/lo.2014.59.4.1256

Copernicus Climate Change Service (C3S), 2017. ERA5: Fifth generation of ECMWF atmospheric reanalyses of the global climate [WWW Document]. Copernic. Clim. Change Serv. Clim. Data Store CDS. URL https://cds.climate.copernicus.eu/cdsapp#!/home (accessed 7.6.20).

Craig, H., Hayward, T., 1987. Oxygen Supersaturation in the Ocean: Biological Versus Physical Contributions. Science 235, 199–202. https://doi.org/10.1126/science.235.4785.199

Daewel, U., Schrum, C., 2013. Simulating long-term dynamics of the coupled North Sea and Baltic Sea ecosystem with ECOSMO II: Model description and validation. J. Mar. Syst. 119–120, 30–49. https://doi.org/10.1016/j.jmarsys.2013.03.008

Daszykowski, M., Kaczmarek, K., Vander Heyden, Y., Walczak, B., 2007. Robust statistics in data analysis — A review. Chemom. Intell. Lab. Syst. 85, 203–219. https://doi.org/10.1016/j.chemolab.2006.06.016

Davey, N.G., Krogh, E.T., Gill, C.G., 2011. Membrane-introduction mass spectrometry (MIMS). TrAC Trends Anal. Chem. 30, 1477–1485. https://doi.org/10.1016/j.trac.2011.05.003

Desmit, X., Nohe, A., Borges, A.V., Prins, T., De Cauwer, K., Lagring, R., Van der Zande, D., Sabbe, K., 2020. Changes in chlorophyll concentration and phenology in the North Sea in relation to de-eutrophication and sea surface warming. Limnol. Oceanogr. 65, 828–847. https://doi.org/10.1002/lno.11351

Desprez, M., Rybarczyk, H., Wilson, J.G., Ducrotoy, J.P., Sueur, F., Olivesi, R., Elkaim, B., 1992. Biological impact of eutrophication in the bay of somme and the induction and impact of anoxia. Neth. J. Sea Res. 30, 149–159. https://doi.org/10.1016/0077-7579(92)90054-I

Diaz, R.J., Rosenberg, R., 2008. Spreading Dead Zones and Consequences for Marine Ecosystems. Science 321, 926–929. https://doi.org/10.1126/science.1156401

Dickinson, A.G., 1996. Determination of dissolved oxygen in seawater by Winkler titration, World Ocean Circulation Experiment, in: WOCE Operations Manual. Woods Hole, Massachussetts, USA, pp. 1–13.

Duarte, C.M., Conley, D.J., Carstensen, J., Sánchez-Camacho, M., 2009. Return to Neverland: Shifting Baselines Affect Eutrophication Restoration Targets. Estuaries Coasts 32, 29–36. https://doi.org/10.1007/s12237-008-9111-2

Ducklow, H.W., Harris, R.P., 1993. Introduction to the JGOFS North Atlantic bloom experiment. Deep Sea Res. Part II Top. Stud. Oceanogr. 40, 1–8. https://doi.org/10.1016/0967-0645(93)90003-6

Eisenstadt, D., Barkan, E., Luz, B., Kaplan, A., 2010. Enrichment of oxygen heavy isotopes during photosynthesis in phytoplankton. Photosynth. Res. 103, 97–103. https://doi.org/10.1007/s11120-009-9518-z

Emeis, K.-C., van Beusekom, J., Callies, U., Ebinghaus, R., Kannen, A., Kraus, G., Kröncke, I., Lenhart, H., Lorkowski, I., Matthias, V., Möllmann, C., Pätsch, J., Scharfe, M., Thomas, H., Weisse, R., Zorita, E., 2015. The North Sea — A shelf sea in the Anthropocene. J. Mar. Syst. 141, 18–33. https://doi.org/10.1016/j.jmarsys.2014.03.012

Emerson, S., 1987. Seasonal oxygen cycles and biological new production in surface waters of the subarctic Pacific Ocean. J. Geophys. Res. 92, 6535. https://doi.org/10.1029/JC092iC06p06535

Emerson, S., Quay, P., Stump, C., Wilbur, D., Knox, M., 1991. O_2 , Ar, N_2 , and ^{222} Rn in surface waters of the subarctic Ocean: Net biological O_2 production. Glob. Biogeochem. Cycles 5, 49–69. https://doi.org/10.1029/90GB02656

EU, 2008. Directive 2008/56/EC of the European Parliament and of the Council of 17 June 2008 establishing a framework for community action in the field of marine environmental policy (Marine Strategy Framework Directive). Off J Eur Union 164, 19–40.

EU, 2000. Directive 2000/60/EC of the European Parliament and of the Council of 23 October 2000 establishing a framework for community action in the field of water policy. Off J Eur Communities 327, 1–72.

Falkowski, P.G., Raven, J.A., 2007. Aquatic photosynthesis, 2nd ed. ed. Princeton University Press, Princeton.

Fernand, L., Weston, K., Morris, T., Greenwood, N., Brown, J., Jickells, T., 2013. The contribution of the deep chlorophyll maximum to primary production in a seasonally stratified shelf sea, the North Sea. Biogeochemistry 113, 153–166. https://doi.org/10.1007/s10533-013-9831-7

Ferreira, J.G., Andersen, J.H., Borja, A., Bricker, S.B., Camp, J., Cardoso da Silva, M., Garcés, E., Heiskanen, A.-S., Humborg, C., Ignatiades, L., Lancelot, C., Menesguen, A., Tett, P., Hoepffner, N., Claussen, U., 2011. Overview of eutrophication indicators to assess environmental status within the European Marine Strategy Framework Directive. Estuar. Coast. Shelf Sci. 93, 117–131. https://doi.org/10.1016/j.ecss.2011.03.014

Fishwick, J., 2018. CTD profiles (depth, pressure, temperature, salinity, potential temperature, density, fluorescence, transmissance, downwelling PAR, dissolved oxygen concentration) binned to 0.5 m and 0.25 m at sites L4 and E1 in the Western English Channel between January 2002 and December 2015. https://doi.org/10.5285/54820666-B5DF-266E-E053-6C86ABC02283

Gaarder, T., 1927. Investigations of the Production of Phytoplankton in the Oslo Fjord. Rapp. Procès-Verbaux Réun. Int. Pour L'exploration Mer 42, 1–48.

Gaichas, S., Skaret, G., Falk-Petersen, J., Link, J.S., Overholtz, W., Megrey, B.A., Gjøsæter, H., Stockhausen, W.T., Dommasnes, A., Friedland, K.D., Aydin, K., 2009. A comparison of community and trophic structure in five marine ecosystems based on energy budgets and system metrics. Prog. Oceanogr. 81, 47–62. https://doi.org/10.1016/j.pocean.2009.04.005

García, H.E., Gordon, L.I., 1992. Oxygen solubility in seawater: Better fitting equations. Limnol. Oceanogr. 37, 1307–1312. https://doi.org/10.4319/lo.1992.37.6.1307

Ghosh, P., Brand, W.A., 2003. Stable isotope ratio mass spectrometry in global climate change research. Int. J. Mass Spectrom. 228, 1–33. https://doi.org/10.1016/S1387-3806(03)00289-6

Giesbrecht, K.E., Hamme, R.C., Emerson, S.R., 2012. Biological productivity along Line P in the subarctic northeast Pacific: In situ versus incubation-based methods. Glob. Biogeochem. Cycles 26, 2012GB004349. https://doi.org/10.1029/2012GB004349

Glibert, P.M., Allen, J.I., Bouwman, A.F., Brown, C.W., Flynn, K.J., Lewitus, A.J., Madden, C.J., 2010. Modeling of HABs and eutrophication: Status, advances, challenges. J. Mar. Syst. 83, 262–275. https://doi.org/10.1016/j.jmarsys.2010.05.004

Glibert, P.M., Maranger, R., Sobota, D.J., Bouwman, L., 2014. The Haber Bosch–harmful algal bloom (HB–HAB) link. Environ. Res. Lett. 9, 105001. https://doi.org/10.1088/1748-9326/9/10/105001

Gloël, J., 2012. Triple oxygen isotopes and oxygen/argon ratio measurements to enhance coastal and open ocean production/respiration comparisons. University of East Anglia, Norwich.

Gonzalez-Pola, C.; Larsen, K. M. H. ; Fratantoni, P.; And Beszczynska-M?Ller, A. (Eds.), 2019. ICES Report on Ocean Climate 2018. https://doi.org/10.17895/ICES.PUB.5461

González-Posada, A.M., 2012. Biological oxygen production from oxygen-to-argon ratios and oxygen isotopologues in the Atlantic Ocean. University of East Anglia, Norwich.

Greenwood, N., Parker, E.R., Fernand, L., Sivyer, D.B., Weston, K., Painting, S.J., Kröger, S., Forster, R.M., Lees, H.E., Mills, D.K., Laane, R.W.P.M., 2010. Detection of low bottom water oxygen concentrations in the North Sea; implications for monitoring and assessment of ecosystem health. Biogeosciences 7, 1357–1373. https://doi.org/10.5194/bg-7-1357-2010

Große, F., Kreus, M., Lenhart, H.-J., Pätsch, J., Pohlmann, T., 2017. A Novel Modeling Approach to Quantify the Influence of Nitrogen Inputs on the

Oxygen Dynamics of the North Sea. Front. Mar. Sci. 4, 383. https://doi.org/10.3389/fmars.2017.00383

Guy, R.D., Fogel, M.L., Berry, J.A., 1993. Photosynthetic Fractionation of the Stable Isotopes of Oxygen and Carbon. Plant Physiol. 101, 37–47. https://doi.org/10.1104/pp.101.1.37

Håkanson, L., Bryhn, A.C., Eklund, J.M., 2007. Modelling phosphorus and suspended particulate matter in Ringkøbing Fjord in order to understand regime shifts. J. Mar. Syst. 68, 65–90. https://doi.org/10.1016/j.jmarsys.2006.10.010

Halpern, B.S., Frazier, M., Potapenko, J., Casey, K.S., Koenig, K., Longo, C., Lowndes, J.S., Rockwood, R.C., Selig, E.R., Selkoe, K.A., Walbridge, S., 2015. Spatial and temporal changes in cumulative human impacts on the world's ocean. Nat. Commun. 6, 7615. https://doi.org/10.1038/ncomms8615

Hamme, R.C., Cassar, N., Lance, V.P., Vaillancourt, R.D., Bender, M.L., Strutton, P.G., Moore, T.S., DeGrandpre, M.D., Sabine, C.L., Ho, D.T., Hargreaves, B.R., 2012a. Dissolved O_2/Ar and other methods reveal rapid changes in productivity during a Lagrangian experiment in the Southern Ocean. J. Geophys. Res. Oceans 117, 1–19. https://doi.org/10.1029/2011JC007046

Hamme, R.C., Emerson, S.R., 2006. Constraining bubble dynamics and mixing with dissolved gases: Implications for productivity measurements by oxygen mass balance. J. Mar. Res. 64, 73–95. https://doi.org/10.1357/002224006776412322

Hamme, R.C., Emerson, S.R., 2004. The solubility of neon, nitrogen and argon in distilled water and seawater. Deep Sea Res. Part Oceanogr. Res. Pap. 51, 1517–1528. https://doi.org/10.1016/j.dsr.2004.06.009

Harris, C.R., Millman, K.J., van der Walt, S.J., Gommers, R., Virtanen, P., Cournapeau, D., Wieser, E., Taylor, J., Berg, S., Smith, N.J., Kern, R., Picus, M., Hoyer, S., van Kerkwijk, M.H., Brett, M., Haldane, A., del Río, J.F., Wiebe, M., Peterson, P., Gérard-Marchant, P., Sheppard, K., Reddy, T., Weckesser, W., Abbasi, H., Gohlke, C., Oliphant, T.E., 2020. Array programming with NumPy. Nature 585, 357–362. https://doi.org/10.1038/s41586-020-2649-2

Harris, G.P., Griffiths, F.B., Thomas, D.P., 1989. Light and dark uptake and loss of 14C: methodological problems with productivity measurements in oceanic waters. Hydrobiologia 173, 95–105. https://doi.org/10.1007/BF00015519

Harris, P.T., 2020. The fate of microplastic in marine sedimentary environments: A review and synthesis. Mar. Pollut. Bull. 158, 111398. https://doi.org/10.1016/j.marpolbul.2020.111398

Haskell, W.Z., Fleming, J.C., 2018. Concurrent estimates of carbon export reveal physical biases in ΔO2/Ar-based net community production estimates in the Southern California Bight. J. Mar. Syst. 183, 23–31. https://doi.org/10.1016/j.jmarsys.2018.03.008

Haskell, W.Z., Prokopenko, M.G., Hammond, D.E., Stanley, R.H.R., Sandwith, Z.O., 2017. Annual cyclicity in export efficiency in the inner Southern California Bight. Glob. Biogeochem. Cycles 31, 357–376. https://doi.org/10.1002/2016GB005561

Helman, Y., Barkan, E., Eisenstadt, D., Luz, B., Kaplan, A., 2005. Fractionation of the Three Stable Oxygen Isotopes by Oxygen-Producing and Oxygen-Consuming Reactions in Photosynthetic Organisms. Plant Physiol. 138, 2292–2298. https://doi.org/10.1104/pp.105.063768

Hendricks, M.B., Bender, M.L., Barnett, B.A., 2004. Net and gross O2 production in the southern ocean from measurements of biological O2 saturation and its triple isotope composition. Deep Sea Res. Part Oceanogr. Res. Pap. 51, 1541–1561. https://doi.org/10.1016/j.dsr.2004.06.006

Hinrichs, I., Gouretski, V., Pätsch, J., Emeis, K.-C., Stammer, D., 2017. North Sea Biogeochemical Climatology (Version 1.1) [WWW Document]. URL https://www.cen.uni-hamburg.de/en/icdc/data/ocean/nsbc.html#zitat

Holt, J., Butenschön, M., Wakelin, S.L., Artioli, Y., Allen, J.I., 2012. Oceanic controls on the primary production of the northwest European continental shelf: model experiments under recent past conditions and a potential future scenario. Biogeosciences 9, 97–117. https://doi.org/10.5194/bg-9-97-2012

Holt, J., Schrum, C., Cannaby, H., Daewel, U., Allen, I., Artioli, Y., Bopp, L., Butenschon, M., Fach, B.A., Harle, J., Pushpadas, D., Salihoglu, B., Wakelin, S., 2016. Potential impacts of climate change on the primary production of regional seas: A comparative analysis of five European seas. Prog. Oceanogr. 140, 91–115. https://doi.org/10.1016/j.pocean.2015.11.004

Holt, J., Wakelin, S., Lowe, J., Tinker, J., 2010. The potential impacts of climate change on the hydrography of the northwest European continental shelf. Prog. Oceanogr. 86, 361–379. https://doi.org/10.1016/j.pocean.2010.05.003

Hsu, S.A., Meindl, E.A., Gilhousen, D.B., 1994. Determining the Power-Law Wind-Profile Exponent under Near-Neutral Stability Conditions at Sea. J. Appl. Meteorol. 33, 757–765. https://doi.org/10.1175/1520-0450(1994)033<0757:DTPLWP>2.0.CO;2

Hull, T., Greenwood, N., Birchill, A., Beaton, A., Palmer, M., Kaiser, J., 2021. Simultaneous assessment of oxygen- and nitrate-based net community production in a temperate shelf sea from a single ocean glider. Biogeosciences 18, 6167–6180. https://doi.org/10.5194/bg-18-6167-2021

Hydes, D.J., Gowen, R.J., Holliday, N.P., Shammon, T., Mills, D., 2004. External and internal control of winter concentrations of nutrients (N, P and Si) in north-west European shelf seas. Estuar. Coast. Shelf Sci. 59, 151–161. https://doi.org/10.1016/j.ecss.2003.08.004

Iijima, H., Nakaya, Y., Kuwahara, A., Hirai, M.Y., Osanai, T., 2015. Seawater cultivation of freshwater cyanobacterium Synechocystis sp. PCC 6803 drastically alters amino acid composition and glycogen metabolism. Front. Microbiol. 6. https://doi.org/10.3389/fmicb.2015.00326

Izett, R.W., Manning, C.C., Hamme, R.C., Tortell, P.D., 2018. Refined Estimates of Net Community Production in the Subarctic Northeast Pacific Derived From ΔO_2 /Ar Measurements With N_2O-Based Corrections for Vertical Mixing. Glob. Biogeochem. Cycles 32, 326–350. https://doi.org/10.1002/2017GB005792

Janssen, F., Schrum, C., Backhaus, J.O., 1999. A climatological data set of temperature and salinity for the Baltic Sea and the North Sea. Dtsch. Hydrogr. Z. 51, 5–245. https://doi.org/10.1007/BF02933676

Johnson, D., 2008. Environmental indicators: their utility in meeting the OSPAR Convention's regulatory needs. ICES J. Mar. Sci. 65, 1387–1391. https://doi.org/10.1093/icesjms/fsn154

Jolliff, J.K., Kindle, J.C., Shulman, I., Penta, B., Friedrichs, M.A.M., Helber, R., Arnone, R.A., 2009. Summary diagrams for coupled hydrodynamic-ecosystem model skill assessment. J. Mar. Syst. 76, 64–82. https://doi.org/10.1016/j.jmarsys.2008.05.014

Jonsson, B.F., Doney, S.C., Dunne, J., Bender, M., 2013a. Evaluation of the Southern Ocean O_2/Ar-based NCP estimates in a model framework. J. Geophys. Res. Biogeosciences 118, 385–399. https://doi.org/10.1002/jgrg.20032

Juranek, L.W., Quay, P.D., 2013. Using Triple Isotopes of Dissolved Oxygen to Evaluate Global Marine Productivity. Annu. Rev. Mar. Sci. 5, 503–524. https://doi.org/10.1146/annurev-marine-121211-172430

Jurikova, H., Abe, O., Shiah, F.-K., Liang, M.-C., 2022. New constraints on biological production and mixing processes in the South China Sea from triple isotope composition of dissolved oxygen. Biogeosciences 19, 2043–2058. https://doi.org/10.5194/bg-19-2043-2022

Kaiser, J., 2011. Technical note: Consistent calculation of aquatic gross production from oxygen triple isotope measurements. Biogeosciences 8, 1793–1811. https://doi.org/10.5194/bg-8-1793-2011

Kaiser, J., Abe, O., 2012. Reply to Nicholson's comment on "Consistent calculation of aquatic gross production from oxygen triple isotope measurements" by Kaiser (2011). Biogeosciences 9, 2921–2933. https://doi.org/10.5194/bg-9-2921-2012

Kaiser, J., Reuer, M.K., Barnett, B., Bender, M.L., 2005. Marine productivity estimates from continuous O2/Ar ratio measurements by membrane inlet mass spectrometry. Geophys. Res. Lett. 32, 1–5. https://doi.org/10.1029/2005GL023459

Kaiser, J., Röckmann, T., 2008. Correction of mass spectrometric isotope ratio measurements for isobaric isotopologues of O_2, CO, CO_2, N_2O and SO_2. Rapid Commun. Mass Spectrom. 22, 3997–4008. https://doi.org/10.1002/rcm.3821

Kerby, T.K., Cheung, W.W.L., Engelhard, G.H., 2012. The United Kingdom's role in North Sea demersal fisheries: a hundred year perspective. Rev. Fish Biol. Fish. 22, 621–634. https://doi.org/10.1007/s11160-012-9261-y

Knight, J.R., Folland, C.K., Scaife, A.A., 2006. Climate impacts of the Atlantic Multidecadal Oscillation. Geophys. Res. Lett. 33, L17706. https://doi.org/10.1029/2006GL026242

Knox, M., Quay, P.D., Wilbur, D., 1992. Kinetic isotopic fractionation during air-water gas transfer of O_2, N_2, CH_4, and H_2. J. Geophys. Res. 97, 20335. https://doi.org/10.1029/92JC00949

Kraberg, A., Kieb, U., Peters, S., Wiltshire, K.H., 2019. An updated phytoplankton check-list for the Helgoland Roads time series station with eleven new records of diatoms and dinoflagellates. Helgol. Mar. Res. 73, 9. https://doi.org/10.1186/s10152-019-0528-8

Lane, G.A., Dole, M., 1956. Fractionation of Oxygen Isotopes during Respiration. Science 123, 574–576. https://doi.org/10.1126/science.123.3197.574

Laws, E.A., 1991. Photosynthetic quotients, new production and net community production in the open ocean. Deep Sea Res. Part Oceanogr. Res. Pap. 38, 143–167. https://doi.org/10.1016/0198-0149(91)90059-O

Laws, E.A., Landry, M.R., Barber, R.T., Campbell, L., Dickson, M.-L., Marra, J., 2000. Carbon cycling in primary production bottle incubations: inferences from grazing experiments and photosynthetic studies using and in the Arabian Sea. Deep Sea Res. Part II Top. Stud. Oceanogr. 47, 1339–1352. https://doi.org/10.1016/S0967-0645(99)00146-0

Le Fèvre, J., 1987. Aspects of the Biology of Frontal Systems, in: Advances in Marine Biology. Elsevier, pp. 163–299. https://doi.org/10.1016/S0065-2881(08)60109-1

Lee, A.J., 1980. Chapter 14 North Sea: Physical Oceanography, in: Elsevier Oceanography Series. Elsevier, pp. 467–493. https://doi.org/10.1016/S0422-9894(08)71359-X

Lefebvre, A., Guiselin, N., Barbet, F., Artigas, F.L., 2011. Long-term hydrological and phytoplankton monitoring (1992–2007) of three potentially eutrophic systems in the eastern English Channel and the Southern Bight of the North Sea. ICES J. Mar. Sci. 68, 2029–2043. https://doi.org/10.1093/icesjms/fsr149

Legendre, L., Demers, S., Yentsch, C.M., Yentsch, C.S., 1983. The ^{14} C method: Patterns of dark CO_2 fixation and DCMU correction to replace the dark bottle1,2: ^{14} C method: DCMU correction. Limnol. Oceanogr. 28, 996–1003. https://doi.org/10.4319/lo.1983.28.5.0996

Li, B., Hu, H., Berelson, W.M., Adkins, J.F., Yeung, L.Y., 2022. On the Use of Dissolved Oxygen Isotopologues as Biogeochemical Tracers in the Northeast Pacific Ocean. J. Geophys. Res. Oceans 127. https://doi.org/10.1029/2022JC018617

Linkov, I., Satterstrom, F.K., Kiker, G., Batchelor, C., Bridges, T., Ferguson, E., 2006. From comparative risk assessment to multi-criteria decision analysis and adaptive management: Recent developments and applications. Environ. Int. 32, 1072–1093. https://doi.org/10.1016/j.envint.2006.06.013

Llope, M., Chan, K.-S., Ciannelli, L., Reid, P.C., Stige, L.C., Stenseth, N.C., 2009. Effects of environmental conditions on the seasonal distribution of phytoplankton biomass in the North Sea. Limnol. Oceanogr. 54, 512–524. https://doi.org/10.4319/lo.2009.54.2.0512

Loder, J.W., Drinkwater, K.F., Oakey, N.S., Horne, E.P.W., 1994. Circulation, hydrographic structure and mixing at tidal fronts: the view from Georges Bank, in: Charnock, H., Dyer, K.R., Huthnance, J.M., Liss, P.S., Simpson, J.H., Tett, P.B. (Eds.), Understanding the North Sea System. Springer

Netherlands, Dordrecht, pp. 69–82. https://doi.org/10.1007/978-94-011-1236-9_6

Loveday, B.R., Smyth, T., Akpinar, A., Hull, T., Inall, M.E., Kaiser, J., Queste, B.Y., Tobermann, M., Williams, C.A.J., Palmer, M.R., 2022. Application of a new net primary production methodology: a daily to annual-scale data set for the North Sea, derived from autonomous underwater gliders and satellite Earth observation. Earth Syst. Sci. Data 14, 3997–4016. https://doi.org/10.5194/essd-14-3997-2022

Luz, B., Barkan, E., 2011. Proper estimation of marine gross O_2 production with $^{17}O/^{16}O$ and $^{18}O/^{16}O$ ratios of dissolved O_2: Estimation of marine gross O_2 prod. Geophys. Res. Lett. 38, n/a-n/a. https://doi.org/10.1029/2011GL049138

Luz, B., Barkan, E., 2009. Net and gross oxygen production from O_2/Ar, $^{17}O/^{16}O$ and $^{18}O/^{16}O$ ratios. Aquat. Microb. Ecol. 56, 133–145. https://doi.org/10.3354/ame01296

Luz, B., Barkan, E., 2005. The isotopic ratios $^{17}O/^{16}O$ and $^{18}O/^{16}O$ in molecular oxygen and their significance in biogeochemistry. Geochim. Cosmochim. Acta 69, 1099–1110. https://doi.org/10.1016/j.gca.2004.09.001

Luz, Boaz, Barkan, E., 2000. Assessment of oceanic productivity with the triple-isotope composition of dissolved oxygen. Science. https://doi.org/10.1126/science.288.5473.2028

Luz, B., Barkan, E., Bender, M.L., Thiemens, M.H., Boering, K.A., 1999. Triple-isotope composition of atmospheric oxygen as a tracer of biosphere productivity. Nature 400, 547–550. https://doi.org/10.1038/22987

Luz, B., Barkan, E., Sagi, Y., Yacobi, Y.Z., 2002. Evaluation of community respiratory mechanisms with oxygen isotopes: A case study in Lake Kinneret. Limnol. Oceanogr. 47, 33–42. https://doi.org/10.4319/lo.2002.47.1.0033

Manning, C.C., Howard, E.M., Nicholson, D.P., Ji, B.Y., Sandwith, Z.O., Stanley, R.H.R., 2017. Revising Estimates of Aquatic Gross Oxygen Production by the Triple Oxygen Isotope Method to Incorporate the Local Isotopic Composition of Water: GOP ESTIMATES INCORPORATING H $_2$ O ISOTOPES. Geophys. Res. Lett. 44, 10,511-10,519. https://doi.org/10.1002/2017GL074375

Mathis, M., Elizalde, A., Mikolajewicz, U., 2019. The future regime of Atlantic nutrient supply to the Northwest European Shelf. J. Mar. Syst. 189, 98–115. https://doi.org/10.1016/j.jmarsys.2018.10.002

Mayzaud, P., Boutoute, M., Gasparini, S., Mousseau, L., Lefevre, D., 2005. Respiration in marine zooplankton-the other side of the coin: CO $_2$ production. Limnol. Oceanogr. 50, 291–298. https://doi.org/10.4319/lo.2005.50.1.0291

Mehler, A.H., 1951. Studies on reactions of illuminated chloroplasts. Arch. Biochem. Biophys. 33, 65–77. https://doi.org/10.1016/0003-9861(51)90082-3

Mészáros, L., van der Meulen, F., Jongbloed, G., El Serafy, G., 2021. Climate Change Induced Trends and Uncertainties in Phytoplankton Spring Bloom Dynamics. Front. Mar. Sci. 8, 669951. https://doi.org/10.3389/fmars.2021.669951

Moore, C.M., Mills, M.M., Arrigo, K.R., Berman-Frank, I., Bopp, L., Boyd, P.W., Galbraith, E.D., Geider, R.J., Guieu, C., Jaccard, S.L., Jickells, T.D., La Roche, J., Lenton, T.M., Mahowald, N.M., Marañón, E., Marinov, I., Moore, J.K., Nakatsuka, T., Oschlies, A., Saito, M.A., Thingstad, T.F., Tsuda, A., Ulloa, O., 2013. Processes and patterns of oceanic nutrient limitation. Nat. Geosci. 6, 701–710. https://doi.org/10.1038/ngeo1765

Nicholson, D., Stanley, R.H.R., Doney, S.C., 2014. The triple oxygen isotope tracer of primary productivity in a dynamic ocean model: Triple oxygen isotopes in a global model. Glob. Biogeochem. Cycles 28, 538–552. https://doi.org/10.1002/2013GB004704

Nicholson, D.P., Stanley, R.H.R., Barkan, E., Karl, D.M., Luz, B., Quay, P.D., Doney, S.C., 2012. Evaluating triple oxygen isotope estimates of gross primary production at the Hawaii Ocean Time-series and Bermuda Atlantic Time-series Study sites: MODELING TRIPLE OXYGEN ISOTOPES. J. Geophys. Res. Oceans 117, n/a-n/a. https://doi.org/10.1029/2010JC006856

Nielsen, E.S., 1952. The Use of Radio-active Carbon (C14) for Measuring Organic Production in the Sea. ICES J. Mar. Sci. 18, 117–140. https://doi.org/10.1093/icesjms/18.2.117

Nightingale, P.D., Malin, G., Law, C.S., Watson, A.J., Liss, P.S., Liddicoat, M.I., Boutin, J., Upstill-Goddard, R.C., 2000. In situ evaluation of air-sea gas exchange parameterizations using novel conservative and volatile tracers. Glob. Biogeochem. Cycles 14, 373–387. https://doi.org/10.1029/1999GB900091

Odum, H.T., 1956. Primary Production in Flowing Waters1. Limnol. Oceanogr. 1, 102–117. https://doi.org/10.4319/lo.1956.1.2.0102

OSPAR Commission, 2003. OSPAR Integrated Report 2003 on the Eutrophication Status of the OSPAR Maritime Area Based Upon the First Application of the Comprehensive Procedure, Eutrophication Series.

OSPAR Commission, Axe, P., Claussen, P., Leujak, W., Stephens, M., Prins, T., Ruiter, H., 2017. Third Integrated Report on the Eutrophication Status of the OSPAR Maritime Area Eutrophication Series.

Painting, S.J., Forster, R.M., 2013. Marine Ecosystem Connections: essential indicators of healthy, productive and biologically diverse seas. Biogeochemistry 113, 1–7. https://doi.org/10.1007/s10533-013-9838-0

Pätsch, J., Radach, G., 1997. Long-term simulation of the eutrophication of the North Sea: temporal development of nutrients, chlorophyll and primary production in comparison to observations. J. Sea Res. 38, 275–310. https://doi.org/10.1016/S1385-1101(97)00051-8

Pauly, D., Christensen, V., Guénette, S., Pitcher, T.J., Sumaila, U.R., Walters, C.J., Watson, R., Zeller, D., 2002. Towards sustainability in world fisheries. Nature 418, 689–695. https://doi.org/10.1038/nature01017

Peinert, R., Saure, A., Stegmann, P., Stienen, C., Haardt, H., Smetacek, V., 1982. Dynamics of primary production and sedimentation in a coastal ecosystem. Neth. J. Sea Res. 16, 276–289. https://doi.org/10.1016/0077-7579(82)90036-9

Phillips, N.A., 1957. A coordinate system having some special advantages for numerical forecasting. J. Meteorol. 14, 184–185. https://doi.org/10.1175/1520-0469(1957)014<0184:ACSHSS>2.0.CO;2

Pingree, R.D., Griffiths, D.K., 1978. Tidal fronts on the shelf seas around the British Isles. J. Geophys. Res. 83, 4615. https://doi.org/10.1029/JC083iC09p04615

Pinkau, A., Schiele, K.S., 2021. Strategic Environmental Assessment in marine spatial planning of the North Sea and the Baltic Sea – An implementation tool for an ecosystem-based approach? Mar. Policy 130, 104547. https://doi.org/10.1016/j.marpol.2021.104547

Possenti, L., Skjelvan, I., Atamanchuk, D., Tengberg, A., Humphreys, M.P., Loucaides, S., Fernand, L., Kaiser, J., 2021. Norwegian Sea net community production estimated from O_2 and prototype CO_2 optode measurements on a Seaglider. Ocean Sci. 17, 593–614. https://doi.org/10.5194/os-17-593-2021

Powley, H.R., Bruggeman, J., Hopkins, J., Smyth, T., Blackford, J., 2020. Sensitivity of Shelf Sea Marine Ecosystems to Temporal Resolution of Meteorological Forcing. J. Geophys. Res. Oceans 125. https://doi.org/10.1029/2019JC015922

Pratt, D.M., Berkson, H., 1959. Two Sources of Error in the Oxygen Light and Dark Bottle Method1. Limnol. Oceanogr. 4, 328–334. https://doi.org/10.4319/lo.1959.4.3.0328

Prokopenko, M.G., Pauluis, O.M., Granger, J., Yeung, L.Y., 2011. Exact evaluation of gross photosynthetic production from the oxygen triple-isotope composition of O_2 : Implications for the net-to-gross primary production ratios: evaluation of GPP from O_2 isotopes. Geophys. Res. Lett. 38, n/a-n/a. https://doi.org/10.1029/2011GL047652

Queste, B.Y., Fernand, L., Jickells, T.D., Heywood, K.J., 2013. Spatial extent and historical context of North Sea oxygen depletion in August 2010. Biogeochemistry 113, 53–68. https://doi.org/10.1007/s10533-012-9729-9

Radach, G., Pätsch, J., 2007. Variability of continental riverine freshwater and nutrient inputs into the North Sea for the years 1977–2000 and its consequences for the assessment of eutrophication. Estuaries Coasts 30, 66–81. https://doi.org/10.1007/BF02782968

Reuer, M.K., Barnett, B.A., Bender, M.L., Falkowski, P.G., Hendricks, M.B., 2007. New estimates of Southern Ocean biological production rates from O_2/Ar ratios and the triple isotope composition of O_2. Deep Sea Res. Part Oceanogr. Res. Pap. 54, 951–974. https://doi.org/10.1016/j.dsr.2007.02.007

Rinko-III sensor description [WWW Document], n.d. . JFE Adventech Co Ltd. URL https://www.jfe-advantech.co.jp/eng/ocean/rinko/rinko3.html (accessed 4.29.20).

Rodhe, J., 1996. On the dynamics of the large-scale circulation of the Skagerrak. J. Sea Res. 35, 9–21. https://doi.org/10.1016/S1385-1101(96)90731-5

Sarmiento, J.L., Gruber, N., 2006. Ocean Biogeochemical Dynamics, 1st ed. Princeton University Press, Princeton.

Schlesinger, M.E., Ramankutty, N., 1994. An oscillation in the global climate system of period 65–70 years. Nature 367, 723–726. https://doi.org/10.1038/367723a0

Seguro, I., Marca, A.D., Painting, S.J., Shutler, J.D., Suggett, D.J., Kaiser, J., 2019. High-resolution net and gross biological production during a Celtic Sea spring bloom. Prog. Oceanogr. 177, 101885. https://doi.org/10.1016/j.pocean.2017.12.003

Seguro, I., Marca, A.D., Painting, S.J., Shutler, J.D., Suggett, D.J., Kaiser, J., 2018. High-resolution net and gross biological production during a Celtic Sea spring bloom. Prog. Oceanogr. https://doi.org/10.1016/j.pocean.2017.12.003

Seguro Requejo, M.I., 2017. Shelf-sea gross and net production estimates from triple oxygen isotopes and oxygen-argon ratios in relation with phytoplankton physiology. University of East Anglia, Norwich.

Sharples, J., Mayor, D.J., Poulton, A.J., Rees, A.P., Robinson, C., 2019. Shelf Sea Biogeochemistry: Nutrient and carbon cycling in a temperate shelf sea water column. Prog. Oceanogr. 177, 102182. https://doi.org/10.1016/j.pocean.2019.102182

Sharples, J., Moore, M.C., Rippeth, T.P., Holligan, P.M., Hydes, D.J., Fisher, N.R., Simpson, J.H., 2001. Phytoplankton distribution and survival in the thermocline. Limnol. Oceanogr. 46, 486–496. https://doi.org/10.4319/lo.2001.46.3.0486

Sims, R.P., Bedington, M., Schuster, U., Watson, A.J., Kitidis, V., Torres, R., Findlay, H.S., Fishwick, J.R., Brown, I., Bell, T.G., 2022. Tidal mixing of estuarine and coastal waters in the western English Channel is a control on spatial and temporal variability in seawater CO_2. Biogeosciences 19, 1657–1674. https://doi.org/10.5194/bg-19-1657-2022

Skákala, J., Ford, D., Brewin, R.J.W., McEwan, R., Kay, S., Taylor, B., Mora, L., Ciavatta, S., 2018. The Assimilation of Phytoplankton Functional Types for Operational Forecasting in the Northwest European Shelf. J. Geophys. Res. Oceans 123, 5230–5247. https://doi.org/10.1029/2018JC014153

Smaal, A.C., Schellekens, T., van Stralen, M.R., Kromkamp, J.C., 2013. Decrease of the carrying capacity of the Oosterschelde estuary (SW Delta, NL) for bivalve filter feeders due to overgrazing? Aquaculture 404–405, 28–34. https://doi.org/10.1016/j.aquaculture.2013.04.008

Smith, W.O., Zhang, W.G., Hirzel, A., Stanley, R.M., Meyer, M.G., Sosik, H., Alatalo, P., Oliver, H., Sandwith, Z., Crockford, E.T., Peacock, E.E., Mehta, A., McGillicuddy, D.J., 2021. A Regional, Early Spring Bloom of *Phaeocystis pouchetii* on the New England Continental Shelf. J. Geophys. Res. Oceans 126, 2020JC016856. https://doi.org/10.1029/2020JC016856

Smyth, T.J., Fishwick, J.R., AL-Moosawi, L., Cummings, D.G., Harris, C., Kitidis, V., Rees, A., Martinez-Vicente, V., Woodward, E.M.S., 2010. A broad spatio-temporal view of the Western English Channel observatory. J. Plankton Res. 32, 585–601. https://doi.org/10.1093/plankt/fbp128

Southward, A.J., Langmead, O., Hardman-Mountford, N.J., Aiken, J., Boalch, G.T., Dando, P.R., Genner, M.J., Joint, I., Kendall, M.A., Halliday, N.C., Harris,

R.P., Leaper, R., Mieszkowska, N., Pingree, R.D., Richardson, A.J., Sims, D.W., Smith, T., Walne, A.W., Hawkins, S.J., 2004. Long-Term Oceanographic and Ecological Research in the Western English Channel, in: Advances in Marine Biology. Elsevier, pp. 1–105. https://doi.org/10.1016/S0065-2881(04)47001-1

Stanley, R.H.R., Kirkpatrick, J.B., Cassar, N., Barnett, B.A., Bender, M.L., 2010. Net community production and gross primary production rates in the western equatorial Pacific: Western Equatorial Pacific production. Glob. Biogeochem. Cycles 24, n/a-n/a. https://doi.org/10.1029/2009GB003651

Stanley, R.H.R., Sandwith, Z.O., Williams, W.J., 2015. Rates of summertime biological productivity in the Beaufort Gyre: A comparison between the low and record-low ice conditions of August 2011 and 2012. J. Mar. Syst. 147, 29–44. https://doi.org/10.1016/j.jmarsys.2014.04.006

Steckbauer, A., Duarte, C.M., Carstensen, J., Vaquer-Sunyer, R., Conley, D.J., 2011. Ecosystem impacts of hypoxia: thresholds of hypoxia and pathways to recovery. Environ. Res. Lett. 6, 025003. https://doi.org/10.1088/1748-9326/6/2/025003

Strang, G., 1968. On the Construction and Comparison of Difference Schemes. SIAM J. Numer. Anal. 5, 506–517. https://doi.org/10.1137/0705041

Teeter, L., Hamme, R.C., Ianson, D., Bianucci, L., 2018. Accurate Estimation of Net Community Production From O_2 /Ar Measurements. Glob. Biogeochem. Cycles. https://doi.org/10.1029/2017GB005874

Tett, P., Gowen, R., Mills, D., Fernandes, T., Gilpin, L., Huxham, M., Kennington, K., Read, P., Service, M., Wilkinson, M., Malcolm, S., 2007. Defining and detecting undesirable disturbance in the context of marine eutrophication. Mar. Pollut. Bull. 55, 282–297. https://doi.org/10.1016/j.marpolbul.2006.08.028

Tilstone, G.H., Land, P.E., Pardo, S., Kerimoglu, O., Van der Zande, D., 2023. Threshold indicators of primary production in the north-east Atlantic for assessing environmental disturbances using 21 years of satellite ocean colour. Sci. Total Environ. 854, 158757. https://doi.org/10.1016/j.scitotenv.2022.158757

Topcu, H.D., Brockmann, U.H., 2015. Seasonal oxygen depletion in the North Sea, a review. Mar. Pollut. Bull. 99, 5–27. https://doi.org/10.1016/j.marpolbul.2015.06.021

Uncles, R.J., Clark, J.R., Bedington, M., Torres, R., 2020. On sediment dispersal in the Whitsand Bay Marine Conservation Zone, in: Marine Protected Areas. Elsevier, pp. 599–629. https://doi.org/10.1016/B978-0-08-102698-4.00031-9

van Haren, H., Mills, D.K., Wetsteyn, L.P.M.J., 1998. Detailed observations of the phytoplankton spring bloom in the stratifying central North Sea. J. Mar. Res. 56, 655–680. https://doi.org/10.1357/002224098765213621

van Leeuwen, S., Tett, P., Mills, D., van der Molen, J., 2015. Stratified and nonstratified areas in the North Sea: Long-term variability and biological and policy implications: North Sea stratification regimes. J. Geophys. Res. Oceans 120, 4670–4686. https://doi.org/10.1002/2014JC010485

Vermaat, J.E., McQuatters-Gollop, A., Eleveld, M.A., Gilbert, A.J., 2008. Past, present and future nutrient loads of the North Sea: Causes and consequences. Estuar. Coast. Shelf Sci. 80, 53–59. https://doi.org/10.1016/j.ecss.2008.07.005

Volk, T., Hoffert, M.I., 2013. Ocean Carbon Pumps: Analysis of Relative Strengths and Efficiencies in Ocean-Driven Atmospheric CO_2 Changes, in: Sundquist, E.T., Broecker, W.S. (Eds.), Geophysical Monograph Series. American Geophysical Union, Washington, D. C., pp. 99–110. https://doi.org/10.1029/GM032p0099

Wanninkhof, R., 2014. Relationship between wind speed and gas exchange over the ocean revisited: Gas exchange and wind speed over the ocean. Limnol. Oceanogr. Methods 12, 351–362. https://doi.org/10.4319/lom.2014.12.351

Williams, P.J. leB., Jenkinson, N.W., 1982. A transportable microprocessor-controlled precise Winkler titration suitable for field station and shipboard use1. Limnol. Oceanogr. 27, 576–584. https://doi.org/10.4319/lo.1982.27.3.0576

Williams, P.J.L., 1981. Microbial contribution to overall marine plankton metabolism-direct measurements of respiration. Oceanologica Acta 4, 359–364.

Winkler, L.W., 1888. Die Bestimmung des im Wasser gelösten Sauerstoffes. Berichte Dtsch. Chem. Ges. 21, 2843–2854. https://doi.org/10.1002/cber.188802102122

Winther, N.G., Johannessen, J.A., 2006. North Sea circulation: Atlantic inflow and its destination. J. Geophys. Res. 111, C12018. https://doi.org/10.1029/2005JC003310

Zhao, C., Daewel, U., Schrum, C., 2019. Tidal impacts on primary production in the North Sea. Earth Syst. Dyn. 10, 287–317. https://doi.org/10.5194/esd-10-287-2019

Zhu, Z., Wang, J., Zhang, G., Liu, S., Zheng, S., Sun, X., Xu, D., Zhou, M., 2021. Using triple oxygen isotopes and oxygen-argon ratio to quantify ecosystem production in the mixed layer of northern South China Sea slope region. Acta Oceanol. Sin. 40, 1–15. https://doi.org/10.1007/s13131-021-1846-7